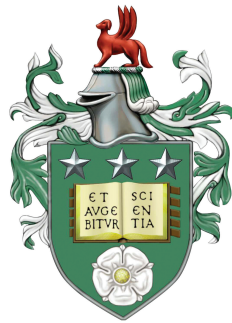


The Interaction of Astrophysical Flows with Clouds and Filaments



Kathryn Jane Alexandra Goldsmith

School of Physics and Astronomy

University of Leeds

Submitted in accordance with the requirements for the degree of
Doctor of Philosophy

February 2019

Declaration

The candidate confirms that the work submitted is her own, except where work which has formed part of jointly authored publications has been included. The contribution of the candidate and the other authors of this work has been explicitly indicated. The candidate confirms that appropriate credit has been given within this thesis where reference has been made to the work of others.

This copy has been supplied on the understanding that it is copyright material and that no quotation from the thesis may be published without proper acknowledgement.

© 2019 The University of Leeds and Kathryn Jane Alexandra Goldsmith

Preface

Within this thesis, some chapters have been based on work presented in the following jointly authored publications:

- I.** “The interaction of a magnetohydrodynamical shock with a filament”, K.J.A. Goldsmith, J.M. Pittard, 2016, MNRAS, 461, 578.
- II.** “A comparison of shock-cloud and wind-cloud interactions: the longer survival of clouds in winds”, K.J.A. Goldsmith, J.M. Pittard, 2017, MNRAS, 470, 2427.
- III.** “A comparison of shock-cloud and wind-cloud interactions: effect of increased cloud density contrast on cloud evolution”, K.J.A. Goldsmith, J.M. Pittard, 2018, MNRAS, 476, 2209.

Paper I forms the basis of Chapter 3. The magnetohydrodynamical code used to perform the simulations in this Chapter was written and developed by S.A.E.G. Falle. Routines setting up the initial conditions for the particular problem were written by J.M. Pittard. The primary author (K.J.A. Goldsmith) was responsible for small modifications to the code to enable the filament to be set up in a magnetic field. The primary author performed convergence studies, a resolution test, and the subsequent high-resolution simulations, analysed the data, and wrote the initial draft of the publication before incorporating comments from the co-author and reviewer into the final draft.

Papers II and III form the basis of Chapters 4 and 5. The hydrodynamical code used to perform the simulations in these chapters was written and developed by S.A.E.G. Falle. J.M. Pittard wrote the initial routines, and the primary author adapted these for the particular problem in each chapter. The simulations and analysis presented in these chapters were carried out by the primary author. The primary author also made small modifications to the code, wrote the initial draft of the publications, and then incorporated comments from the co-author and reviewers into the final drafts.

Acknowledgements

This thesis would not have been possible without the guidance, encouragement, and boundless patience of my supervisor, Julian Pittard, particularly when dealing with my incompetence when attempting to code. I have thoroughly enjoyed collaborating with him in the production of this and our published papers, even if much of my work was covered in red pen. Thanks are also due to Sam Falle for sharing his code.

In addition, I'd like to thank my fellow PhD students for keeping me sane on the few occasions I made it into the office. I'd also like to thank the staff and students of the College of the Resurrection, Mirfield, West Yorkshire for their patience and generosity in allowing me to complete this PhD even though I had inadvisedly begun training to be an Anglican priest several months before the submission of this thesis.

Finally, thanks go to my family and friends who have offered me their support and put up with me when everything (frequently) went wrong.

Thank you.

Abstract

This thesis presents numerical simulations of the interaction of winds and shocks with clouds and filaments. Firstly, the shock-driven evolution of a 3D filament in a magnetised medium is investigated by varying the shock Mach number, cloud density contrast (χ), magnetic field strength and orientation, and cloud aspect ratio and angle to the shock. The morphology and lifetime of the filament is compared between simulations and the conditions that best extend the lifetime of the filament (e.g. a mild shock and a perpendicular/oblique magnetic field) are noted. The orientation of the magnetic field has a significant effect on the lifetime of the filament. Moreover, filaments in a parallel magnetic field can survive for longer if they are orientated ‘broadside’ to the shock front.

Secondly, a comparison of shock-cloud and wind-cloud interactions with increasing wind Mach number at both low and high χ is presented. This is the first study to demonstrate Mach scaling in a wind-cloud study and differences between wind-cloud and shock-cloud simulations at low χ . It also notes the shorter normalised cloud mixing time for the wind case, as well as the lack of Mach number dependence for that time-scale and the normalised cloud drag time at higher χ . Additionally, there are significant morphological differences between the two processes, particularly in the progress of the shock through the cloud and in the formation of tails in the higher χ simulations.

Finally, previous shock-filament studies are extended into the isothermal regime. The most significant finding is the large variation in the normalised evolution of the

filament at high Mach numbers. Furthermore, the ‘three-rolled’ structure observed in previous adiabatic studies is present only in sideways-oriented filaments with $\chi = 10^2$.

Abbreviations

AMR	Adaptive Mesh Refinement
CNM	Cold Neutral Medium
GMC	Giant Molecular Cloud
HD	Hydrodynamic
HIM	Hot Ionised Medium
IR	Infrared
ISM	Interstellar Medium
KH	Kelvin-Helmholtz
MHD	Magnetohydrodynamic
PAH	Polycyclic Aromatic Hydrocarbon
RH	Rankine-Hugoniot
RM	Richtmyer-Meshkov
RT	Rayleigh-Taylor
SN	Supernova
SNR	Supernova Remnant
UV	Ultraviolet
WIM	Warm Ionised Medium
WNM	Warm Neutral Medium

Contents

1	Introduction	1
1.1	The Interstellar Medium	2
1.1.1	ISM phases	3
1.1.1.1	Atomic clouds	3
1.1.1.2	Molecular clouds	4
1.1.1.3	Ionised medium	6
1.1.1.4	Dust	9
1.1.2	Filamentary structures	10
1.2	Shocks in the ISM	12
1.2.1	Feedback processes	12
1.2.2	HD shocks	13
1.2.3	MHD shocks	15
1.2.4	Radiative shocks	17
1.3	Shock-cloud interactions	19
1.3.1	The shock-cloud problem	20
1.3.2	Early numerical studies	23
1.3.3	Adiabatic HD shock-cloud simulations	24
1.3.3.1	Non-spherical clouds	27
1.3.4	MHD shock-cloud simulations	30
1.3.5	Radiative/isothermal simulations	33

Contents

1.4	Wind-cloud interactions	36
1.4.1	Wind-cloud simulations	37
1.4.2	Other related numerical studies	39
1.5	Overview of this thesis	39
2	Numerical Methods	40
2.1	Basic equations	40
2.2	Finite volume method	42
2.3	The Riemann problem	45
2.3.1	Second order accuracy	49
2.4	Adaptive Mesh Refinement	50
2.5	MHD	51
3	Magnetohydrodynamic Filament Simulations	55
3.1	Introduction	55
3.2	Method	57
3.2.1	Numerical setup	57
3.2.1.1	Initial conditions	57
3.2.1.2	Global quantities	60
3.2.1.3	Timescales	61
3.2.2	Convergence studies	62
3.3	Results	65
3.3.1	Parallel field	69
3.3.1.1	Filament morphology	69
3.3.1.2	Effect of filament length and orientation on the evolution of the core mass	71
3.3.1.3	Effect of filament length and orientation on the mean velocity and the velocity dispersion	75

3.3.1.4	Effect of filament length and orientation on the mean density	76
3.3.1.5	χ dependence of the filament evolution	79
3.3.1.6	Mach dependence of the filament evolution	82
3.3.1.7	β_0 dependence of the filament evolution	83
3.3.2	Perpendicular field	85
3.3.2.1	Filament morphology	85
3.3.2.2	Effect of filament length and orientation on the evolution of the core mass	91
3.3.2.3	Effect of filament length and orientation on the mean velocity and the velocity dispersion	91
3.3.2.4	Effect of filament length and orientation on the mean density	93
3.3.2.5	χ dependence of the filament evolution	93
3.3.2.6	Mach dependence of the filament evolution	98
3.3.2.7	β_0 dependence of the filament evolution	98
3.3.3	Oblique field	99
3.3.3.1	Filament morphology	99
3.3.3.2	Effect of filament length and orientation on the core mass, mean velocity, velocity dispersion, and mean density	100
3.3.3.3	χ , M , and β_0 dependence of the filament evolution	103
3.3.4	Timescales	104
3.4	Discussion	108
3.4.1	Entrainment of filament material	109
3.5	Summary and Conclusions	111

4	A comparison of shock-cloud and wind-cloud interactions: the longer survival of clouds in winds	113
4.1	Introduction	113
4.2	The numerical setup	114
4.2.1	Initial conditions	115
4.2.2	The shock-cloud model	116
4.2.3	The wind-cloud model	117
4.2.4	Global quantities	118
4.2.5	Time-scales	119
4.3	Results	120
4.3.1	Stages	120
4.3.2	Shock-cloud interaction	121
4.3.3	Wind-cloud interaction	122
4.3.3.1	Comparison of wind-cloud and shock-cloud interactions	122
4.3.3.2	Effect of increasing M_{wind} on the evolution	125
4.3.4	Statistics	127
4.3.4.1	Cloud mass	127
4.3.4.2	Cloud velocity	131
4.3.4.3	Centre of mass of the cloud	132
4.3.4.4	Cloud shape	133
4.3.4.5	Time-scales	134
4.4	Discussion	136
4.4.1	Mach scaling	138
4.4.2	Longer survivability of clouds	139
4.5	Summary and Conclusions	140

5	A comparison of shock-cloud and wind-cloud interactions: effect of increased cloud density contrast on cloud evolution	142
5.1	Introduction	142
5.2	The numerical setup and initial conditions	144
5.3	Results	144
5.3.1	Shock-cloud interaction	145
5.3.2	Wind-cloud interaction	148
5.3.2.1	Comparison of wind-cloud and shock-cloud interactions	148
5.3.2.2	Effect of increasing M_{wind} on the evolution	150
5.3.3	Statistics	153
5.3.4	Time-scales	158
5.3.4.1	t_{drag}	158
5.3.4.2	t_{mix}	158
5.3.5	Comparison to existing literature	159
5.4	Summary and Conclusions	160
6	Isothermal shock-filament interactions	164
6.1	Introduction	164
6.2	Problem definition	165
6.2.1	Previous work	166
6.3	The numerical setup	168
6.3.1	Diagnostics	169
6.3.2	Dynamical time-scales	169
6.4	Results	169
6.4.1	Interaction of a filament with $\chi = 10^2$ and a sideways orientation with a shock of $M = 3$	170
6.4.2	Effect of filament orientation on the interaction	174

Contents

6.4.3	Mach number dependence	178
6.4.4	χ dependence	181
6.4.5	Statistics	182
6.4.5.1	Time-scales	190
6.5	Discussion	192
6.6	Summary and Conclusions	194
7	Conclusions	196
7.1	Summary	196
7.2	Future work	202
7.3	Concluding remarks	203
	References	204

List of figures

1.1	Image of the Rosette Nebula	8
1.2	Logarithmic H_α image of the western edge of the Cygnus Loop and H_α image showing the interaction of the shock front with an isolated cloud in the southwest region of the Cygnus Loop	21
1.3	Shock-sphere shadowgrams taken from an experimental study	22
1.4	Volumetric renderings of the log of the density of a spherical (left), aligned prolate (middle), and inclined prolate (right) cloud	28
1.5	Volumetric renderings of the cloud density for a parallel magnetic field (top) and isosurface and horizontal slice at $y = 0$ of the cloud density for a perpendicular magnetic field	32
2.1	Space-time diagram of the Riemann problem solution.	46
2.2	Example of an AMR grid.	50
3.1	The interaction at $t = 0t_{cs}$ for model <i>m10c1b1/4o45pa</i>	59
3.2	Convergence tests for 3D MHD simulations of a Mach 10 shock hitting a filament with density contrast $\chi = 10$ in a parallel field.	66
3.3	Resolution test for a Mach 10 shock overrunning a filament, using the initial setup shown in Fig. 3.1.	67

List of figures

3.4	Relative error versus spatial resolution for a number of global quantities measured from a shock-filament interaction with $\chi = 10$, $M = 10$, and $\beta_0 = 1$	67
3.5	The time evolution of the logarithmic density, scaled with respect to the ambient density, for model <i>m10c1b1l4o45pa</i>	71
3.6	The time evolution of the logarithmic density, scaled with respect to the ambient density, for model <i>m10c1b1l4o90pa</i>	72
3.7	The time evolution of the logarithmic density, scaled with respect to the ambient density, for model <i>m10c1b1l4o0pa</i>	73
3.8	3D volumetric renderings of models <i>m10c1b1l4o45pa</i> (top), <i>m10c1b1l4o90pa</i> (middle), and <i>m10c1b1l4o0pa</i> (bottom)	74
3.9	Time evolution of the core mass for (a) a filament with variable length and an orientation of 45° , and (b) $l = 4$ with variable orientation, in an initial parallel magnetic field.	75
3.10	Time evolution of the filament mean velocity for (a) a filament with variable length and an orientation of 45° , and (b) $l = 4$ with variable orientation, in an initial parallel magnetic field.	77
3.11	Time evolution of the filament velocity dispersion in the x , y , and z directions for a filament with variable length and an orientation of 45° (left-hand column), and $l = 4$ with variable orientation (right-hand column), struck by a parallel shock.	77
3.12	Time evolution of the mean density of the filament (top) and filament core for filaments with (left-hand column) variable length and an orientation of 45° , and (right-hand column) $l = 4$ and a variable orientation, in a parallel magnetic field.	78
3.13	The time evolution of the logarithmic density, scaled with respect to the ambient density, for model <i>m10c2b1l4o45pa</i>	80

3.14 The time evolution of the logarithmic density, scaled with respect to the ambient density, for model <i>m10c3b1l4o45pa</i> using a resolution of R_{16}	81
3.15 χ dependence of the evolution for filaments with $l = 4$ and $\theta = 45^\circ$ in a parallel magnetic field.	82
3.16 Mach number dependence of the evolution for filaments with $l = 4$ and $\theta = 45^\circ$ in a parallel magnetic field.	84
3.17 Plasma beta dependence of the evolution for filaments with $l = 4$ and $\theta = 45^\circ$ in a parallel magnetic field.	84
3.18 The time evolution of the logarithmic density, scaled with respect to the ambient density, for model <i>m10c1b1l4o45pe</i>	87
3.19 As per Fig. 3.18 but showing the xy plane and magnetic fieldlines.	87
3.20 The time evolution of the logarithmic density, scaled with respect to the ambient density, for model <i>m10c1b1l4o90pe</i>	88
3.21 As per Fig. 3.20 but showing the xy plane and magnetic fieldlines.	88
3.22 The time evolution of the logarithmic density, scaled with respect to the ambient density, for model <i>m10c1b1l4o0pe</i>	89
3.23 As per Fig. 3.22 but showing the xy plane and magnetic fieldlines.	89
3.24 3D volumetric renderings of models <i>m10c1b1l4o45pe</i> (top), <i>m10c1b1l4o90pe</i> (middle), and <i>m10c1b1l4o0pe</i> (bottom).	90
3.25 Time evolution of the core mass for (a) a filament with variable length and an orientation of 45° , and (b) $l = 4$ with variable orientation, in an initial perpendicular magnetic field.	92
3.26 Time evolution of the filament mean velocity for (a) a filament with variable length and an orientation of 45° , and (b) $l = 4$ with variable orientation, in an initial perpendicular magnetic field.	93

List of figures

3.27	Time evolution of the filament velocity dispersion in the x , y , and z directions for a filament with variable length and an orientation of 45° (left-hand column), and $l = 4$ with variable orientation (right-hand column) in an initial perpendicular magnetic field.	94
3.28	Time evolution of the mean density of the filament (top) and filament core (bottom) for filaments with (left-hand column) variable length and $\theta = 45^\circ$, and (right-hand column) $l = 4$ and a variable orientation, in an initial perpendicular magnetic field.	95
3.29	The time evolution of the logarithmic density, scaled with respect to the ambient density, for models $m10c2b1l4o45pe$ (left-hand column) and $m10c3b1l4o45pe$ (right-hand column).	96
3.30	Top row: as per Fig. 3.29 (left-hand panels) but showing the xy plane and magnetic fieldlines. The evolution proceeds left to right with $t = 1.08t_{cs}$, $t = 1.98t_{cs}$, and $t = 3.65t_{cs}$. Bottom row: as per Fig. 3.29 (right-hand panels) but showing the xy plane and magnetic fieldlines.	97
3.31	χ dependence of the evolution for filaments with $l = 4$ and $\theta = 45^\circ$ in a perpendicular magnetic field.	97
3.32	Mach number dependence of the evolution for filaments with $l = 4$ and $\theta = 45^\circ$ in a perpendicular magnetic field.	99
3.33	Plasma beta dependence of the evolution for filaments with $l = 4$ and $\theta = 45^\circ$ in a perpendicular magnetic field.	100
3.34	Time evolution of the core mass for (a) a filament with variable length and an orientation of 45° , and (b) $l = 4$ with variable orientation, in a magnetic field orientated at 45° to the shock normal.	101
3.35	Time evolution of the filament mean velocity for (a) a filament with variable length and an orientation of 45° , and (b) $l = 4$ with variable orientation, in a magnetic field orientated 45° to the shock normal.	101

3.36	Time evolution of the filament velocity dispersion in the x , y , and z directions for a filament with variable length and an orientation of 45° (left-hand column), and $l = 4$ with variable orientation (right-hand column) in a magnetic field orientated 45° to the shock normal.	102
3.37	Time evolution of the mean density of the filament (top) and filament core (bottom) for filaments with (left-hand column) variable length and $\theta = 45^\circ$, and (right-hand column) $l = 4$ and a variable orientation, in a magnetic field orientated 45° to the shock normal.	103
3.38	χ dependence of the evolution for filaments with $l = 4$ and $\theta = 45^\circ$ in a magnetic field orientated 45° to the shock normal.	104
3.39	Mach number dependence of the evolution for filaments with $l = 4$ and $\theta = 45^\circ$ in a magnetic field orientated 45° to the shock normal.	105
3.40	Plasma beta dependence of the evolution for filaments with $l = 4$ and $\theta = 45^\circ$ in a magnetic field orientated 45° to the shock normal.	105
3.41	t_{drag} as a function of filament length (a), where the filament has an orientation of $\theta = 45^\circ$, and orientation (b), where the filament has a length $l = 4$, for simulations with $M = 10$, $\chi = 10$, and $\beta = 1$.	107
3.42	t_{mix} as a function of filament length (top panels), where the filament has an orientation of $\theta = 45^\circ$, and orientation (bottom panels), where the filament has a length $l = 4$, for simulations with $M = 10$, $\chi = 10$, and $\beta = 1$, in a perpendicular/oblique field (left) and a parallel field (right).	107
4.1	The time evolution of the logarithmic density for models (top) <i>c1shock</i> and (bottom) <i>c1wind1</i>	123
4.2	The time evolution of the logarithmic density for models (top) <i>c1wind1a</i> , (middle) <i>c1wind1b</i> , and (bottom) <i>c1wind1c</i>	128

List of figures

4.3	The time evolution of the linear density (left), advected scalar κ which identifies only the cloud material (middle), and advected scalar \times linear density which allows the density of only the cloud to be shown (right) for model <i>c1wind1c</i>	129
4.4	Time evolution of the global quantities	135
4.5	Cloud drag time, t_{drag} , and mixing time of the core, t_{mix} , as a function of the wind Mach number	137
5.1	The time evolution of the logarithmic density for model <i>c3shock</i> . .	147
5.2	The time evolution of the logarithmic density for model <i>c3wind1</i> . .	150
5.3	The time evolution of the logarithmic density for models <i>c3wind1a</i> (top row), <i>c3wind1b</i> (middle row), and <i>c3wind1c</i> (bottom row) . . .	152
5.4	Time evolution of the global quantities	154
5.5	Cloud drag time, t'_{drag} , and mixing time of the core, t_{mix} , as a function of the wind Mach number	161
6.1	The time evolution of the logarithmic density for model <i>m3c2l8s</i> . .	173
6.2	A 3D volumetric rendering of model <i>m3c2l8s</i>	174
6.3	The time evolution of the logarithmic density for model <i>m3c2l830</i> .	175
6.4	A 3D volumetric rendering of model <i>m3c2l830</i>	176
6.5	The time evolution of the logarithmic density for model <i>m3c2l860</i> .	177
6.6	A 3D volumetric rendering of model <i>m3c2l860</i>	177
6.7	The time evolution of the logarithmic density for model <i>m3c2l885</i> .	178
6.8	A 3D volumetric rendering of model <i>m3c2l885</i>	179
6.9	The time evolution of the logarithmic density for model <i>m10c2l8s</i> .	180
6.10	The time evolution of the logarithmic density for model <i>m1.5c2l8s</i> .	181
6.11	The time evolution of the logarithmic density for model <i>m3c3l8s</i> . .	182
6.12	The time evolution of the logarithmic density for model <i>m3c1l8s</i> . .	183

6.13	Time evolution of the core mass, m_{core} , normalised to its initial value, for various simulations with $M = 3$ and $\chi = 10^2$	184
6.14	The time evolution of the x and z centre-of-mass position of the filament for various simulations (the same simulations as in Fig. 6.13)	185
6.15	As Fig. 6.13 but showing the time evolution of the filament mean velocity in the direction of shock propagation ($\langle v_{x,\text{cloud}} \rangle$) and in the z -direction ($\langle v_{z,\text{cloud}} \rangle$)	187
6.16	As Fig. 6.13 but showing the time evolution of the filament velocity dispersion in each direction	188
6.17	The Mach number dependence of the evolution of m_{core} , $\langle v_{x,\text{cloud}} \rangle$, and $\langle x_{\text{cloud}} \rangle$, for filaments with $l = 8 r_c$ and oriented sideways to the shock front.	189
6.18	The χ dependence of the evolution of m_{core} , $\langle v_{x,\text{cloud}} \rangle$, and $\langle x_{\text{cloud}} \rangle$, for $M = 3$ and filaments with $l = 8 r_c$ and oriented sideways to the shock front.	190
6.19	t_{drag} as a function of the filament length (left-hand panel) and orientation (right-hand panels)	190
6.20	t_{mix} as a function of the filament length (left-hand panel) and orientation (right-hand panels)	191

List of tables

1.1	A summary of the main numerical simulations of shock-cloud interactions discussed in Section 1.3.	35
1.2	A summary of the main numerical simulations of wind-cloud interactions discussed in Section 1.4.1.	38
3.1	The 3D grid extent for each of the MHD simulations.	58
3.2	A summary of the shock-filament simulations performed for a parallel magnetic field.	68
3.3	As Table 3.2 but for perpendicular and oblique magnetic fields. . . .	68
4.1	The grid extent for each of the simulations	118
4.2	Values of the density jump and bow shock stand-off distance (in units of r_c) for each of the simulations.	127
4.3	A summary of the cloud-crushing time, t_{cc} for a cloud with $\chi = 10$ and $r_c = 1$	130
5.1	The grid extent for each of the simulations presented in this chapter	145
5.2	A summary of the cloud-crushing time, t_{cc} , and key time-scales . . .	153
6.1	A summary of the shock-filament simulations presented in this work, along with key time-scales.	171

Chapter 1

Introduction

This thesis concerns simulations of the interaction of shocks and winds with spherical clouds and filaments. Interstellar gas (as will be described in Section 1.1) is inhomogeneous and therefore stellar feedback processes such as shocks and winds can cause it to evolve in a multitude of differing ways. It is therefore important, from both a theoretical and observational point of view, to understand the effect of these processes in order to form a more complete picture of the nature and evolution of the interstellar medium and, potentially, the process of star formation.

Several questions could be asked with regard to the above interactions, and these motivate the research contained within this thesis. For example, how does the presence of a magnetic field affect the interaction of a shock with a filament, and is the orientation of the field with respect to the filament important? Do filaments embedded in a magnetised medium have increased lifetimes compared to those of spherical clouds? To what extent is the density contrast between the filament and the ambient medium important? Could an increased density contrast slow or prevent the destruction of the filament? What are the conditions which would allow filaments to survive indefinitely? Previous numerical studies have examined the evolution of filaments or tail-like structures from spherical clouds in both magnetised and non-magnetised media but there has been no comprehensive exploration of the evolution

Introduction

of a filamentary structure in a magnetised medium using such a large parameter space as intimated from the above questions.

Furthermore, how do the effects of winds and shocks on spherical clouds differ, given the superficial similarity of the flow in these two processes? Are such processes broadly compatible? To what extent would increasing the wind Mach number and the density contrast of the cloud affect the nature of the interaction? No comparative exploration of shock-cloud and wind-cloud simulations has previously been published, and some studies in the literature have assumed that the two types of interaction are broadly interchangeable; thus, the degree to which these types of interaction are similar/dissimilar remains to be determined and is important in order that observations of these processes are interpreted correctly.

Finally, does the evolution of a filament in an isothermal or quasi-isothermal medium differ from that of one in an adiabatic medium? Although previous studies have used a softened equation of state to mimic the effects of radiative cooling on shock-cloud interactions, the extent to which an isothermal or near-isothermal equation of state affects a shock-filament interaction has yet to be understood.

In the following chapters, I attempt to answer these questions and add to the current understanding of feedback processes and cloud evolution in the interstellar medium.

1.1 The Interstellar Medium

The Milky Way Galaxy¹ comprises not only stars but also a tenuous, inhomogenous medium (the interstellar medium; ISM) spread out across interstellar space. The ISM manifests itself primarily via the extinction, reddening, and polarisation of starlight. For example, the detection by [Hartmann \(1904\)](#) of static absorption lines in Ca II in the spectrum of the spectroscopic binary system δ Orionis indicates the presence

¹referred to with an uppercase G to distinguish it from other galaxies

of a diffuse cloud of cold interstellar gas along the line of sight, since analogous absorption lines originating from the binary stars themselves would shift according to the movement of the stars as they orbited each other. [Trumpler \(1930\)](#) showed that such clouds do not exist in isolation but are part of a much wider distribution of interstellar material.

In the following subsections, I will outline the composition of the ISM and the physical processes occurring within it. I will then review the literature on shock- and wind-cloud interactions in terms of both observations and numerical simulations.

1.1.1 ISM phases

The ISM (along with the intergalactic medium and circumstellar environments) is inhomogeneous and is comprised of dust along with gas clouds with large density and temperature distributions embedded in a hotter, low-density, magnetised, turbulent flow (see e.g. [Pittard et al. 2009](#) for a more detailed discussion). The ISM has traditionally been described in terms of phases (delineated by the state of hydrogen), each of which are described below (see also review papers by [McKee 1995](#); [Ferrière 2001](#); and [Cox 2005](#)).

1.1.1.1 Atomic clouds

Atomic hydrogen (H I) is useful observationally because, unlike molecular hydrogen, it is able to be directly observed via the 21 cm spin transition, allowing the distribution of H I in the Milky Way Galaxy (for example) to be mapped. According to the thermal model of the ISM, H I exists in two distinct thermally-stable phases: the cold neutral medium (CNM; $T \lesssim 300$ K) and warm neutral medium (WNM; peak temperature $T \simeq 8000$ K) ([Field et al. 1969](#); [Heiles and Troland 2003](#); [Cox 2005](#)). The two phases are able to coexist in pressure equilibrium which is regulated by the radiative cooling and heating balance ([Draine 1978](#); [Wolfire et al. 1995, 2003](#)).

Introduction

1.1.1.2 Molecular clouds

Observations of molecular gas show that it comprises discrete clouds extending from giant molecular clouds (GMC; with masses of up to $10^6 M_{\odot}$ and a mean hydrogen number density of around $100 - 1000 \text{ cm}^{-3}$, the latter relating to higher-density regions within the cloud) down to much smaller dense cores (of masses up to $\sim 10^3 M_{\odot}$ and a mean density of up to 10^6 cm^{-3}) (McKee and Ostriker, 2007). GMCs, in particular, are important since an understanding of their formation and properties can inform our understanding of star formation. They appear to be discrete systems with well-defined boundaries, but are inhomogeneous with clumps and cores (regions within which single stars are formed) and are therefore sources of most of the star formation in the Galaxy. GMCs are dynamic systems that include self-gravity, magnetic fields, and turbulence, with the role played by gravity allowing them to be distinguished from other phases of the ISM. Molecular clouds are extremely difficult to observe since they are cold and dark and thus cannot be observed directly in visible light. However, high concentrations of dust within denser cores serve to block light from background stars and allow some GMCs to be observed in silhouette. Whilst GMCs do emit millimetre wavelength radiation via changes in the rotational state of the molecules, the spectral lines of the most abundant molecule, H_2 , are extremely weak and therefore difficult to detect by infrared and radio observations, partly because the amount of energy needed to change the molecule's rotational state is dependent upon its mass and, with molecular hydrogen being the lightest molecule, a significantly large amount of energy would be needed; in a cold cloud, such a change in state would be unlikely and therefore the majority of H_2 would remain in the ground state and therefore undetectable. The primary method for locating GMCs, therefore, utilises CO molecules (another abundant species), which can be observed in both emission and absorption. It is estimated that there is one CO molecule for

every 10,000 hydrogen molecules, meaning that H₂ (and, thus, the GMC itself) can be easily traced.

There are two contrasting views regarding the formation of GMCs (McKee and Ostriker, 2007). The first suggests that GMCs are formed by large-scale colliding flows which coagulate to form clouds. Elmegreen (1993) notes, however, that a large number of generations of collisions are needed in order to generate the observed power-law mass distribution, something that the short lifetime of such molecular clouds would seem to prohibit. In the second view, GMCs are formed within spiral arms, where gas is able to gather along the arm due to the low shear and high densities present. Consideration of the volume from which the gas in a GMC is accumulated and the cloud surface density has elicited values comparable to observations. Larson (1981) summarised the main characteristics of GMCs, often referred to as ‘Larson’s laws’. The first of these describes the line width–size relation, i.e that GMCs are generally supersonically turbulent and have line widths of δv that tend to increase as a power of the size, $\delta v \propto R^p$, where $p = 0.38$. Secondly, GMCs are large enough to be gravitationally bound and satisfy the virial theorem, $GM/R \sim \sigma^2$, where G , M , R and σ refer to the gravitational constant, cloud mass, cloud radius, and internal velocity dispersion, respectively (Larson 1981; Myers 1987). Larson concluded that clumps within GMCs were also gravitationally bound. The third ‘law’ is that all GMCs have the same column density. In addition to Larson’s ‘laws’, McKee (1999) suggests that a further characteristic of GMCs is that they appear to have magnetic fields that are dynamically significant. Given the above, the nature of GMCs and properties such as their lifetime remain unclear.

In general, molecular clouds exhibit large variations in density (e.g. Blitz and Stark 1986), with high-density regions (or cores) prone to collapse under gravity, leading to star formation. Given that stars associated with such clouds tend to be young and that much older stellar associations lack molecular gas it is suggested that molecular clouds are, in general, fleeting, temporary structures with a short span

Introduction

between the formation of the cloud itself and star formation (Ballesteros-Paredes and Hartmann 2007; van Loo et al. 2010).

The formation of H_2 occurs via the recombination of hydrogen atoms mediated by interstellar dust particles (Hollenbach and Salpeter, 1971). However, such molecules can only survive in significant quantities inside clouds which are shielded from UV radiation which might otherwise lead to dissociation and which are cold enough to limit collisions. H_2 is not able to be directly observed using radio spectroscopy since it has no permanent dipole moment and thus all its allowed transitions fall outside the radio part of the spectrum (Field et al., 1966). However, CO *does* transition in the radio domain and can therefore be used to trace molecular gas. Measurements of the peak specific intensity of CO emission lines show that molecular gas is very cold, with temperatures in the range 10 – 20 K (Goldsmith, 1987). Other molecular tracers include HCN, CS, and NH_3 , all of which have optically thick, and therefore bright, emission lines.

Whilst many analytical and numerical studies have investigated the destruction of clouds (see Section 1.3) van Loo et al. (2010, 2007) and Lim et al. (2005) considered cold molecular cloud formation via the response of a warm atomic cloud to a pressure increase (caused by converging flows or weakly-interacting shocks) in the medium in which it is embedded.

1.1.1.3 Ionised medium

The formation of ionised hydrogen occurs through the emission of strong UV radiation by O and B stars, some of the brightest and hottest stars in the Galaxy. This radiation is energetic enough to ionise hydrogen atoms; thus, the regions around such stars are called “H II” regions (see Fig. 1.1). The boundary between these regions and the rest of the ISM tends to be sharp since the UV photons are quickly absorbed by the neutral hydrogen. The ionisation first expands into the neutral medium until

the rate of ionisations and recombinations within the nebula are equal. In a uniform medium, this balance is achieved when the H II region is at its Strömgen radius

$$r_S = (30 \text{ pc}) \left(\frac{N_{48}}{n_H n_e} \right)^{1/3}, \quad (1.1)$$

where n_H and n_e are the free-proton and free-electron number densities (in cm^{-3}) in the H II region, respectively, and N_{48} is the number of ionising photons emitted per unit time by the star.

Transitions between energy levels during recombination lead to the emission of optical Balmer lines, especially the H_α line which arises from transitions between the $n = 3$ and $n = 2$ energy levels. H_α -emitting gas has been detected in all directions outside H II regions (Roesler et al., 1978), and H_α mapping has revealed the existence of structures such as filaments within the gas (Reynolds, 1987; Reynolds et al., 1999). H_α emissions and other optical emission lines can be used to probe a cylindrical volume of radius 2-3 kpc around the Sun owing to the effect of extinction arising from interstellar dust.

The temperature of the bounded H II regions and the diffuse, H_α -emitting gas has been determined as ~ 8000 K; thus, together these two components form the Warm Ionised Medium (WIM). In addition to this, the presence of hot interstellar gas has been detected through the use of UV observations. These observations have identified highly ionised species such as O^{5+} (O VI) and N^{4+} (N V) which are excellent tracers of hot collisionally-ionised gas since their high ionisation potentials make it unlikely that they were produced through photoionisation. The temperature of this gas has been found to be in the region of $\sim 10^6$ K; thus, this gas has been termed the Hot Ionised Medium (HIM). Formation of the HIM is now generally accepted as arising from supernova explosions and stellar winds (e.g. McCray and Snow 1979; Spitzer 1990), the former of which are capable of driving powerful shockwaves through the ISM.

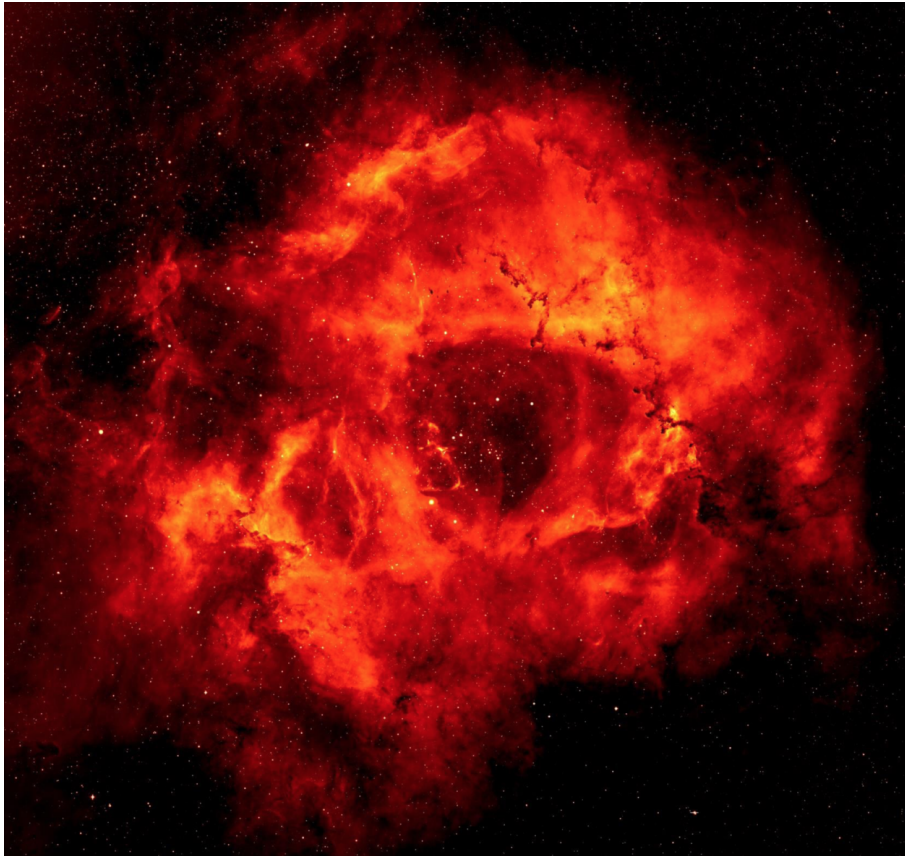


Fig. 1.1 Image of the Rosette Nebula, an area of ionised gas located in a GMC in the Monoceros constellation, shown as a three-colour image. Taken from [Drew et al. \(2005\)](#).

1.1.1.4 Dust

In addition to gas in its various states, the ISM also comprises dust, which consists of tiny particles of solid material. The size of these particles can range from a few molecules to ‘grains’ of up to 0.1 mm in size. The composition of dust particles includes silicate minerals but can also include metals and carbonaceous material such as diamond or graphite. Dust is formed in stars and is transported into the ISM via stellar winds or supernovae explosions. The importance of dust in the ISM has been alluded to in previous subsections in terms of its ability to obscure or redden starlight passing through it, and the subsequent necessity for the use of radio wavelengths to probe the ISM has been discussed. Previous studies (e.g. [Jenkins and Savage 1974](#); [Bohlin 1975](#)) have determined that the distribution of dust is inhomogeneous throughout the ISM and is coterminous with the inhomogeneities present in the interstellar gas, i.e. it follows the distribution of gas. Since dust absorbs energy from stellar photons, is heated, and re-emits energy in the infrared (IR), dust is capable of being mapped. Such maps show that there are good dust-gas correlations in the ISM (see [Schlegel et al. \(1998\)](#)). The dust-to-gas ratio has been calculated as ~ 0.01 for the Galaxy ([Draine and Li, 2007](#)), though a variation corresponding to a factor of 3 has been found in this ratio ([Burstein, 2003](#)).

The type and distribution of the dust grains can be understood from the presence of extinction in stellar spectra. The total extinction, A_λ , is given by

$$A_\lambda \equiv 2.5 \log_{10} (F_\lambda^0 / F_\lambda), \quad (1.2)$$

where F_λ is the observed flux and F_λ^0 is the flux expected in the absence of any extinction. Extinction curves can be used to indicate the particular species of grain present in each region. For example, a small peak at a UV wavelength of around 217.5 nm is attributed to graphite grains ([Gilra 1972](#); [Mathis et al. 1977](#)), whilst IR bands at 9.7 μm and 18 μm may represent silicate grains ([Knacke and Thomson](#)

1973; [Draine and Lee 1984](#)). A further identified species are polycyclic aromatic hydrocarbons (PAHs).

Larger, silicate dust grains can help determine the orientation of the magnetic field at that particular point in the ISM through their elongated nature, since they preferentially absorb light along their long axis. Elongated grains tend to align themselves such that their long axis lies perpendicular to the magnetic field. Therefore, starlight passing through dust becomes polarized and the magnetic field orientation can be inferred ([Hoang and Lazarian, 2008](#)).

Dust grains help to alter the chemistry of the ISM. In cold dense clouds they allow gas particles to accrete on their surface whilst in the warmer medium they are able to lose their volatile shell to the gas. Dust grains act as catalysts in the recombination of hydrogen atoms (e.g. [Hollenbach and Salpeter 1971](#)) and can also help shield H₂ molecules from UV photodissociation ([Shull and Beckwith, 1982](#)). Dust also contributes towards the heating and cooling of the gas through the ejection of photoelectrons and through collisions with gas particles. The ionising rate is highly dependent on the size of the dust grains (see references in [Ferrière \(2001\)](#)).

1.1.2 Filamentary structures

Networks of cold, dense filamentary structures are known to be ubiquitous throughout the universe; *Spitzer* (e.g. [Benjamin et al. 2003](#); [Carey et al. 2009](#); [Churchwell et al. 2009](#); [Courtois et al. 2015](#); [Katushkina et al. 2018](#)) and *Herschel* have both revealed the presence of filamentary networks in galactic discs and interstellar clumps, respectively. Recent observations from *Herschel* in particular have revealed filaments in both star-forming and non-star-forming regions of interstellar clouds (e.g. [André et al. 2010](#); [Henning et al. 2010](#); [Men'shchikov et al. 2010](#); [Molinari et al. 2010](#); [Motte et al. 2010](#); [Schneider et al. 2012](#); [Rayner et al. 2017](#)), and such observations suggest the central role played by filaments in the process of star-formation

(Schneider and Elmegreen 1979; Arzoumanian et al. 2011; André et al. 2014; see also Federrath (2016) for theoretical and numerical studies of such observations). Filaments have also been observed throughout the Galaxy in e.g. the Taurus molecular cloud (Panopoulou et al., 2014), the Lupus molecular clouds (Benedettini et al., 2015), and Orion A (Polychroni et al., 2013). Simulations of molecular clouds show the formation of filamentary structure in support of observations (e.g. Klessen and Burkert 2000; Ballesteros-Paredes and Mac Low 2002; Padoan et al. 2006; Federrath et al. 2010; Hennebelle 2013; Kirk et al. 2015), whilst the lifetime of such features exposed to stellar feedback processes has been investigated by Rogers and Pittard (2013).

Filamentary structures are observed in e.g. galactic outflows as $H\alpha$ - and H I-emitting filaments (Shopbell and Bland-Hawthorn 1998; Martin et al. 2002; Strickland et al. 2004; Veilleux et al. 2005; Heesen et al. 2011; Westmoquette et al. 2011; Bolatto et al. 2013), as a consequence of the ram-pressure stripping of galaxies in gravitationally-bound clusters (Conselice et al. 2001; Crawford et al. 2005; Forman et al. 2007; Canning et al. 2011; Abramson and Kenney 2014; Kenney et al. 2015), the pillars observed in molecular clouds (Benedettini et al., 2015), young protoclusters (Vig et al., 2007), and supernova remnants (Koo et al. 2007; Dopita et al. 2010; Vogt and Dopita 2011; Nynka et al. 2015) and span a whole range of scales.

The formation of filaments has yet to be definitively established but is thought to occur through the compression of gas due to the convergence of flows driven by e.g. interstellar turbulence or gravitational disc instabilities, or the interaction of high-velocity shocks or winds with clouds driven by dynamic processes such as turbulence, gravitational collapse, or magnetism (see e.g. Vazquez-Semadeni et al. 2007; Banerjee et al. 2009; Peters et al. 2012; Moeckel and Burkert 2015; Banda-Barragán et al. 2016; Federrath 2016). For example, OB stars in the Cygnus X region (Cygnus OB2 and Cygnus OB9) interact with nearby molecular clouds via radiation and winds (Schneider et al., 2006) whilst in the Pipe Nebula, the B59 region,

Introduction

which comprises a complex network of filaments, is being shaped by high-velocity outflows from embedded protostars (Duarte-Cabral et al. 2012; Peretto et al. 2012).

Whilst some filaments may have very short lifetimes before they dissipate or are destroyed, others are known to collapse under gravity and fragment into star-forming cores. Recent observational studies have shown that a large number of prestellar cores are found within dense filaments (André et al. 2010; Arzoumanian et al. 2011; Roy et al. 2015), with some filaments displaying several cores strung out along their length (Schisano et al. 2014; Könyves et al. 2015). In addition, young stellar clusters appear at the intersections of colliding filaments (Myers 2011; Schneider et al. 2012; Mallick et al. 2013). The presence of young stellar objects embedded within the filament can lead to the dispersal and destruction of the filament through the action of shocks, winds, and ionizing radiation (see e.g. Colín et al. 2013).

1.2 Shocks in the ISM

1.2.1 Feedback processes

Stars play a major role in shaping the ISM. Massive O and B stars create wind-blown shells and cavities, and H II regions which expand into the ambient ISM as a result of ionisation and heating by stellar photons. Winds, H II regions, and supernova (SN) explosions all sweep up and compress interstellar matter, impart mechanical energy to the ISM, and help shape it. Stellar winds and SNe tend to act in very similar ways, though there are more subtle differences in terms of the time-scale over which they act as well as their energy output. Winds and SNe are sources of direct mass injection into the ISM; indirect mass injection occurs when dense clumps are photoevaporated, thermally evaporated, or ablated by the action of ionising radiation, winds, and shocks. These three feedback mechanisms are mainly responsible for the multi-phase nature of the ISM and the presence of turbulence within it (e.g. Pittard

[et al. \(2009\)](#); see also [Ferrière \(2001\)](#) for a brief review of feedback processes in the ISM).

The formation of new stars can be modified by the presence of such feedback processes since stellar winds and ionising radiation can disperse the surrounding parental molecular gas and inhibit star formation. Conversely, new stars may be formed in the presence of massive stars ([Elmegreen and Lada 1977](#); [Koenig et al. 2012](#)). Feedback processes result in the presence of shocks throughout the ISM.

A shock is a pressure-driven compressive disturbance propagating faster than the local speed of sound ([Draine, 2010](#)). In the absence of magnetic fields in the ISM, information travels at sound speed. Therefore, shocks have speeds greater than a Mach number of 1 (i.e. they are supersonic). In the presence of a magnetic field, shocks will travel along the magnetic field lines at the Alfvén speed (see Subsubsection 1.2.3.). Shocks produce an irreversible change in the state of the fluid (i.e. an increase in entropy); such changes in the fluid properties (density, temperature, velocity) occur faster than the rate at which the shocked medium can react, causing discontinuities in the fluid variables. Shocks lead to compression, heating, and acceleration of the medium. Shocks are driven by energetic processes such as stellar winds, SNe, cloud-cloud collisions, and expanding H II regions, for example, and are ubiquitous since the the temperature of much of the ISM is maintained at a much lower level than that of the feedback processes due to radiative cooling.

1.2.2 HD shocks

In essence, a shock is a physical discontinuity which conserves mass, energy, and momentum, with the flux of each of these quantities being equal on each side of the discontinuity (see [Landau and Lifshitz 1987](#)). The balance of these fluxes is governed by the Rankine-Hugoniot (RH) jump conditions which describe the

Introduction

relationship between the state either side of a discontinuity. This balance can be most easily achieved when the flux across the discontinuity is zero, i.e. when there is a contact discontinuity (i.e. a surface separating two fluids with different physical properties), for example. Where there *is* a flow across the discontinuity, the result is a shock.

In the frame of the shock, the RH conditions (the ratios of post- to pre-shock density, pressure, and temperature) for an ideal gas are,

$$\frac{\rho_2}{\rho_1} = \frac{v_1}{v_2} = \frac{(\gamma+1)M_1^2}{(\gamma-1)M_1^2+2}, \quad (1.3)$$

$$\frac{P_2}{P_1} = \frac{2\gamma M_1^2}{\gamma+1} - \frac{\gamma-1}{\gamma+1}, \quad (1.4)$$

$$\frac{T_2}{T_1} = \frac{[2\gamma M_1^2 - (\gamma-1)][(\gamma-1)M_1^2 + 2]}{[(\gamma+1)M_1]^2}, \quad (1.5)$$

where ρ , P , and T represent density, pressure, and temperature, the subscripts 1 and 2 refer to values of the quantities downstream and upstream of the shock, respectively, v is the velocity perpendicular to the shock front (in the frame of reference of the shock), γ is the heat capacity of the gas, and $M_1 = v_1/c_1$ is the shock Mach number in the downstream region.

For an adiabatic shock with $\gamma = 5/3$, the equations reduce to

$$\frac{\rho_2}{\rho_1} = \frac{v_1}{v_2} = \left(\frac{1}{4} + \frac{3}{4M_1^2} \right)^{-1}, \quad (1.6)$$

$$\frac{P_2}{P_1} = \frac{5}{4}M_1^2 - \frac{1}{4}, \quad (1.7)$$

$$\frac{T_2}{T_1} = \frac{5M_1^2 + 14M_1^2 - 3}{16M_1^2}, \quad (1.8)$$

while for an isothermal ($\gamma = 1$) shock, they reduce to

$$\frac{\rho_2}{\rho_1} = \frac{v_1}{v_2} = M_{\text{iso}}^2, \quad (1.9)$$

$$\frac{P_2}{P_1} = M_{\text{iso}}^2, \quad (1.10)$$

$$\frac{T_2}{T_1} = 1. \quad (1.11)$$

where $M_{\text{iso}} = v_1/c_{\text{iso}}$ and c_{iso} is the isothermal sound speed. Motion (i.e. sound waves) in a hydrodynamic (HD) fluid is purely longitudinal.

1.2.3 MHD shocks

It was shown above that in a HD medium there are only longitudinal (sound) waves. However, in a magnetohydrodynamic (MHD) medium the presence of the magnetic field allows waves to propagate in both longitudinal and transverse directions. In the presence of a supersonic disturbance these waves are unable to propagate ahead of the disturbance and (as in the case of sound waves encountering such a disturbance in a HD medium) the response of the medium to the disturbance is non-smooth and is termed a shock. In a MHD medium transverse waves (also called Alfvén waves) propagate through the restoring force provided by tension in the magnetic field lines, are non-compressive, and have a characteristic velocity

$$v_{\text{trans}} = v_A \cos \theta, \quad (1.12)$$

where θ is the angle between the magnetic field and the shock normal and v_A is the Alfvén velocity

$$v_A = \frac{B}{\sqrt{\mu_0 \rho}}, \quad (1.13)$$

Introduction

where B is the strength of the magnetic field, μ_0 is the magnetic permeability of free space, and ρ is the density (Alfvén, 1942). In addition, there are two other waves in an MHD fluid: fast-mode and slow-mode waves. In the former, the variation of these waves is in phase and the waves propagate faster than an Alfvén wave. In the latter, the variation is out of phase and they propagate slower than an Alfvén wave. These magnetosonic waves have characteristic velocities that relate the Alfvén velocity to the sound speed, c_s (see e.g. Falle and Komissarov 1999)

$$v_{ms, \text{fast}}^2 = \frac{1}{2} \left[(c_s^2 + v_A^2) + \sqrt{(c_s^2 + v_A^2)^2 - 4c_s^2 v_A^2 \cos^2 \theta} \right], \quad (1.14)$$

$$v_{ms, \text{slow}}^2 = \frac{1}{2} \left[(c_s^2 + v_A^2) - \sqrt{(c_s^2 + v_A^2)^2 - 4c_s^2 v_A^2 \cos^2 \theta} \right]. \quad (1.15)$$

The Alfvén wave is often referred to as the ‘intermediate’ wave since its velocity lies between those of the slow and fast waves. Since the intermediate wave has no impact on the density or the strength of the magnetic field, its velocity is constant and it is able to rotate the tangential component of the magnetic field. Thus, the intermediate wave can be classed instead as a rotational discontinuity.

The RH equations were presented in subsection 1.2.2. The presence of a magnetic field, however, requires some modification to these equations, though the MHD RH equations in full are complicated due to the three wave modes. The MHD jump conditions can be given as a set of conservation equations

$$[\rho v_x] = 0, \quad (1.16)$$

$$\left[\rho v_x^2 + p + \frac{B^2}{2\mu_0} - \frac{B_x^2}{\mu_0} \right] = 0, \quad (1.17)$$

$$\left[\rho v_x v_t - \frac{B_x}{\mu_0} B_t \right] = 0, \quad (1.18)$$

$$\left[\left(\frac{1}{2} \rho v^2 + \frac{\gamma}{\gamma-1} p + \frac{B^2}{\mu_0} \right) v_x - (v \cdot \mathbf{B}) \frac{B_x}{\mu_0} \right] = 0, \quad (1.19)$$

$$[B_x] = 0, \quad (1.20)$$

$$[v_x B_t - B_x v_t] = 0, \quad (1.21)$$

where p is the pressure, v is the velocity, and the subscripts t and x refer to the transverse component and the normal component, respectively. These equations can then be rewritten to give the MHD RH equations for perpendicular and oblique shocks. The above sets of jump conditions give six unknown quantities: ρ , v_x , v_t , p , B_x , B_t . Thus, if the upstream values are known, the downstream values can be calculated.

Two special cases of fast and slow shocks are of interest: switch-on and switch-off shocks, respectively. These occur when B_t is either created or cancelled out across a shock (i.e. they either switch on the tangential component of the field or switch it off).

1.2.4 Radiative shocks

So far I have dealt with non-radiative shocks. However, since the temperature and density of a fluid is raised by the action of the shock, it is likely that (astrophysically, at least) the post-shock fluid will be radiative. Indeed, radiative shocks have been found to occur ubiquitously in, for example, jets, bubbles, and SNRs, and over a wide range of scales. Assuming that the fluid radiates energy in an optically thin radiative relaxation layer (RRL) after the shock has travelled downstream, the post-shock

Introduction

fluid properties (density, pressure, velocity, and temperature) remain the same as the properties in the HD shock case immediately behind the shock front. However, further downstream in the radiative relaxation layer they settle to new values. Within the RRL the cooling function, $\Lambda(T)$, is greater than zero, the temperature drops, and compression of the fluid leads to increased density. The most important distinction between a radiative shock and a non-radiative shock is that the former can increase the density to a much greater extent than the latter.

The radiative cooling time-scale is given by

$$t_{\text{cool}} \sim \frac{nk_B T}{n^2 \Lambda(T)}, \quad (1.22)$$

where n is the number density, k_B is the Boltzmann constant, and T is the temperature. The cooling length (the distance over which shocked cloud material cools radiatively) is given by

$$L_{\text{cool}} = t_{\text{cool}} v_c, \quad (1.23)$$

where v_c is the velocity of the shocked cloud.

In the special case of an isothermal shock, the temperature in the RRL is equal to the upstream temperature, which can occur when the cooling time is very short. This leads to some minor modifications of the RH jump relations.

[Falle \(1975\)](#) and [McCray et al. \(1975\)](#) first showed that radiative shocks were susceptible to cooling instabilities whilst [Langer et al. \(1981\)](#) found such shocks to be affected by overstability arising from oscillations (see [Pittard et al. \(2003\)](#) and [Pittard et al. \(2005a\)](#) and references therein). Some radiative shocks perturbed from steady state are subject to a cooling overstability arising from oscillations ([Langer et al. 1981](#); [Chevalier and Imamura 1982](#); [Imamura et al. 1984](#)). [Chevalier and Imamura \(1982\)](#) found that stable shocks are produced by positive increasing linear cooling functions, i.e. when $\alpha \lesssim 0.8$ for the power-law cooling function $\Lambda = \Lambda_0 T^\alpha$.

If there is a rapid increase in cooling with temperature then a perturbation within the RRL that increases the velocity of the shock will lead to more rapid cooling and thus shorter cooling lengths, ensuring that the shock is stable. However, if the cooling function does not increase sufficiently rapidly with temperature the cooling length then oscillates overstably between slow shocks that have shorter cooling lengths and fast shocks that have longer cooling lengths (Kimoto and Chernoff, 1997). In addition, Strickland and Blondin (1995) found that radiative shock stability decreases with increasing Mach number. Pittard et al. (2005a) investigated the overstability of low Mach number ($M < 5$) radiative shocks and found that overstability can occur for low Mach numbers if α is sufficiently negative.

1.3 Shock-cloud interactions

The ISM is known to be a highly dynamic and non-uniform entity containing regions of varying temperature and density (see Section 1.1) where the maintenance of thermal equilibrium is attempted through heating and cooling processes. Studies of the interaction of hot, high-velocity gas originating from events such as SNe with cooler, dense clumps of material (often referred to as ‘clouds’) are of great interest for a complete understanding of the gas dynamics of the ISM, since it is evident that the evolution and morphology of large-scale flows can be determined or modified by the far smaller clouds (Elmegreen and Scalo 2004; Mac Low and Klessen 2004; Scalo and Elmegreen 2004; McKee and Ostriker 2007; Hennebelle and Falgarone 2012; Padoan et al. 2014). Such studies are also important for understanding galaxy formation (e.g. Sales et al. 2010; Barnes et al. 2014) and the evolution of SNRs and other diffuse sources (e.g. McKee and Ostriker 1977; Cowie et al. 1981; White and Long 1991; Dyson et al. 2002; Pittard et al. 2003).

Clouds may either accrete material from, or lose material to, the ambient medium: clouds that are hit by shocks or winds are likely to be destroyed, with such destruction

Introduction

affecting the flow by ‘mass-loading’ it via processes such as hydrodynamic ablation, whereas clouds may also become compressed and gravitationally collapse after being struck by a shock and therefore trigger star formation, thus removing material from the ISM (Elmegreen and Lada 1977; Elmegreen 1998; Federrath et al. 2010; Federrath and Klessen 2012). In addition, clouds embedded in a hot flow may also be entrained by the flow and moved over considerable distances. This entrainment shapes the morphology of the cloud and can ultimately cause the destruction of the cloud, altering the gas dynamics of the ISM (see Chapter 3 for cases where the cloud is not destroyed on the usual dynamical time-scales).

Shock-cloud interactions have previously been inferred from observations (e.g. Baade and Minkowski, 1954; van den Bergh, 1971) while more recent observations have provided direct evidence, e.g. bow shocks, of shock waves interacting with clouds (e.g. Levenson et al., 2002; Patnaude et al., 2002). Figure 1.2 shows the interaction of a SN blast wave with the inhomogeneous ISM. In addition to observations, shock-cloud interactions have also been studied experimentally. For instance, the evolution of a sphere of dense material interacting with a laser-induced shock has been probed by X-ray radiography (Klein et al. 2000; Klein et al. 2003; Hansen et al. 2007; Rosen et al. 2009; see also Fig. 1.3).

This section introduces the shock-cloud problem and reviews the literature pertaining to the shock-cloud problem and relevant numerical studies of such interactions.

1.3.1 The shock-cloud problem

The shock-cloud problem, at its most basic level, comprises the idealised scenario of a HD adiabatic planar shock striking a spherical cloud. The interaction can be described by three dimensionless parameters: 1) the shock Mach number, M (i.e. the ratio of the speed of the shock along the shock normal to the speed of sound in the

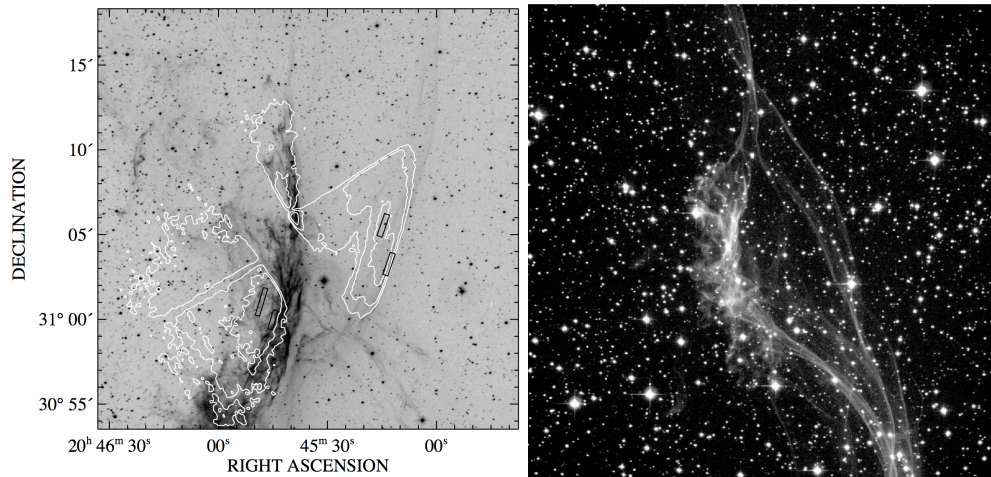


Fig. 1.2 *Left*, Logarithmic H_α image of the western edge of the Cygnus Loop, showing a network of bright, elongated filaments at the centre of the image produced by fully radiative shocks. Fainter emission to the right of the image is produced by Balmer-dominated shocks and traces the edge of the blast wave. Taken from [Levenson et al. \(2002\)](#). *Right*, H_α image showing the interaction of the shock front with an isolated cloud in the southwest region of the Cygnus Loop. Taken from [Patnaude et al. \(2002\)](#).

medium upstream of the shock), 2) the cloud density contrast, χ

$$\chi = \frac{\rho_{\max}}{\rho_{\text{amb}}}, \quad (1.24)$$

where ρ_{\max} is the maximum density of the cloud and ρ_{amb} is the density of the ambient medium, and 3) the ratio of specific heats (‘adiabatic gas index’), γ

$$\gamma = \frac{c_p}{c_v}, \quad (1.25)$$

where c_p is the specific heat capacity at constant pressure and c_v is the specific heat capacity at constant volume. [Klein et al. \(1994\)](#) and [Nakamura et al. \(2006\)](#) demonstrated that for $M \gg 1$ Mach scaling applies and the interaction can be described solely by χ and γ .

Introduction

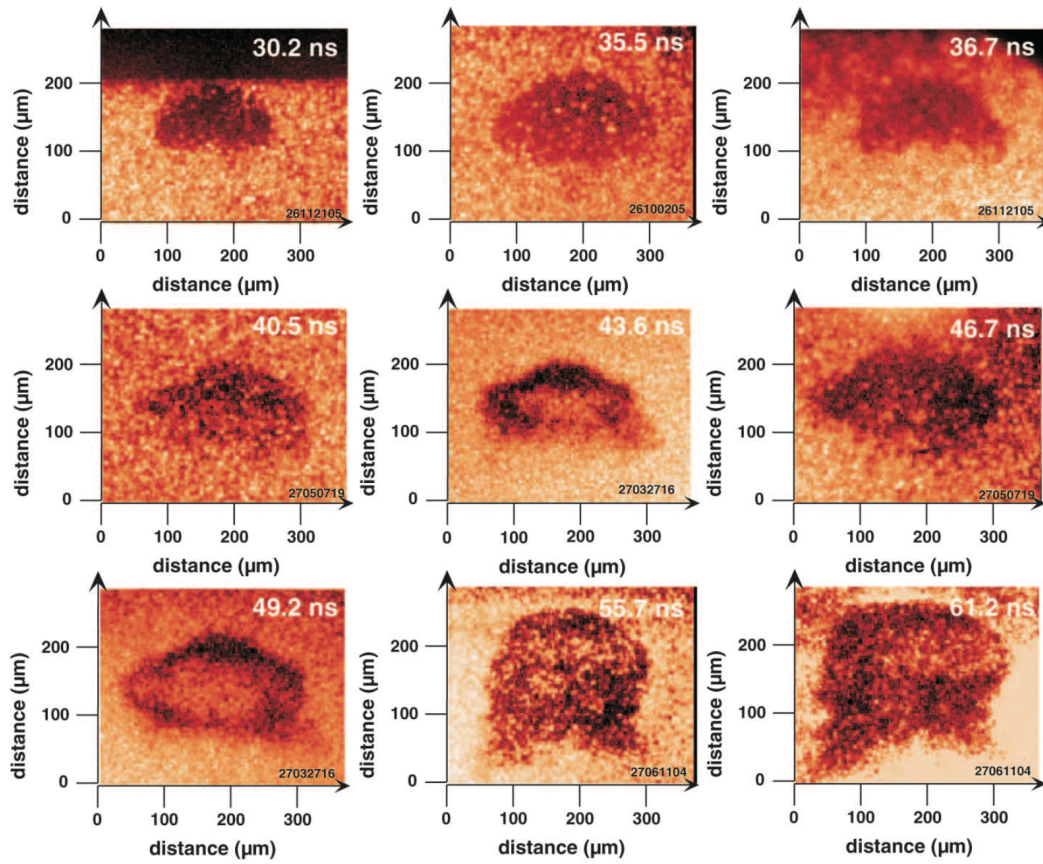


Fig. 1.3 Shock-sphere shadowgrams taken from an experimental study. Images show the evolution of a copper sphere from its initial interaction with the laser-induced shock wave until its eventual destruction. Taken from [Klein et al. \(2003\)](#).

In MHD models, a fourth parameter is used to describe the interaction: the ratio of thermal pressure to magnetic pressure (i.e. the ‘plasma beta’),

$$\beta_0 = 8\pi \frac{P_0}{B_0^2}, \quad (1.26)$$

where P_0 is the ambient thermal pressure and B_0 is the ambient magnetic field strength. Additionally, the Alfvénic Mach number,

$$M_A = \frac{v_b}{v_A}, \quad (1.27)$$

can be used, where v_b is the shock speed. Finally, the orientation of the magnetic field to the shock normal is considered in MHD models.

In addition to the above, other parameters to be considered for non-spherical clouds include the aspect ratio of the cloud and the angle of orientation of its major axis to the shock normal.

1.3.2 Early numerical studies

There is now a large amount of literature, beginning in the 1970s, concerning the idealised case of a planar adiabatic shock striking an isolated spherical cloud. The initial focus of the papers had been on shocks propagating within a uniform medium. However, observations subsequently revealed the ISM to be clumpy in nature, thus complicating the problem of modelling such interactions.

Analytical studies were conducted by e.g. [McKee and Cowie \(1975\)](#) (who analysed the properties of the flow), [Spitzer \(1982\)](#) (who investigated reflected acoustic waves from shock waves interacting with clouds), and [Hartquist et al. \(1986\)](#) (who explored how a wind evolved when embedded clouds evaporate; i.e. the post-shock flow becomes ‘mass-loaded’ by the cloud material). The motivation for the majority of these studies was observational evidence of the interaction of SNRs with

Introduction

a shock, e.g. Cassiopeia A and the Cygnus Loop (Baade and Minkowski, 1954; van den Bergh, 1971), where parts of the SNR were found to be moving at much lower velocities than the rest of the expanding shell, leading researchers to seek to determine the processes that occur when a shock overruns a cloud, as well as the conditions under which the interaction evolves.

Whilst these analytical studies were important in helping to define the nature of the interactions taking place within the ISM, the complexity of such problems can only really be described by numerical calculations. Throughout the late 70s until the early 90s several numerical studies were published. For example, Sgro (1975) ran 2D calculations of the interaction of an adiabatic planar shock with both cold and hot clouds and investigated the cloud morphology as well as the relationship between the shock and the cloud. However, their results were deemed to be preliminary since the flow within the cloud was not able to be fully resolved. Woodward (1976) also ran 2D calculations of the implosion of a cloud after it has been struck by a shock, but their simulations stopped before the interaction had been fully evolved. Another early numerical study by Nittmann et al. (1982) identified four distinct stages in the interaction of a strong shock with a cloud.

The main limitations of the above studies were the reduced computing power available and the low resolution of the calculations which prevented the interaction from being clearly followed. From the 1990s onwards, more complex studies in both 2D and 3D began to be published that sought to overcome these limitations.

1.3.3 Adiabatic HD shock-cloud simulations

Klein et al. (1994) sought to address the many outstanding questions regarding the morphology and hydrodynamic evolution of a cloud embedded in a shocked medium. With the increase in available computing power since the 1970s, they were able to perform a comprehensive 2D axisymmetric numerical study of the problem of a

shock-cloud interaction and focused on the idealised case of a planar shock wave hitting a single spherical cloud. They also defined the characteristic time-scale for a spherical cloud to be crushed by the shock being driven into it (the ‘cloud-crushing time-scale’),

$$t_{cc} = \frac{\chi^{1/2} r_c}{v_b}. \quad (1.28)$$

They determined that small clouds could be destroyed by Kelvin-Helmholtz (KH) and Rayleigh-Taylor (RT) instabilities in several cloud-crushing times ([Chandrasekhar, 1961](#)), thus allowing such instabilities to play a significant part in fragmenting the cloud. Their paper is significant for numerical studies of shock-cloud interactions. Firstly, because it provides a benchmark against which other, more realistic, studies can be compared and secondly, because it simplifies a complex problem into one determined purely by two dimensionless parameters: M and χ . [Klein et al. \(1994\)](#) then demonstrated that for a highly supersonic flow (i.e. $M \geq 5$) M scales out, leaving the problem to be described almost entirely by χ . In addition, they also suggested that a spatial resolution of at least 100 cells per cloud radius is required in order for the simulation quantities under consideration to be fully converged and the main features of the interaction, i.e. the growth of hydrodynamic instabilities, clearly resolved; this latter requirement has been revisited in later studies.

The first study to present the results of three-dimensional simulations was [Stone and Norman \(1992\)](#). They revealed that the cloud fragments in all directions, that the level of fragmentation is resolution-dependent, and that vortex rings which had been observed in 2D simulations are actually unstable when viewed in three dimensions.

A small number of studies have attempted to apply the findings of single-cloud-shock/wind interactions to the problem of multiple embedded clouds. [Poludnenko et al. \(2002\)](#), for example, attempted a detailed analysis of the dynamics of the interaction of shocks with multiple dense clouds with high Mach numbers. They found that the thickness of the cloud layer, and the distribution of the clouds within

Introduction

it, defines the evolution of the system (i.e. a small separation between the clouds leads to their merger into a single structure before they are destroyed, whereas a larger separation could be described instead by the single-cloud regime). [Alūzas et al. \(2012\)](#) and [Alūzas et al. \(2014\)](#) similarly considered multiple clouds. In this case the interaction was studied using a range of Mach numbers. Whilst [Poludnenko et al. \(2002\)](#) considered multiple clouds in terms of “layers” and suggested that the total cloud mass and number density of the clouds were not significant, [Alūzas et al. \(2012\)](#) and [Alūzas et al. \(2014\)](#) looked at the placing of such clouds and found that (when magnetic fields were taken into consideration) upstream clouds can shield clouds further downstream from the full effects of the flow. They also determined that as the number density of the clouds declines, the clumpy region becomes more “porous”.

In addition to the above adiabatic studies, other papers have considered the additional effects of turbulence on the interaction. [Pittard et al. \(2009\)](#) included a $k - \epsilon$ turbulence model in their code, in contrast to previous studies that had assumed the shocked flow was inviscid. They compared their results to those of an inviscid model and found that with a density contrast $\chi \lesssim 100$ and a smooth post-shock flow, cloud destruction occurs on approximately the same time-scale as that of an inviscid cloud owing to the length of time required for turbulence to be generated. Higher density contrasts, however, provided a far greater divergence in results. A second paper, [Pittard et al. \(2010\)](#), considered the impact of varying the Mach number on the interaction, as well as the conditions leading to the formation of tail-like structures behind the cloud, and found that higher Mach numbers ($M > 2.76$) lead to the post-shock conditions becoming almost independent of the Mach number (i.e. Mach-scaling is achieved). It was further found that low Mach numbers hold back the production of tails, and that such tails are produced only for density contrasts of $\chi \gtrsim 10^3$. The most recent paper that considered the role of turbulence, [Pittard and Parkin \(2016\)](#), compared 2D and 3D simulations and found that there is very

little difference between the simulations in terms of key global quantities such as the cloud lifetime. Moreover, they found that $k - \varepsilon$ and inviscid simulations show very good agreement in 3D.

1.3.3.1 Non-spherical clouds

As discussed in Section 1.1.2, observations have shown filamentary structures to be highly prevalent in areas of star formation. Thus, studies of non-spherical clouds interacting with shocks are important. However, it is necessary to simulate less complex scenarios (e.g. adiabatic, and without gravity, radiative cooling, etc.) before more realistic cases can be addressed. [Klein et al. \(1994\)](#) briefly investigated the interaction of a shock with a cylindrically-shaped cloud and defined a modified cloud-crushing time-scale for such interactions,

$$t'_{cc} = \frac{(\chi a_0 c_0)^{1/2}}{v_b}, \quad (1.29)$$

where a_0 and c_0 are the initial radii of the cloud in the radial and axial directions, respectively. [Klein et al. \(1994\)](#) was the first numerical study to investigate how the nature of the interaction changes when the aspect ratio of the cloud (3:1 in their study) is changed. Their 2D axisymmetric cloud was set so that it was hit from one end by the propagating shock, and the orientation and length of the ‘filament’ were unaltered. They determined that there was reasonable agreement between the spherical case and simulations using a non-spherical cloud and their modified cloud-crushing time-scale, and stated that modest changes to the shape of the cloud would not affect their overall conclusions.

The first 3D non-spherical shock-cloud study was conducted by [Xu and Stone \(1995\)](#) for a prolate cloud of aspect ratio 2:1. In that study, the cloud was able to be orientated at different angles and directions relative to the shock front. They defined

Introduction

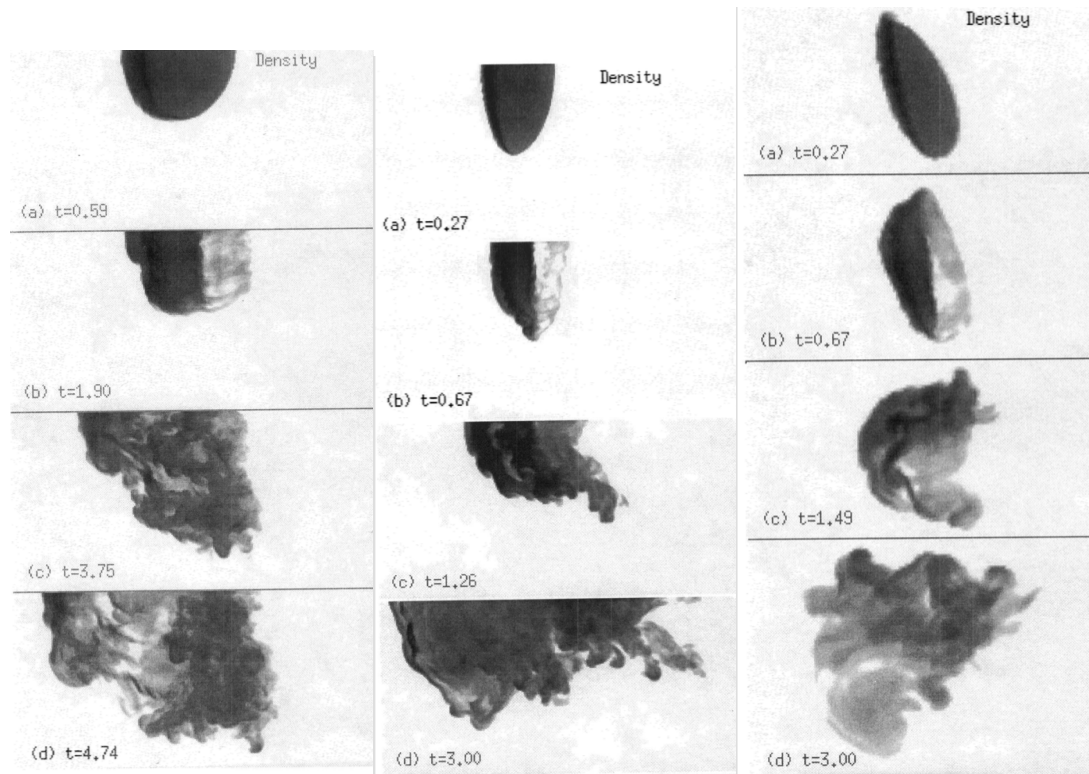


Fig. 1.4 Volumetric renderings of the log of the density of a spherical (left), aligned prolate (middle), and inclined prolate (right) cloud at different times (scaled by the modified cloud-crushing timescale, t_{cs} - see Eq. 1.30). Taken from [Xu and Stone \(1995\)](#).

a modified cloud-crushing time for prolate clouds,

$$t_{cs} = \frac{r_s \chi^{1/2}}{v_b}, \quad (1.30)$$

where r_s is the radius of a sphere of equivalent mass. They found that by modifying the cross-section of the cloud its evolution could be significantly altered depending on the cloud geometry. In particular, the mixing rate of their prolate cloud was found to be much faster than that of a spherical cloud of the same mass because of the greater surface-to-volume ratio. They also found that, whilst the formation of a vortex ring is a feature of interactions with spherical clouds, a prolate cloud aligned perpendicularly to the shock normal does not form a vortex ring since the interaction of the shock is more complex. Additionally, the prolate cloud is accelerated to a near-constant velocity far more quickly than the spherical cloud. In contrast, the evolution of an inclined prolate cloud is substantially different to that of the aligned cloud: in this case the cloud's inclination causes it to be spun around, drastically altering the development of hydrodynamical instabilities. Figure 1.4 shows the difference in the evolution between a spherical cloud and aligned and inclined prolate clouds.

[Pittard and Goldsmith \(2016\)](#) investigated 3D shock-filament interactions where the filament's aspect ratio, density contrast, and its angle of orientation to the shock front were varied. They found that varying the filament length and angle of orientation significantly changes the nature of the interaction; for example, slightly oblique filaments tend to spill the high vorticity flow around the upstream end of the filament, allowing a long wake to form behind the filament, whilst highly oblique filaments have a dominant vortex ring at the upstream end, aiding their subsequent fragmentation. Filaments presented sideways-on to the shock front are accelerated more quickly and initially lose mass more quickly than spherical clouds.

Of the few other studies covering non-spherical clouds, [Patnaude and Fesen \(2005\)](#) considered cloud models with some substructure within them, whilst [Mellema](#)

[et al. \(2002\)](#) studied spherical and elliptical cloud geometries and found that the initial geometry of the cloud can significantly alter the cloud evolution. [Cooper et al. \(2009\)](#) investigated wind-cloud interactions involving three-dimensional non-axisymmetric clouds and found that these could eventually form filaments.

1.3.4 MHD shock-cloud simulations

The presence of magnetic fields can strongly change the nature of the interaction. Prior to [Mac Low et al. \(1994\)](#), it was already known that in many places in the ISM the magnetic pressure could equal or exceed the thermal pressure of the gas and suppress instabilities, thus tempering cloud fragmentation. [Mac Low et al. \(1994\)](#) ran 2D axisymmetric simulations and showed that if a magnetic field is present then the formation of KH and Richtmyer-Meshkov (RM) instabilities are impeded and the mixing of the cloud with the flow is reduced. Thus, the presence of a magnetic field can prevent the complete destruction of the cloud, allowing it to survive as a coherent structure, as opposed to mixing completely with the ambient flow (as in the field-free case). A parallel field (the orientation of the magnetic field is given with respect to the direction of shock propagation, i.e. the shock front normal) allows a ‘flux rope’ to form behind the cloud, since the field is preferentially amplified at that point due to shock-focussing. Thus, in a magnetised medium, shock-cloud interactions are capable of creating linear structures.

[Fragile et al. \(2005\)](#) conducted 2D simulations and found that magnetic fields concentrated near the cloud surface suppress the growth of destructive HD instabilities. Moreover, external fields compress the cloud by confining it between the stretched field lines. These processes dramatically affect the radiative cooling efficiency, increasing it with increasing field strength, as well as the size of the condensed cooled cloud fragments. [Orlando et al. \(2008\)](#) investigated the effects of thermal conduction, with a focus on magnetised clouds. They found that when the field was parallel, the

rate of reduction of thermal conduction is at a minimum, thereby prolonging the lifetime of the cloud; conversely, when the field is perpendicular to the cylindrical cloud instabilities are able to be efficiently suppressed by thermal conduction, thus reducing the rate at which the cloud mixes with the surrounding flow.

The combination of magnetic fields and radiative cooling was explored in [van Loo et al. \(2007\)](#), where fast mode, followed by slow mode, shocks propagated into the cloud. As the shock interacts with the front of the cloud, it provides conditions sufficient for the formation of massive, gravitationally-bound clumps which may be precursors to star-formation.

[Shin et al. \(2008\)](#) found that at low cloud-crushing times the structure of the shocked cloud was largely insensitive to either field orientation or strength - the evolution is driven purely by the mechanical energy of the shock. However, at late times magnetic fields do affect the evolution of the cloud. Strong fields lead to different cloud morphologies depending upon the field geometry, but even weak fields have a substantial effect in terms of turbulent stripping and fragmentation when compared to the non-magnetised cases. In a strong parallel field, the cloud takes on a disc-like appearance, whilst in a perpendicularly or obliquely aligned shock, the cloud takes on a sheet-like appearance at late times and becomes orientated parallel to the post-shock field (see Figure 1.5, which shows the difference in cloud structure between a strong parallel or perpendicular magnetic field).

[van Loo et al. \(2010\)](#) explored the interaction of a weak, radiative shock with a magnetised cloud in order to better understand the formation of a magnetically dominated molecular cloud. They investigated the effect of different orientations of the magnetic field and determined that obliquely-oriented fields can be sub-divided into quasi-perpendicular (i.e. angled at 45°) and quasi-parallel (i.e. angled at 15°) fields. The former produce low-density clouds resembling H I clouds whilst the latter generate high-density clumps.

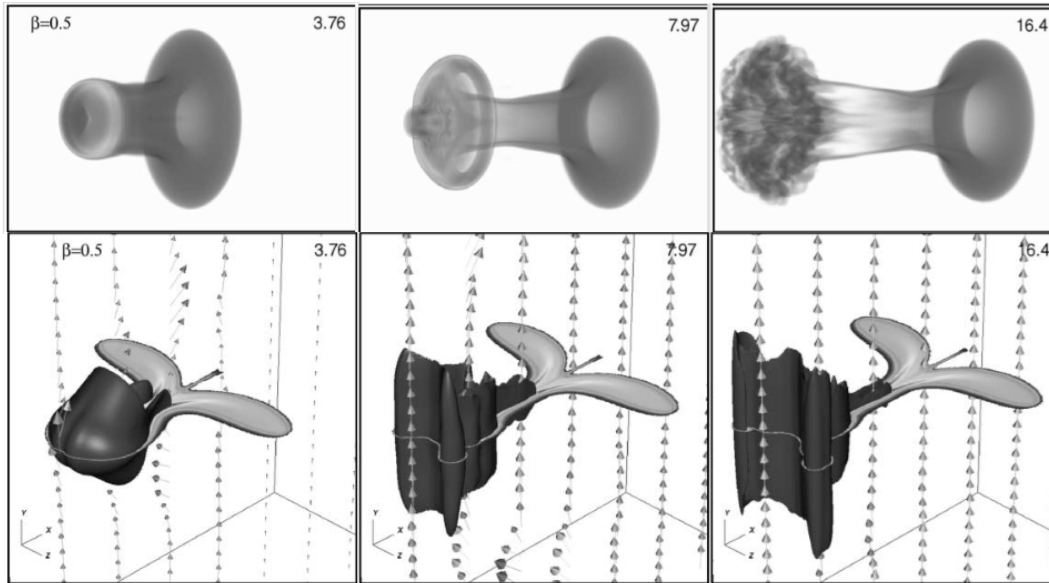


Fig. 1.5 Volumetric renderings of the cloud density for a parallel magnetic field (top) and isosurface and horizontal slice at $y = 0$ of the cloud density for a perpendicular magnetic field (bottom) in a strong field at different times (measured in units of the cloud-crushing timescale, t_{cc} - see Eq. 3.10). Taken from [Shin et al. \(2008\)](#).

In addition, [Li et al. \(2013\)](#) showed that a perpendicular field can better deflect the flow around the cloud and reduce mixing, whereas a parallel field allows the cloud to be permeated by the flow, thus enhancing mixing. This effect was also noted in the paper on wind-cloud interactions by [Banda-Barragán et al. \(2016\)](#), who found that cloud models where the magnetic field component is transverse to the wind direction have lower mixing fractions and velocity component dispersions than models where the field component is aligned with the flow.

More recent work has considered the optimum field strength needed to produce cloud fragments which can survive the destructive processes and has found that intermediate-strength fields are most effective, since strong fields prevent compression and weak fields do not insulate the cloud from cooling ([Johansson and Ziegler, 2013](#)).

The magnetic field cases detailed so far have assumed a field with uniform geometry extending throughout the ambient medium and the cloud. It is worth noting that [Li et al. \(2013\)](#) attempted to simulate more realistic magnetic fields and

looked at complex field topologies (i.e. tangled fields) embedded within the cloud and how these might alter the evolution of the shocked cloud.

1.3.5 Radiative/isothermal simulations

A number of studies have included the effects of radiative cooling in their calculations. [Mellema et al. \(2002\)](#) showed that rapid cooling leads to the break up of the cloud into a number of fragments which are able to survive for a long time. [Fragile et al. \(2004\)](#) showed that for moderate cloud densities and for shock Mach numbers $\lesssim 20$, cooling processes can be highly efficient, allowing more than 50% of the initial cloud mass to cool to below 100 K. [Orlando et al. \(2005\)](#) considered both radiative cooling and thermal conduction and found that whilst the latter leads to the evaporation of clouds and the suppression of HD instabilities, the former amplifies such instabilities and allows the cloud to cool and fragment. Radiative cooling tends to dominate when there is a low shock Mach number, whilst for high Mach numbers the evolution is dominated by thermal conduction. [Melioli et al. \(2005\)](#) performed 3D radiative HD simulations using up to three spherical clouds and found that such interactions cause the formation of elongated filaments. They also noted that mass-loading of the flow is less efficient as a result.

Whilst a full radiative cooling model would provide more realistic results applicable to observations, such models can be computationally expensive (see [Yirak et al. \(2010\)](#), who demonstrated that whilst a resolution of 100 cells per cloud radius allowed the evolution of the cloud to be well captured, the removal of thermal energy through radiative cooling meant that a resolution of between 100-200 cells per cloud needed to be adopted). Instead, softening the equation of state so that it is isothermal ($\gamma = 1$) or quasi-isothermal can mimic the effects of cooling in the ISM. Several studies have explored the effect of an isothermal equation of state on the interaction between a shock or wind and a cloud. [Klein et al. \(1994\)](#) briefly

Introduction

explored a 2D shock-cloud interaction using $\gamma = 1.1$ for the cloud only and found that a softened equation of state leads to greater compression in the cloud, with the cross-section of the radiative cloud much smaller than that of a non-radiative cloud. Moreover, the cloud drag is smaller than when an adiabatic equation of state is used. In addition, they found that isothermal clouds survive for longer due to the higher density of the shocked cloud. An investigation of similarity solutions for cloud collapse ([Kawachi and Hanawa, 1998](#)) using values for the equation of state in the range $0.9 < \gamma < 1$ found that the collapse of a cylindrical cloud asymptotes toward $\gamma = 1$ when approached from below this value. [Li et al. \(2003\)](#) explored self-gravitating turbulent clouds over a range of values for γ and found that the ability of interstellar gas clouds to fragment under the action of self-gravity decreased in the range $0.2 < \gamma < 1.4$. [Larson \(2005\)](#), in a review paper, noted that the above result had particular importance for filamentary clouds, and that a value of $\gamma = 1$ denotes a critical value for filament collapse. [Nakamura et al. \(2006\)](#), in their 3D study in which they compared adiabatic and isothermal interactions, used $\gamma = 1.1$ for both the cloud and the intercloud gas. Their results supported those of [Klein et al. \(1994\)](#) and underlined the fact that the cloud experiences much milder destruction by HD instabilities. Finally, [Banda-Barragán et al. \(2016\)](#) briefly explored the effect of a quasi-isothermal equation of state ($\gamma = 1.1$) on a MHD wind-cloud interaction and noted that an isothermal filament survives for longer than an adiabatic one. Other studies to have utilised an isothermal equation of state for the cloud include [Raga et al. \(2005\)](#) and [Pittard et al. \(2005b\)](#).

A summary of relevant shock-cloud studies in the literature can be found in Table 1.1, whilst a similar summary of wind-cloud studies can be found in Table 1.2.

1.3 Shock-cloud interactions

Table 1.1 A summary of the main numerical simulations of shock-cloud interactions discussed in Section 1.3.

Authors	Interaction type	Geometry	Typical (max) resolution	χ	M	RC	TC	MF
SN92 ^a	SC	3D XYZ	60 (60)	10	10			
KMC94 ^b	SC	2D RZ	120 (240)	$3 - 4 \times 10^2$	$10, 10^2, 10^3$			
MC94 ^c	SC	2D RZ, XY	50 (240)	10	$10, 10^2$			✓
XS95 ^d	SC	3D XYZ	25 (53)	10	10			
MKR02 ^e	SC	2D RZ, XY	200 (200)	10^3	10	✓		
PFB02 ^f	SCM	2D XY	32 (32)	5×10^2	10			
F04 ^g	SC, SCM	2D XY	200	10^3	5 - 40	✓		
PF05 ^h	SC	2D XY	450 (500)	3, 6, 8, 10	10, 20			
O05 ⁱ	SC	2D RZ, 3D XYZ	132 (132)	10	30, 50	✓	✓	
N06 ^j	SC	2D RZ, 3D XYZ	120 (960)	$10, 10^2$	$1.5 - 10^3$			
V07 ^k	SC	2D RZ	640	45	1.5, 2.5, 5	✓		✓
O08 ^l	SC	2.5D XYZ	132 (528)	10	50	✓	✓	✓
SSS08 ^m	SC	3D XYZ	68 (68)	10	10			✓
P09 ⁿ	SC	2D RZ	64 (256)	$10, 10^2, 10^3$	10			
P10 ^o	SC	2D RZ	128 (128)	$10, 10^2, 10^3$	1.5 - 40			
V10 ^p	SC	3D XYZ	120 (480)	45	2.5	✓		✓
A12 ^q	SCM	2D XY	8 (32)	$10^2, 10^3$	1.5, 2, 3, 10			
LFB13 ^r	SC	3D XYZ	54	10^2	10	✓		✓
JZ13 ^s	SC	3D XYZ	100	10^2	30	✓	✓	✓
A14 ^t	SCM	2D XY	32 (128)	10^2	3			✓
PP16 ^u	SC	3D XYZ	64 (128)	$10, 10^3$	1.5, 10			
PG16 ^v	SF	3D XYZ	32 (32)	$10, 10^2, 10^3$	1.5, 3, 10			
Chapter 3	SF	3D XYZ	32	$10, 10^2, 10^3$	1.5, 3, 10			✓
Chapter 4	SC, WC	2D RZ	128	10	10			
Chapter 5	SC, WC	2D RZ	128	10^3	10			
Chapter 6	SF	3D XYZ	32	$10, 10^2, 10^3$	1.5, 3, 10	✓*		

Notes. The interaction types are given as SC = shock-cloud, SCM = shock-multiple clouds, SF = shock-filament, and WC = wind-cloud. The headings in columns 7-9 are: RC = radiative cooling, TC = thermal conduction, and MF = magnetic fields.

The references are as follows: ^aStone & Norman (1992), ^bKlein, McKee & Colella (1994), ^cMac Low et al. (1994), ^dXu & Stone (1995), ^eMellema, Kurk & Röttgering (2002), ^fPoludnenko, Frank & Blackman (2002), ^gFragile, Murray & Anninos (2004), ^hPatnaude & Fesen (2005), ⁱOrlando et al. (2005), ^jNakamura et al. (2006), ^kvan Loo et al. (2007), ^lOrlando et al. (2008), ^mShin, Stone & Snyder (2008), ⁿPittard et al. (2009), ^oPittard et al. (2010), ^pvan Loo, Falle & Hartquist (2010), ^qAlūzas et al. (2012), ^rLi, Frank & Blackman (2013), ^sJohannson & Ziegler (2013), ^tAlūzas et al. (2014), ^uPittard & Parkin (2016), ^vPittard & Goldsmith (2016).

* Chapter 6 uses a softened equation of state rather than a full radiative cooling model.

1.4 Wind-cloud interactions

Wind-cloud interactions have generally been considered to be a particular case of the shock-cloud problem where the cloud interacts with the post-shock flow rather than the shock itself; thus, many studies have assumed both processes to be similar in nature (see Chapter 5 for scenarios when this assumption does not hold). These interactions occur between a stationary cloud and a hot, high-velocity wind or, conversely, between a static ambient medium and a moving cloud ('bullet'). Observational studies have provided evidence of the interaction of hot flows or winds with molecular clouds (e.g. [Koo et al., 2001](#); [Westmoquette et al., 2010](#)). High-velocity winds and shocks in regions of star formation are capable of strongly affecting molecular clouds. For example, the B59 filament in the Pipe nebula is thought to be undergoing distortion by a wind ([Peretto et al., 2012](#)) and molecular cloud complexes in the Cygnus X region are being shaped by winds and radiation ([Schneider et al., 2006](#)), whilst winds lead to the disruption, fragmentation or dispersion of clouds such as the Rosette molecular cloud ([Bruhweiler et al. 2010](#); see also [Rogers and Pittard \(2013\)](#) and [Wareing et al. \(2017\)](#) for relevant numerical studies). Another effect of the interaction of a flow with a dense cloud is the entrainment of the cloud into the flow and acceleration of cloud material towards the flow's velocity. Several studies have revealed large outflow velocities from rapidly star-forming galaxies (e.g. [Heckman et al. 2000](#); [Pettini et al. 2001](#); [Rupke et al. 2002](#); [Martin 2005](#); [Martin et al. 2012](#)) and clouds have been typically observed at distances of a few kpc from the driving region (e.g. [Soto and Martin 2012](#)). However, it has proved less easy to reconcile observations that clouds can travel distances on the order of 100 kpc (e.g. [Turner et al. 2014](#)) without being destroyed by flows of such high velocity; [Scannapieco and Brügger \(2015\)](#) determined that in order to achieve these velocities clouds would need to be the size of entire galaxies.

Similar to the parameters used to define the shock-cloud problem, the wind-cloud problem can be defined by the Mach number of the post-shock flow or wind,

$$M_{ps/wind} = \frac{v_{ps/wind}}{c_{ps/wind}}, \quad (1.31)$$

where $v_{ps/wind}$ is the velocity of the post-shock flow or wind and $c_{ps/wind}$ is the adiabatic sound speed of the post-shock flow or wind and is given by

$$c_{ps/wind} = \sqrt{\gamma \frac{P_{ps/wind}}{\rho_{ps/wind}}}, \quad (1.32)$$

with $P_{ps/wind}$ and $\rho_{ps/wind}$ denoting the pressure and density of the post-shock flow or wind, respectively. This is in addition to the usual parameters of χ , etc.

1.4.1 Wind-cloud simulations

In addition to the large body of literature concerning shock-cloud interactions, many computational studies over the last two decades have considered the particular case of a hot, tenuous wind interacting with a cool, dense cloud (for example, [Klein et al. \(1994\)](#) briefly addressed the simple case of the 2D adiabatic interaction of a spherical cloud with a wind where the the initial shock has been removed - i.e. a cloud embedded within a post-shock flow). These studies have tended to focus on scenarios involving radiative cooling (see e.g. [Schiano et al. 1995](#); [Poludnenko et al. 2004](#); [Raga et al. 2007, 2005](#); [Cooper et al. 2009](#); [Scannapieco and Brügger 2015](#); [Brügger and Scannapieco 2016](#)) or magnetic fields (e.g. [Jones et al. 1996](#); [Miniati et al. 1999](#); [Gregori et al. 1999, 2000](#); [McCourt et al. 2015](#); [Banda-Barragán et al. 2016](#); [Banda-Barragán et al. 2018](#)). Other wind-cloud numerical studies have included self-gravity ([Murray et al. 1993](#)) and thermal conduction ([Marcolini et al. 2005](#); [Vieser and Hensler 2007](#); [Brügger and Scannapieco 2016](#)), whilst [Pittard et al. \(2005b\)](#) considered the interaction of a wind with multiple clouds.

Introduction

Table 1.2 A summary of the main numerical simulations of wind-cloud interactions discussed in Section 1.4.1.

Authors	Interaction type	Geometry	Typical (max) resolution	χ	M_{wind}	RC	TC	MF
M93 ^a	WC	2D XY	25	$5 \times 10^2, 10^3$	0.25 - 1			
J94 ^b	WC	2D XY	43	$30, 10^2$	3, 10			
S95 ^c	WC	2D RZ	128 (270)	$10 - 2 \times 10^3$	10	✓		
J96 ^d	WC	2D XY	50 (100)	$10, 40, 10^2$	10			✓
M99 ^e	WC	2D XY	26	$10, 10^2$	1.5, 10			✓
G99 ^f	WC	3D XYZ	26	10^2	1.5			✓
G00 ^g	WC	3D XYZ	26	10^2	1.5			✓
P04 ^h	WC	2D RZ	128	10^2	$10 - 2 \times 10^2$	✓		
R5 ⁱ	WC	3D XYZ	25	50	2.6	✓		
P05 ^j	WC, WCM	2D XY	32	350	1, 20			
M05 ^k	WC	2D RZ	75, 150	$10^2, 5 \times 10^2$	2.98, 6.66		✓	
R07 ^l	WC	3D XYZ	76	10	242	✓		
VH07 ^m	WC	2D RZ	28 - 33	5900 - 61000	0.3		✓	
C09 ⁿ	WC, WFC	3D XYZ	6 - 38	630, 910, 1260	4.6	✓		
K11 ^o	WC	2D RZ	64	10^3	0.6 - 2			
M15 ^p	WC	3D XYZ	32	50	1.5			✓
SB15 ^q	WC	3D XYZ	32 - 128	$3 \times 10^2 - 10^4$	0.5 - 11.4	✓		
BS16 ^r	WC	3D XYZ	32 - 96	$3 \times 10^2 - 10^4$	0.99 - 11.4	✓	✓	
B16 ^s	WC	3D XYZ	128	10^3	4, 4.9			✓*
B18 ^t	WFC	3D XYZ	128	10^3	4			✓

Notes. The interaction types are given as WC = wind-cloud, WCM = wind-multiple clouds, and WFC = wind-fractal cloud. The headings in columns 7-9 are: RC = radiative cooling, TC = thermal conduction, and MF = magnetic fields.

The references are as follows: ^aMurray et al. (1993), ^bJones et al. (1994), ^cSchiano et al. (1995), ^dJones et al. (1996), ^eMiniati et al. (1999), ^fGregori et al. (1999), ^gGregori et al. (2000), ^hPoludnenko et al. (2004), ⁱRaga et al. (2005), ^jPittard et al. (2005), ^kMarcolini et al. (2005), ^lRaga et al. (2007), ^mVieser & Hensler (2007), ⁿCooper et al. (2009), ^oKwak et al. (2011), ^pMcCourt et al. (2015), ^qScannapieco & Brüggén (2015), ^rBrüggén & Scannapieco (2016), ^sBanda-Barragán et al. (2016), ^tBanda-Barragán et al. (2018).

* Banda-Barragán et al. (2016) also use a softened equation of state in addition to their adiabatic simulations.

1.4.2 Other related numerical studies

Related studies not discussed in this chapter include shell-cloud (e.g. [Pittard, 2011](#)), jet-cloud (e.g. [Fragile et al., 2017](#)), and cloud-cloud (e.g. [Duarte-Cabral et al., 2011](#)) interactions, as well as ram-pressure stripping of the ISM from galaxies (e.g. [Close et al., 2013](#)).

1.5 Overview of this thesis

This work covers both HD and MHD simulations and spherical/non-spherical clouds; thus, there is inevitably a large and complex parameter space to be investigated, including, for example, the orientation of the filament, the orientation of the magnetic field lines, and Mach number of the shock/wind, etc. My work is, by nature, simplified. However, I believe that it lays much-needed groundwork for future simulations of more complicated scenarios.

The remainder of the thesis is organised as follows: in Chapter 2, I introduce the numerical methods and code that will be used in this thesis. In Chapter 3, I present the results of 3D MHD simulations of shock-filament interactions. Chapter 4 provides a comparison of 2D shock-cloud and wind-cloud interactions at varying wind Mach numbers and at low cloud density contrasts. Chapter 5 continues the simulations presented in the previous chapter and extends the investigation into higher cloud density contrasts. Chapter 6 expands the work in Chapter 3 to include 3D HD shock-filament interactions using a softened equation of state to mimic the effects of radiative cooling. Finally, Chapter 7 provides a summary of the conclusions drawn in this thesis and addresses the motivation for future work.

Chapter 2

Numerical Methods

This chapter presents the basic equations and structure of HD and ideal MHD codes. Since the numerical code MG was used to perform the calculations presented in this work, I focus on the implementation of these components within MG.

2.1 Basic equations

In order to solve a mathematical problem, various mathematical techniques can be employed to provide an analytical solution. However, this type of solution tends to work only for simple models. Numerical methods are used to provide approximate solutions to differential equations which cannot otherwise be solved analytically. In the HD case the equations being solved are the Euler equations of inviscid flow or the Navier-Stokes equations for a viscous flow. I will deal only with the Eulerian equations in this work and thus assume there to be zero thermal conductivity and viscosity. The full set of equations in Cartesian coordinates consist of the continuity equation,

$$\frac{\partial \rho}{\partial t} + \nabla \cdot (\rho \mathbf{u}) = 0, \quad (2.1)$$

the momentum equations for each component of momentum,

$$\frac{\partial \rho u}{\partial t} + \nabla \cdot (\rho u \mathbf{u}) + \frac{\partial P}{\partial x} = 0, \quad (2.2)$$

$$\frac{\partial \rho v}{\partial t} + \nabla \cdot (\rho v \mathbf{u}) + \frac{\partial P}{\partial y} = 0, \quad (2.3)$$

$$\frac{\partial \rho w}{\partial t} + \nabla \cdot (\rho w \mathbf{u}) + \frac{\partial P}{\partial z} = 0, \quad (2.4)$$

the energy equation,

$$\frac{\partial E}{\partial t} + \nabla \cdot [(E + P)\mathbf{u}] = 0, \quad (2.5)$$

and an equation to obtain an advected scalar, κ , in order to distinguish different regions within the solution,

$$\frac{\partial \rho \kappa}{\partial t} + \nabla \cdot (\rho \kappa \mathbf{u}) = 0. \quad (2.6)$$

κ has no physical meaning and does not affect the other fluid variables. In the above equations, P denotes the thermal pressure, \mathbf{u} is the velocity vector with components u , v , w in the x , y , z directions, respectively, and ρ represents the mass density. The total (thermal + kinetic) energy density, E , is given by the following equation of state,

$$E = \frac{P}{\gamma - 1} + \frac{1}{2} \rho \mathbf{u}^2, \quad (2.7)$$

where γ represents the adiabatic index, or heat capacity, of the gas (I assume a value of $\gamma = 5/3$ for an ideal monoatomic gas throughout this thesis, apart from Chapter 6 where I use $\gamma = 1.01$ for an isothermal filament).

In this thesis, I ignore the effects of gravity in all my calculations. This is because my calculations are intentionally scale-free (thereby enabling them to be scaled to

any physical size or timescale) and simple, whereas the inclusion of gravity would add a physical scale and complexity to the simulations. In any case, not all clouds or filaments may be gravitationally bound.

A sub-grid turbulence model (the k - ϵ model, which is commonly used in fluid dynamics to model the mean flow in fully developed, high Reynolds number turbulence - see [Dash and Wolf \(1983\)](#) for a description of this model and [Falle \(1994\)](#) for details of its implementation in MG. Here, two additional fluid variables are used to represent the turbulent motion of the flow: k represents the turbulence kinetic energy and ϵ represents the rate of dissipation of turbulence energy) can also be supplemented into the above set of equations in order to model turbulent viscosity in the flow (see [Pittard et al. \(2009\)](#) for the full set of equations, including the k - ϵ model, in cylindrical coordinates). The sub-grid turbulence model is not discussed in detail here since it has not been specifically used in any of the successive chapters. However, the term “inviscid” is used when discussing simulations performed without the k - ϵ model in other works that have featured this model; various chapters will make reference to some of these works.

2.2 Finite volume method

In order to numerically solve the Euler equations, an approximate solution (achieved via a numerical method) is needed. Firstly, the differential equations must be discretised. One method used to perform such discretisation is the finite-volume method. The domain over which the calculations are to be performed is subdivided into finite volumes, or cells, which have single values for each of the conserved quantities (e.g. density, momentum, energy, advected scalar) before the equations are integrated over each particular cell volume. For example, the integration over

Equation 2.1 is given by,

$$\iiint_V \frac{\partial \rho}{\partial t} dV + \iiint_V \nabla \cdot (\rho \mathbf{u}) dV = 0. \quad (2.8)$$

Using the divergence theorem, this can be re-written as,

$$\frac{\partial \rho V}{\partial t} + \oint_A \rho (\mathbf{u} \cdot \hat{\mathbf{n}}) dA = \frac{\partial \rho V}{\partial t} + F(\rho) = 0, \quad (2.9)$$

where A is the area bounding the cell. The above equation states that the rate of change of mass contained in a volume V during time interval dt is equal to the net mass flux through the surface $F(\rho)$ bounding that volume. Thus, whilst mass is able to move from one volume to another, the overall mass is conserved (certain boundary conditions, however, may mean that the equation is not conservative at the edges of the domain; for example, in cases where mass is allowed to flow into or out of the system).

Secondly, the equations must also be discretised in time. This allows the solution to be advanced from one point in time (t_n) to another (t_{n+1}) so that the mass in a particular cell can be calculated at the next time step using the current state of the cell. The change from one discrete time to another over a given time step is found by integrating the flux over the time step,

$$(\rho_{ijk}^{n+1} - \rho_{ijk}^n)V + \int_{t_n}^{t_{n+1}} F_{ijk}(\rho) dt = 0, \quad (2.10)$$

where n is the time step index and F_{ijk} is the sum of the fluxes across the six surfaces bounding the cubic cell indexed by the spatial coordinates ijk .

For the sake of simplicity, I consider a one-dimensional flow. Assuming that the velocity is constant across the face of a particular cell, the total flux in the x direction is the difference between the fluxes of both the left and right faces of a cubic cell of

Numerical Methods

length h ,

$$F_i(\rho) = F_{i-1/2}(\rho) - F_{i+1/2}(\rho), \quad (2.11)$$

where

$$F_{i\pm 1/2} = h^2(\rho u)_{i\pm 1/2}. \quad (2.12)$$

In order for the equation to be fully discretised, F needs to be approximated by its average value, \bar{F} ,

$$\int_{t_n}^{t_{n+1}} F_i(\rho) dt = \Delta t \bar{F}_i(\rho). \quad (2.13)$$

Thus, by combining Equations 2.9, 2.11, and 2.13, the mass advection step in the x direction is given by,

$$\rho_{ijk}^{n+1} = \rho_{ijk}^n + \Delta t \bar{F}_{i-1/2,jk}(\rho) - \Delta t \bar{F}_{i+1/2,jk}(\rho), \quad (2.14)$$

where the index i has been replaced by ijk in order to denote the three-dimensional index of the cubic domain. Similarly, the advection of both momentum and energy is given by,

$$(\rho u)_{ijk}^{n+1} = (\rho u)_{ijk}^n + \Delta t \bar{F}_{i-1/2,jk}(\rho u) - \Delta t \bar{F}_{i+1/2,jk}(\rho u), \quad (2.15)$$

and

$$E_{ijk}^{n+1} = E_{ijk}^n + \Delta t \bar{F}_{i-1/2,jk}(E + P) - \Delta t \bar{F}_{i+1/2,jk}(E + P). \quad (2.16)$$

The final step involves calculating the average fluxes, \bar{F} , by solving the Riemann problem across each cell boundary (the Godunov scheme, [Godunov, 1959](#)). This procedure will be discussed in the following section.

2.3 The Riemann problem

The Riemann problem concerns two distinct states, each with constant density, velocity, and pressure, and delineates what happens once the boundary between them is removed and the flow allowed to evolve. A vector, \mathbf{W} , is used to represent the set of primitive values,

$$\mathbf{W} = \begin{bmatrix} \rho \\ u \\ p \end{bmatrix}, \quad (2.17)$$

and the initial values of the Riemann problem are given by,

$$\mathbf{W}(x, 0) = \begin{cases} \mathbf{W}_L & \text{if } x < 0 \\ \mathbf{W}_R & \text{if } x > 0. \end{cases} \quad (2.18)$$

Solving the Riemann problem allows the fluxes for each variable between the two states to be calculated and the cell values updated using Equations 2.14, 2.15, and 2.16.¹

The Riemann problem solution has three waves. These waves split the flow into four regions, W_L , W_{*L} , W_{*R} , and W_R , where the subscripts L and R denote the left and right states, respectively (see Fig. 2.1). The inner two of these four regions, separated by a contact discontinuity, are maintained at the same pressure and velocity, i.e. $P_{*L} = P_{*R} = p_*$ and $u_{*L} = u_{*R} = u_*$. Thus, we are left with four unknown quantities (p_* , u_* , ρ_{*L} , and ρ_{*R}). The pressure, p_* , is found by solving the following equation,

$$f(p_*, \mathbf{W}_L, \mathbf{W}_R) = f_{L/R}(p_*, \mathbf{W}_L) + f_{L/R}(p_*, \mathbf{W}_R) + u_R - u_L = 0 \quad (2.19)$$

¹This is valid only as long as the waves originating from one boundary do not interact with those from another. To avoid this, the *Courant-Friedrichs-Lewy* condition is employed and is given by $\Delta t \leq C \frac{h}{u}$, where C is the Courant number and varies depending on the nature of the problem. MG uses a conservative value of the Courant number, $C = 0.4$, in order to completely avoid wave interactions and, thus, provide greater numerical stability.

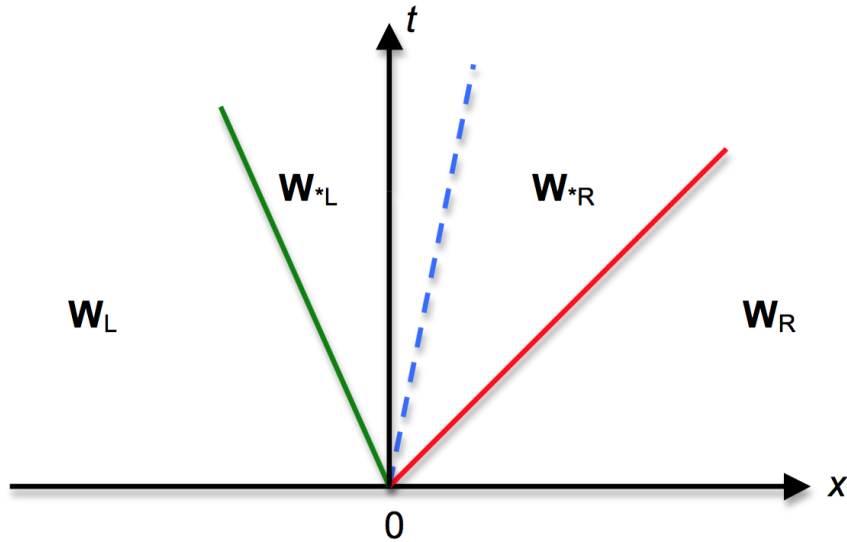


Fig. 2.1 Space-time diagram indicating the solution to the Riemann problem. Here, a contact discontinuity is represented by a blue dashed line, while the red and green lines to either side of this denote the waves.

(Toro, 2009), where

$$f_{L/R}(p_*, \mathbf{W}) = \begin{cases} (p_* - p) \left[\frac{2}{((\gamma+1)p_* + (\gamma-1)p)\rho} \right]^{1/2} & \text{if } p_* > p \text{ (shock),} \\ \frac{2}{\gamma-1} \sqrt{\frac{\gamma p}{\rho}} \left[\left(\frac{p_*}{p} \right)^{\frac{\gamma-1}{2\gamma}} - 1 \right] & \text{if } p_* \leq p \text{ (rarefaction).} \end{cases} \quad (2.20)$$

The case that has left and right waves as rarefactions is linear and solvable directly. In the case of a shock, however, the equation must be solved by an iterative method, i.e.,

$$p_{*i+1} = p_{*i} - \frac{f(p_{*i}, \mathbf{W}_L, \mathbf{W}_R)}{f'(p_{*i}, \mathbf{W}_L, \mathbf{W}_R)}. \quad (2.21)$$

The initial guess is provided by a linear solver, similar to the two shock approximation given in Toro (2009),

$$\begin{cases} p_0 = \max(p_{floor}, PTS) \\ PTS = \frac{g_L(\hat{p})p_L + g_R(\hat{p})p_R - (u_R - u_L)}{g_L(\hat{p}) + g_R(\hat{p})}, \\ g_K(p) = \left(\frac{2}{[(\gamma+1)p + (\gamma-1)p_K]\rho_K} \right)^{1/2} \end{cases} \quad (2.22)$$

2.3 The Riemann problem

where p_{floor} is a small positive value used to maintain the positivity of the pressure and \hat{p} is an initial guess. MG uses the variables p_L and p_R as guesses in g_L and g_R , respectively. The above equation can be reduced to

$$p_0 = \frac{\rho_R a_R p_L + \rho_L a_L p_R - \rho_R \rho_L a_R a_L (u_R - u_L)}{\rho_R a_R + \rho_L a_L}, \quad (2.23)$$

where a is the adiabatic sound speed and is given by $a = \sqrt{\gamma p / \rho}$. The determination of p_* to the desired accuracy requires many arbitrary iterations and is computationally slow. In order to mitigate against this slowness, MG iterates until the difference between p_{*i+1} and p_{*i} is less than 0.01%. Thus, unless the value of p_* given by the linear solver differs by more than 10% from either p_L or p_R , p_0 is taken to be the final result and the iterative method is not used. This initial guess can also be used in Equation 2.20 to delineate whether the wave is a shock or a rarefaction

When the pressure of the intermediate region is known, the wave velocity, u_* , can be calculated as follows,

$$u_* = \frac{1}{2}(u_L + u_R) + \frac{1}{2}[f_{R/L}(p_*, \mathbf{W}_R) - f_{R/L}(p_*, \mathbf{W}_L)]. \quad (2.24)$$

The density either side of the contact discontinuity (e.g. regions W_{*L} and W_{*R}) can now be found, depending on the type of wave. In the case of a shock, the RH conditions can be used. Combining the three RH conditions for mass, momentum, and energy gives,

$$\rho_{*K} = \rho_K \left[\frac{\frac{p_*}{p_K} + \frac{\gamma-1}{\gamma+1}}{\frac{\gamma-1}{\gamma+1} \frac{p_*}{p_K} + 1} \right], \quad (2.25)$$

where K represents either the left or right waves (L or R , respectively). In the case of a rarefaction wave, and assuming isentropic expansion,

$$\rho_{*K} = \rho_K \left(\frac{p_*}{p_K} \right). \quad (2.26)$$

Numerical Methods

The boundary of the cell (at $x = 0$) can be placed in one of the four regions if the speed of each wave is calculated. A positive wave speed places it to the right of the boundary, whilst a negative wave speed places it to the left. For a rarefaction, there are two wave speeds: one for the head and one for the tail.

The wave speeds for all possible waves are given by,

$$S_{cd} = u_*, \quad (2.27)$$

$$S_{shock,K} = u_K \mp a_K \left[\frac{\gamma+1}{2\gamma} \frac{p_*}{p_K} + \frac{\gamma-1}{2\gamma} \right]^{1/2}, \quad (2.28)$$

$$S_{rf,head,K} = u_K \mp a_K, \quad (2.29)$$

$$S_{rf,tail,K} = u_{*K} \mp a_{*K}, \quad (2.30)$$

where the subscripts cd , $shock$, rf , $head$, and $tail$ refer to the contact discontinuity, a shock, a rarefaction wave, and the head and tail of the rarefaction, respectively. Here, \mp takes the upper sign for a left wave and the lower sign for a right wave. If the signs of $S_{rf,head,K}$ and $S_{rf,tail,K}$ are in opposition, the interface falls within the rarefaction fan. The values within the fan are not uniform and are given by,

$$\mathbf{W}_{rf,K}(x,t) = \begin{cases} \rho_{rf,K}(x,t) = \rho_K \left[\frac{2}{\gamma+1} \pm \frac{\gamma-1}{(\gamma+1)a_K} \left(u_K - \frac{x}{t} \right) \right]^{\frac{2}{\gamma-1}}, \\ u_{rf,K}(x,t) = \frac{2}{\gamma+1} \left[\frac{\gamma-1}{2} u_K \pm a_K + \frac{x}{t} \right], \\ p_{rf,K}(x,t) = p_K \left[\frac{2}{\gamma+1} \pm \frac{\gamma-1}{(\gamma+1)a_K} \left(u_K - \frac{x}{t} \right) \right]^{\frac{2}{\gamma-1}}, \end{cases} \quad (2.31)$$

where \pm takes the upper sign for a left wave and the lower sign for a right wave. $\mathbf{W}_{rf,K}$ is constant over time at the cell boundary ($x = 0$) and therefore the flux across the boundary is also constant. If the region where the cell boundary lies is known,

the average flux can then be calculated. The total flux is the sum of the flux across each of the six cell faces. Once the total flux has been calculated, the fluid variables are then updated with the contributions from Equations 2.14, 2.15, and 2.16.

2.3.1 Second order accuracy

The above subsections describe the Godunov method, which is first-order in time and space. First-order methods such as this tend to be diffusive, and in order to counteract this, MG uses methods that are second-order accurate in space and time in order to speed up the calculations. The above first-order method for spatial reconstruction uses the piecewise constant method under the assumption that the fluid variables are constant within the cells. Second-order accuracy is obtained under the assumption that the variables vary linearly within the cells. However, such accuracy requires the gradients within each cell to be known. Here, the average value across the entire cell is the stored value. MG achieves second-order accuracy via the piecewise linear method which interpolates between cell values. Determination of the slope can take a variety of forms. However, MG uses the steepest slope whilst simultaneously ensuring the condition that the values at the cell boundaries fall between the constant cell values. Once the gradients have been determined suitably for each cell, the left and right states for the Riemann problem can be set up in order to compute the fluxes across the complete time-step.

The achievement of second-order accuracy in time is performed using a second-order Runge-Kutta method. Here, the piecewise constant method is used to advance the solution by half a time-step, with the resulting state then used to determine the fluxes needed to advance the initial state by a complete time-step using a piecewise linear method.

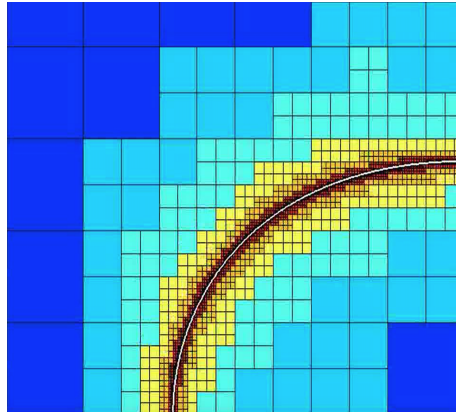


Fig. 2.2 An example of an AMR grid using six levels of refinement. The density of the region is denoted by the colour scale. Refined (small squares) and derefined (large squares) areas are shown.

2.4 Adaptive Mesh Refinement

In many numerical studies, the flow over most of the numerical domain might be relatively uniform. However, if small areas of the computational grid are more detailed than their surroundings a much finer grid is required. To refine the entire grid would be computationally expensive and would slow the calculations down significantly. If the locations where a greater level of precision is needed are known in advance, it is possible to use a static non-uniform grid with a much finer mesh at these positions in order to resolve these features, though such a grid would obviously have limitations. However, generally, such requirements for refinement evolve as the solution evolves. Adaptive Mesh Refinement (AMR) is a method that creates increasingly fine grid levels only where/when required, as determined by the solution, thus increasing the accuracy and speed of the calculation. Figure 2.2 shows an example of an AMR grid with refined and derefined areas. Here, unrefined areas show a much larger grid, while regions with greater detail show an increasingly finer grid at points where the solution is continuously changing.

In MG, a hierarchy of n grid levels, $G^0 \dots G^{n-1}$, is used and the two coarsest (or largest) grids (G^0 and G^1) cover the entire domain, with finer grids being added where needed and removed where they are not. The time step on grid G^n is $\Delta t_0/2^n$,

where Δt_0 is the time step on grid G^0 . The amount of refinement is increased at points in the mesh where shocks or discontinuities exist, i.e. where the variables associated with the fluid show steep gradients that are unable to be resolved by the coarser grid. At these points, the number of computational grid cells produced by the previous level is increased by a factor of 2 in each spatial direction. Thus, fine grids are only utilised in regions where the flow is highly variable, with much coarser grids used where the flow is relatively uniform. Refinement and derefinement are performed on a cell-by-cell basis and are controlled by the differences in the solutions on the two coarsest grids. Each refinement level solves the Riemann problem and calculates the fluxes and then updates the fluid variables. Refinement occurs when there is a difference of more than 1 percent between a conserved variable in the finest grid and its projection from a grid one level down. If the difference in the two preceding levels falls to below 1 percent, the cell is derefined. In order to maintain accuracy and ensure a smooth transition between multiple levels, the refinement criteria are, to an extent, diffused, with the code attempting to refine neighbouring cells in order to prevent steep jumps in the resolution between the two cells that would impact the refinement process. AMR can be computationally very expensive in situations where the entire grid requires a high resolution, although for situations where this is not the case AMR provides the perfect balance between computational speed and the required resolution.

2.5 MHD

In addition to solving the Euler equations, MG can also solve the ideal MHD equations,

$$\frac{\partial \rho}{\partial t} + \nabla \cdot (\rho \mathbf{u}) = 0, \quad (2.32)$$

$$\frac{\partial \rho u}{\partial t} + \nabla \cdot (\rho u \mathbf{u} - B_x \mathbf{B} + P) = 0, \quad (2.33)$$

$$\frac{\partial \rho v}{\partial t} + \nabla \cdot (\rho v \mathbf{u} - B_y \mathbf{B} + P) = 0, \quad (2.34)$$

$$\frac{\partial \rho w}{\partial t} + \nabla \cdot (\rho w \mathbf{u} - B_z \mathbf{B} + P) = 0, \quad (2.35)$$

$$\frac{\partial E}{\partial t} + \nabla \cdot [(E + P) \mathbf{u} - (\mathbf{B} \cdot \mathbf{u}) \mathbf{B}] = 0, \quad (2.36)$$

again, consisting of the continuity, momentum, and energy equations, respectively. In addition, the ideal MHD equations also include the induction equation,

$$\frac{\partial \mathbf{B}}{\partial t} - \nabla \times (\mathbf{u} \times \mathbf{B}) = 0. \quad (2.37)$$

In the above equations, $E = \frac{p_g}{\gamma-1} + p_m + \frac{1}{2} \rho u^2$ is the total energy per unit volume, \mathbf{B} is the magnetic field strength, and P is the total pressure (given by the gas pressure p_g plus the magnetic pressure $p_m = \frac{1}{2} B^2$). A factor of $1/\sqrt{4\pi}$ has been incorporated into the definition of the magnetic field in the above equations in order to simplify them. As in the hydrodynamic case, the ideal MHD equations are solved by solving the Riemann problem at each interface.

The MHD problem presents difficulties when ensuring that the condition

$$\nabla \cdot \mathbf{B} = 0 \quad (2.38)$$

remains true when using the conservative form of the MHD equations. $\nabla \cdot \mathbf{B}$ is typically not zero (but remains small) in numerical calculations, but the equations used to approximate the MHD equations use the conservative form which requires

the above condition to be true. Therefore, while the condition holds initially, it begins to evolve as errors are introduced. Unless explicitly enforced, the condition misbehaves in regions where the forces are close to equilibrium and fails if there is a discontinuity in the magnetic field in the initial state. Thus, the condition is prone to violation by magnetic monopoles introduced by numerical errors which are able to break the solution in the region of discontinuities (Brackbill and Barnes, 1980). Although Brackbill and Barnes (1980) proposed using the non-conservative form of the momentum equation to solve this problem, this was not found to be effective when the flow contained a shock. To get around this, Falle et al. (1998) instead used a second-order upwind scheme which uses a linear approximation for all Riemann problems except for those which involve strong rarefactions, and added source terms to remove the effect of the numerical monopoles. Thus, MG_M (the MHD version of MG) utilises the divergence cleaning scheme of Dedner et al. (2002) to transport these divergence errors to the domain boundaries and coincidentally dampen them.

Another complicating factor is the use of primitive variables in the MHD code. Whilst the Riemann problem is governed by the conservative form of the MHD equations, MG uses primitive variables, \mathbf{P} , in order to more easily solve the linear Riemann problem,

$$\mathbf{P} = [\rho, v_x, v_y, v_z, p_g, B_y, B_z]^t, \quad (2.39)$$

where ρ and p_g denote the density and gas pressure, and v and B denote the components of the velocity and magnetic field in the x, y, z directions. t denotes the transpose of the vector. The primitive variables satisfy

$$\frac{\partial \mathbf{P}}{\partial t} + \bar{\mathbf{A}} \frac{\partial \mathbf{P}}{\partial x} = 0. \quad (2.40)$$

Numerical Methods

The matrix, \mathbf{A} , is given by,

$$\mathbf{A} = \begin{pmatrix} v_x & \rho & 0 & 0 & 0 & 0 & 0 \\ 0 & v_x & 0 & 0 & \frac{1}{\rho} & \frac{B_y}{\rho} & \frac{B_z}{\rho} \\ 0 & 0 & v_x & 0 & 0 & -\frac{B_x}{\rho} & 0 \\ 0 & 0 & 0 & v_x & 0 & 0 & -\frac{B_x}{\rho} \\ 0 & \rho a^2 & 0 & 0 & v_x & 0 & 0 \\ 0 & B_y & -B_x & 0 & 0 & v_x & 0 \\ 0 & V_z & 0 & -B_x & 0 & 0 & v_x \end{pmatrix} \quad (2.41)$$

where a is the adiabatic sound speed. The above matrix represents the Jacobian matrix of fluxes with respect to the primitive variables. A mean matrix,

$$\bar{\mathbf{A}}(P_L, P_R) = \mathbf{A} \left[\frac{1}{2}(P_L + P_R) \right], \quad (2.42)$$

is used to construct an approximate solution to the linear problem, and is dependent on the left and right states. Use of the primitive variable equations only requires seven variables because the condition $\nabla \cdot \mathbf{B} = 0$ renders the x component of the magnetic field constant if there is no dependence on y or z . Therefore, there are seven waves (the speeds of which are given by the eigenvalues of \mathbf{A}) which need computing, thus adding a degree of complexity to the MHD equations in comparison to the HD equations. [Falle et al. \(1998\)](#) discuss in detail how the fluxes are computed from the eigenvectors of $\bar{\mathbf{A}}$ using a simple linear Riemann solver.

Chapter 3

Magnetohydrodynamic Filament Simulations

3.1 Introduction

The ISM is known to be a highly dynamic and non-uniform entity containing regions of varying temperature and density (see Section 1.1). Studies of the interaction of hot, high-velocity gas (e.g. shocks or winds) with cooler, dense material (i.e. clouds) are of great interest for a complete understanding of the gas dynamics of the ISM. Recently, *Herschel* images have revealed the ubiquitous presence of filamentary structures throughout the ISM in both star-forming and non-star-forming regions (e.g. [André et al. 2010](#), [André et al. 2014](#)). Since filaments harbour dense clumps or cores that may eventually become stars, investigations into their origin and evolution are important for understanding star-formation (§ 1.1.2).

The interactions of spherical molecular clouds with SNR shockwaves have been well observed and studied (see [Pittard and Parkin \(2016\)](#) for a comprehensive overview of the characteristics of such interactions). Whilst there are instances in the literature of the interactions of jets and winds with filaments, there have been very few studies devoted to shock-filament interactions. Therefore, a wide-ranging

Magnetohydrodynamic Filament Simulations

discussion of such observations presents difficulties. [Zhou et al. \(2014\)](#) discuss the interaction of SNR G127.1+0.5 with an external filament. However, in this case the filament is very large and significant changes in the shock properties can be expected as it sweeps over the filament. This precludes a detailed comparison with my work.

The presence of magnetic fields can strongly change the nature of a shock-cloud interaction. 2D axisymmetric simulations have shown that if there is a magnetic field present then the formation of the KH and RM instabilities are impeded and the mixing of the cloud with the flow is reduced ([Mac Low et al., 1994](#)). Furthermore, 3D simulations have revealed that the orientation of the field with respect to the cloud has a significant effect on the evolution of the cloud's morphology ([Shin et al., 2008](#)).

There is now a large body of literature, beginning in the 1970s, concerning the idealised case of a planar adiabatic shock striking an isolated spherical cloud (see § 1.3). However, there are very few numerical studies in the current literature which consider interactions involving non-spherical clouds, and (to my knowledge) none which describe in detail the effects of a magnetic field on these interactions. This chapter extends the purely hydrodynamic work conducted by [Pittard and Goldsmith \(2016\)](#). By nature, it represents an idealised scenario before more realistic simulations of filaments are conducted. I investigate the effects that magnetic fields have on shock-filament interactions by varying the Mach number (M), density contrast (χ), and plasma beta (β_0), in addition to varying the orientation and length of the filament, θ and l , respectively, for parallel, perpendicular, and oblique magnetic fields. In § 3.2 I introduce the initial conditions and the results of a convergence study. In § 3.3 I present the results of my simulations. A discussion of the relevance of my work to shock-filament and wind-filament studies is given in § 3.4, and § 3.5 summarises and concludes, and addresses the motivation for further work.

3.2 Method

3.2.1 Numerical setup

The computations were performed using the MG magnetohydrodynamic code, details of which can be found in Chapter 2.

3.2.1.1 Initial conditions

A three-dimensional XYZ cartesian grid was used with constant inflow from the negative x direction and free inflow/outflow conditions at other boundaries. The numerical domain was set to be large enough so that the main features of the interaction occurred before the shock reached the edge of the grid. Since the grid extent is χ -dependent (because, for example, a larger value of χ means that a hydrodynamical cloud takes longer to be destroyed, and therefore a larger grid is needed - see [Pittard et al. \(2010\)](#) §4.1.2. for a discussion on how the nature of the interaction changes with χ for hydrodynamic cases) and M -dependent the grid extent for each simulation is given in Table 3.1. The number of grid levels used was 7 (see § 2.4). All length scales are measured in units of the filament radius, r_c , where $r_c = 1$, the unit of density is taken to be the density of the surrounding unshocked gas, $\rho_{\text{amb}} = 1.9 \times 10^{-5}$ (in computational units), and the ambient pressure is $P_{\text{amb}} = 2.2 \times 10^{-5}$ (also in computational units). The effective resolution is taken to be the resolution of the finest grid and is given as R_{cr} , where ‘cr’ is half the number of cells per filament semi-minor axis in the finest grid, equivalent to the number of cells per cloud radius for a spherical cloud. In this chapter, the resolution used is R_{32} (see § 3.2.2). I impose no inherent scale on my simulations, thus my results are applicable to a broad range of scenarios.

The simulated cloud is a cylinder of length l with hemispherical caps, representing an idealised filament, and the total length of the filament is given by $(l + 2)r_c$.

Magnetohydrodynamic Filament Simulations

Table 3.1 The grid extent for each of the simulations. M is the sonic Mach number and χ is the cloud density contrast. The unit of length is the initial filament radius, r_c .

M	χ	X	Y	Z
10	10	$-20 < X < 560$	$-10 < Y < 10$	$-12 < Z < 10$
10	$10^{2,\dagger}$	$-20 < X < 500$	$-14 < Y < 14$	$-23 < Z < 15$
10	$10^{2,\ddagger}$	$-20 < X < 1000$	$-14 < Y < 14$	$-30 < Z < 14$
10	$10^{3,\dagger}$	$-20 < X < 300$	$-14 < Y < 14$	$-41 < Z < 15$
10	$10^{3,\ddagger}$	$-20 < X < 800$	$-14 < Y < 14$	$-40 < Z < 20$
3	10	$-20 < X < 500$	$-14 < Y < 14$	$-15 < Z < 13$
1.5	10	$-20 < X < 800$	$-12 < Y < 20$	$-20 < Z < 20$

Notes: \dagger parallel magnetic field; \ddagger perpendicular/oblique magnetic field

I am therefore able to vary the aspect ratio and orientation of the filament in order to investigate how such changes might alter the interaction. The filament has been given smooth edges over about 10% of its radius,

$$\rho(r) = \rho_{\text{amb}}[\psi + (1 - \psi)\eta] \quad (3.1)$$

(see Pittard et al., 2009), where

$$\eta = \frac{1}{2} \left(1 + \frac{\alpha - 1}{\alpha + 1} \right), \quad (3.2)$$

$$\alpha = \exp\{\min[20.0, p_1((r/r_c)^2 - 1)]\}. \quad (3.3)$$

Here, r is the distance from the cloud centre, r_c is the cloud radius, $\psi \simeq \chi = \rho_{\text{max}}/\rho_{\text{amb}}$, and the parameter p_1 controls the steepness of the profile at the cloud edge. Throughout this chapter I use a value of $p_1 = 10$ to give a reasonably sharp-edged cloud. The filament and surrounding ambient medium are in pressure equilibrium. The filament is centred on the grid origin $x, y, z = (0, 0, 0)$ with the planar shock front (propagating through a magnetised ambient medium) imposed on the grid at $x = -10$. Figure 3.1 shows the interaction at $t = 0t_{cs}$ (see Eq. 3.12 for the

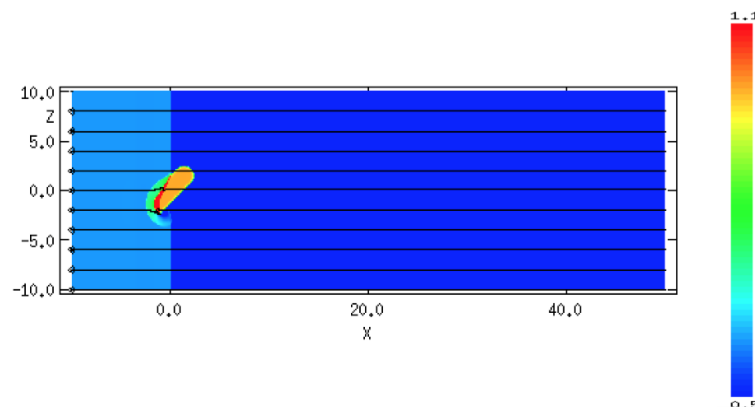


Fig. 3.1 The interaction at $t = 0t_{cs}$ for model *m10c1b1l4o45pa* (see § 3.3 for the model naming convention). The scale shows logarithmic density, from red (highest density) to blue (lowest density). The density has been scaled with respect to the ambient density so that a value of 0 represents the value of ρ_{amb} and 1 represents $10 \times \rho_{\text{amb}}$. The filament is initially positioned at the origin, with the spatial scale in units of the initial filament radius r_c . The shock front moves from $-x$ to $+x$ and the magnetic field lines are parallel to the shock front.

definition of this timescale). The simulations are described by the sonic Mach number of the shock M , the cloud density contrast χ , the filament length l , and the ratio of thermal to magnetic pressure (also known as the “plasma beta”) $\beta_0 = 8\pi P_{\text{amb}}/B_0^2$, where P_{amb} is the ambient thermal pressure and B_0 is the ambient magnetic field strength. The filament orientation with respect to the z axis (or shock front), θ , and the magnetic field orientation with respect to the shock normal in the xz plane, are also considered. In the following simulations, the magnetic field is given a parallel, perpendicular, or oblique (i.e. oriented at 45° to the shock normal) orientation. It should be noted, however, that only one specific perpendicular or oblique orientation of the field was included in this chapter owing to the already large parameter space under consideration, and that other perpendicular/oblique orientations may produce different effects on the evolution of the filament to those described in this study. The simulations are scale-free and expressed in dimensionless units. The properties of the flow behind the shock front are described by the RH jump conditions (see § 1.2).

3.2.1.2 Global quantities

Various diagnostic quantities are used to follow the evolution of the interaction (see [Klein et al., 1994](#); [Nakamura et al., 2006](#); [Pittard et al., 2009](#); [Pittard and Parkin, 2016](#)). These quantities include the filament mass (m), mean density ($\langle \rho \rangle$), filament volume (V), mean velocity along each axis (e.g. $\langle v_x \rangle$), and velocity dispersions along each orthogonal axis (e.g. δv_x). Averaged quantities, $\langle f \rangle$, are calculated according to

$$\langle f \rangle = \frac{1}{m_\beta} \int_{\kappa \geq \beta} \kappa \rho f \, dV, \quad (3.4)$$

where m_β , the mass which is identified as being part of the cloud, is given by

$$m_\beta = \int_{\kappa \geq \beta} \kappa \rho \, dV. \quad (3.5)$$

The mass-weighted mean velocity of the filament in each direction ($\langle v_x \rangle$, $\langle v_y \rangle$, $\langle v_z \rangle$) and the velocity dispersions in all three directions, defined as

$$\delta v_x = (\langle v_x^2 \rangle - \langle v_x \rangle^2)^{1/2}, \quad (3.6)$$

$$\delta v_y = (\langle v_y^2 \rangle - \langle v_y \rangle^2)^{1/2}, \quad (3.7)$$

$$\delta v_z = (\langle v_z^2 \rangle - \langle v_z \rangle^2)^{1/2}, \quad (3.8)$$

are monitored, as well as the mean density, which is given as

$$\langle \rho \rangle = \frac{m_\beta}{V_\beta}, \quad (3.9)$$

where V_β is the volume of a region having $\kappa \geq \beta$.

An advected scalar, κ , is used to trace the filament material in the flow, allowing the whole filament along with its denser core to be distinguished from the ambient medium. κ has an initial value of $\rho/(\chi\rho_{\text{amb}})$ for cells located a distance of $2.25 r_c$ from the cloud centre, and $\kappa = 0$ for distances greater than this. Thus at the centre of the cloud $\kappa = 1$, and it declines for cells further out, reducing to a value of zero for the surrounding ambient material. β is the threshold value, and integrations are performed over cells where $\kappa \geq \beta$. Two related sets of quantities can thus be investigated: setting $\beta = 0.5$ explores the densest part of the cloud and its associated fragments (termed the ‘core’), and setting $\beta = 2/\chi$ explores the entire cloud, the surrounding low-density envelope, and regions where a low percentage of material shows mixing with the ambient flow (termed the ‘cloud’). Therefore, each of the global quantities is able to be computed for the cells associated with either the filament core (using the subscript “core”, e.g. m_{core}) or the entire filament (using the subscript “cloud”, e.g. m_{cloud}).

3.2.1.3 Timescales

Time zero in my calculations is taken to be the time when the inter-cloud shock is level with the centre of the filament. Klein et al. (1994) defined a characteristic timescale for a spherical cloud to be crushed by the shock being driven into it (the “cloud-crushing time”),

$$t_{cc} = \frac{\chi^{1/2} r_c}{v_b}, \quad (3.10)$$

where v_b is the shock velocity in the ambient medium. A second timescale was defined by Klein et al. (1994), namely a modified cloud-crushing time for cylindrically-shaped clouds,

$$t'_{cc} = \frac{(\chi a_0 c_0)^{1/2}}{v_b}, \quad (3.11)$$

where a_0 and c_0 are the initial radii of the cloud in the radial and axial directions respectively. Xu and Stone (1995) instead provided a modified cloud-crushing time

for prolate clouds,

$$t_{cs} = \frac{r_s \chi^{1/2}}{v_b}, \quad (3.12)$$

where r_s is the radius of a sphere of equivalent mass. [Pittard and Goldsmith \(2016\)](#) compared all three timescales and found that the one defined by [Xu and Stone \(1995\)](#) for prolate clouds gave a slightly better reduction in variance between the simulations. Therefore, this timescale, t_{cs} , has been adopted for this Chapter, with the assumption that the smooth edges to the filament can be approximated as reasonably sharp edges ([Pittard et al. 2009](#)).

Several other timescales are available. For example, the “drag time”, t_{drag} , is the time taken for the average cloud velocity relative to the post-shock flow to decrease by a factor of e (i.e. the time when the average cloud velocity $\langle v \rangle_{\text{cloud}} = (1 - 1/e) v_{ps}$, where v_{ps} is the velocity of the post-shock flow as measured in the frame of the pre-shock ambient medium); the “mixing time”, t_{mix} , is the time when the filament core mass is half that of its initial value, and the cloud “lifetime”, t_{life} , is the time taken for the filament core mass to reach 1% of its initial value.

3.2.2 Convergence studies

In numerical studies it is important to show that the quantities from the simulation under consideration are converged and do not change as the resolution increases, and that therefore the calculations are being performed at a resolution great enough to resolve clearly the main features of the interaction, e.g. the growth of magnetohydrodynamic instabilities. The growth of such instabilities at the cloud surface generates turbulence and any increase in resolution could lead to increasingly small scales with respect to the turbulence. Diagnostic quantities such as the mixing rate between cloud and ambient medium are sensitive to small-scale instabilities and are therefore less likely to show convergence. Resolution tests of numerical shock-cloud interactions for 2D adiabatic, hydrodynamic, spherical clouds have revealed that

such simulations require a resolution of at least 100 cells per cloud radius (R_{100}) for converged results (e.g. Klein et al. 1994; Nakamura et al. 2006), with more complex cases requiring even higher resolutions (e.g. Yirak et al. 2010). However, it is very computationally expensive to run 3D simulations to such high resolutions.

3D studies of spherical clouds have shown that convergence at resolutions as low as R_{32} is achievable, though to properly capture the behaviour of the interaction a resolution of R_{64} is necessary (Pittard and Parkin, 2016). Even more encouragingly, these authors found very little difference between inviscid and $k - \varepsilon$ turbulence model¹ simulations (it had previously been established that 2D studies which include the $k - \varepsilon$ model are convergent at lower resolutions, in contrast with inviscid studies - see Pittard et al. 2009). The non-turbulent, hydrodynamic 3D Xu and Stone (1995) study found that the evolution of the effective size of a prolate cloud was resolution-dependent and that a resolution of at least R_{27} was needed for convergence of all the diagnostic quantities. However, because a large grid was required for their cloud they were unable to run a “high” resolution simulation to test this. One of the few 3D MHD resolution tests in the literature was performed by Shin et al. (2008) for a spherical cloud using a non-AMR code at resolutions of R_{120} and R_{60} and concluded that most aspects of the MHD shock-cloud interaction were well converged at both resolutions. To my knowledge, the only resolution tests for a 3D purely hydrodynamic shock-filament interaction were performed by Pittard and Goldsmith (2016), who demonstrated that convergence was possible at a resolution of R_{32} .

I extend these resolution tests to a 3D MHD shock-filament interaction. I focus on two measures, the mean cloud velocity, $\langle v_x \rangle$, and the core mass of the cloud, m_{core} , which are affected by the cloud material becoming mixed with the flow and which

¹The subgrid $\kappa - \varepsilon$ turbulence model is used to model the mean flow in fully-developed, high Reynolds number turbulence. It has been calibrated by comparing the growth of shear layers determined experimentally with computed values (Dash and Wolf, 1983). Details of its implementation in MG can be found in Falle (1994).

Magnetohydrodynamic Filament Simulations

are therefore suitable indicators of convergence. In choosing these two quantities I follow the convention of previous papers such as [Pittard et al. \(2009\)](#), [Pittard and Parkin \(2016\)](#), and especially [Pittard and Goldsmith \(2016\)](#). However, it should be noted that although the latter paper included convergence tests that considered the resolution dependence of t_{drag} and t_{mix} for inviscid shock-filament calculations (as well as the evolution of the filament centre of mass in the x and z directions), no such tests have been run for filaments embedded in a magnetised medium in this chapter. Thus, the inclusion of these quantities in the resolution tests of future similar calculations should be considered.

It is known that simulations run with lower density contrasts are much more resolution-dependent. When $\chi = 10$ (which is the case for the majority of my simulations) the filament is destroyed more quickly at lower resolutions. Figure 3.2 shows the time evolution of the core mass (a) and mean cloud velocity (b) as a function of the spatial resolution for simulations with $M = 10$, $\beta_0 = 1$, $\chi = 10$, $l = 4$, a parallel field orientation, and a filament orientation of 45° to the z axis. Figure 3.3 illustrates the difference in resolution, in terms of the main features of the evolution of the filament, between resolutions R_8 and R_{32} . It can be seen from Fig. 3.2(b) that, with the exception of R_4 , all resolutions are reasonably convergent until approximately $30t_{cs}$, after which there is some slight divergence. However, from Fig. 3.2(a), it is clear that there are much larger differences between each of the simulations. There appears to be some convergence between R_{32} and R_{64} , at least until approximately $15t_{cs}$ when a fifth of the core mass has been lost, and the filaments in these simulations initially lose their core mass much more slowly than the filaments in the lower resolution simulations. However, I was restricted from comparing even higher resolution runs because of the large computational requirements.

Figure 3.4 shows the relative error, which is defined as the fractional difference between the value of a global parameter measured at a resolution N and that measured at the finest resolution f :

$$\Delta Q_N = \frac{|Q_N - Q_f|}{|Q_f|}, \quad (3.13)$$

where $f = 64$ for simulations with $M = 10$, $\chi = 10$, and $\beta_0 = 1$. It can be seen that, in general, the relative error decreases with increasing resolution, and thus manifests convergence. This is in line with the results from [Pittard and Parkin \(2016\)](#) and [Pittard and Goldsmith \(2016\)](#). Figure 3.4(a) shows that for a resolution of R_{32} all quantities have a relative error of below 5% at $t = 2t_{cs}$. As the simulations progress, the relative error in the core mass increases overall. However, for R_{32} , the relative error in the mass is still $\sim 5\%$ (and is even lower for the other quantities), indicating that a resolution of R_{32} provides reasonably-converged results, and adding support for the adoption of this resolution in all subsequent simulations.

3.3 Results

In this section I present the results of various simulations where I have varied M , χ , β_0 , l , and θ . Tables 3.2 and 3.3 summarise the calculations performed. I adopt a naming convention for each simulation such that *m10c1b1/2o45pa* refers to a simulation with $M = 10$, $\chi = 10$, $\beta_0 = 1$, $l = 2$, a filament orientation of $\theta = 45^\circ$ and a parallel magnetic field. The majority of the simulations performed are for $M = 10$, $\chi = 10$, and $\beta_0 = 1$, whilst the length and orientation of the filament are varied. Towards the end of each section I will also discuss the results from simulations with different Mach numbers, density contrasts, and plasma betas. A simulation of a spherical cloud of radius $r_c = 1$ is also included for comparison with filaments of varying length (note that these simulations were run with a resolution of R_{16}).

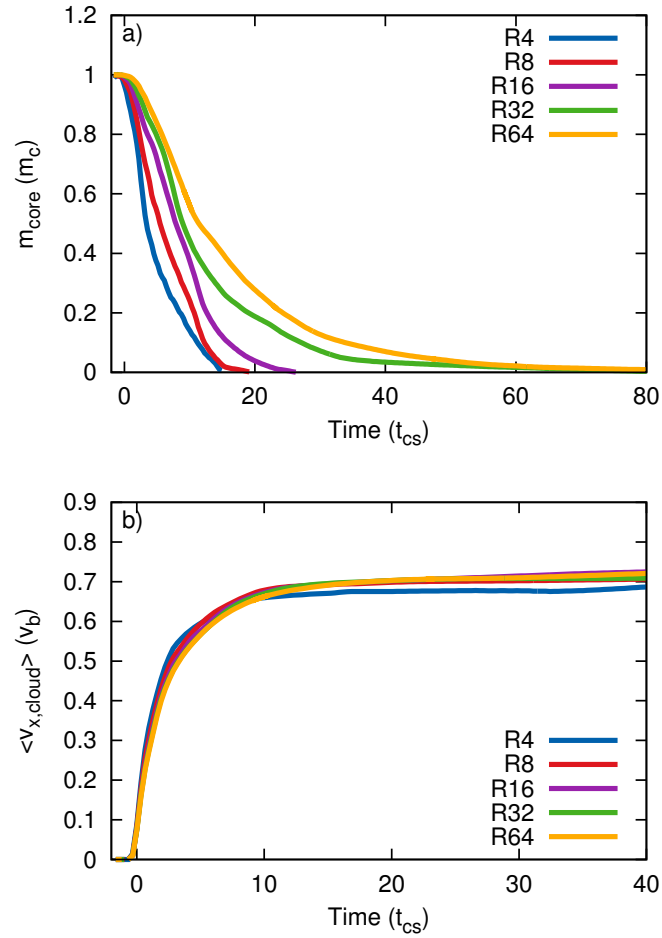


Fig. 3.2 Convergence tests for 3D MHD simulations of a Mach 10 shock hitting a filament with density contrast $\chi = 10$ in a parallel field. The time evolution of (a) the core mass (normalised to the value of the initial filament mass, $m_{\text{core},0}$), and (b) mean cloud velocity are shown.

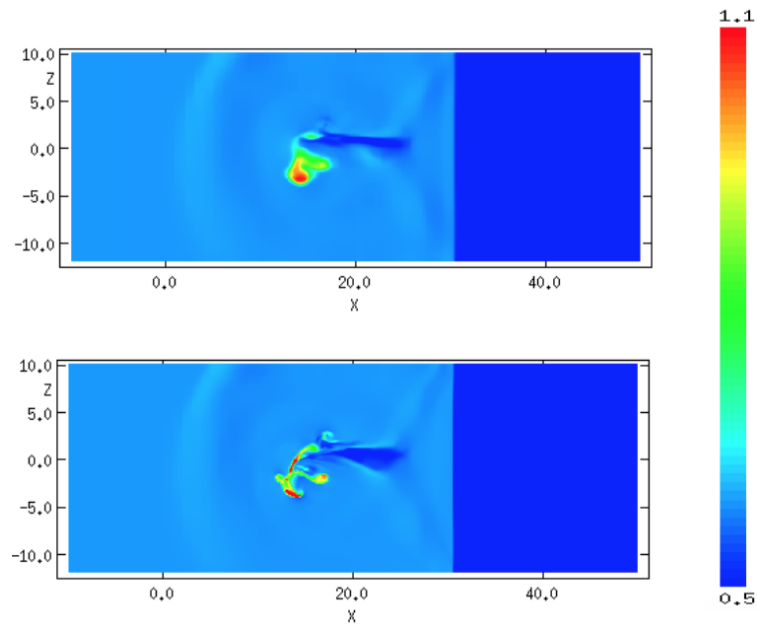


Fig. 3.3 Resolution test for a Mach 10 shock overrunning a filament, using the initial setup shown in Fig. 3.1. A logarithmic density plot, scaled in terms of the ambient density, is shown at $t = 6.11 t_{cs}$ for resolutions R_8 (top) and R_{32} (bottom).

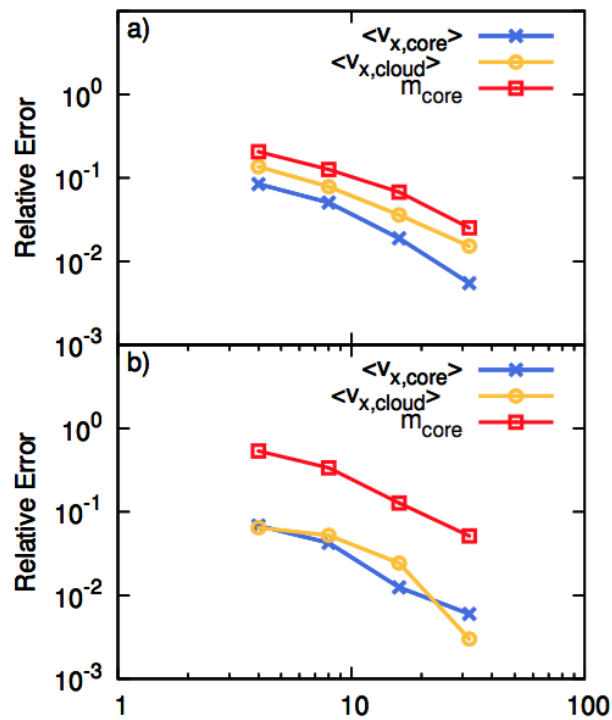


Fig. 3.4 Relative error (compared to the highest resolution simulation) versus spatial resolution (the number of cells per filament radius on the finest grid) for a number of global quantities measured from a shock-filament interaction with $\chi = 10$, $M = 10$, and $\beta_0 = 1$ at $t = 2 t_{cs}$ (top) and $t = 5 t_{cs}$ (bottom).

Magnetohydrodynamic Filament Simulations

Table 3.2 A summary of the shock-filament simulations performed for a parallel magnetic field. M is the sonic Mach number, χ is the density contrast of the filament to the surrounding ambient medium, β_0 is the ratio of thermal to magnetic pressure, l defines the length of the filament, and θ defines the angle of orientation of the filament between its major-axis and the shock surface. v_b is the shock speed through the inter-cloud medium (in code units). v_{ps} is the post-shock flow velocity, and is given in units of v_b . M_A is the Alfvénic Mach number, $M_{\text{slow/fast}}$ are the slow/fast magnetosonic Mach numbers. t_{cc} is the cloud-crushing time-scale of Klein et al. (1994), while t_{cs} is the cloud-crushing time-scale for a spherical cloud of equivalent mass introduced by Xu and Stone (1995). Key filament timescales are additionally noted. Values appended by † denote that the true value was greater than that given but that the simulation had ended before this point was reached.

Simulation	M	χ	β_0	l (r_c)	θ ($^\circ$)	v_b	$v_{ps}(v_b)$	M_A	M_{slow}	M_{fast}	t_{cs}/t_{cc}	t_{drag}/t_{cs}	t_{mix}/t_{cs}	t_{life}/t_{cs}
m10c1b112o45	10	10	1	2	45°	13.6	0.74	9.13	10.0	9.13	1.36	2.98	8.32	25.4
m10c1b114o45	10	10	1	4	45°	13.6	0.74	9.13	10.0	9.13	1.59	2.55	9.06	69.5
m10c1b118o45	10	10	1	8	45°	13.6	0.74	9.13	10.0	9.13	1.91	2.36	8.86	37.4
m10c1b114o0	10	10	1	4	0°	13.6	0.74	9.13	10.0	9.13	1.59	1.27	7.10	91.1
m10c1b114o30	10	10	1	4	30°	13.6	0.74	9.13	10.0	9.13	1.59	1.90	10.4	104
m10c1b114o70	10	10	1	4	70°	13.6	0.74	9.13	10.0	9.13	1.59	3.19	7.10	20.7
m10c1b114o85	10	10	1	4	85°	13.6	0.74	9.13	10.0	9.13	1.59	2.56	6.46	19.1
m10c1b114o90	10	10	1	4	90°	13.6	0.74	9.13	10.0	9.13	1.59	2.56	6.11	19.1
m10c2b114o45	10	10 ²	1	4	45°	13.6	0.74	9.13	10.0	9.13	1.59	4.35	5.17	11.7
m10c3b114o45	10	10 ³	1	4	45°	13.6	0.74	9.13	10.0	9.13	1.59	4.72	4.49	7.30
m10c1b0.514o45	10	10	0.5	4	45°	13.6	0.74	6.45	10.0	6.46	1.59	2.55	35.7	79.1
m10c1b1014o45	10	10	10	4	45°	13.6	0.74	28.9	28.9	10.0	1.59	2.55	7.42	19.1
m1.5c1b114o45	1.5	10	1	4	45°	2.04	0.42	1.37	1.50	1.37	1.59	2.26	127 [†]	127 [†]
m3c1b114o45	3	10	1	4	45°	4.07	0.67	2.74	3.00	2.74	1.59	2.70	212	213 [†]

Table 3.3 As Table 3.2 but for perpendicular and oblique magnetic fields. All columns apply to both perpendicular and oblique fields, except columns which contain parentheses - in these columns, values without (with) parentheses indicate perpendicular (oblique) simulations. Values appended by † denote that the true value was greater than that given but that the simulation had ended before this point was reached.

Simulation	M	χ	β_0	l (r_c)	θ ($^\circ$)	v_b	$v_{ps}(v_b)$	M_A	M_{slow}	M_{fast}	t_{cs}/t_{cc}	t_{drag}/t_{cs}	t_{mix}/t_{cs}	t_{life}/t_{cs}
m10c1b112o45	10	10	1	2	45°	13.6	0.73 (0.74)	9.13	∞ (17.7)	6.74 (7.29)	1.36	1.86 (2.23)	181 (112)	181.70 [†] (149.48 [†])
m10c1b114o45	10	10	1	4	45°	13.6	0.73 (0.74)	9.13	∞ (17.7)	6.74 (7.29)	1.59	1.59 (1.91)	128 (128 [†])	127.71 [†] (127.81 [†])
m10c1b118o45	10	10	1	8	45°	13.6	0.73 (0.74)	9.13	∞ (17.7)	6.74 (7.29)	1.91	1.32 (1.58)	104 [†] (106 [†])	104.08 [†] (106.06 [†])
m10c1b114o0	10	10	1	4	0°	13.6	0.73 (0.74)	9.13	∞ (17.7)	6.74 (7.29)	1.59	0.95 (1.27)	71.7 (73.3)	128 [†] (128 [†])
m10c1b114o30	10	10	1	4	30°	13.6	0.73 (0.74)	9.13	∞ (17.7)	6.74 (7.29)	1.59	1.28 (1.59)	119 (80.8)	1190 [†] (128 [†])
m10c1b114o70	10	10	1	4	70°	13.6	0.73 (0.74)	9.13	∞ (17.7)	6.74 (7.29)	1.59	2.55 (3.19)	107 (87.9)	111 [†] (116 [†])
m10c1b114o85	10	10	1	4	85°	13.6	0.73 (0.74)	9.13	∞ (17.7)	6.74 (7.29)	1.59	2.55 (2.56)	53.5 (90.8)	112 [†] (128 [†])
m10c1b114o90	10	10	1	4	90°	13.6	0.73 (0.74)	9.13	∞ (17.7)	6.74 (7.29)	1.59	2.56 (2.56)	62.0 (47.4)	95.7 [†] (128 [†])
m10c2b114o45	10	10 ²	1	4	45°	13.6	0.73 (0.74)	9.13	∞ (17.7)	6.74 (7.29)	1.59	4.15 (4.15)	78.5 (30.0)	92.7 (89.5 [†])
m10c3b114o45	10	10 ³	1	4	45°	13.6	0.73 (0.74)	9.13	∞ (17.7)	6.74 (7.29)	1.59	4.89 (5.42)	14.8 (1.58)	24.4 [†] (18.8 [†])
m10c1b0.514o45	10	10	0.5	4	45°	13.6	0.72 (0.73)	6.45	∞ (1.58)	5.42 (5.77)	1.59	1.27 (1.59)	128 [†] (98.5)	128 [†] (128 [†])
m10c1b1014o45	10	10	10	4	45°	13.6	0.74 (0.74)	28.9	∞ (4.21)	9.45 (9.70)	1.59	2.87 (2.87)	13.3 (12.0)	128 [†] (128 [†])
m1.5c1b114o45	1.5	10	1	4	45°	2.04	0.02 (0.12)	1.37	∞ (2.66)	1.01 (1.09)	1.59	1.10 (1.49)	90.4 [†] (229 [†])	90.4 [†] (229 [†])
m3c1b114o45	3	10	1	4	45°	4.07	0.55 (0.59)	2.74	∞ (5.31)	2.02 (2.19)	1.59	0.91 (1.24)	183 [†] (114 [†])	183 [†] (114 [†])

3.3.1 Parallel field

3.3.1.1 Filament morphology

I first review the morphology of filaments embedded in an initially parallel (i.e. at 0° to the shock normal) magnetic field. Figure 3.5 presents snapshots of the time evolution of the density distribution for simulation *m10c1b1l4o45pa*. The evolution of the filament broadly follows the stages outlined in §4.1 of Pittard et al. (2009). Firstly, the filament is struck and compressed by the shock front, and a bow shock is formed. Then the filament expands until $t \approx 6.46t_{cs}$. However, unlike the hydrodynamical spherical cloud case where the cloud broadly maintains its shape, the filament is instead contorted out of shape and the expansion of the cloud is less evident. The filament is swept downstream in the ambient flow, showing very little fragmentation due to the parallel magnetic field but continually being stripped of material. The presence of parallel magnetic field lines means that, unlike the hydrodynamic case, the MHD filament exhibits little or no surface instabilities, ensuring that the filament core survives for a far longer timescale than would otherwise be possible. MHD filaments in a parallel field do not tend to form long tails of cloud material, but instead a linear “void” is created which comprises an area of low density and high magnetic pressure. In non-oblique filaments (henceforth known as “axisymmetric” filaments), and in particular filaments orientated at $\theta = 90^\circ$, this region forms a very clear “flux rope”, but where the filament is angled to the shock front (“oblique” filaments) such a structure is less well defined because the contortion of the filament in the ambient flow is not symmetric.

Figures 3.6 and 3.7 show the density distribution at various times for simulations *m10c1b1l4o90pa* and *m10c1b1l4o0pa*, respectively. The orientation of these two filaments leads to many more interesting features than those seen with the obliquely-orientated clouds. For the interaction in Fig. 3.6 the filament is struck end-first, while in Fig. 3.7 the filament is struck on its broadside. The initial filament structure in

Magnetohydrodynamic Filament Simulations

Fig. 3.6, after it has been struck by the shock, is very similar to that of the other runs, since the mechanical energy of the shock is driving the interaction rather than the magnetic energy of the filament. Compressed filament material is seen to form a column or “flux rope” behind the filament head but the level of compression is limited in comparison with the purely hydrodynamic case due to the magnetic field lines which surround the filament and resist compression by the converging flow. The post-shock flow is prevented from entering the flux rope by the build-up of magnetic pressure in that area. The surface of the filament, by contrast, shows shear instabilities (though damped because of the field) which serve to create “wings” - areas either side of the filament where the material is being ablated and bent by the surrounding flow (see §3.1.1. of [Alūzas et al. 2014](#)). Although the level of instability is greater than in the cases where the filament was orientated obliquely, the filament nonetheless remains relatively coherent and does not fragment. Instead it undergoes continual ablation to the surrounding flow until no substantial mass remains. The filament with $l = 4$ and $\theta = 85^\circ$ begins to follow this evolution, and an initial well-defined flux rope is formed. However, since the filament is oriented at a slight angle to the shock front the structures forming on the axis behind the filament are quickly destabilised and the evolution proceeds as in the obliquely-orientated cases described above.

The filament in Fig. 3.7 also forms “wings”. However, since the shock front strikes the entire length of the filament, the wings are far more substantial and act to shield the far side of the filament from the flow. Therefore, the column of compressed material forming the flux rope in this instance is much broader than in the previous case. The filament is then dragged downstream by the post-shock flow, becoming elongated before finally being destroyed.

Figure 3.8 shows a 3D volumetric rendering of the time evolution of the density of filament material in simulations *m10c1b1l4o45pa*, *m10c1b1l4o90pa*, and *m10c1b1l4o0pa*, showing clearly the flux rope associated with the filament orien-

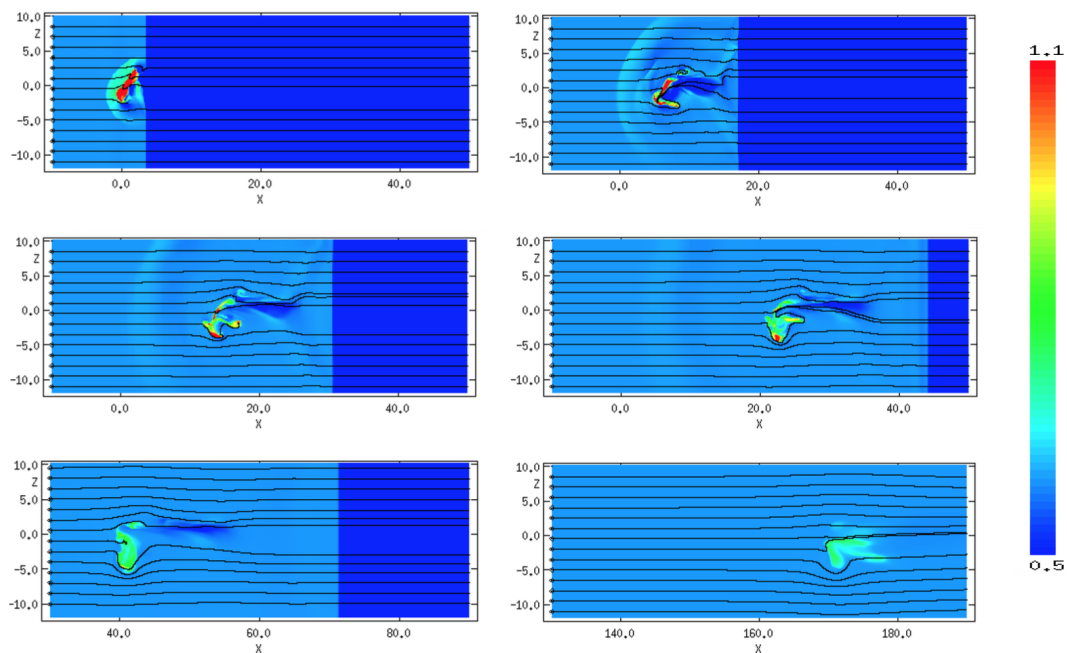


Fig. 3.5 The time evolution of the logarithmic density, scaled with respect to the ambient density, for model *m10c1b1l4o45pa*. The evolution proceeds left to right, top to bottom, with $t = 0.95 t_{cs}$, $t = 3.54 t_{cs}$, $t = 6.11 t_{cs}$, $t = 9.06 t_{cs}$, $t = 14.2 t_{cs}$, and $t = 52.5 t_{cs}$. Note the shift in the x axis scale for the final two panels. The initial magnetic field is parallel to the shock normal.

tated at $\theta = 90^\circ$, and also that material is forced out of the side of the filament in simulation *m10c1b1l4o45pa*. Because only the filament material is shown, other features such as the bow shock are not displayed in these plots.

3.3.1.2 Effect of filament length and orientation on the evolution of the core mass

In a purely hydrodynamical case with a Mach 10 shock the filament is destroyed within a short timescale of $t \sim 10 t_{cs}$ (the filament survives for longer when hit by a weaker shock - see [Pittard and Goldsmith \(2016\)](#)). This is because turbulent instabilities are able to build up at the surface of the filament and encourage the ablation of mass from it. However, when magnetic fields are present instabilities are damped, and filaments survive over far longer timescales. Figure 3.9 shows the evolution of the filament core mass over time for filaments with different lengths

Magnetohydrodynamic Filament Simulations

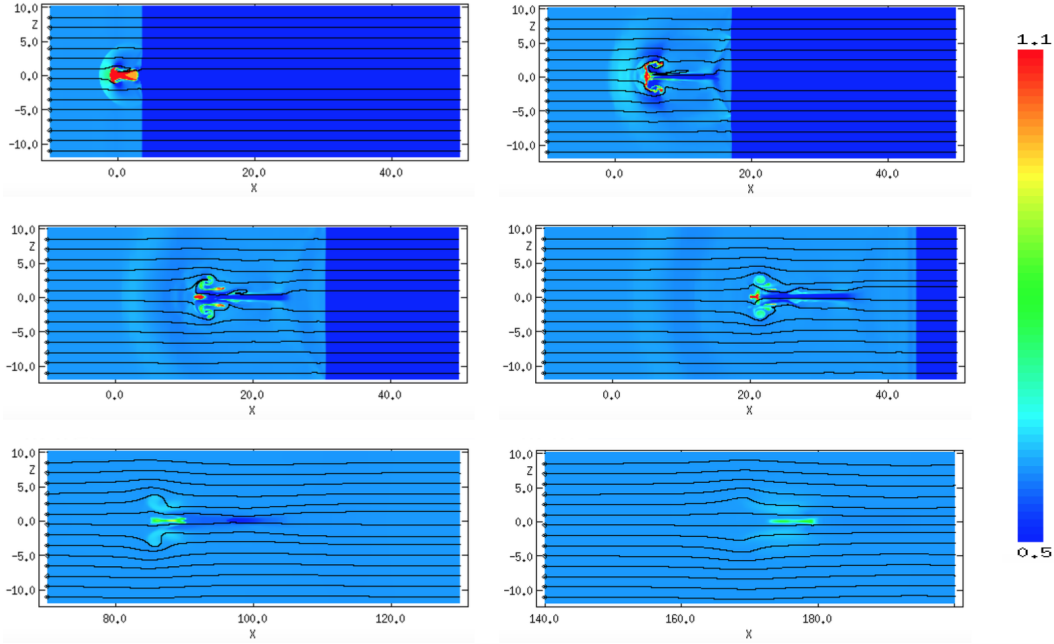


Fig. 3.6 The time evolution of the logarithmic density, scaled with respect to the ambient density, for model *m10c1b1l4o90pa*. The evolution proceeds left to right, top to bottom, with $t = 0.95 t_{CS}$, $t = 3.54 t_{CS}$, $t = 6.11 t_{CS}$, $t = 9.06 t_{CS}$, $t = 27.9 t_{CS}$, and $t = 52.2 t_{CS}$. Note the shift in the x axis scale for the bottom two panels. The initial magnetic field is parallel to the shock normal.

and orientations. It can be seen that the timescale for destruction in these cases is far greater than in the hydrodynamical scenario presented in [Pittard and Goldsmith \(2016\)](#).

It can be seen that in terms of the core mass, the filament with $l = 4$ and an orientation of $\theta = 90^\circ$, and that with a length of $l = 2$ and an orientation of $\theta = 45^\circ$, are destroyed at $t \approx 31 t_{CS}$ and $t \approx 28 t_{CS}$, respectively. However, the filament with $l = 4$ and $\theta = 0^\circ$, and that with $l = 8$ and $\theta = 45^\circ$, are not destroyed until $t \approx 104 t_{CS}$ (not visible in the figure) and $t \approx 61 t_{CS}$, respectively.

The orientation of the filament to the shock normal plays an important role in the core mass evolution and the lifetime of the filament (Fig. 3.9(b)). Whilst all filament orientations show a similar initial decrease in mass until $t \approx 5 t_{CS}$ the filament orientated at $\theta = 90^\circ$ (i.e. end on), although initially the slowest to lose mass, thereafter shows the most rapid drop in mass until its destruction (cf. Fig.

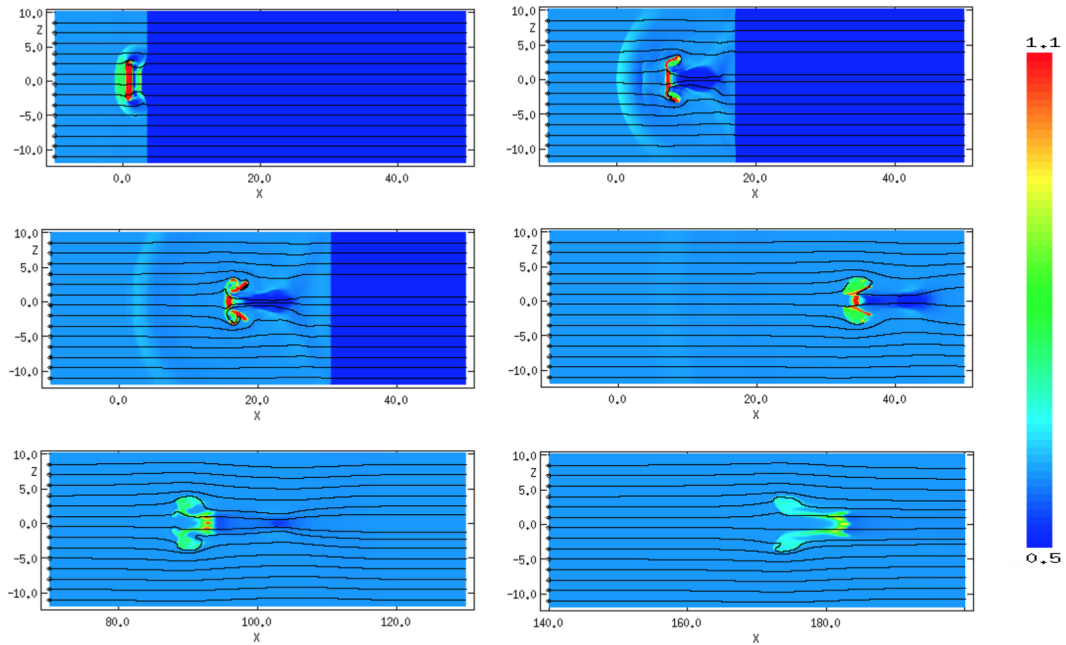


Fig. 3.7 The time evolution of the logarithmic density, scaled with respect to the ambient density, for model *m10c1b1l4o0pa*. The evolution proceeds left to right, top to bottom, with $t = 0.95t_{CS}$, $t = 3.54t_{CS}$, $t = 6.11t_{CS}$, $t = 11.7t_{CS}$, $t = 27.9t_{CS}$, and $t = 52.2t_{CS}$. Note the shift in the x axis scale for the bottom two panels. The initial magnetic field is parallel to the shock normal.

28(i) in Pittard and Goldsmith (2016)). It is noticeable that those filaments with orientations of $0^\circ < \theta \lesssim 45^\circ$ are much slower overall to lose the majority of their core mass (with the mass loss rate decreasing significantly once less than 5% of the initial filament mass remains), whilst those with orientations of $\theta > 45^\circ$ are destroyed much more quickly.

Unless the filament is very short (in which case it begins to approximate a spherical cloud), the length of the filament has less of an influence on the mass loss than the orientation. From Fig. 3.9(a) it can be seen that all three filaments initially show a similar decrease in their core mass. However, the filament with length $l = 2$ subsequently loses mass at a much faster rate than the other two lengths. This differs from the hydrodynamic case in Pittard and Goldsmith (2016), where the filament of length $l = 8$ loses mass faster than the other filaments. Interestingly, the spherical cloud, whilst incurring a faster mass-loss rate than the filament with $l = 2$, begins

Magnetohydrodynamic Filament Simulations

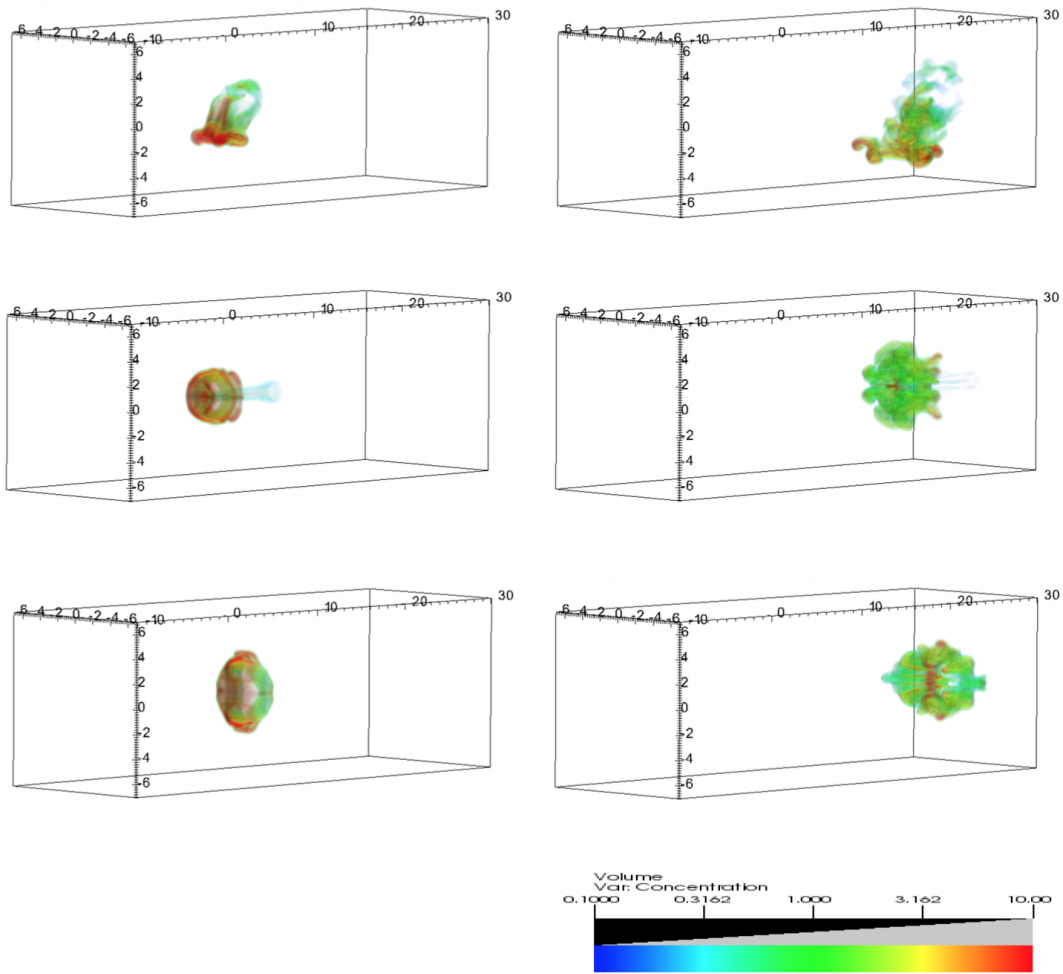


Fig. 3.8 3D volumetric renderings of models *m10c1b1l4o45pa* (top), *m10c1b1l4o90pa* (middle), and *m10c1b1l4o0pa* (bottom) at $t = 3.54t_{cs}$ (left-hand column) and $t = 9.06t_{cs}$ (right-hand column). The initial magnetic field is parallel to the shock normal.

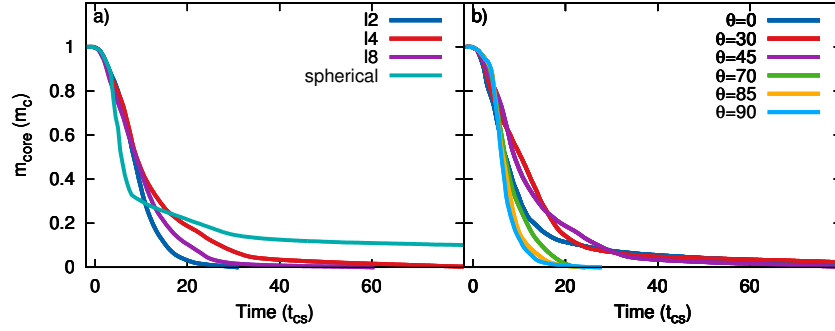


Fig. 3.9 Time evolution of the core mass, m_{core} , for (a) a filament with variable length and an orientation of 45° , and (b) $l = 4$ with variable orientation, in an initial parallel magnetic field.

to level off at $\sim 7t_{cs}$ and retains approximately one tenth of its initial mass by the end of the simulation. In this case, although the “length” of the filament is short, it is axisymmetric to the shock front and behaves in a similar manner to the filament of length $l = 4$ and $\theta = 0^\circ$.

3.3.1.3 Effect of filament length and orientation on the mean velocity and the velocity dispersion

There are two stages to the acceleration of the filament through the ambient flow. The filament is first accelerated to the velocity of the transmitted shock, $\propto v_b/\sqrt{\chi}$, as the shock is driven through it, and then further accelerated by the flow of post-shock gas until it reaches the velocity of the flow, e.g. $0.74v_b$ for $M = 10$, $\beta_0 = 1$ and a parallel field. Figure 3.10 shows the time evolution of the mean cloud velocity in the x direction, $\langle v_x \rangle$. It can be seen that filaments with orientations of $\theta \lesssim 45^\circ$ are initially accelerated faster than those with orientations of $\theta > 45^\circ$; this is likely to be because there is a greater surface area presented to the shock front with these orientations, i.e. the filament is ‘broadside’ to the shock front. It is interesting to note that the filament hit end on is initially accelerated the least rapidly, but that the rate of velocity gain does not level off as much as in some of the other models until the filament experiences a reduction in acceleration at $v \simeq 0.6v_b$. It is clear that the

Magnetohydrodynamic Filament Simulations

filaments with $l = 4$ and $\theta = 0^\circ, 90^\circ$ display more overtly the two-stepped nature of the acceleration. At $t > 40t_{cs}$, the filaments with $\theta = 30^\circ$ and $\theta = 90^\circ$ slightly overshoot and then decelerate to the velocity of the post-shock flow (not visible in Fig. 3.10), possibly due to the release of some built-up tension in the field lines.

In comparison with the filament orientation, the length appears to have no significant effect on the mean velocity, with all filaments being accelerated at approximately the same rate. This is in contrast to the spherical cloud which displays a profile similar to the end on filament in Fig. 3.10(b).

The interaction of shocks with filaments creates substantial velocity dispersions and reveals the presence of instabilities. In the x direction, the filaments with orientations $\theta \gtrsim 70^\circ$ have the highest peaks (Fig. 3.11(d)), with the $\theta = 0^\circ$ and $\theta = 30^\circ$ filaments showing the least dispersion in the x direction. This is in agreement with Pittard and Goldsmith (2016) where, for end on or nearly end on filaments, their $\delta v_x/v_b$ also reaches $\simeq 0.2$ (cf. their Fig. 28(e)). Figures 3.11(e,f), by contrast, indicate much less overall dispersion in the y and z directions. This is because, in the x direction, the initial peak occurs as the transmitted shock travels through the filament. Thus, there is a large dispersion between the shocked and unshocked filament material at that time. A similar effect is produced in the y and z directions, although slightly later, when the filament is undergoing compression.

A comparison of the top and bottom panels of Fig. 3.11 reveals that the velocity dispersion is more sensitive to filament orientation than length in the x direction, and more sensitive to length rather than orientation in the z direction.

3.3.1.4 Effect of filament length and orientation on the mean density

Figure 3.12 shows the time evolution of the mean density of the filament, $\langle \rho_{\text{cloud}} \rangle$, and filament core, $\langle \rho_{\text{core}} \rangle$. The peak mean densities, after the shock has hit and compressed the filament, for various lengths and orientations of the filament are

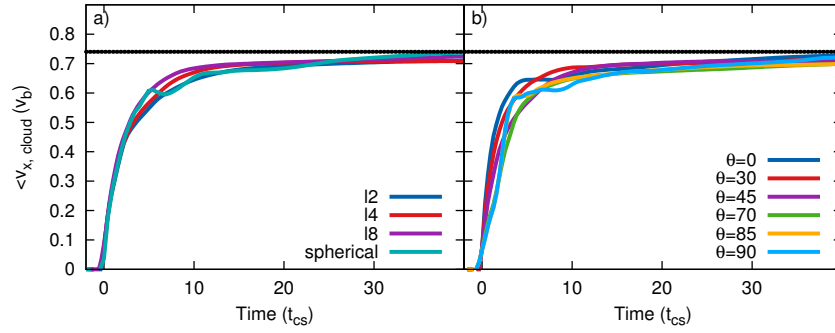


Fig. 3.10 Time evolution of the filament mean velocity, $\langle v_x \rangle$, for (a) a filament with variable length and an orientation of 45° , and (b) $l = 4$ with variable orientation, in an initial parallel magnetic field. The dotted black line indicates the velocity of the post-shock flow.

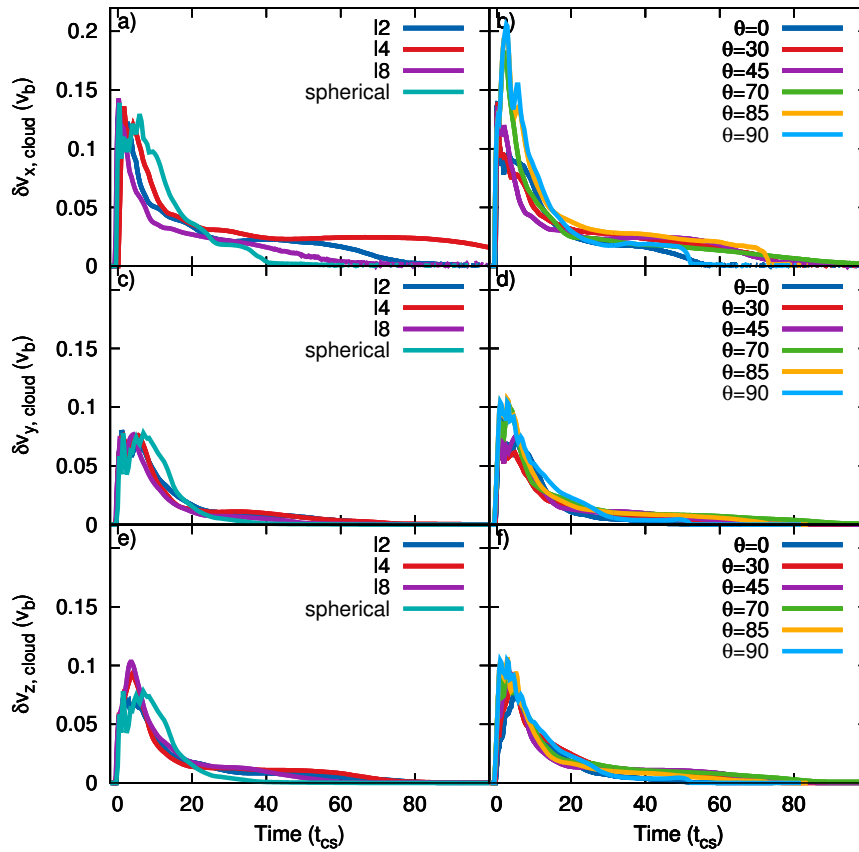


Fig. 3.11 Time evolution of the filament velocity dispersion in the x , y , and z directions, $\delta v_{x,y,z}$, for a filament with variable length and an orientation of 45° (left-hand column), and $l = 4$ with variable orientation (right-hand column), struck by a parallel shock.

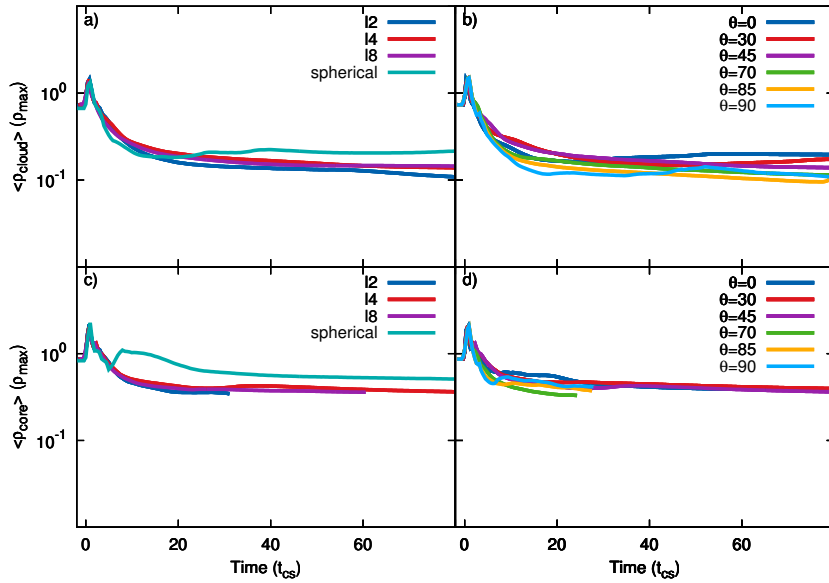


Fig. 3.12 Time evolution of the mean density of the filament, $\langle \rho_{\text{cloud}} \rangle$ (top), and filament core, $\langle \rho_{\text{core}} \rangle$ (bottom), normalised to the initial maximum filament density, for filaments with (left-hand column) variable length and an orientation of 45° , and (right-hand column) $l = 4$ and a variable orientation, in a parallel magnetic field.

similar. However, the mean densities of filaments with $l = 4$ and $\theta = 90^\circ$, or $l = 2$ and $\theta = 45^\circ$, decline more rapidly, with a lower final value of $\langle \rho \rangle / \rho_{\text{max}}$ being reached in these cases (though in Fig. 3.12(d) the filament with $\theta = 70^\circ$ reaches a lower mean density level by the end of the simulation). It is noticeable in Fig. 3.12(b) that for filaments with orientations of $\theta = 0^\circ$, $\theta = 30^\circ$, or $\theta = 90^\circ$ there is a subsequent increase in the mean density after reaching their lowest value, and this is mirrored in the spherical cloud mean density in Fig. 3.12(a). The initial peak of the spherical cloud mean density in Fig. 3.12(c) is slightly higher than for the filaments, and a second, broader peak is present also. The difference in the height of the peak mean densities may be due to the fact that the shocks driven into the filaments do not converge as well as those driven into the spherical cloud.

3.3.1.5 χ dependence of the filament evolution

Varying the cloud density contrast radically alters the evolution of the filament. This is clearly seen in Figs. 3.13 and 3.14, where the filament downstream of the bow shock evolves in a highly turbulent manner, not dissimilar to previous hydrodynamical shock-cloud simulations (e.g. [Pittard and Goldsmith 2016](#)). The tail of turbulent cloud material follows the pattern of the field lines at that point which are highly contorted and tangled. Since instabilities are able to form on the surface of the filament to a much greater degree than the other simulations run with a parallel magnetic field, the core mass of the filaments in these cases are destroyed in very short timescales of $t = 17.2t_{cs}$ and $t = 8.4t_{cs}$ for $\chi = 100$ and $\chi = 1000$, respectively, though they are first drawn out into long strands, or tails, of cloud material before being broken up into clumps and eventually mixed with the post-shock flow. Indeed, the development of turbulent instabilities increases with increasing χ . This is in complete contrast to the $\chi = 10$ case shown in Fig. 3.5, where the evolving filament in that case forms a compact and smooth structure and does not display pronounced turbulent instabilities. The decreased destruction time of the filament (in units of t_{cs}) with increasing χ follows the trend in [Pittard and Goldsmith \(2016\)](#), where t_{life} reduces as χ increases when $M = 10$.² However, this is in direct contrast with [Pittard and Parkin \(2016\)](#), who revealed that spherical clouds do not show a clear trend with χ for t_{life} at $M = 10$. This shows that t_{mix} and t_{life} do not exhibit monotonic behaviour with varying χ when $M = 10$.

The demise of the $\chi = 100$ and $\chi = 1000$ filaments is seen in the mean density plot (Fig. 3.15(c)), which shows that although these two filaments initially have a much higher mean density in comparison with ρ_{amb} , their mean density thereafter quickly reduces, while the filament with $\chi = 10$ maintains a much higher mean

²It should be noted that, owing to computational difficulties with running the $\chi = 1000$ simulation at such a high resolution, I used a slightly lower resolution of R_{16} for this case. Thus, it should be borne in mind that this filament may be destroyed more rapidly than would be the case with a resolution of R_{32} .

Magnetohydrodynamic Filament Simulations

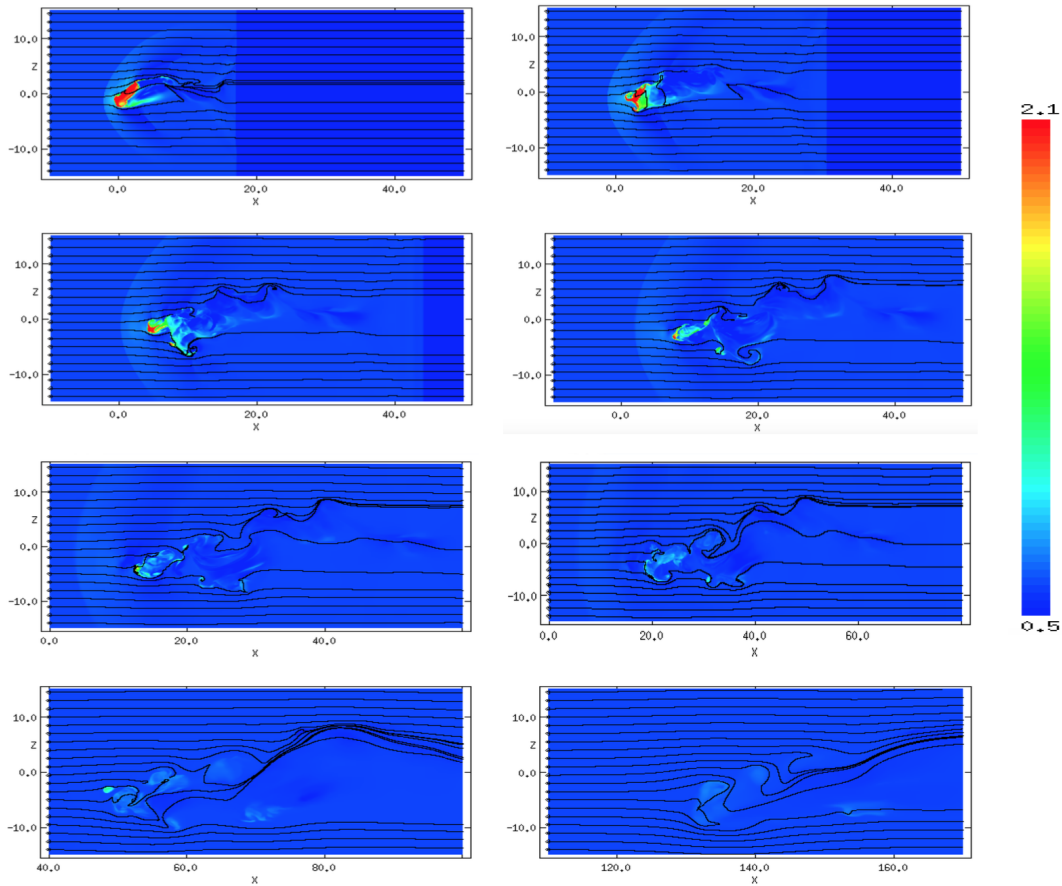


Fig. 3.13 The time evolution of the logarithmic density, scaled with respect to the ambient density, for model *m10c2b1l4o45pa*. The evolution proceeds left to right, top to bottom, with $t = 1.09t_{CS}$, $t = 1.97t_{CS}$, $t = 2.86t_{CS}$, $t = 3.65t_{CS}$, $t = 4.57t_{CS}$, $t = 5.36t_{CS}$, $t = 8.85t_{CS}$, and $t = 16.5t_{CS}$. Note the shift in the x axis scale for the final four panels, and the change in the logarithmic density scale compared to previous cases. The initial magnetic field is parallel to the shock normal.

density after its initial compression by the shock front. In addition, Fig. 3.15(b) shows that the filament with $\chi = 1000$ is destroyed before it has reached the velocity of the post-shock flow. The presence of instabilities is, however, present in the velocity dispersion plots (Fig. 3.15(d-f)) with both the higher χ filaments producing a higher dispersion peak in the x direction than the $\chi = 10$ filament. In addition, the peak dispersion for higher values of χ is shifted from the $\chi = 10$ case in the x and y directions, indicating that turbulent instabilities take longer to form and are more important for the dispersal of the filament than its initial compression.

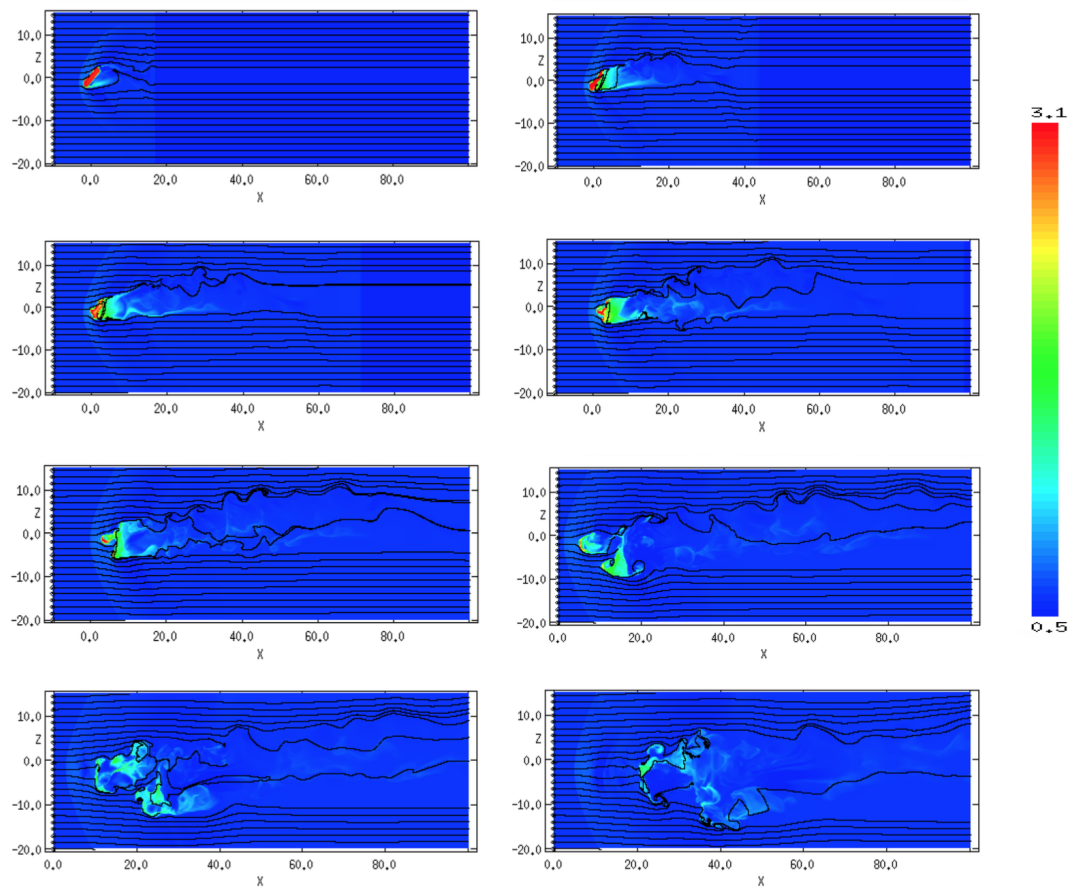


Fig. 3.14 The time evolution of the logarithmic density, scaled with respect to the ambient density, for model *m10c3b114o45pa* using a resolution of R_{16} . The evolution proceeds left to right, top to bottom, with $t = 0.33t_{cs}$, $t = 0.88t_{cs}$, $t = 1.43t_{cs}$, $t = 1.95t_{cs}$, $t = 2.50t_{cs}$, $t = 3.03t_{cs}$, $t = 3.57t_{cs}$, and $t = 4.11t_{cs}$. Note the shift in the x axis scale for the final three panels, and the change in the logarithmic density scale compared to previous cases. The initial magnetic field is parallel to the shock normal.

Magnetohydrodynamic Filament Simulations

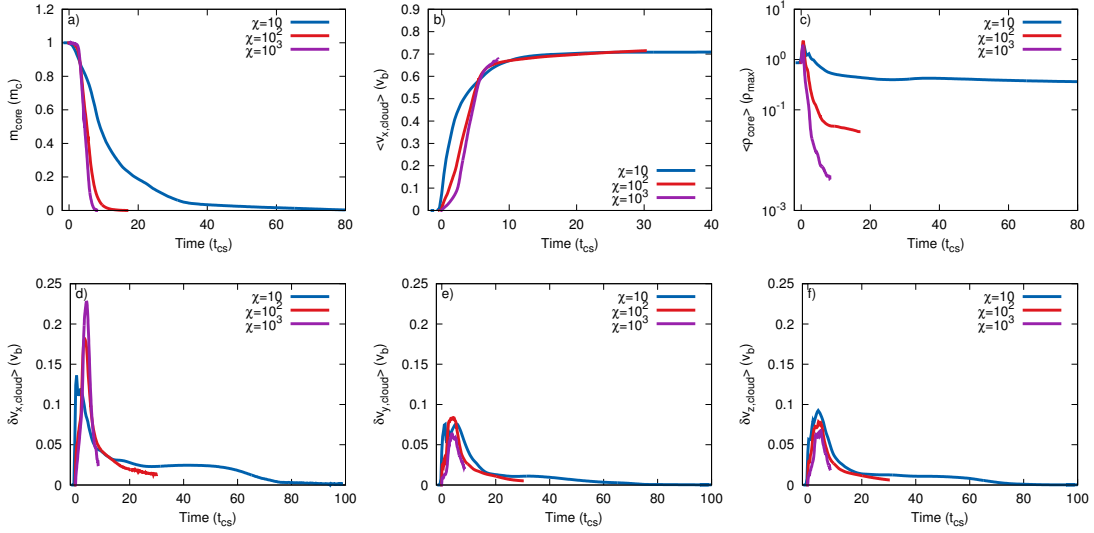


Fig. 3.15 χ dependence of the evolution for filaments with $l = 4$ and $\theta = 45^\circ$. The initial magnetic field is parallel to the shock normal, $M = 10$, and $\beta_0 = 1$. Note that model *m10c3b1l4o45pa* was run at a resolution of R_{16} .

3.3.1.6 Mach dependence of the filament evolution

The Mach number of the shock can affect the growth rate of KH and RT instabilities (the formation of wave-like structures at the filament surface due to the presence of a velocity shear from the surrounding post-shock flow, and instabilities of the interface between the filament and surrounding flow - each with a different density - formed when the less dense flow pushes the more dense filament leading to ‘fingers’ of filament material protruding away from the surface, respectively), and can also affect the speed at which material is stripped from the filament and the time taken for the filament to become fully mixed with the surrounding flow. The post-shock conditions are dependent on the Mach number. In the purely hydrodynamic case, low Mach numbers (i.e. $M \leq 2.76$, see [Pittard et al. 2010](#)) lead to a subsonic post-shock flow with respect to a stationary obstacle. Conversely, high Mach numbers provide a supersonic post-shock flow.

I investigated three values for the shock Mach number: $M = 1.5, 3$, and 10 . Figure 3.16 shows the Mach number dependence of the evolution. It is evident

from Fig. 3.16(a) that the core mass declines much more rapidly for $M = 10$ than for $M = 1.5$, indicating that core material exists for far longer with a low Mach number because of the milder interaction of the shock with the filament. The morphology of the filaments with $M = 1.5$ and $M = 3$ does not radically alter over time, with the filament merely being bent into a horseshoe shape and experiencing very little compression or ablation of cloud material until the end of the simulation at $t = 126.9t_{cs}$ (for $M = 1.5$) and $t = 212.7t_{cs}$ (for $M = 3$). It is clear, therefore, that the interaction of the shock with the cloud is much more gentle in these cases than for $M = 10$. Figure 3.16(b) illustrates the differing values for the velocity of the post-shock flow according to Mach number, with very low Mach numbers resulting in a much slower acceleration to the (smaller) normalised velocity of the post-shock flow. The more gentle interaction at the lower Mach numbers results in the acceleration of the filament up to the post-shock flow velocity while it is still intact and coherent in structure. In addition, a bow wave is formed ahead of the filament for shocks with $M = 1.5$, rather than the bow shock visible for $M = 10$ in Fig. 3.5.

The velocity dispersion plots (Figs. 3.16(d,e,f)) show that $M = 1.5$ and $M = 3$ have a faster decay of velocity dispersions in all directions, in comparison to $M = 10$. Indeed, the difference in the height of the initial peak indicates that the filament has been struck by a shock of differing strength, since for the milder shocks there is far less of a contrast between the velocity of the shocked and unshocked portions of the filament when the shock front first hits the cloud.

3.3.1.7 β_0 dependence of the filament evolution

Figure 3.17 shows the effect of varying the plasma beta on the evolution of the filament. Figure 3.17(a) shows that the core mass of the model with $\beta_0 = 10$ (i.e. a weak magnetic field) is destroyed far quicker than for filaments with smaller values

Magnetohydrodynamic Filament Simulations

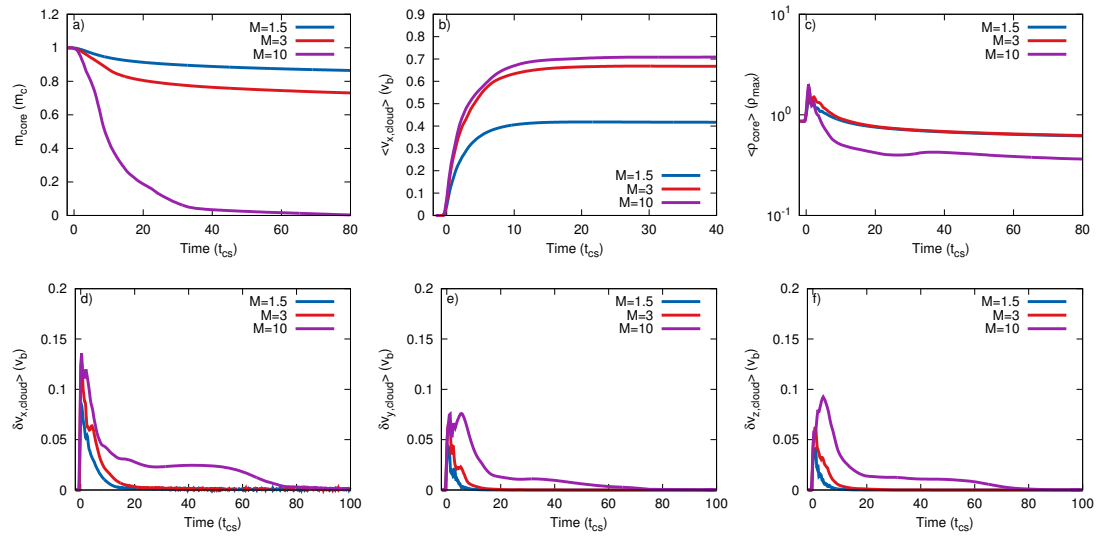


Fig. 3.16 Mach number dependence of the evolution for filaments with $l = 4$ and $\theta = 45^\circ$. The initial magnetic field is parallel to the shock normal, $\chi = 10$, and $\beta_0 = 1$.

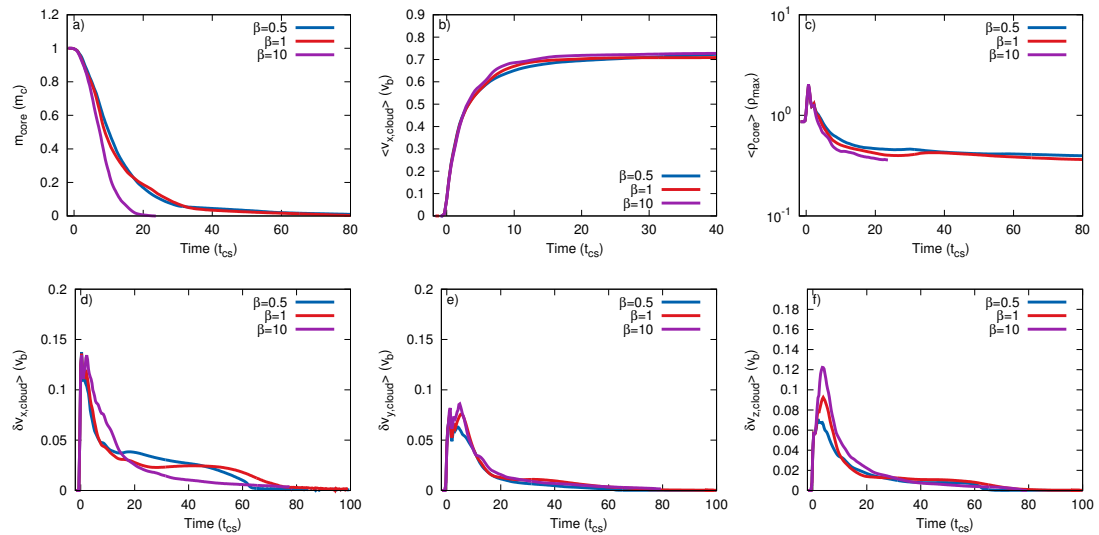


Fig. 3.17 Plasma beta dependence of the evolution for filaments with $l = 4$ and $\theta = 45^\circ$. The initial magnetic field is parallel to the shock normal, $M = 10$, and $\chi = 10$.

of β_0 (i.e. strong fields), since a weaker magnetic field is less able to damp the emergence of instabilities on the surface of the filament. The evolution with $\beta_0 = 0.5$ and $\beta_0 = 1$ is, however, broadly the same, and the filament morphologies for these two cases are very similar, whereas that for $\beta_0 = 10$ shows greater dispersal of the cloud material. Figures 3.17(b-f) show that there is not a great amount of divergence between the three simulations with respect to the filament velocity, mean density, or velocity dispersion in the y direction. However, the velocity dispersion in the x direction does show some divergence at later times, once the structure and dynamics of the shocked filament become sensitive to the magnetic field strength, and the peak of the dispersion in the z direction increases with decreasing field strength.

3.3.2 Perpendicular field

3.3.2.1 Filament morphology

The time evolution of the density distribution for simulation *m10c1b1l4o45pe* is presented in Fig. 3.18, with the magnetic fieldlines visible in the xy plane in Fig. 3.19. The presence of the perpendicular (i.e. 90° to the shock normal) magnetic field lines helps to protect the filament from the effects of the shock front and subsequent post-shock flow. Here, the field lines bend around the filament, allowing the flow to move along them and shielding the filament from rapid mass loss via ablation. In the filaments set at an initial angle to the shock front (the “oblique” filaments), the filaments are drawn out into long tendrils and are swept downstream in the flow. These filaments lose very little mass until near the end of the simulation. A small linear void is formed downstream of the filament, but this is much smaller than the void created in the parallel field scenario. As with the parallel field, oblique filaments do not form any significant linear structure along their axis because they are asymmetrical to the shock front. Compared to the parallel field case in Fig. 3.5, it can be observed that the perpendicular field ensures that the filament maintains a higher

Magnetohydrodynamic Filament Simulations

density, and produces a more rapid initial acceleration of the filament downstream. The latter is caused by the release of the tension that builds up in the field lines as they re-straighten.

Figure 3.20 shows snapshots of the density distribution for model *m10c1b1l4o90pe*, again with the fieldlines in the xy plane shown in Fig. 3.21. In the parallel field case, a flux rope would be expected to form on the axis behind the filament. However, with a perpendicular magnetic field this is not observed. Instead, low density filament material forms a linear structure along the axis and, in line with the parallel field scenario's flux rope, this structure persists for some time. As in the parallel field case, the filament with $l = 4$ and $\theta = 85^\circ$ begins to form a similar structure to this filament but the symmetrical nature of the evolving filament is quickly destabilised.

The density distribution for the filament in simulation *m10c1b1l4o0pe* is depicted in Fig. 3.22 and Fig. 3.23. The morphology of this filament at early times (i.e. $t = 3.54t_{cs}$) is very similar to that with a parallel field, except that the wings of this filament are swept backwards into the flow. From an observational point of view it may appear as if the filament has been struck by a shock travelling toward the $-x$ direction, and this may render the observational interpretation of such structures problematic. The beginnings of a very short, but broad, flux rope are present but this feature does not grow over time.

Figure 3.24 shows a 3D volumetric rendering of the time evolution of the density of filament material in simulations *m10c1b1l4o45pe*, *m10c1b1l4o90pe*, and *m10c1b1l4o0pe*, clearly showing a “sheet-like” structure at the upstream end of the filament. Because only the filament material is shown, other features such as the bow shock are not displayed in these plots.

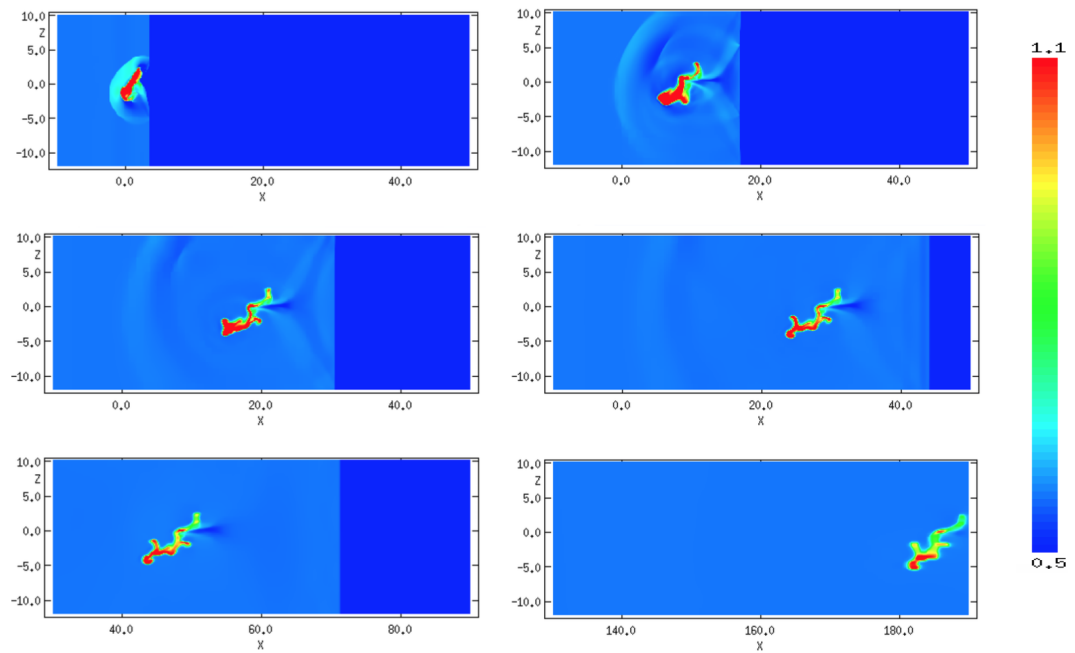


Fig. 3.18 The time evolution of the logarithmic density, scaled with respect to the ambient density, for model *m10c1b1/4o45pe* (cf. the parallel field case in Fig. 3.5). The evolution proceeds left to right, top to bottom, with $t = 0.95 t_{CS}$, $t = 3.44 t_{CS}$, $t = 6.36 t_{CS}$, $t = 8.95 t_{CS}$, $t = 14.5 t_{CS}$, and $t = 52.1 t_{CS}$. Note the shift in the x axis scale for the final two panels. The initial magnetic field is perpendicular to the shock normal.

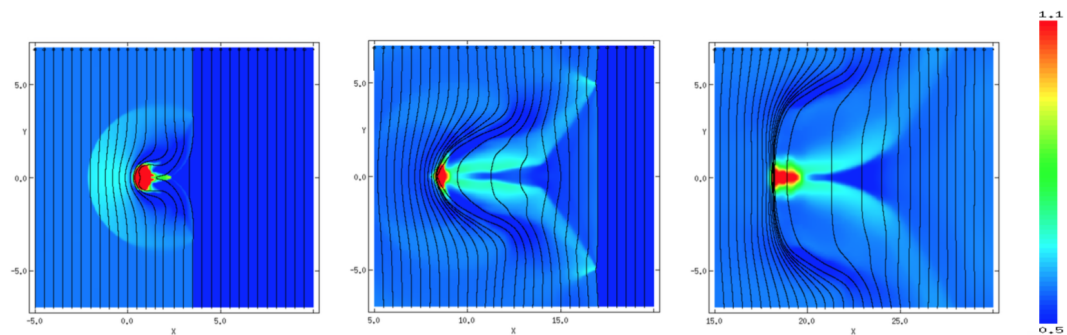


Fig. 3.19 As per Fig. 3.18 but showing the xy plane and magnetic fieldlines. The evolution proceeds left to right with $t = 0.95 t_{CS}$, $t = 3.44 t_{CS}$, and $t = 6.36 t_{CS}$. Note the shift in the x axis scale for the final panel.

Magnetohydrodynamic Filament Simulations

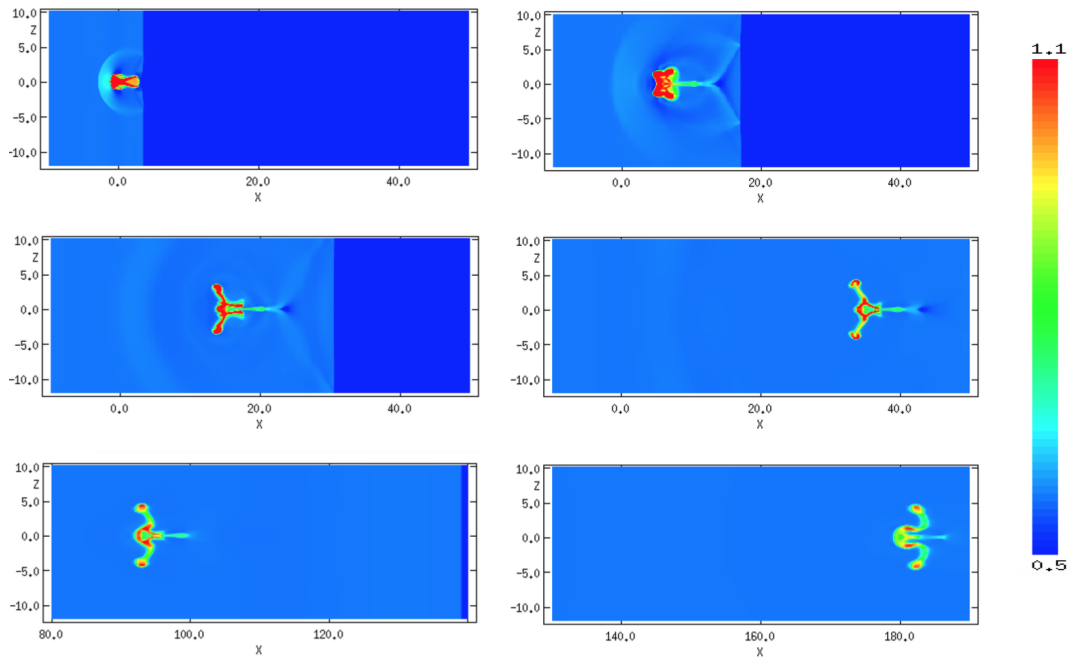


Fig. 3.20 The time evolution of the logarithmic density, scaled with respect to the ambient density, for model *m10c1b1l4o90pe* (cf. the parallel field case in Fig. 3.6). The evolution proceeds left to right, top to bottom, with $t = 0.95t_{CS}$, $t = 3.55t_{CS}$, $t = 6.10t_{CS}$, $t = 11.7t_{CS}$, $t = 27.9t_{CS}$, and $t = 52.2t_{CS}$. Note the shift in the x axis scale for the bottom two panels. The initial magnetic field is perpendicular to the shock normal.

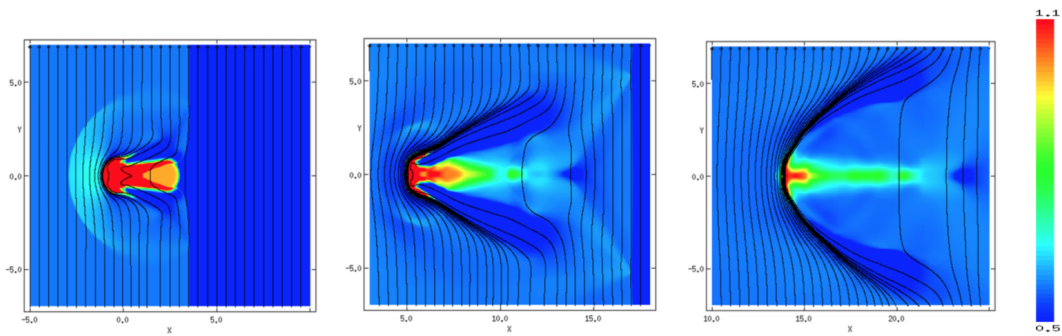


Fig. 3.21 As per Fig. 3.20 but showing the xy plane and magnetic fieldlines. The evolution proceeds left to right with $t = 0.95t_{CS}$, $t = 3.55t_{CS}$, and $t = 6.10t_{CS}$. Note the shift in the x axis scale for the final panel.

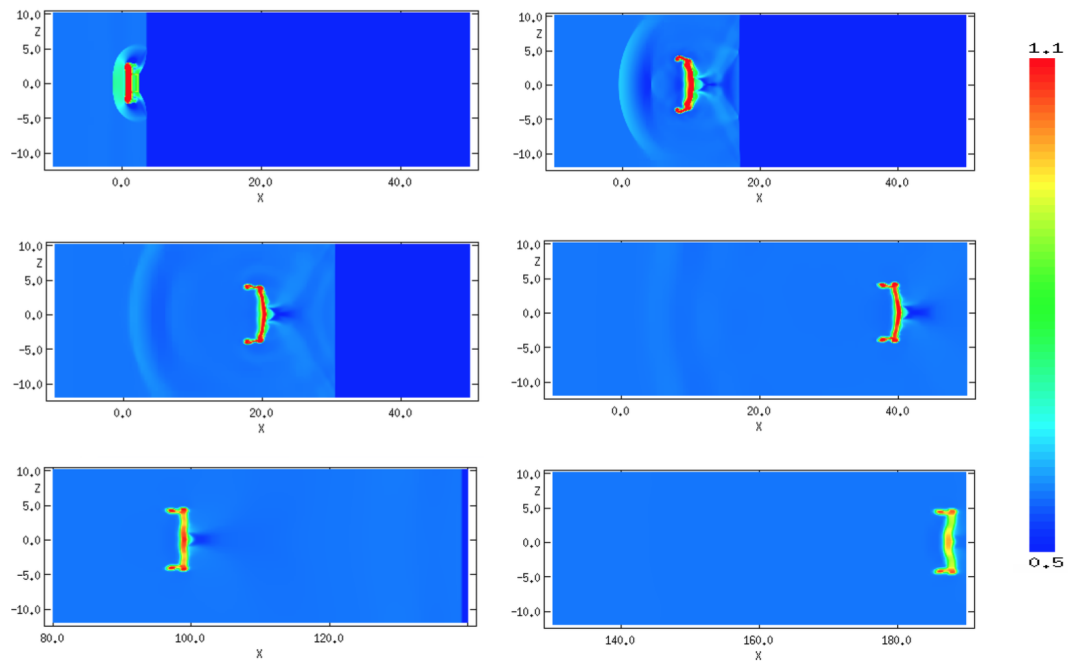


Fig. 3.22 The time evolution of the logarithmic density, scaled with respect to the ambient density, for model *m10c1b114o0pe* (cf. the parallel field case in Fig. 3.7). The evolution proceeds left to right, top to bottom, with $t = 0.95 t_{CS}$, $t = 3.54 t_{CS}$, $t = 6.12 t_{CS}$, $t = 11.7 t_{CS}$, $t = 27.9 t_{CS}$, and $t = 52.2 t_{CS}$. Note the shift in the x axis scale for the bottom two panels. The initial magnetic field is perpendicular to the shock normal.

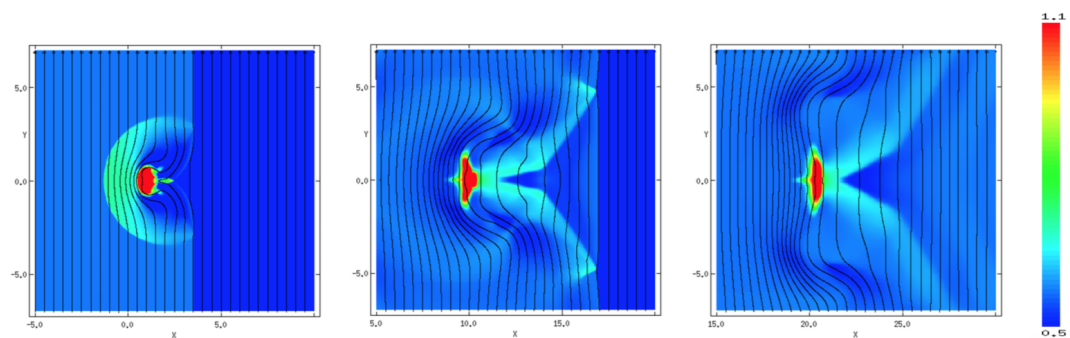


Fig. 3.23 As per Fig. 3.22 but showing the xy plane and magnetic fieldlines. The evolution proceeds left to right with $t = 0.95 t_{CS}$, $t = 3.54 t_{CS}$, and $t = 6.12 t_{CS}$. Note the shift in the x axis scale for the final panel.

Magnetohydrodynamic Filament Simulations

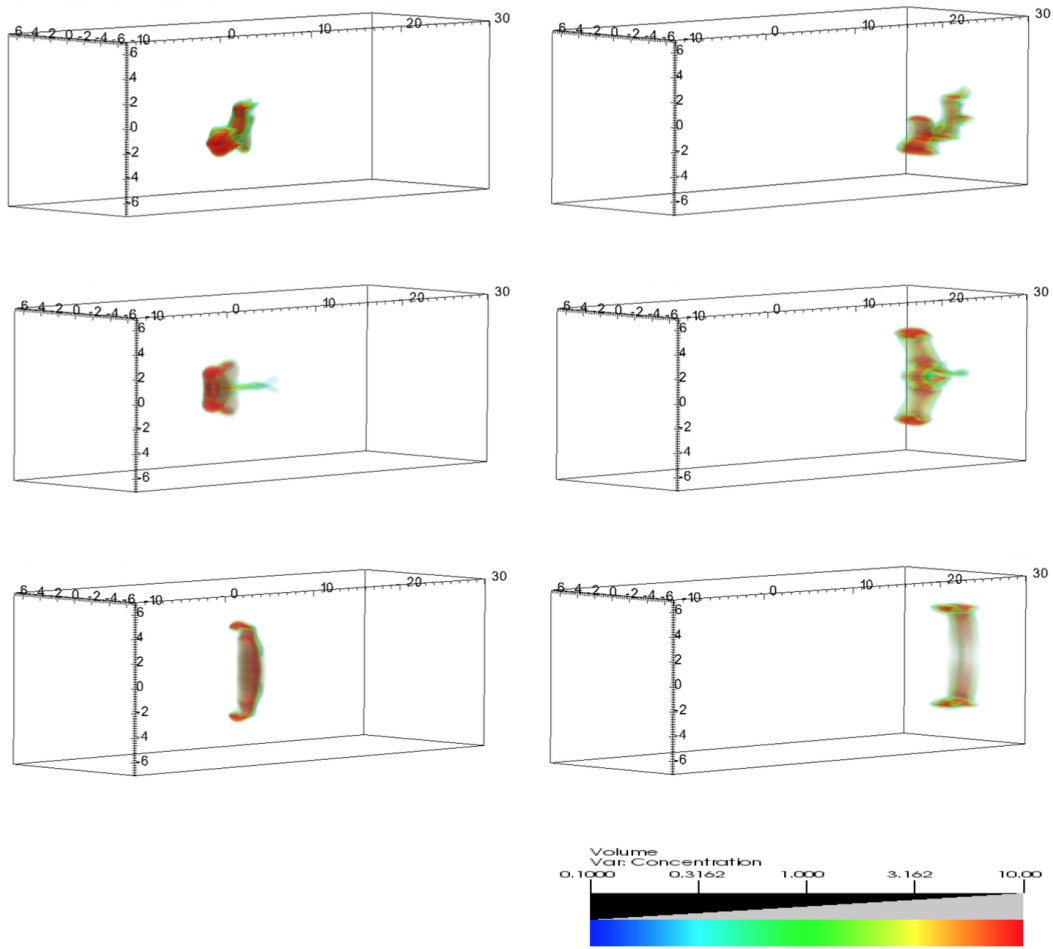


Fig. 3.24 3D volumetric renderings of models *m10c1b1l4o45pe* (top), *m10c1b1l4o90pe* (middle), and *m10c1b1l4o0pe* (bottom) at $t = 3.44 t_{cs}$ (left-hand column) and $t = 8.95 t_{cs}$ (right-hand column). The initial magnetic field is perpendicular to the shock normal.

3.3.2.2 Effect of filament length and orientation on the evolution of the core mass

Amongst all the quantities being tracked, the reduction in the filament core mass shows the most dramatic difference between simulations with parallel and perpendicular magnetic fields. Figure 3.25 shows the evolution of the core mass for filaments in a perpendicular field. The first point of note is that these filaments are very slow to lose their mass. Indeed, in all cases the filaments still comprised a significant amount of mass (between two and three fifths of the initial mass) by $t = 80t_{CS}$. This is in direct contrast to the filaments in a parallel field. Whilst filaments with $l = 4$ and $\theta = 85^\circ$ and 90° lose their mass more quickly (in agreement with the parallel field cases) it is interesting that the filament with $l = 4$ and $\theta = 0^\circ$ has lost the most mass by $t = 80t_{CS}$: in the parallel field simulations it was one of the filaments which conserved their mass the longest.

Considering Fig. 3.25(a), the length of the filament does not appear to have a large influence over the evolution of the core mass, since all three filaments lose mass at approximately the same rate. The spherical cloud, in comparison, loses mass much more quickly, having lost approximately three fifths of its initial mass by the end of the simulation, as opposed to the two fifths that the other filaments have lost. Similar to the parallel magnetic field case, where the spherical cloud evolved in a similar manner to the filaments with $\theta = 0^\circ$, the spherical cloud in this case evolves in a similar manner to the filament with $\theta = 90^\circ$.

3.3.2.3 Effect of filament length and orientation on the mean velocity and the velocity dispersion

The plots showing the mean filament velocity in the x direction (Fig. 3.26) reveal that the filaments in all cases are accelerated to the velocity of the post-shock flow more rapidly than those in a parallel magnetic field. The acceleration is expected to

Magnetohydrodynamic Filament Simulations

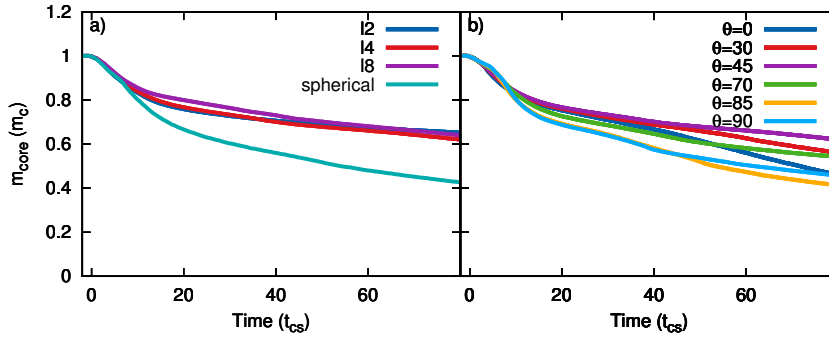


Fig. 3.25 Time evolution of the core mass, m_{core} , for (a) a filament with variable length and an orientation of 45° , and (b) $l = 4$ with variable orientation, in an initial perpendicular magnetic field.

be faster due to i) the increased magnetic pressure which builds up on the upstream side of the filament, and ii) the ‘snapping back’ of the field lines due to the magnetic tension which builds up as the field is dragged around the filament. In contrast to Fig. 3.10(b), the filament with $l = 4$ and $\theta = 30^\circ$ levels off after the initial acceleration, before accelerating again to reach the post-shock flow velocity. Additionally, the filament with $l = 4$ and $\theta = 0^\circ$ overshoots, before asymptoting to the velocity of the post-shock flow.

The length of the filament has little effect on the mean velocity, with all three filaments initially accelerating at the same rate. However, the filament with $l = 8$ and $\theta = 45^\circ$ exhibits the “levelling-off” seen in plot (b), a feature not present in Fig. 3.10(a). The spherical cloud continues to smoothly and rapidly accelerate without levelling off and thus reaches the post-shock flow velocity earlier than the three filaments.

With regard to the velocity dispersion plots, the length of the cloud is shown to have even less of an influence on the evolution of this parameter than in the case of a parallel field (compare Figs. 3.27(a-c) to Figs. 3.11(a-c)). However, there is a clear split in Figs. 3.27(d,f) between those filaments which are more “end on” to the shock front, and those which are more “broadside” to it. As in the parallel field case, those filaments with orientations of $\theta > 45^\circ$ have a greater initial dispersion in the x and z

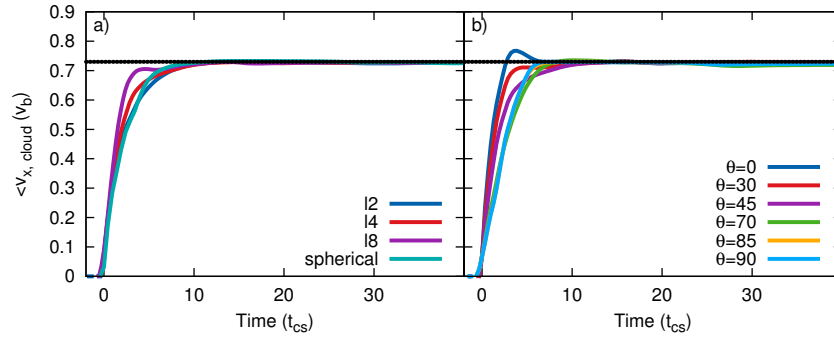


Fig. 3.26 Time evolution of the filament mean velocity, $\langle v_x \rangle$, for (a) a filament with variable length and an orientation of 45° , and (b) $l = 4$ with variable orientation, in an initial perpendicular magnetic field. The dotted black line indicates the velocity of the post-shock flow.

directions, whilst filaments of varying length have very similar velocity dispersions in all directions. In all the velocity dispersion plots the peak of the dispersions is lower than those with a parallel field, indicating that the section of filament closest to the shock front has undergone less compression in the perpendicular field case.

3.3.2.4 Effect of filament length and orientation on the mean density

The mean density plots (Fig. 3.28) for both $\langle \rho_{\text{cloud}} \rangle$ and $\langle \rho_{\text{core}} \rangle$, in terms of the filament orientation, show very little difference between the simulations. However, as in the parallel magnetic field case, the filaments with orientations greater than $\theta = 45^\circ$ have a slightly larger drop in mean density, overall. Plots (a) and (c) of Fig. 3.28 show almost no change in the mean density between the simulations while the spherical cloud reduces to a much lower mean density consistent with the filaments with $\theta = 0^\circ$, and 90° , indicating that the filament length is not important for the evolution of the mean density.

3.3.2.5 χ dependence of the filament evolution

The evolution of filaments in a perpendicular field with increasing cloud density contrasts is radically different to those in a parallel magnetic field. Figure 3.29

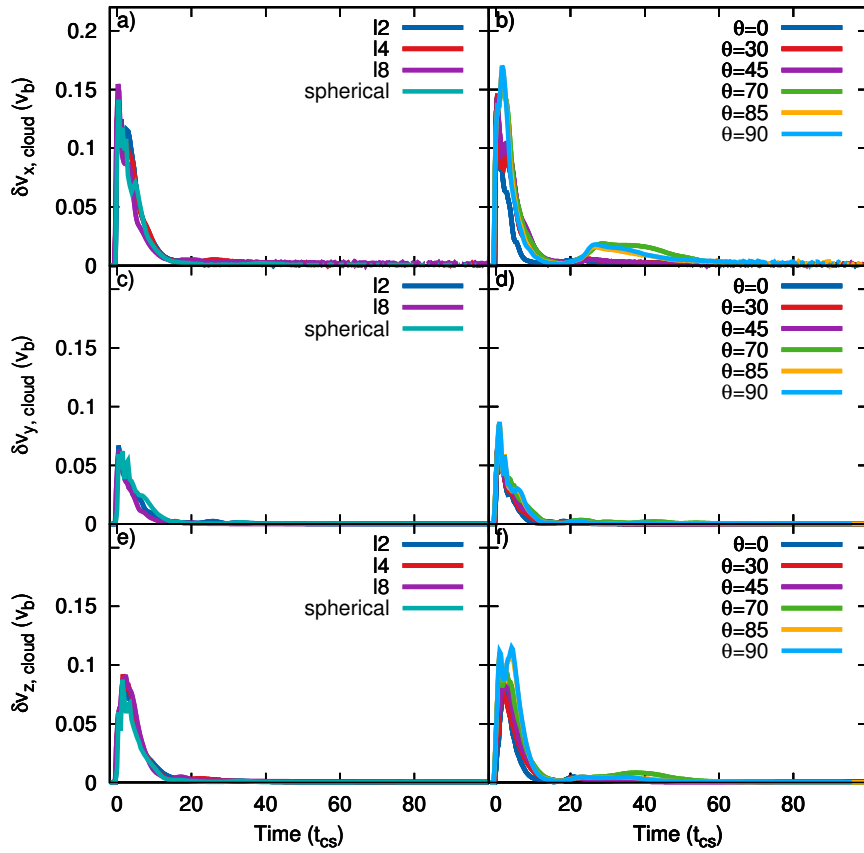


Fig. 3.27 Time evolution of the filament velocity dispersion in the x , y , and z directions, $\delta v_{x,y,z}$, for a filament with variable length and an orientation of 45° (left-hand column), and $l = 4$ with variable orientation (right-hand column) in an initial perpendicular magnetic field.

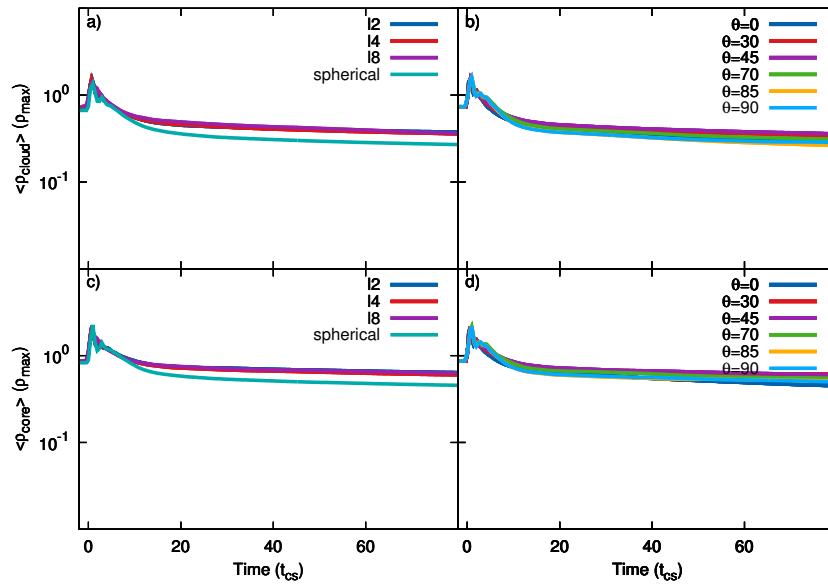


Fig. 3.28 Time evolution of the mean density of the filament, $\langle \rho_{\text{cloud}} \rangle$ (top), and filament core, $\langle \rho_{\text{core}} \rangle$ (bottom), normalised to the initial maximum filament density, for filaments with (left-hand column) variable length and $\theta = 45^\circ$, and (right-hand column) $l = 4$ and a variable orientation, in an initial perpendicular magnetic field.

shows that the filament is drawn out into long, smooth, tendril-like shapes which persist for far longer than the filaments in the parallel case (cf. Fig. 3.13), while the highly-turbulent features present with a parallel field are not in evidence. In addition, the magnetic fieldlines are increasingly stretched around the filament and bunched together, as seen in Fig. 3.30. The higher the value of χ , the more drawn-out the filament is along the x axis. This is evident in Fig. 3.31(a), where the filaments with higher values of χ retain almost two fifths of their initial mass at the end of the simulation, though that with $\chi = 1000$ still has a faster mass-loss rate in agreement with the parallel field case. The mean velocity and mean density plots for both parallel and perpendicular fields are very similar. However, the velocity dispersion plots show some differences, with much less dispersion in the x and y directions in Figs. 3.31(d,e).

Magnetohydrodynamic Filament Simulations

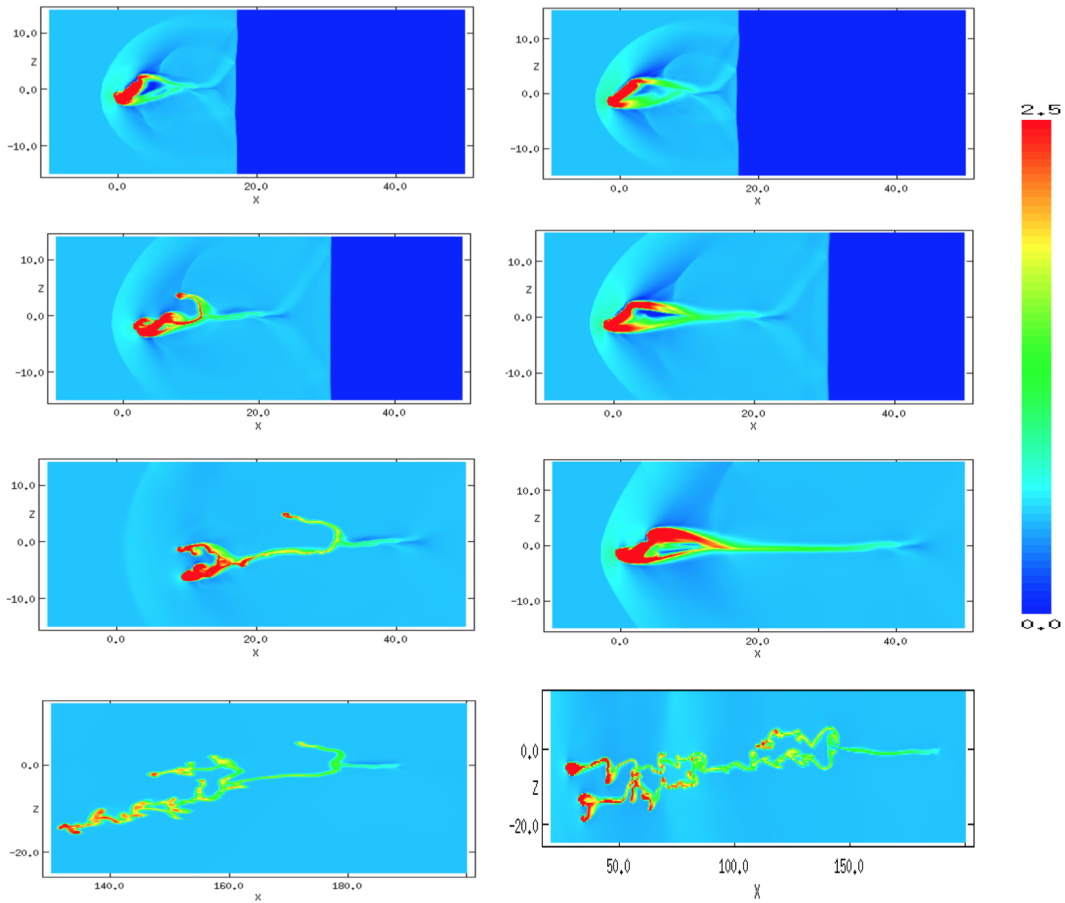


Fig. 3.29 The time evolution of the logarithmic density, scaled with respect to the ambient density, for models *m10c2b1l4o45pe* (left-hand column) and *m10c3b1l4o45pe* (right-hand column). The evolution proceeds top to bottom, with $t = 1.08t_{CS}$, $t = 1.98t_{CS}$, $t = 3.65t_{CS}$, and $t = 16.6t_{CS}$ for the $\chi = 100$ case, and $t = 0.34t_{CS}$, $t = 0.61t_{CS}$, $t = 1.15t_{CS}$, and $t = 5.23t_{CS}$ for the $\chi = 1000$ case. Note the shift in the x and y axis scales for the final panel in each column, and the change in the logarithmic density scale compared to previous cases. The initial magnetic field is perpendicular to the shock normal.

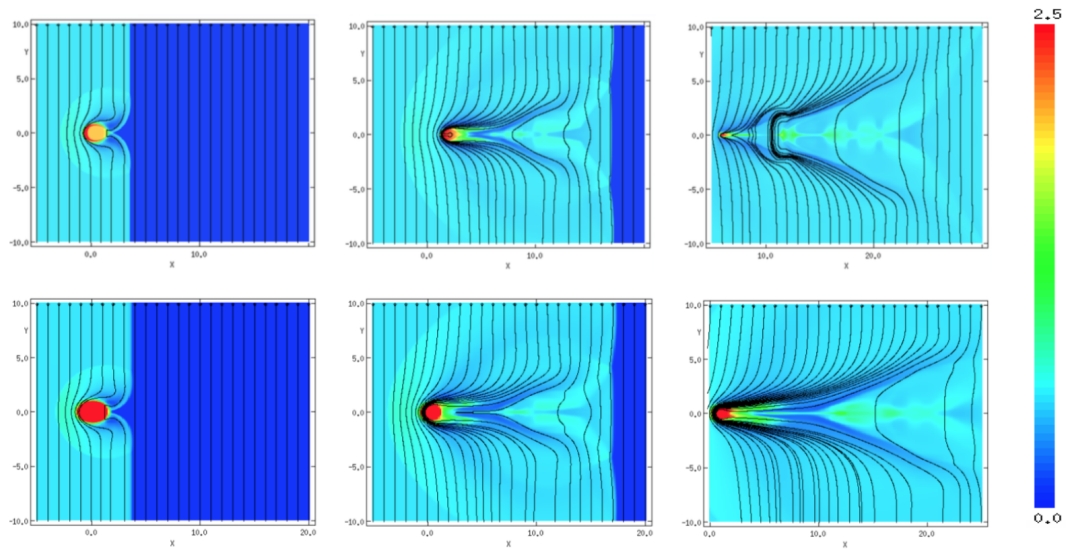


Fig. 3.30 Top row: as per Fig. 3.29 (left-hand panels) but showing the xy plane and magnetic fieldlines. The evolution proceeds left to right with $t = 1.08 t_{CS}$, $t = 1.98 t_{CS}$, and $t = 3.65 t_{CS}$. Bottom row: as per Fig. 3.29 (right-hand panels) but showing the xy plane and magnetic fieldlines. The evolution proceeds left to right with $t = 0.34 t_{CS}$, $t = 0.61 t_{CS}$, and $t = 1.15 t_{CS}$. Note the shift in the x axis scale for the final panels.

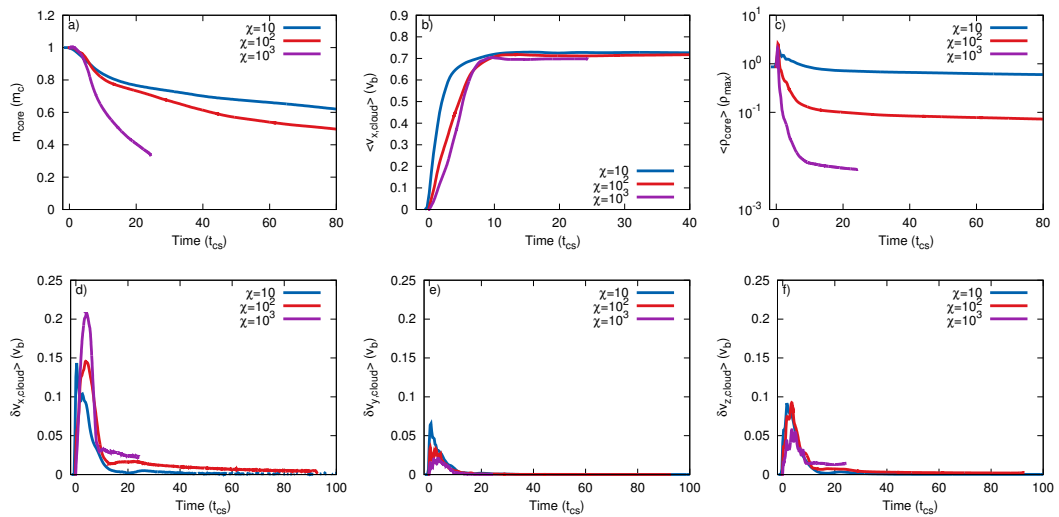


Fig. 3.31 χ dependence of the evolution for filaments with $l = 4$ and $\theta = 45^\circ$. The initial magnetic field is perpendicular to the shock normal, $M = 10$, and $\beta_0 = 1$. Note that although model *m10c3b1l4o45pe* was run at a reduced resolution of R_{16} it was computationally difficult to run. Therefore, the filament in this model moved off the grid before the simulation was complete.

3.3.2.6 Mach dependence of the filament evolution

The shock Mach number dependence of the evolution displays similar trends to that of the parallel magnetic field case. However, it can be seen from Fig. 3.32(a) that the filament which has been struck by a $M = 1.5$ shock has lost almost no mass for the duration of the simulation (in contrast with the filament struck by an $M = 10$ shock, which has lost two fifths of its mass by $t = 80t_{cs}$). Fig. 3.32(b) shows that the post-shock velocity in the $M = 1.5$ case is very small (and much smaller than that of the same case in a parallel field). This suggests that the combination of a mild shock and the magnetic field lines bent around the filament serve to protect the filament from compression and ablation by the flow for a considerable time. This is borne out by the morphology of the low Mach filaments, which retain the same footprint for much of the simulation (indeed, the filament with $M = 1.5$ does not significantly alter its morphology at all). The velocity dispersion plots (d, e, f) show that there is far less dispersion in all directions compared with the parallel magnetic field case, though again the simulation with $M = 1.5$ has almost no dispersion since its morphology has not been significantly changed by the post-shock flow during the period that the simulation was run.

3.3.2.7 β_0 dependence of the filament evolution

Figure 3.33 shows the effect of varying the plasma beta on the filament evolution. As in the parallel field case, the filament with a weak magnetic field ($\beta = 10$) loses mass much more quickly than the other two, stronger, fields. The morphology of the filament in the weaker field displays similar patterns of instability to that of the parallel field, with material being stripped from the surface of the filament. In contrast, the filament in the other two strengths of field remains tightly bound for the duration of the simulation. In addition, there is again a very low amount of divergence between the simulations with regard to the velocity, velocity dispersions,

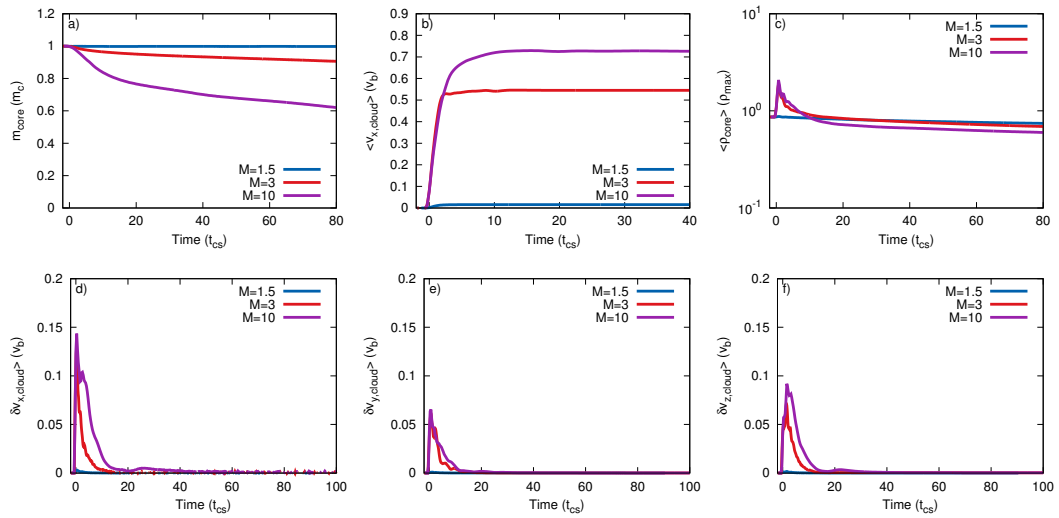


Fig. 3.32 Mach number dependence of the evolution for filaments with $l = 4$ and $\theta = 45^\circ$. The initial magnetic field is perpendicular to the shock normal, $\chi = 10$, and $\beta_0 = 1$.

and mean density, though the filament in a $\beta = 10$ field takes longer to be accelerated to the velocity of the post-shock flow due to the lower upstream magnetic pressure and decreased tension in the field lines. Furthermore, its velocity dispersions decay more slowly, compared to those filaments with stronger field strengths.

3.3.3 Oblique field

3.3.3.1 Filament morphology

The simulations run with an obliquely-orientated (i.e. at 45° to the shock normal) magnetic field have very similar morphologies to those run with a perpendicularly-orientated field. For this reason, I have not included snapshots of the logarithmic density for the oblique field case. As before, filaments set at an angle to the shock front in an oblique field take on a tendril-like appearance, whilst those orientated either broadside, or end on, to the shock front produce linear features along the axis behind the filament.

Magnetohydrodynamic Filament Simulations

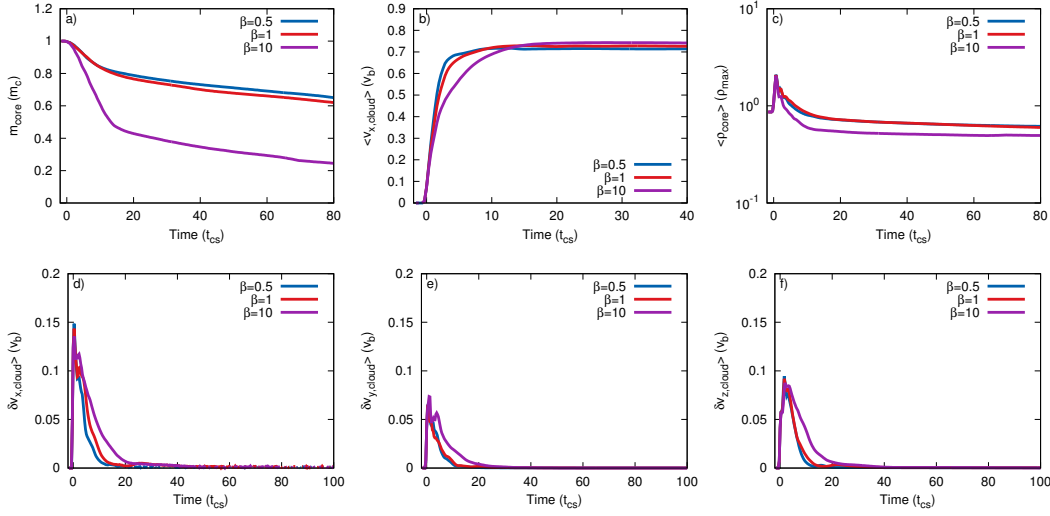


Fig. 3.33 Plasma beta dependence of the evolution for filaments with $l = 4$ and $\theta = 45^\circ$. The initial magnetic field is perpendicular to the shock normal, $M = 10$, and $\chi = 10$.

3.3.3.2 Effect of filament length and orientation on the core mass, mean velocity, velocity dispersion, and mean density

In terms of the evolution of the core mass, there is only a slight difference between Fig. 3.34(a) and Fig. 3.25(a). In the oblique field case, the filament with $l = 4$ and $\theta = 45^\circ$ has the most mass remaining at the end of the simulation whilst that with $l = 8$ and $\theta = 45^\circ$ loses the most mass. In the perpendicular field case, however, the rate at which each filament loses mass is reversed. Considering Fig. 3.34(b) and Fig. 3.25(b), the only difference between the two field orientations is that in the perpendicular field case the filament with $l = 4$ and $\theta = 85^\circ$ is one of two filaments which lose the most mass by the end of the simulation, but in the oblique case this filament loses mass far slower (at a similar rate to the filaments with $\theta = 30^\circ$ and $\theta = 70^\circ$).

The mean velocity plots for filaments in oblique and perpendicular fields (Fig. 3.35 and Fig. 3.26, respectively) are almost identical, though the filament in the oblique field with $l = 8$ and $\theta = 45^\circ$ is accelerated to the velocity of the post-shock flow much more smoothly than the same filament in the perpendicular field. The ve-

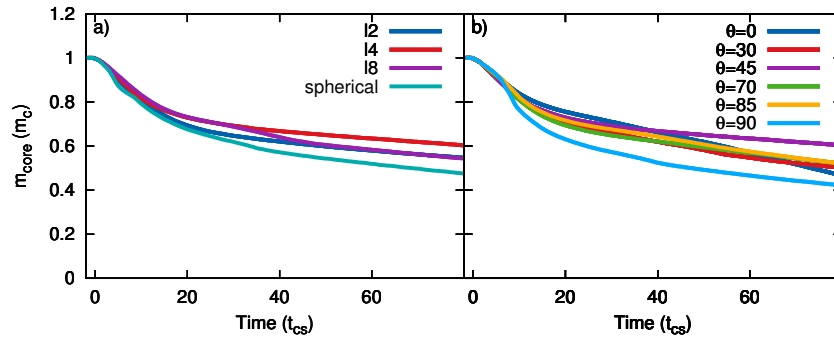


Fig. 3.34 Time evolution of the core mass, m_{core} , for (a) a filament with variable length and an orientation of 45° , and (b) $l = 4$ with variable orientation, in an initial magnetic field orientated at 45° to the shock normal.

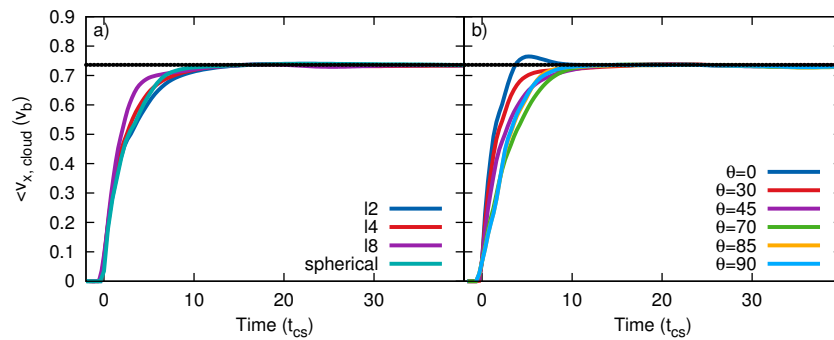


Fig. 3.35 Time evolution of the filament mean velocity, $\langle v_x \rangle$, for (a) a filament with variable length and an orientation of 45° , and (b) $l = 4$ with variable orientation, in an initial magnetic field orientated 45° to the shock normal. The dotted black line indicates the velocity of the post-shock flow.

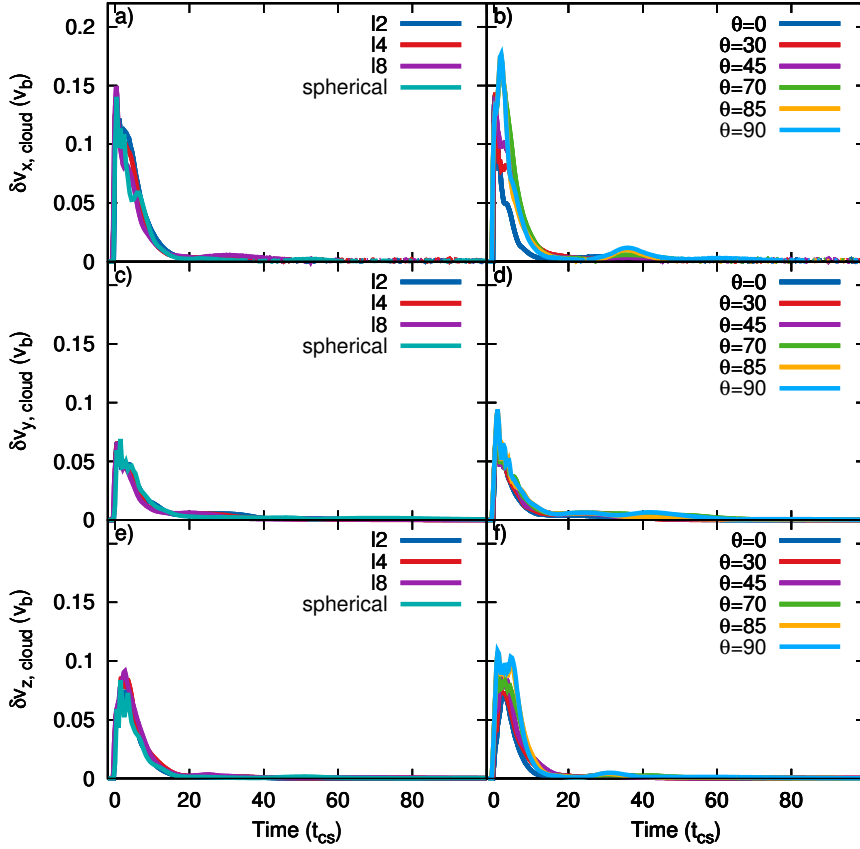


Fig. 3.36 Time evolution of the filament velocity dispersion in the x , y , and z directions, $\delta v_{x,y,z}$, for a filament with variable length and an orientation of 45° (left-hand column), and $l = 4$ with variable orientation (right-hand column) in an initial magnetic field orientated 45° to the shock normal.

locity dispersions for both orientations of the magnetic field are also very similar, though Fig. 3.36(d) does not display as large a dispersion in the x direction between $t = 30 - 40 t_{cs}$ as Fig. 3.27(d) does. In terms of the mean density (cf. Fig. 3.37 with Fig. 3.28), the filaments with different orientations provide very similar plots in both the oblique and perpendicular field cases, whereas those filaments with varying lengths in the oblique field case reach a much lower mean density after the initial peak.

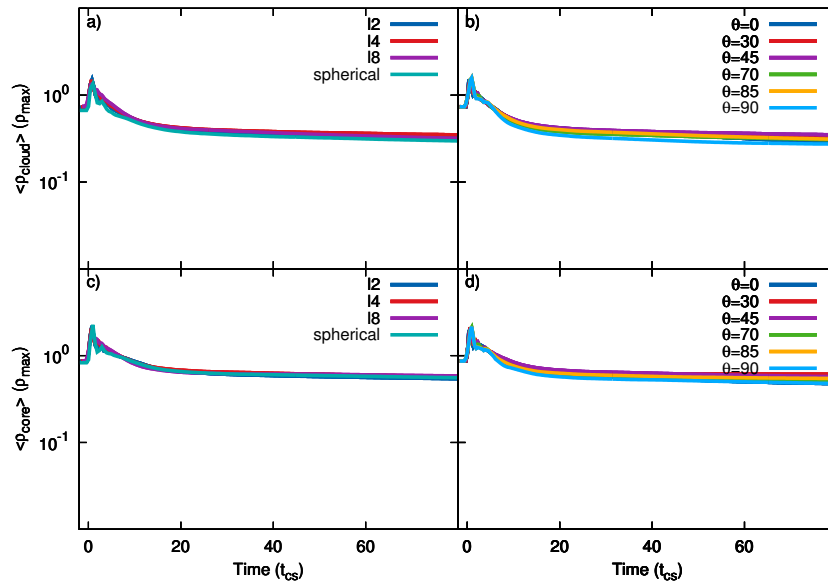


Fig. 3.37 Time evolution of the mean density of the filament, $\langle \rho_{\text{cloud}} \rangle$ (top), and filament core, $\langle \rho_{\text{core}} \rangle$ (bottom), normalised to the initial maximum filament density, for filaments with (left-hand column) variable length and $\theta = 45^\circ$, and (right-hand column) $l = 4$ and a variable orientation, in an initial magnetic field orientated 45° to the shock normal.

3.3.3.3 χ , M , and β_0 dependence of the filament evolution

As with the time evolution of the filaments with varying length and orientation, the dependence of the evolution on the density contrast, shock Mach number, and magnetic field strength does not significantly differ between the perpendicular and oblique field cases. In terms of the change in χ , the only difference between Figs. 3.38 and 3.31 is that the filaments with higher values of χ in the oblique field are destroyed much faster than those in a perpendicular field (though still not as rapidly as for a parallel field). Figure 3.39 shows that the velocity of the post-shock flow is higher in the oblique field case, and thus the filament hit by a $M = 1.5$ shock reaches a higher final velocity compared to the perpendicular field case. In addition, this filament has much greater velocity dispersions than the same filament in the perpendicular field case (cf. Fig. 3.32). The filament struck by a $M = 3$ shock also loses mass at a slightly faster rate than in a perpendicular field. Considering the

Magnetohydrodynamic Filament Simulations

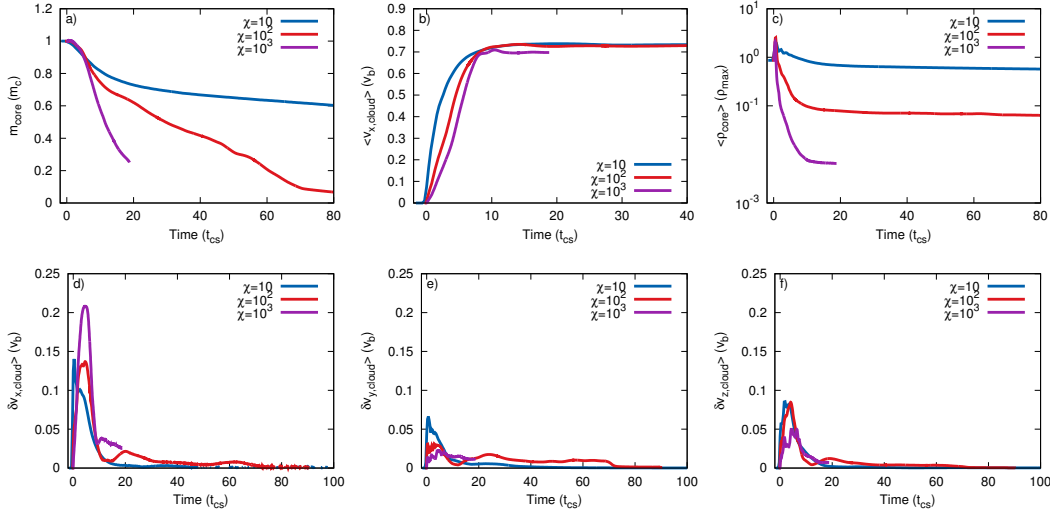


Fig. 3.38 χ dependence of the evolution for filaments with $l = 4$ and $\theta = 45^\circ$. The initial magnetic field is orientated 45° to the shock normal, $M = 10$, and $\beta_0 = 1$. Note that although model *m10c3b1l4o45ob* was run at a reduced resolution of R_{16} it was computationally difficult to run. Therefore, the filament in this model moved off the grid before the simulation was complete.

magnetic field strength, the main difference between the perpendicular and oblique field cases is that the filament in a field of strength $\beta_0 = 0.5$ undergoes much greater velocity dispersions in the y direction at $t \simeq 40t_{cs}$, compared with the perpendicular field (cf. Fig. 3.40(e) to Fig. 3.33(e)).

3.3.4 Timescales

Values of t_{drag} , t_{mix} , and t_{life} are noted in Tables 3.2 and 3.3. With the exception of the simulations with a cloud density contrast of 1000 in both the parallel and oblique field cases, in all other cases $t_{\text{drag}} < t_{\text{mix}}$. Figure 3.41 shows the values of t_{drag} for filaments of varying length and an orientation of $\theta = 45^\circ$ and filaments with a length $l = 4$ and varying orientations, with $M = 10$, $\chi = 10$, and $\beta = 1$. It can be seen from Fig. 3.41(a) that t_{drag} decreases at a similar rate with increasing filament length for all orientations of the magnetic field. However, the field orientation also has an influence on the value of t_{drag} , with filaments in a parallel field exhibiting higher values compared to those in a perpendicular field. Figure 3.41(b), in contrast, shows that

3.3 Results

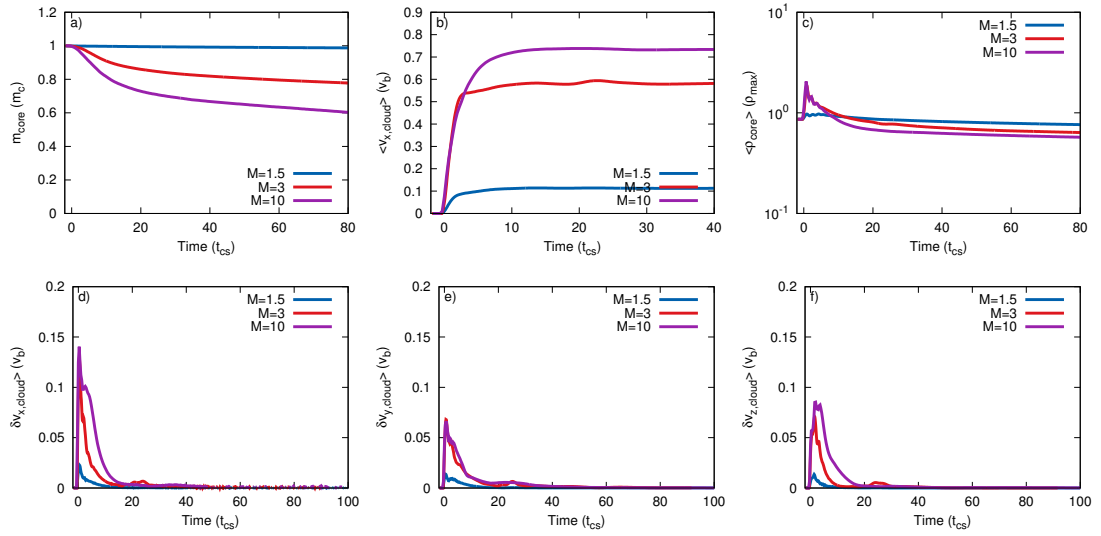


Fig. 3.39 Mach number dependence of the evolution for filaments with $l = 4$ and $\theta = 45^\circ$. The initial magnetic field is orientated 45° to the shock normal, $\chi = 10$, and $\beta_0 = 1$.

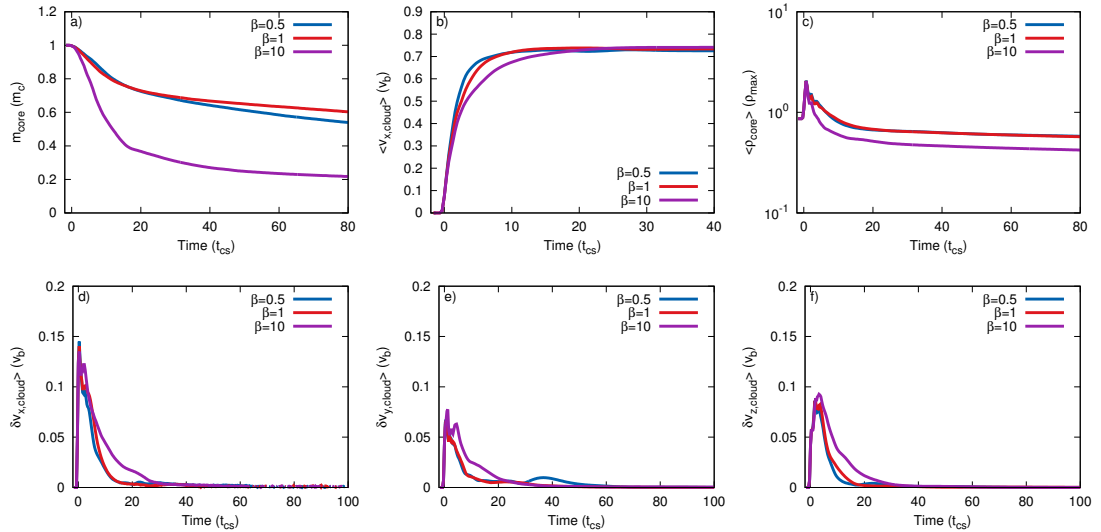


Fig. 3.40 Plasma beta dependence of the evolution for filaments with $l = 4$ and $\theta = 45^\circ$. The initial magnetic field is orientated 45° to the shock normal, $M = 10$, and $\chi = 10$.

Magnetohydrodynamic Filament Simulations

while the field orientation has the same effect for filaments with varying θ as those with varying length, t_{drag} in this case increases with increasing filament orientation, with filaments of $\theta = 0^\circ$ exhibiting the lowest value of t_{drag} (i.e. these filaments accelerate faster than the others). In addition, there is a downturn/plateauing in the value of t_{drag} for filaments with orientations of $\theta \geq 70^\circ$. For both plots, t_{drag} varies by a factor of ~ 2.5 . t_{drag} is an important indicator of the filament's acceleration within the post-shock flow; thus, in the above cases, longer filaments oriented broadside to the shock front are able to be accelerated more quickly up to the velocity of the post-shock flow.

Figure 3.42 shows the change in t_{mix} according to filament length and orientation, respectively. It should be noted that because MHD filaments generally exist for far longer than hydrodynamic filaments t_{mix} in some of the simulations occurred after the end of the simulation. I have, therefore, plotted the simulation's final value of t as t_{mix} whilst emphasising that the actual t_{mix} was in fact greater than this (see Tables 3.2 and 3.3 for an indication of the relevant simulations). The results from [Pittard and Goldsmith \(2016\)](#) showed that t_{mix} displayed the same behaviour as t_{drag} for filaments of varying length or orientation. However, my results displayed much more complex behaviour (cf. Fig. 3.42 with Fig. 34 in [Pittard and Goldsmith \(2016\)](#)). The results for filaments of differing length broadly showed the same trends as for t_{drag} , but those for filaments of varying orientation in either a perpendicular or oblique field did not. It is clear that filaments of $\theta = 45^\circ$ in perpendicular/oblique fields are far more slow to mix in with the surrounding flow than filaments of any other orientation. t_{mix} is relevant to the survival of the filament; therefore, in the above cases, filaments of length $l \leq 4$ and oriented at $\theta = 45^\circ$ in either a perpendicular or oblique field are able to survive for significant periods of time.

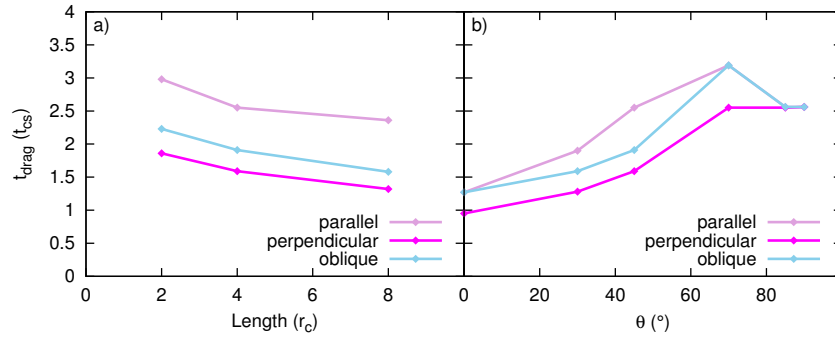


Fig. 3.41 t_{drag} (in terms of the cloud) as a function of filament length (a), where the filament has an orientation of $\theta = 45^\circ$, and orientation (b), where the filament has a length $l = 4$, for simulations with $M = 10$, $\chi = 10$, and $\beta = 1$.

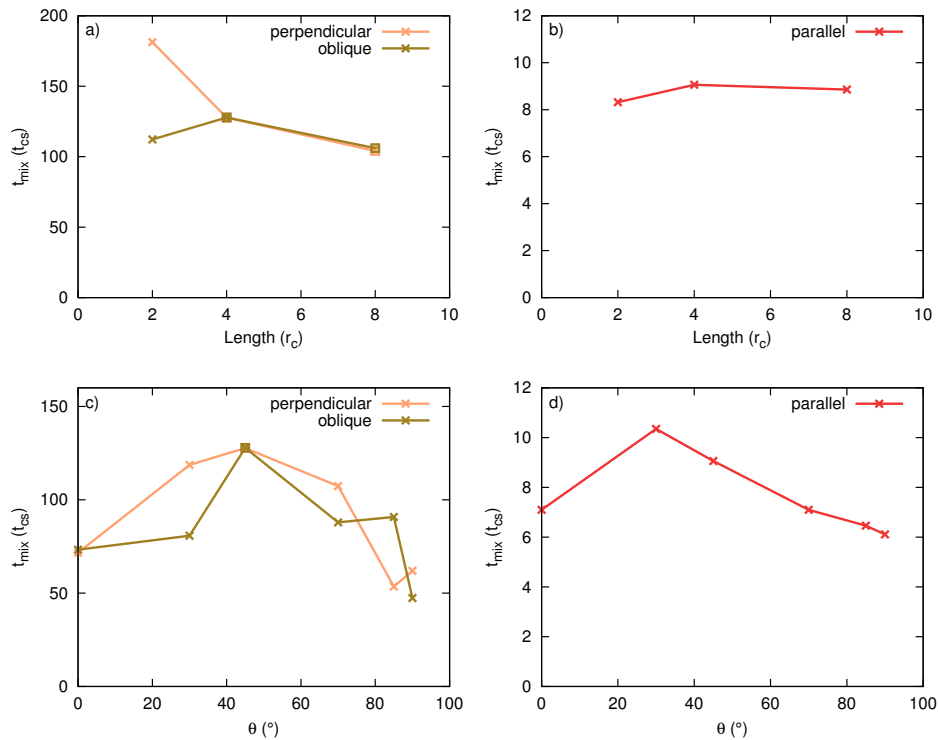


Fig. 3.42 t_{mix} , as a function of filament length (top panels), where the filament has an orientation of $\theta = 45^\circ$, and orientation (bottom panels), where the filament has a length $l = 4$, for simulations with $M = 10$, $\chi = 10$, and $\beta = 1$, in a perpendicular/oblique field (left) and a parallel field (right). Note that data marked with a ‘square’ represent inferred rather than actual values for t_{mix} (see Table 3.3).

3.4 Discussion

Filaments have been observed in regions such as the Taurus molecular cloud ([Panopoulou et al., 2014](#)), the Lupus molecular clouds ([Benedettini et al., 2015](#)), Orion A ([Polychroni et al., 2013](#)), and the Pipe Nebula ([Peretto et al., 2012](#)). Recent observations (e.g. from *Herschel*) have shown filamentary structures to be highly prevalent within star-forming regions and point towards their central role in the process of star formation (e.g. [Arzoumanian et al. 2011](#)). In addition, theoretical and numerical studies ([Federrath, 2016](#)) of such observations which followed the evolution of molecular clouds and the star formation within them, detected complex networks of filaments in all simulations and determined various filament parameters which were in excellent agreement with observations.

A large proportion of prestellar cores are found to be located within dense filaments (e.g. [Schisano et al. 2014](#), [Könyves et al. 2015](#)). Clusters tend to be highly concentrated at filament junctions but cores (and, thus, stars) have also been shown to form along filaments, indicating that the merger of filaments enables the formation of massive stars within clusters ([Schneider et al., 2012](#)). The presence of magnetic fields and their stabilising effects on filaments have been inferred (e.g. the alignment of a filament to the ambient magnetic field ([Benedettini et al., 2015](#)) and the smooth morphology of some filaments ([Crawford et al., 2005](#))), though there has been less discussion of this subject in the literature. Such stabilisation may have a role to play in enabling the subsequent formation of cores.

In light of the importance of filamentary structures, studies of the interaction of high-speed flows with filaments, as well as the physics of filament evolution and destruction, are important for a complete understanding of the magnetohydrodynamical nature of the ISM and the process of star formation.

3.4.1 Entrainment of filament material

In the current study, I found that almost all the filaments had been accelerated to the velocity of the post-shock flow by the end of the simulations. The entrainment of cold, molecular filaments has been noted in the literature (e.g. in jet-filament interactions (O’Dea et al., 2013)). Although the current work concerns the interaction of a shock with a filament there is some relevance to wind-filament/cloud interactions, since the majority of the filaments in the simulations presented in this Chapter survived the passage of the initial shock and were then overrun by the post-shock flow, which can be thought of as resembling a wind of the same velocity. A more detailed comparison of shock-cloud and wind-cloud interactions will be presented in Chapters 4 and 5.

Zhang et al. (2015) investigated hydrodynamic isothermal wind-cloud interactions. In their simulations, they found that the ram pressure from a hot wind was not able to accelerate the cloud to observed velocities since the cloud was rapidly shredded by KH instabilities whilst it was still at a relatively low velocity. This called into question how cool gas was able to be entrained and accelerated by the surrounding flow. The authors proposed an alternative theory whereby magnetic fields could prolong the cloud’s life, allowing the build-up of turbulent instabilities to occur over a much longer timescale than that implied by the hydrodynamic simulations. McCourt et al. (2015) also found that tangled internal magnetic fields suppressed mixing and allowed clouds to accelerate up to the wind speed.

In a similar vein, Scannapieco and Brüggén (2015) investigated the evolution of cold spherical clouds embedded in flows of hot and fast material. They found that the velocity of the cloud was dependent on the density contrast and the velocity of the hot wind; one implication being that if $\chi \gtrsim 100$, the cloud would not be accelerated to the hot wind speed before being destroyed. In addition, these authors considered the distance travelled by the cloud and found that this was proportional to the square of the lifetime. Thus, the suppression of KH instabilities can be important

Magnetohydrodynamic Filament Simulations

in determining the distance over which the cloud moves before its destruction. In the hydrodynamic case, the distance depended almost completely on the initial cloud radius. This presented problems in that for clouds to travel distances of ~ 100 kpc, as observed in nearby galaxies, they would need to be the size of a galaxy in order to do so without first being destroyed. The authors suggested that magnetic fields may be one way in which the cloud's lifetime could be extended to allow them to travel such large distances.

In the work presented in this chapter, I found that the cloud density contrast, shock Mach number, and magnetic field orientation are important for determining the lifetime of filaments. A χ of 1000 in a parallel field and a shock Mach number of 10 led to the rapid destruction of the filament by turbulent instabilities before it had reached the velocity of the post-shock flow, whereas low values of χ in a weak shock and a perpendicular or oblique field provided the best conditions for the long-term survival of the filament. Filaments struck by a weak (e.g. $M = 1.5$) shock, regardless of the orientation of the magnetic field, were easily able to reach the much lower post-shock flow velocity. It should be noted, however, that my simulations did not include the effects of evaporation on the filament, which [Zhang et al. \(2015\)](#) consider to be important for the destruction of the cloud in the presence of a magnetic field. My simulations also reveal that the presence of a magnetic field dramatically affects the filament lifetime. A perpendicular or oblique field allows the field lines to wrap around the edge of the filament, protecting it from the flow and allowing it to move a distance downstream of many tens, hundreds, or thousands of r_c before the filament is finally destroyed (and in some cases the filament may not be destroyed at all). Thus, the preserving effect that the orientation of the field has on the filament is the key take-away result of this chapter.

3.5 Summary and Conclusions

The material in this Chapter forms the basis for the second in a series of papers investigating the interaction between astrophysical shocks and filaments. In this Chapter, I employed a magnetohydrodynamic code to investigate the evolution and destruction by an adiabatic shock of a filament embedded within a magnetised medium. In comparison to the results from the previous hydrodynamical study of filaments by [Pittard and Goldsmith \(2016\)](#) I found that the presence of magnetic fields, their orientation with respect to the shock normal, and an increase in the density contrast of the filament all had significant effects on the evolution and lifetime of the filament; this is the key and novel result arising from this chapter. I summarise my main results for each orientation of the magnetic field as follows, noting that in all comparisons the time is normalised by t_{CS} :

- *Parallel fields:*
 - (i) Filaments which are orientated either broadside, or nearly-broadside, on to the shock front survive for far longer than those orientated end on. Unless the filament is very small, the length of the filament has no significant effect on its evolution;
 - (ii) Well-defined linear structures situated on the axis behind the filament are formed only when the filament is end on with respect to the shock front (i.e. orientated at $\theta = 90^\circ$);
 - (iii) An increase in the cloud density contrast hastens the destruction of the cloud through the increased presence of turbulent instabilities located on the filament surface. As the density contrast increases, so does the amount of turbulence;
 - (iv) Low shock Mach numbers restrict the filament from fragmenting, thus significantly prolonging its life.

Magnetohydrodynamic Filament Simulations

- *Perpendicular/oblique fields:*
 - (vi) Even if the filament is end on with respect to the shock front, filaments in a perpendicularly/obliquely-orientated magnetic field do not form flux ropes;
 - (vii) Compared with parallel-orientated fields, perpendicular/oblique fields shield the filament to a degree from the surrounding flow, allowing the filament lifetime to be considerably extended. The filament is more greatly confined by the field and maintains a higher average density;
 - (viii) Filaments are more rapidly accelerated to the velocity of the post-shock flow due to the effects of the magnetic pressure and field line tension;
 - (ix) An increase in the filament density contrast does not initiate large turbulent instabilities, compared to the case of a parallel field;
 - (x) A combination of a mild (e.g. $M = 1.5$) shock and a perpendicular/oblique field allows the filament to survive almost intact for a considerable length of time.

The work presented in this Chapter is difficult to apply observationally since the adiabatic simulations do not include realistic physical processes such as thermal conduction, radiative cooling, and self-gravity. Future work should include the effects of radiative cooling, and should also compare synthetic observations of such simulations with actual observations in order to present a more complete picture of the evolution of filaments in the ISM. It should be noted that [Banda-Barragán et al. \(2016\)](#) explored the effects of using a quasi-isothermal equation of state to approximate the effect of radiative cooling in MHD wind-cloud simulations and found that this led to significantly longer cloud lifetimes compared to the adiabatic case; a comparison with isothermal shock-filament interactions (see Chapter 6) would, therefore, be of interest.

Chapter 4

A comparison of shock-cloud and wind-cloud interactions: the longer survival of clouds in winds

4.1 Introduction

The coupling of stellar feedback processes (stellar winds, ionising radiation, shock waves from SNRs, etc.) with clouds can produce superficially-similar dynamical effects. [Pittard et al. \(2009\)](#) noted that clouds with a high density contrast were able to survive the passage of a shock and would then be immersed in a post-shock flow that would resemble a wind with the same Mach number. Since the simulation of a hot, high-velocity wind can therefore be thought of as resembling a post-shock flow, many wind-cloud papers are highly pertinent to the shock-cloud scenario, and vice-versa. Although both wind-cloud and shock-cloud interactions have been well studied, there exists, to my knowledge, no direct comparison of the two processes in the literature. This, therefore, forms the motivation for this chapter.

With respect to the survivability of clouds, [Scannapieco and Brügger \(2015\)](#) noted that in the hydrodynamic, adiabatic situation only the initial cloud radius

A comparison of shock-cloud and wind-cloud interactions: the longer survival of clouds in winds

determines the distance over which clouds can travel. The authors found that the distances over which the clouds were able to travel would enable them to arrive at a few kpc from the driving region (observations have shown these to be typical distances when clouds are seen in absorption against the starbursting host galaxy (see e.g. [Heckman et al., 2000](#); [Pettini et al., 2001](#); [Soto and Martin, 2012](#))). These clouds would therefore require a distinct density (as opposed to the cloud mass being smoothed out and mixed into the flow) in order to be observed in this way. Absorption line observations using background galaxies and quasars have in fact revealed that clouds may travel distances on the order of ≈ 100 kpc or more ([Bergeron 1986](#); [Lanzetta and Bowen 1992](#); [Steidel et al. 1994](#); [Steidel et al. 2002](#); [Steidel et al. 2010](#); [Zibetti et al. 2007](#); [Kacprzak et al. 2008](#); [Chen et al. 2010](#); [Tumlinson et al. 2013](#); [Werk et al. 2013](#); [Werk et al. 2014](#); [Peeples et al. 2014](#); [Turner et al. 2014](#)). This is extremely challenging for current theoretical models.

In this chapter, I investigate a 2D hydrodynamical, adiabatic wind-cloud interaction and compare the results to those of a shock-cloud simulation using similar initial parameters. I then incrementally increase the velocity of the wind to increase its effective Mach number and explore the impact this has on the evolution of the cloud.

The outline of this chapter is as follows: in § 4.2 I introduce the initial conditions. In § 4.3 I present the results of the simulations. A brief discussion of the relevance of my work in terms of Mach scaling and the longevity of the cloud can be found in § 4.4. § 4.5 summarises and concludes.

4.2 The numerical setup

The computations in this chapter were performed using the MG HD code, details of which can be found in Chapter 2.

4.2.1 Initial conditions

All simulations were performed on a two-dimensional RZ cylindrically-symmetric grid at an effective resolution of R_{128} (where the subscript denotes the number of cells per cloud radius on the finest grid), which has been found to be the minimum necessary for key features in the flow to be adequately resolved and for the morphology and global statistical values to begin to show convergence (e.g. [Mac Low et al. 1994](#); [Niederhaus 2007](#); [Pittard et al. 2009](#); [Pittard and Parkin 2016](#)). Nine grid levels (G^0 to G^8) are used for calculations requiring the finest grid. I measure all length scales in units of the cloud radius, r_c , where $r_c = 1$, whilst velocities are measured in terms of the shock speed through the background medium, v_b ($v_b = 13.6$, in computational units). Measurements of the density are given in terms of the density of the background medium, ρ_{amb} , while those of the pressure are given in terms of the ambient medium pressure, P_{amb} (see § 3.2.1.1 for the values of these latter two quantities). The numerical domain is set to be large enough so that the main features of the interaction occur before cloud material reaches the edge of the grid. Table 4.1 details the grid extent for each of the simulations.

I make the following assumptions in order to maintain simplicity: the cloud has an adiabatic equation of state (with $\gamma = 5/3$) and I ignore the effects of thermal conduction, magnetic fields, self-gravity, and radiative cooling. My assumption of adiabacity is consistent with the small-cloud-limit, whereby the cloud-crushing time-scale is much shorter than the cooling time-scale (cf. [Mac Low et al. 1994](#)). Non-radiative interactions between shocks/winds and clouds are expected in the ISM ([McKee and Cowie, 1975](#)). I further justify my simplified set-up by noting that my primary goal is to provide an initial comparison of shock-cloud and wind-cloud simulations and the similarities/differences between the two types of interaction are better isolated without the introduction of additional processes. I do not, therefore, concern myself at this stage with the detail of the processes which led to the cloud

A comparison of shock-cloud and wind-cloud interactions: the longer survival of clouds in winds

being embedded in the wind, nor with the effects of additional processes (e.g. radiative cooling) on the interaction. It should, however, be noted that 3D calculations are necessary in future work and that they are expected to produce slightly different morphologies and statistical values once non-axisymmetric instabilities become important at late times (e.g. $t > 5t_{cc}$, Pittard and Parkin, 2016). More realistic 3D comparative studies that include radiative cooling should be considered in the future.

4.2.2 The shock-cloud model

My reference simulation is the shock-cloud model *c1shock* (see § 4.3 for the model naming convention). The simulated cloud is an idealised sphere and is assumed to have sharp edges which maximises the growth of KH instabilities and sets a lower limit to the cloud’s lifetime (see e.g. Nakamura et al. 2006; Pittard and Parkin 2016 for a discussion of how cloud density profiles affect the formation of hydrodynamic instabilities), in contrast to previous shock-cloud studies that used a soft edge to the cloud (e.g. Pittard and Parkin 2016), and is initially in pressure equilibrium with the surrounding stationary ambient medium. The simulations are described by the shock Mach number, $M_{\text{shock}} = 10$, and the density contrast between the cloud and the stationary ambient medium, $\chi = 10$. The shock-cloud simulation begins with the shock initially located at $z = 1$ (the shock propagates in the negative z direction) and the cloud is centred on the grid origin $r, z = (0, 0)$.

The post-shock¹ density, pressure, and velocity for the shock-cloud case relative to the pre-shock ambient values and to the shock speed are $\rho_{ps/wind}/\rho_{\text{amb}} = 3.9$, $P_{ps/wind}/P_{\text{amb}} = 124.8$, and $v_{ps/wind}/v_b = 0.74$, respectively.

¹I use the subscript *ps/wind* to denote quantities related to either the post-shock flow or the wind.

4.2.3 The wind-cloud model

In order to simulate a wind-cloud interaction, I begin by removing the initial shock and fill the domain external to the cloud with the same post-shock flow properties. At the start of the simulation, the cloud is instantly surrounded by a wind of uniform speed and direction, in line with previous wind-cloud studies (e.g. [Banda-Barragán et al. 2016](#)). Since this is an idealised scenario as a first step towards more realistic simulations, I simplify the initialisation of the wind and make the following assumptions: a) the wind is associated with the post-shock flow properties of the shock-cloud model (i.e. I simulate a mildly supersonic wind using exactly the same post-shock flow conditions as used in the shock-cloud model) and b) that it completely surrounds the cloud at time zero. My aim is to provide comparable initial conditions for both interactions before any of the wind parameters are changed. This means that the cloud is initially under-pressured compared to the wind. Astrophysically, this implies that the wind switches on rapidly.

Although the initial cloud density is the same in both the shock-cloud and wind-cloud simulations, the density contrast between the cloud and the *wind* in the latter case (χ') is given by factoring off the value of the post-shock density jump from the value of χ , i.e. $\chi' = \chi/3.9$ (see § 4.2.2).

In addition to the parameters described in § 4.2.2, the wind-cloud simulations are also described by the effective Mach number of the wind, $M_{ps/wind}$, given by

$$M_{ps/wind} = \frac{v_{ps/wind}}{c_{ps/wind}}, \quad (4.1)$$

where $c_{ps/wind} = \sqrt{\gamma \frac{P_{ps/wind}}{\rho_{ps/wind}}}$ is the adiabatic sound speed of the post-shock flow/wind. For the initial wind-cloud simulation (model *c1wind1*), $M_{ps/wind} = 1.36$. Since the initial, unshocked cloud pressure is equal to P_{amb} , and $P_{amb} \ll P_{ps/wind}$, the cloud does not start off in pressure equilibrium with the wind and is thus under-pressured

A comparison of shock-cloud and wind-cloud interactions: the longer survival of clouds in winds

Table 4.1 The grid extent for each of the simulations (see § 4.3 for the model naming convention). $M_{ps/wind}$ refers to the effective Mach number of the post-shock flow/wind. The unit of length is the initial cloud radius, r_c .

Simulation	$M_{ps/wind}$	R	Z
c1shock	1.36	$0 < R < 10$	$-200 < Z < 5$
c1wind1	1.36	$0 < R < 20$	$-400 < Z < 10$
c1wind1a	4.30	$0 < R < 20$	$-400 < Z < 10$
c1wind1b	13.6	$0 < R < 20$	$-500 < Z < 10$
c1wind1c	43.0	$0 < R < 20$	$-500 < Z < 10$

with respect to the flow. Over the course of one cloud-crushing time-scale the cloud pressure increases until it is equal to or slightly greater than the pressure of the surrounding wind. It should be noted that the wind can travel a long way in the ‘cloud-crushing time’ due to the high density contrast of the cloud. This is a different set-up to other wind-cloud studies (e.g. [Schiano et al. 1995](#)) where the simulations begin with the cloud already in approximate ram pressure equilibrium with the wind, but is necessary in order to allow a more direct comparison to my shock-cloud simulation.

The value of the wind velocity, $v_{ps/wind}$, is given in § 4.2.2. In order to explore the effect of an increasing Mach number on the interaction, the velocity of the flow, $v_{ps/wind}$, is increased by factors of $\sqrt{10}$, $\sqrt{100}$, and $\sqrt{1000}$ in order to increase $M_{ps/wind}$. Values of the wind Mach number are given in Table 4.1.

4.2.4 Global quantities

The various global quantities used to follow the evolution of the interaction are described in § 3.2.1.2. In this chapter, I define motion in the direction of wind/shock propagation as “axial” (the wind/shock propagates in the negative z direction), whilst motion perpendicular to this is termed “radial”. In order to measure the shape of the cloud, the effective radii of the cloud in the radial (a) and axial (c) directions are

defined as

$$a = \left(\frac{5}{2} \langle r^2 \rangle \right)^{1/2}, \quad c = [5(\langle z^2 \rangle - \langle z \rangle^2)]^{1/2}. \quad (4.2)$$

4.2.5 Time-scales

Time zero in my calculations is taken to be the time when the shock is level with the leading edge of the cloud, in the shock-cloud case, whilst for the wind-cloud case the simulation begins with the cloud immediately surrounded by the flow. For the shock-cloud simulation, I use the characteristic time-scale for a cloud to be crushed (the ‘‘cloud-crushing time’’; see Eq. 3.10) given by [Klein et al. \(1994\)](#) whilst for the wind-cloud simulations I redefine this time-scale in terms of the velocity of the wind flowing past the cloud ($v_{ps/wind}$),

$$t_{cc} = \frac{C \sqrt{\chi} r_c}{v_{ps/wind}}, \quad (4.3)$$

where the constant C is given by the ratio of the post-shock flow/wind velocity to the velocity of the shock through the unshocked medium, $v_{ps/wind}/v_b$.² The value of the constant depends on the value of the shock Mach number ($M_{shock} = 10$ in this chapter) used in the shock-cloud simulation, against which the wind simulations are compared. Thus, for my initial shock and wind simulations, models *c1shock* and *c1wind1*, the value of $C = 0.74$ and is specific to this Mach number and my adopted value of γ . The value of C is also dependent on the value of $v_{ps/wind}$ which, in my later wind-cloud models, is varied, resulting in differing values of C . Therefore, t_{cc} also varies depending on the particular simulation under consideration. Values for the cloud crushing time for each simulation are given in Table 4.3. Several other time-scales are also available, and are described in § 3.2.1.3.

²Note that in some wind-cloud studies, t_{cc} is defined slightly differently (e.g. [Jones et al. 1996](#); [Banda-Barragán et al. 2016](#)).

4.3 Results

In this section I present the results from the various simulations. I begin with a brief examination of the interaction of a shock with a cloud in terms of its morphology and then, maintaining the same initial parameters, compare this to the interaction of a wind with a cloud. I then consider in detail the interaction of clouds with winds of increasing Mach number. At the end of this section I consider the impact of the interaction on various global quantities.

I adopt a naming convention for each simulation such that *c1shock* refers to a shock-cloud simulation with $\chi = 10$. Models with *wind1a – c* in their title indicate wind-cloud interactions of increasing wind Mach number.

4.3.1 Stages

The purely adiabatic evolution of a cloud struck by a shock propagating in the $-z$ direction is characterised by four main stages (see e.g. [Pittard et al., 2009](#); [Pittard and Parkin, 2016](#)): (1) the cloud is struck by the shock, causing a transmitted shock to travel at a velocity $v_s = v_b/\chi^{1/2}$ through the cloud, while a bow shock (or bow wave) is formed upstream and the incident shock diffracts around the cloud; (2) the cloud undergoes compression in the z direction (on the whole) by both the transmitted shock and also a shock driven into the back of the cloud due to a dramatic pressure jump as the external shock is focussed onto the axis; (3) the cloud reaches the expansion stage where, under high pressure, it expands in the radial and axial directions; and (4) the cloud is finally destroyed and mixed with the post-shock flow.

In the case of a wind-swept cloud, stages 1-4 remain essentially the same. However, since the cloud immediately begins interacting with the flow, [Banda-Barragán et al. \(2016\)](#) divided the stages for a wind-cloud scenario thus: 1) compression, including the transmission and reflection of shocks within, and external to, the cloud; 2) stripping; 3) expansion; and 4) break-up. They noted that the stripping phase

(when cloud material begins to flow downstream and wraps around the cloud, converging on the axis behind the cloud) occurs at all times, but is more dynamically important up to $t \approx 1.3t_{cc}$.

4.3.2 Shock-cloud interaction

I begin by examining the morphology of the interaction for the shock-cloud scenario, where $M = 10$ and $\chi = 10$ (simulation *c1shock*). The shock is initially located at $z = 1$ (i.e. level with the leading edge of the cloud).

Figure 4.1 (top panels) provides logarithmic density plots of the rz plane as a function of time for the shock-cloud case. The evolution of the cloud broadly follows the above stages. The shock initially strikes the cloud on its leading edge, sending a transmitted shock through the cloud whilst the external shock is bent around the edge of the cloud as it moves downstream. The external shock becomes level with the centre of the cloud at $t \simeq 0.32t_{cc}$. A bow shock is visible upstream of the cloud. The first three upper panels of Fig. 4.1 relate approximately to the first two stages of evolution, which lasts until $t \simeq t_{cc}$. The external shock sweeps around the cloud and becomes focussed on the $r = 0$ axis. A region of higher pressure forms downstream behind the cloud due to the convergence of this shock on the axis and this serves to drive secondary shocks back through the cloud towards its leading edge. These secondary shocks create additional waves and shocks upstream of the cloud (note the faint secondary shock front just ahead of the cloud in the upper panel at $t = 2.0t_{cc}$ in Fig. 4.1) when they exit the leading edge of the cloud, accelerating as they do so.

At $t \simeq 1.6t_{cc}$ the transmitted shock has exited the back of the cloud and accelerates into the downstream gas. This action initiates a rarefaction wave which propagates in the upstream direction. The secondary shocks deposit vorticity as they progress back through the cloud. This deposition begins to disrupt the smooth morphology of the cloud, forcing the right-hand edge of the cloud upwards and

A comparison of shock-cloud and wind-cloud interactions: the longer survival of clouds in winds

leading to a modest expansion of the cloud in the transverse direction. At the same time, a supersonic vortex ring forms downstream of the cloud on the $r = 0$ axis. In a similar manner to e.g. Pittard et al. (2009) and Pittard and Parkin (2016), the cloud exhibits a low-density interior surrounded by a thick, high-density shell (see upper panel at $t = 1.6t_{cc}$ in Fig. 4.1). At $t \simeq 2.0t_{cc}$, the shell begins to collapse. Cloud material is now ablated by the surrounding flow and shear instabilities at the side of the cloud result in a “rolling-up” of cloud material in the transverse direction - over time this becomes shredded into long strands by the action of KH instabilities on the surface of the cloud. In addition, there is some circulation of the flow on the axis behind the cloud which serves to strip material from the rear of the cloud, allowing it to mix in with the flow. After $t \simeq 3.3t_{cc}$, a long, turbulent wake forms on the axis downstream of the cloud, and the cloud is quickly ablated.

4.3.3 Wind-cloud interaction

4.3.3.1 Comparison of wind-cloud and shock-cloud interactions

Figure 4.1 (bottom panels) shows logarithmic density plots of the rz plane as a function of time for the wind-cloud case with $M_{\text{wind}} = 1.36$ and $\chi = 10$ (simulation *c1wind1*). The velocity, density, and pressure of the wind are exactly the same as the post-shock values in simulation *c1shock* (i.e. the cloud is surrounded by ‘post-shock’ material). Hence, the density jump between the cloud and the wind is given by $\chi/3.9$ (see § 4.2.2).

The morphology of the cloud and its evolution share some broad similarities with the shock-cloud case (e.g. both clouds form dense shells surrounding lower density interiors, both are squeezed in the radial direction, and both are eventually drawn into long, filamentary wakes in the axial direction), but there are also some key differences.

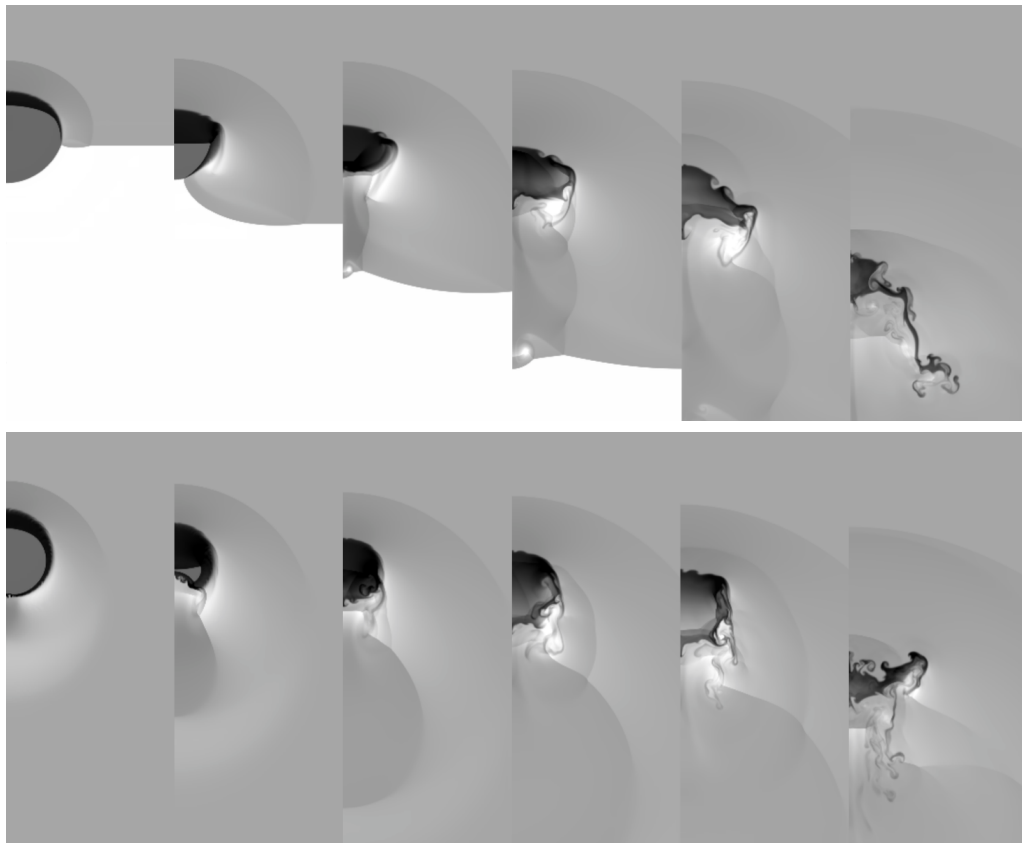


Fig. 4.1 The time evolution of the logarithmic density for models (top) *c1shock* and (bottom) *c1wind1*. The greyscale shows the logarithm of the mass density, from white (lowest density) to black (highest density). The density in this and subsequent figures has been scaled with respect to the ambient density, so that a value of 0 represents the value of ρ_{amb} and 1 represents $10 \times \rho_{\text{amb}}$, and the density scale used for this figure extends from 0 to 1.7. The evolution proceeds left to right with $t = 0.43 t_{cc}$, $t = 0.82 t_{cc}$, $t = 1.2 t_{cc}$, $t = 1.6 t_{cc}$, $t = 2.0 t_{cc}$, and $t = 3.3 t_{cc}$. The r axis (plotted horizontally) extends $3 r_c$ off-axis in each plot. All frames in the top and bottom sets show the same region ($-5 < z < 2$, in units of r_c) so that the motion of the cloud is clear. Note that in this and similar figures the z axis is plotted vertically, with positive towards the top and negative towards the bottom.

A comparison of shock-cloud and wind-cloud interactions: the longer survival of clouds in winds

Firstly, there are clear differences in the behaviour of the external medium. Since the simulation begins with the marginally supersonic wind completely surrounding the cloud, a small lower-density, lower-pressure region is immediately formed on the axis downstream of the cloud (as also noted by [Marcolini et al. 2005](#); [Banda-Barragán et al. 2016](#)). This feature is not present in the shock-cloud case and is formed by the initial motion of the wind removing gas from around the rear of the cloud. The low-pressure region is eventually carried downstream of the cloud, allowing an area of higher pressure to form behind the cloud (though not in quite the same manner as in the *c1shock* simulation).

Secondly, whilst the cloud is strongly compressed into the shape of an oblate spheroid in the shock-cloud case, the cloud in the wind-cloud case suffers much less compression in the axial direction, particularly during the initial stages of the interaction, and maintains a more rounded shape. While the leading edge of the cloud undergoes much less compression compared to the shock case, the rear of the cloud is clearly being pushed upwards by the action of a shock driven into the back of the cloud. Plots of the logarithmic pressure (not shown) indicate that a region of high pressure occurs at the leading edge of the cloud in both models, while the back of the cloud remains at a relatively lower pressure in model *c1wind1* compared to *c1shock*. In their study of a wind-cloud interaction with $M_{\text{wind}} = 10$ (i.e. a higher wind Mach number than used in my model *c1wind1*), [Schiano et al. \(1995\)](#) noted generally that when a free-flowing wind encounters a 2D spherical cloud and passes through the bow shock, the wind is compressed, decelerated, heated, and channelled around the cloud. As the shocked gas is accelerated around the periphery of the cloud and rejoins the wind flow along the cloud flanks, the gas pressure is lowered, and there is therefore a commensurate decrease in cloud pressure with increasing distance from the cloud apex; this is similar to the situation in model *c1wind1*.

There are also clear differences between the two simulations in terms of the initial transmitted shock driven through the cloud. In model *c1shock*, the shock is

reasonably flat as it progresses through the cloud, whereas it is much less flat in model *c1wind1* (cf. both panels at $t = 0.43t_{cc}$ and $t = 0.82t_{cc}$ in Fig. 4.1) and curves around the edge of the cloud. As in the shock-cloud case, secondary shocks driven back into the cloud lead to the formation of shocks/waves upstream of the cloud, though in model *c1wind1* these are slightly more pronounced (e.g. at $t = 2.0t_{cc}$).

At $t = 2.8t_{cc}$, the cloud, which has developed a dense shell surrounding a less dense interior, collapses at a slightly later time than in the shock-cloud case. Eventually the cloud takes on a very similar morphology to that in model *c1shock* from $t \simeq 3.3t_{cc}$ onwards, when it is drawn into a long wake in the axial direction (not shown).

4.3.3.2 Effect of increasing M_{wind} on the evolution

Figure 4.2 shows the time evolution of the logarithmic density for models *c1wind1a*, *c1wind1b*, and *c1wind1c*, where the wind has an increasing Mach number ($M_{\text{wind}} = 4.3, 13.6, \text{ and } 43$, respectively). As can be seen from a comparison between Fig. 4.2 and the lower panels of Fig. 4.1, there are a large number of differences between these simulations and *c1wind1* (where $M_{\text{wind}} = 1.36$).

Firstly, as the effective Mach number of the wind increases, the region of low pressure behind the cloud becomes a very low-pressure cavity, is highly supersonic, and expands rapidly in the direction of wind propagation, becoming elongated as it does so. Unlike the initial wind-cloud interaction described above (*c1wind1*), these cavities do not move away from the rear of the cloud, and because they are of a much lower pressure than the region in *c1wind1* they are far more pronounced.

Secondly, a transmitted shock moves inwards from the back of the cloud in *c1wind1* but not in the higher M_{wind} simulations. Whilst the wind flow around the cloud in model *c1wind1* is focussed around the cloud flank and onto the $r = 0$ axis, in models *c1wind1b* and *c1wind1c* the flow is much more linear and suffers very

A comparison of shock-cloud and wind-cloud interactions: the longer survival of clouds in winds

little deflection at the back of the cloud. Because of this, there is no dramatic pressure jump behind the cloud and this helps prevent a transmitted shock being driven into the back of the cloud.

Thirdly, it is noticeable that the density jump at the bow shock and the stand-off distance between the bow shock and the leading edge of the cloud both change according to the Mach number (see Table 4.2). As the Mach number of the wind increases, the density jump increases towards the high Mach number limit and the stand-off distance between the bow shock and cloud decreases (see [Farris and Russell \(1994\)](#) for a discussion of the factors affecting the stand-off distance). The higher post-shock pressure behind the bow shock causes the leading edge of the cloud to be pushed slightly further downstream in the higher M_{wind} simulations, compared to *c1wind1*. The normalised velocity of the shocked gas around the edge of the cloud is also reduced due to the higher compression at the bow shock. The nature of the transmitted shock propagating through the cloud also changes, becoming initially much flatter as the Mach number increases, more akin to the shock-cloud case. All of this serves to compress the cloud in the axial direction, lending it an oblate spheroid shape similar to the cloud in model *c1shock*, rather than the more rounded morphology evident in model *c1wind1*. Although the shape of the cloud in all the wind-cloud simulations with higher values of M_{wind} is similar, compared to that in model *c1wind1*, it is noticeable that the cloud in model *c1wind1a* becomes more kinked on its leading edge with the kink resembling the beginnings of a finger of cloud material moving in the $+z$ direction, and that the development of this kink is different, compared to models *c1wind1b* and *c1wind1c* where the kink is more curled and resembles a KH instability (cf. final two panels in each set of Fig. 4.2). The effect of this kink on the lifetime of the cloud is discussed in § 4.3.4.1

It should be noted that the cloud morphology and statistics in simulations *c1wind1b* and *c1wind1c* are very similar (as expected from Mach scaling - cf. [Klein et al., 1994](#); [Pittard et al., 2010](#)).

Table 4.2 Values of the density jump and bow shock stand-off distance (in units of r_c) for each of the simulations.

Simulation	Density jump	Stand-off distance
<i>c1shock</i>	1.53	1.72
<i>c1wind1</i>	1.53	1.72
<i>c1wind1a</i>	3.44	1.32
<i>c1wind1b</i>	3.94	1.28
<i>c1wind1c</i>	3.99	1.28

Figure 4.3 shows the density, advected scalar κ , and advected scalar \times density for model *c1wind1c* at late times (i.e. $t = 46t_{cc}$ and $t = 101t_{cc}$). It can clearly be seen that the cloud has yet to be smoothed out into the flow and shows some evidence of structure along with a distinct cloud edge. Compared with the lower panels in Fig. 4.2, which show the cloud during the initial stages of the evolution, the cloud in Fig. 4.3 has expanded supersonically into the flow and formed a tail-like structure. Although the cloud is not highly dense at late times, we can infer that it, nonetheless, shows evidence of long-term survival, something that has not been observed in previous wind-cloud studies.

4.3.4 Statistics

I now explore the evolution of various global quantities of the interaction for both the shock-cloud and wind-cloud models. Figure 4.4 shows the time evolution of these key quantities, whilst Table 4.3 lists various time-scales taken from these simulations. The following subsections present a more detailed discussion of these statistics.

4.3.4.1 Cloud mass

Panel (a) of Fig. 4.4 shows the time evolution of the core mass, m_{core} . The core mass decreases as a result of cloud material being ablated by, and mixed into, the surrounding flow. It is clear that models *c1shock* and *c1wind1* share a similar trend in terms of their rate of mass loss, until around two fifths of their core mass has

A comparison of shock-cloud and wind-cloud interactions: the longer survival of clouds in winds

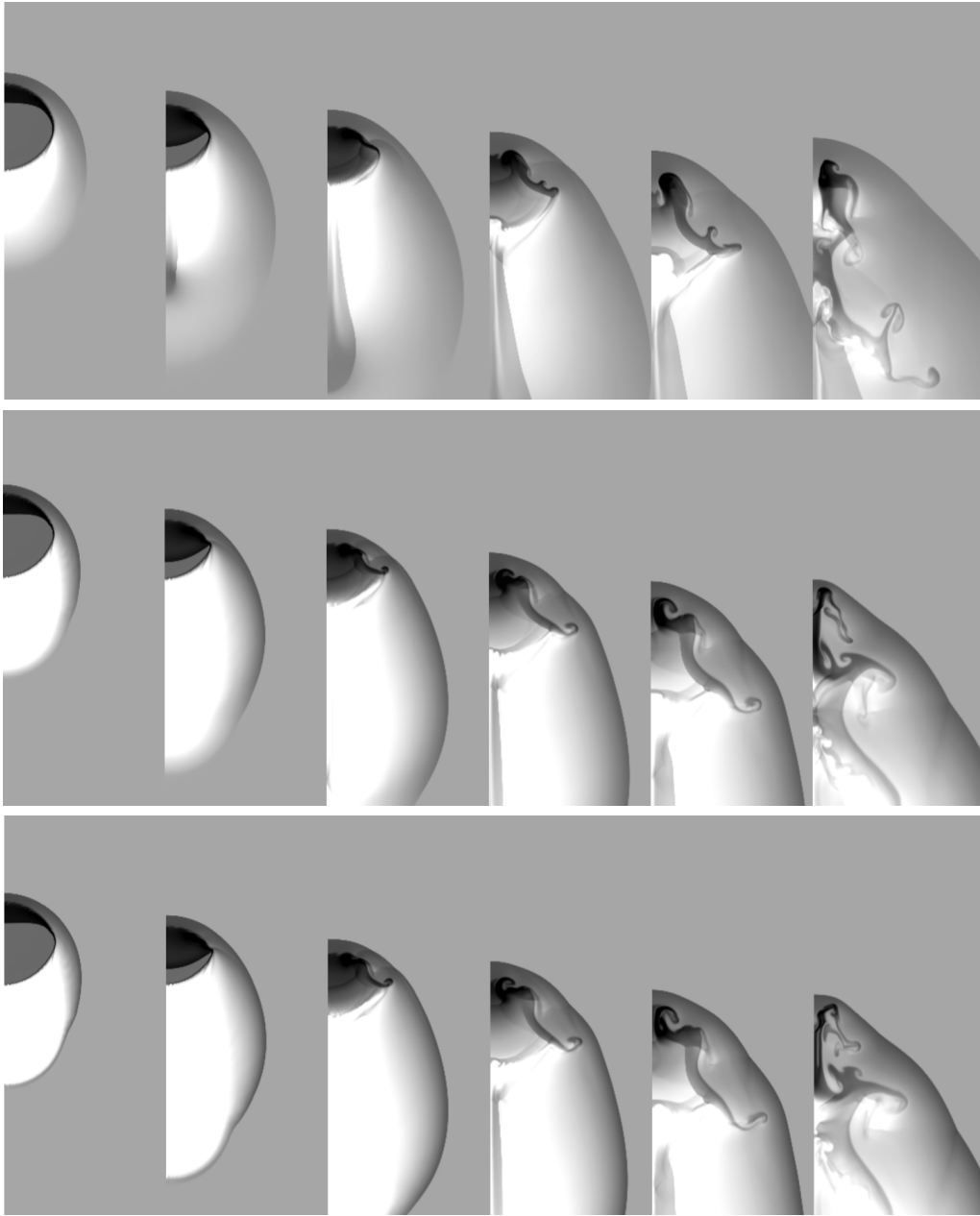


Fig. 4.2 The time evolution of the logarithmic density for models (top) *c1wind1a*, (middle) *c1wind1b*, and (bottom) *c1wind1c*. The greyscale shows the logarithm of the mass density, scaled with respect to the ambient medium. The density scale used in this figure extends from 0 to 1.7. The evolution proceeds left to right with $t = 0.7t_{cc}$, $t = 1.3t_{cc}$, $t = 1.9t_{cc}$, $t = 2.6t_{cc}$, $t = 3.2t_{cc}$, and $t = 5.2t_{cc}$. The r axis (plotted horizontally) extends $3r_c$ off-axis in each plot. The first 5 frames in each set show the same region ($-5 < z < 2$, in units of r_c) so that the motion of the cloud is clear. The displayed region is shifted in the last frame in each set ($-7 < z < 0$) in order to more fully show the cloud.

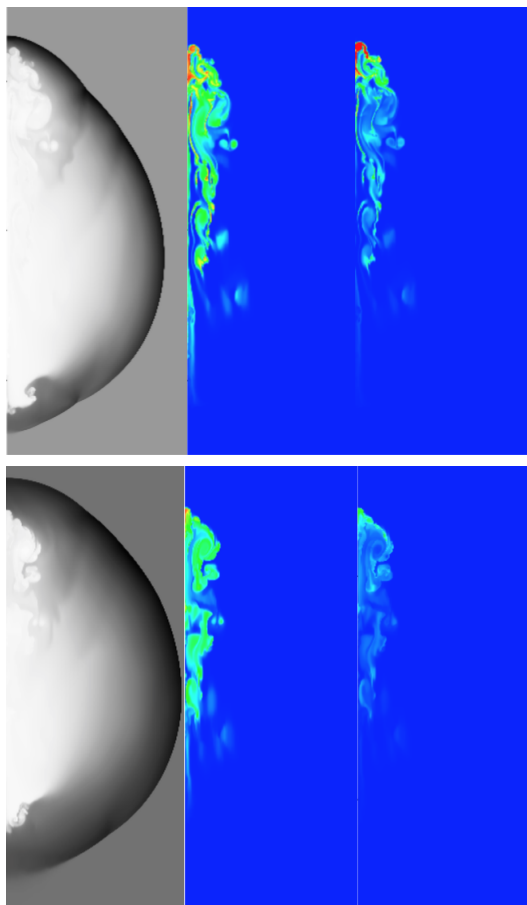


Fig. 4.3 The time evolution of the linear density (left), advected scalar κ which identifies only the cloud material (middle), and advected scalar \times linear density which allows the density of only the cloud to be shown (right) for model *c1wind1c*. The greyscale shows the mass density, scaled with respect to the ambient medium. The density scale used in the left-hand panels of this figure extends from 0 to 9.7 in the upper panels and 0 to 7.0 in the lower panels. The colour scale in the middle frames extends from dark blue (ambient material) to red (cloud material). The scale used in the right-hand panels extends from 0 to 1 (the ambient medium has a density of 1, but an advected scalar of 0, in this plot). All of the top panels are at $t = 46.0t_{cc}$, whilst all the bottom panels are at $t = 101.4t_{cc}$. The r axis (plotted horizontally in each frame) extends $12r_c$ off-axis in the top set of frames and $16r_c$ off-axis in the bottom set of frames. All frames in the top set show the same region ($-115 < z < -85$, in units of r_c) whilst all frames in the bottom set show $-250 < z < -210$.

A comparison of shock-cloud and wind-cloud interactions: the longer survival of clouds in winds

Table 4.3 A summary of the cloud-crushing time, t_{cc} for a cloud with $\chi = 10$ and $r_c = 1$ (see Eqn. 4.3 re the calculation of t_{cc}), and key time-scales, in units of t_{cc} , for the simulations investigated in this work. Note that the value for t_{drag} given here is calculated using the definition given in § 6.3.2, in comparison to the values shown in Fig. 4.5 which were calculated using the definition given in Pittard et al. (2010) in order to compare with the values of t_{drag} presented in that paper.

Simulation	t_{cc}	t_{drag}	t_{mix}	t_{life}
c1shock	0.233	2.35	6.72	23.0
c1wind1	0.233	3.34	6.12	12.9
c1wind1a	0.074	3.88	13.3	35.7
c1wind1b	0.023	3.78	23.5	96.9
c1wind1c	0.0074	4.28	25.6	136.0

been lost (both models have a much steeper rate of mass loss, at least until $t \approx 8t_{cc}$, than the models with higher values of M_{wind}). This is surprising considering that the clouds in these simulations initially evolve very differently; for example, the passage of the shock through the cloud, the degree of compression of the cloud, and the presence or otherwise of a low-pressure region behind the cloud are different between the two simulations, leading to a difference in cloud morphology. In contrast, models *c1wind1b* and *c1wind1c* display very shallow curves which are almost coincident. This reduced rate of mass loss may be due to the lack of a transmitted shock being driven into the back of the cloud (in contrast to models *c1shock* and *c1wind1*), as well as reduced circulation of the flow on the axis behind the cloud as M_{wind} increases. In addition, the normalised wind velocity (in units of v_{wind}) is reduced around the cloud flank due to the increased compression at the bow shock. Thus, there is less stripping of material from the rear of the cloud compared to lower M_{wind} simulations.

Interestingly, model *c1wind1a* appears to bridge the two groups: it is initially slow to lose mass (as per the other high M_{wind} models), but between $t \approx 10 - 20t_{cc}$ its rate of mass loss gradually becomes comparable to that of the *c1shock* and *c1wind1* simulations. In simulations *c1wind1a - c*, a prominent “kink” develops on the leading edge of the cloud; this feature is not evident in Figure 2 of Pittard and Parkin (2016) but the difference may be attributable to the fact that I used a hard edge to

my cloud which is more conducive to the growth of such instabilities. A similar kink is present in the adiabatic cloud modelled in [Marcolini et al. \(2005\)](#). This kink allows a greater expansion of the cloud in the radial direction (i.e., a_{cloud} increases) at later times compared to models *c1shock* and *c1wind1*. The kink develops differently between models *c1wind1a* and *c1wind1b/c*, and the radial expansion of the cloud in model *c1wind1a* occurs earlier than that of the latter two models. This means that the subsequent mixing and ablation of cloud material by the flow takes place earlier than in models *c1wind1b* and *c1wind1c*.

[Pittard and Parkin \(2016\)](#) showed that the mixing time, t_{mix} , for a spherical cloud struck by a Mach 10 shock was $\approx 6t_{cc}$ and increased as the value of the shock Mach number was reduced. Table 4.3 shows that the two models with similar initial parameters (*c1shock* and *c1wind1*) have roughly similar mixing times. However, for *winds* of increasing Mach number the value of t_{mix} *increases* until near to the high Mach number limit (when $M_{ps/wind} \gtrsim 10$). As before, this is due to the less effective stripping of cloud material by the flow around the edge of the cloud as M_{wind} increases. It is surprising, however, to find that the normalised mixing time is 5 times longer for clouds in winds than for clouds hit by shocks in the high Mach number limit.

4.3.4.2 Cloud velocity

Figure 4.4(b) shows the mean velocity of the cloud in the direction of propagation of the shock/wind, normalised by the post-shock/wind velocity. The clouds in models *c1shock* and (from $t \approx 4t_{cc}$) *c1wind1* show slightly faster acceleration towards the asymptotic velocity, with the cloud in *c1wind1* being accelerated to the velocity of the background flow much more quickly than in the other wind simulations. In addition, in model *c1shock* (and to a much lesser extent *c1wind1*), the cloud exhibits a “two-stepped” acceleration at $t \approx 4t_{cc}$. This coincides with the beginning of a

A comparison of shock-cloud and wind-cloud interactions: the longer survival of clouds in winds

‘plateau’ region. At this point, the cloud undergoes significant stretching in the axial direction until $t \approx 8t_{cc}$ (the approximate end of the plateau region), when most of the core material has been ablated and the remaining less dense and filamentary structure is again accelerated by the flow up to the asymptotic velocity.

The acceleration of the cloud in model *c1wind1a* is initially smooth until $t \approx 15t_{cc}$ (at which point the cloud begins to form long strands), but then fluctuates slightly about the velocity of the wind. The clouds in models *c1wind1b* and *c1wind1c* undergo the smoothest acceleration because of the reduction in the growth of turbulent instabilities on the cloud surface, and again are almost identical in behaviour (due to Mach scaling).

4.3.4.3 Centre of mass of the cloud

The distance travelled by the cloud before it becomes fully mixed into the flow is reflected by the movement of the cloud centre of mass. The time evolution of the position of the centre of mass of the cloud in the z direction, normalised by the initial radius of the cloud, is given in Fig. 4.4(c). It is clear that the post-shock flow or wind can transport cloud material over large distances. Up until $t \approx 2t_{cc}$, there is not a great deal of movement in the direction of the flow (the centre of mass has only moved $0.8 - 1.8r_c$). However, by $t = 12t_{cc}$ the clouds have been displaced by 15 – 20 times the initial cloud radius. Over much longer time spans (e.g. up to $t = 30t_{cc}$, as in Fig. 4.4(c)), the cloud displacement shows greater variation between models, with the centre of mass of the cloud in models *c1shock* and *c1wind1* showing considerably more movement. However, there is much less variety in displacement among all the higher wind Mach number simulations, indicating that movement in the axial direction is not strongly dependent upon M_{wind} in these cases (as expected with Mach scaling). Figure 4.4(c) also shows the displacement of each cloud at $t = t_{\text{mix}}$. Clearly, the distance over which the cloud has moved by the time its core

mass has been reduced by half increases dramatically according to the Mach number, with the cloud in model *c1wind1c* having moved by $47 r_c$ at t_{mix} (compared to $8 r_c$ for the cloud in model *c1wind1*). This indicates that clouds in higher Mach number winds can travel significant distances before being fully mixed into the flow.

4.3.4.4 Cloud shape

Figures 4.4(d)-(f) show the time evolution of the effective cloud radii, a and c , and their ratio. The radial dimension of the cloud, a_{cloud} , decreases slightly during the initial compression phase as the cloud is squeezed in the axial direction, but then increases sharply as the cloud undergoes expansion. Model *c1wind1* shows the steepest increase, reaching a maximum value for a_{cloud} of $\approx 2.8 r_c$ at $t = 5.9 t_{cc}$ as the cloud material is squeezed in the radial direction by the various shocks within and around the cloud, and then decreasing gently as the cloud material is drawn along the axis behind the cloud and gradually mixed into the flow. Model *c1shock* follows a similar trend, though it reaches its peak expansion of $1.8 r_c$ at a slightly earlier time ($t = 4.4 t_{cc}$).

The clouds in models *c1wind1b* and *c1wind1c* show completely different behaviour, with a more smoothly increasing expansion over time as M_{wind} increases, rather than an initial peak. The cloud in model *c1wind1a*, as noted earlier, displays traits of both behaviours since it shows a slight initial increase before plateauing and then gently increasing again, eventually peaking at an effective radius of $2.2 r_c$ at $t = 19.5 t_{cc}$.

Since the cloud in simulation *c1shock* rapidly becomes elongated in the axial direction after the initial compression of the cloud, the values of c_{cloud} and $c_{\text{cloud}}/a_{\text{cloud}}$ steadily increase over time until $t \approx 17 t_{cc}$ when they level out. The cloud in simulation *c1wind1*, in contrast, shows a much less steep increase in c_{cloud} and $c_{\text{cloud}}/a_{\text{cloud}}$. However, the ratio of cloud shape, $c_{\text{cloud}}/a_{\text{cloud}}$, shows a much higher value for the

A comparison of shock-cloud and wind-cloud interactions: the longer survival of clouds in winds

cloud in model *c1wind1*, reaching a value of 26 at $t = 97t_{cc}$ (not shown) while that for model *c1shock* reaches a high of 8.5 at $t = 55t_{cc}$. This is in line with Klein et al. (1994), who noted that the combined effect of the lateral expansion associated with the Venturi effect and the axial stretching due to the stripping of material from the side of the cloud led to a much larger cloud aspect ratio for a wind-swept cloud, in comparison to the case of a cloud struck by a shock.

Similar to the above, models *c1wind1b* and *c1wind1c* show a steady increase in both c_{cloud} and $c_{\text{cloud}}/a_{\text{cloud}}$ (with the plots having very similar profiles for both clouds). In contrast to model *c1wind1*, the clouds in these two simulations have maximum aspect ratios of 11.3 (at $t = 221t_{cc}$) and 4.4 ($t = 214t_{cc}$) (not shown), respectively, which do not follow the behaviour predicted by Klein et al. (1994). The cloud in model *c1wind1a* shows different behaviour, again, with an initial peak around $t \approx 10 - 12t_{cc}$ for both c_{cloud} and $c_{\text{cloud}}/a_{\text{cloud}}$ before levelling off. The peak value for the aspect ratio is 16 at $t = 79t_{cc}$.

4.3.4.5 Time-scales

Figure 4.5 shows the Mach dependence of t_{drag} and t_{mix} . These two time-scales are useful indicators of the evolution and destruction of the cloud. In previous shock-cloud studies (e.g. Pittard et al., 2010; Pittard and Parkin, 2016), values of t_{drag} and t_{mix} for a given χ were relatively constant at Mach numbers > 4 (due to Mach scaling), while at lower Mach numbers t_{drag} and t_{mix} both increased sharply. With the wind-cloud simulations, however, it can be seen that the values for t_{mix} increase sharply and nearly linearly (at least for $M_{\text{wind}} < 10$) as the Mach number increases. The values for t_{drag} for the wind-cloud simulations, meanwhile, are relatively constant within the range $2.0 - 2.2t_{cc}$ (using the definition of t_{drag} found in Pittard et al., 2010).³ Within this range the cloud in model *c1wind1* has the lowest

³The calculations performed in Pittard et al. (2010) (against which I compare my results in Fig. 4.5) used the $k-\varepsilon$ turbulence model. In order to ensure that the use of this model had no significant impact on my results, I re-ran my wind simulations using the values for the $k-\varepsilon$ model employed in Pittard

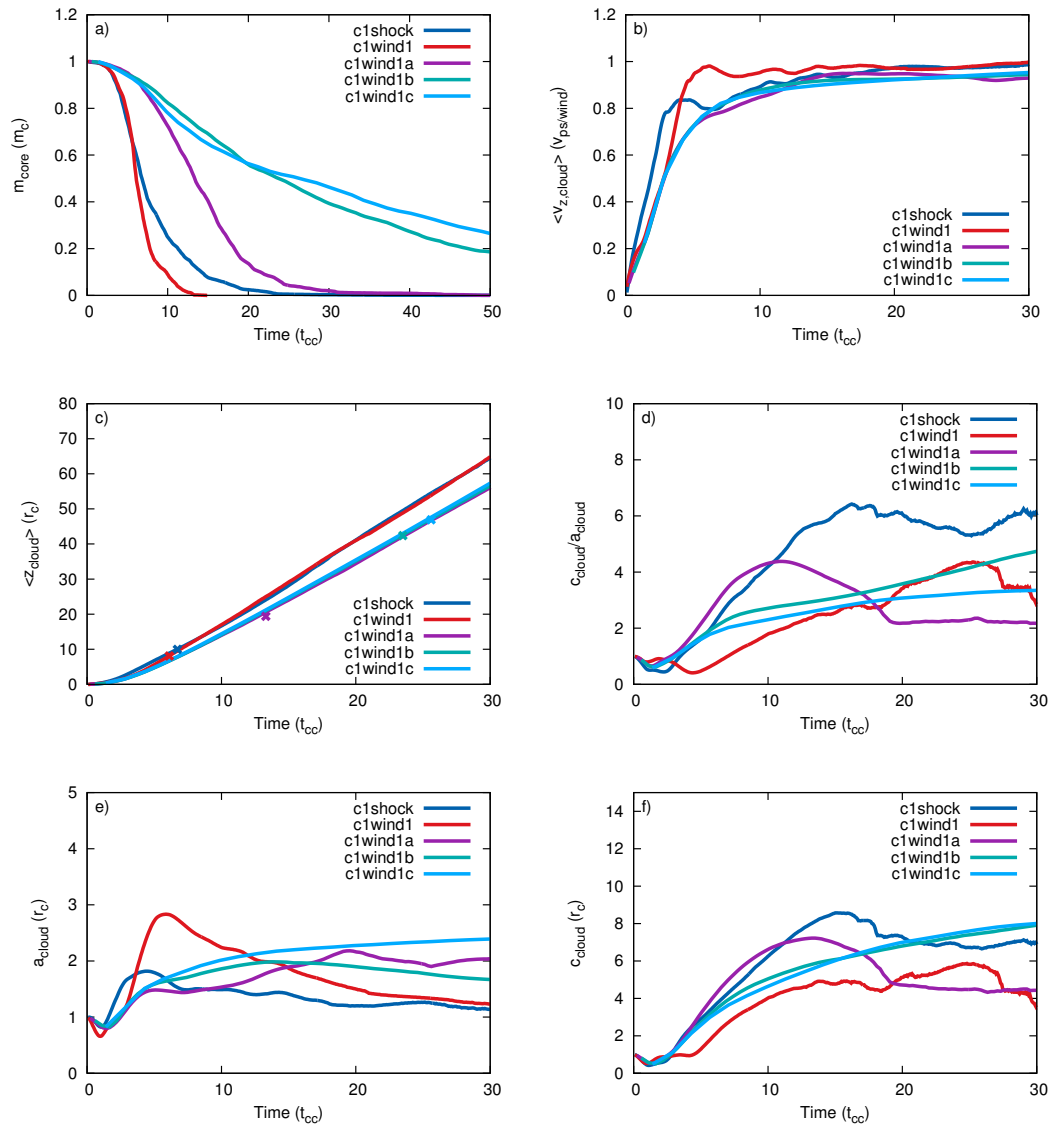


Fig. 4.4 Time evolution of (a) the core mass of the cloud, m_{core} , (b) the mean velocity of the cloud in the z direction, $\langle v_z \rangle$, (c) the centre of mass in the axial direction, $\langle z_{\text{cloud}} \rangle$, (d) the ratio of cloud shape in the axial and transverse directions, $c_{\text{cloud}}/a_{\text{cloud}}$, (e) the effective transverse radius of the cloud, a_{cloud} , and (f) the effective axial radius of the cloud c_{cloud} . Note that panel (a) shows the evolution on an extended time-scale compared to the other panels. Panel (c) also shows the position of each cloud at $t = t_{\text{mix}}$ (indicated by the respective coloured crosses).

A comparison of shock-cloud and wind-cloud interactions: the longer survival of clouds in winds

value for t_{drag} , indicating faster acceleration, and that in model *c1wind1c* has the highest value (slower acceleration), which fits in with the results of [Scannapieco and Brügger \(2015\)](#) who showed that the acceleration of clouds in galaxy outflows was smaller for higher Mach numbers. While the lack of a shock driven into the back of the cloud in the higher wind Mach number simulations would aid the acceleration of the cloud, it is probable that this effect is superseded by the reduction in the stand-off distance leading to greater compression at the bow shock and a reduction in the normalised wind velocity around the edge of the cloud.

Figures 4.4(a) and 4.5(b) show that the mixing of the core is more efficient at *lower* wind Mach numbers. At lower M_{wind} , the growth of KH instabilities is more important and the post-bow shock velocity of the wind around the cloud flanks is greater. At higher M_{wind} , t_{mix} levels off at $\simeq 25t_{cc}$, indicating that Mach scaling is obtained.

Figure 4.5 shows that the “inviscid” and “ k - ϵ ” models generally have comparable t_{drag} and t_{mix} time-scales, indicating that the level of “ambient” turbulence in the latter has little effect on the cloud evolution (higher values are required - see [Pittard et al. \(2009\)](#) and [Goodson et al. \(2017\)](#)). Instead, one sees much larger differences in t_{drag} and t_{mix} between the shock-cloud and wind-cloud cases, indicating that the *nature* of the background flow is important.

4.4 Discussion

The interaction of both shocks and winds with clouds is of great importance in terms of understanding the nature and evolution of the ISM. Shock-cloud and wind-cloud interactions have been studied numerically but there has been no direct comparison

et al. (2009, 2010) (use of these specific values is important since the strength of turbulent mixing depends on the initial values of k and ϵ - see [Pittard et al. \(2009\)](#) and [Goodson et al. \(2017\)](#)). I also calculated a non- k - ϵ model shock-cloud simulation at a shock Mach number of 40. These additional values have been included in Fig. 4.5 in order to show clearly the differences between wind-cloud and shock-cloud simulations.

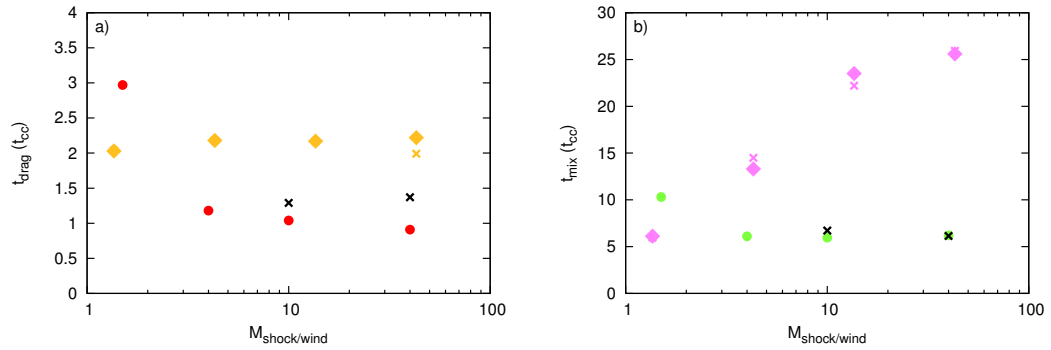


Fig. 4.5 (a) Cloud drag time, t_{drag} , (gold diamonds) and (b) mixing time of the core, t_{mix} , (pink diamonds) as a function of the wind Mach number for the wind-cloud simulations. The time-scales for all wind-cloud simulations in this chapter which were re-run using the $k-\varepsilon$ turbulence model are also shown (gold and pink crosses for panels (a) and (b), respectively). Note that these simulations were run at a slightly lower resolution of R_{64}). Also shown are the corresponding values as a function of the shock Mach number for shock-cloud simulations with $M_{\text{shock}} = 10$ and $M_{\text{shock}} = 40$ (black crosses in each panel), as well as values from the 2D $k-\varepsilon$ simulations in Pittard et al. (2010) for a shock-cloud interaction with $\chi = 10$ (t_{drag} , red circles; t_{mix} , green circles). It should be noted, however, that Pittard et al. (2010) used a slightly different definition of the drag time - defined in their paper as the time when the relative cloud velocity had decreased by a factor of $1/e$. This definition provides smaller values of t_{drag} than the calculation used in this chapter. In order to compare the two time-scales, I re-calculated my values of t_{drag} for both the shock-cloud simulations where the shock Mach number $M = 10$ and $M = 40$ and the wind-cloud simulations in accordance with their definition. See Table 4.3 for values of t_{drag} calculated according to the definition given in § 6.3.2 of the current paper.

A comparison of shock-cloud and wind-cloud interactions: the longer survival of clouds in winds

of the two processes, to date. In the following subsections, I discuss two main outcomes of my work, Mach scaling and the long-term survival of the cloud. These have previously been discussed in terms of shock-cloud interactions and I note their importance to wind-cloud studies.

4.4.1 Mach scaling

One of the main results from this study is the presence of Mach scaling. Mach scaling has been discussed in detail in previous shock-cloud studies (see e.g. [Klein et al., 1994](#); [Pittard et al., 2009, 2010](#)). Briefly, in the strong shock limit, the time evolution of the cloud is independent of the shock Mach number when it is expressed in units of $t/t_{cc} \propto tM$ in the limit $M \rightarrow \infty$. [Klein et al. \(1994\)](#) first demonstrated Mach scaling for sharp-edged clouds, with [Nakamura et al. \(2006\)](#) producing similar results for clouds with smooth edges. Such studies have been able to demonstrate Mach scaling in the shock-cloud case because the shock Mach numbers used in individual studies have encompassed a large range (e.g. [Klein et al. \(1994\)](#) who investigated $M = 10 - 10^3$ and [Nakamura et al. \(2006\)](#) who used the range $M = 1.5 - 10^3$). The same cannot be said for wind-cloud studies. A brief trawl of the literature reveals only a handful of studies where the Mach number of the wind was higher than 10. [Poludnenko et al. \(2004\)](#), in their study of hypersonic radiative bullets, stated that they had used Mach numbers in the range 10-200 but did not go on to discuss the effect of changing the Mach number on the interaction. [Raga et al. \(2007\)](#), who had very similar parameters to those used in the previous study, used a bullet Mach number of 242 which, whilst firmly in the strong shock regime, was not compared to other values of the Mach number. [Pittard et al. \(2005b\)](#) considered wind Mach numbers of 1 and 20 in their study of multiple clouds embedded in a wind, but did not have a great enough range of values for the Mach number in order to detect Mach scaling.

Although there are differences in the initial set-up and the physical processes included, my work is perhaps most easily compared to that of [Scannapieco and Brügger \(2015\)](#), who investigated a range of wind Mach numbers (from 0.5 to 11.4). A key result from these authors was that the mixing time-scale increases with the wind Mach number. However, by extending my investigation to higher wind Mach numbers ($M_{\text{wind}} = 43.0$ vs. 11.4) I am able to show that the mixing time levels off at high Mach numbers. I believe, therefore, that my work is the first to demonstrate Mach scaling in a wind-cloud study.

4.4.2 Longer survivability of clouds

In their study, [Scannapieco and Brügger \(2015\)](#) note that clouds embedded in a wind are unable to travel distances of more than $30 - 40 r_c$ before being disrupted. I find that clouds can travel $40 - 50 r_c$ by $t = t_{\text{mix}}$, which suggests similarities between our works. Moreover, I find that the cloud in simulation *c1wind1c*, i.e. the simulation with the highest wind velocity and a cloud density contrast of 10, still has significant structure and density at late times (e.g. $100t_{cc}$, when it still has $\approx 10\%$ of its core mass; see Fig. 4.3) and that it is able to reach distances of $\simeq 200 r_c$ at this time (see Fig. 4.3). Thus, although my results are still not easily reconciled with observations indicating clouds existing at the 100 kpc distances noted above, they nonetheless show that clouds can survive as distinct structures over much longer distances compared to those presented in [Scannapieco and Brügger \(2015\)](#). The longer survivability of clouds entrained in a wind may be further enhanced when combined with other effects such as magnetic fields or cooling.

Figure 4.3 shows that the cloud in simulation *c1wind1c* is not completely destroyed at late times, though its density has dropped below that of the surrounding wind by $t \approx 100t_{cc}$ (the bottom panels of Fig. 4.3). Since the bow shock around the cloud is denser than the cloud at this time, preferential detection of the cloud

A comparison of shock-cloud and wind-cloud interactions: the longer survival of clouds in winds

may require that the cloud material has enhanced metallicity relative to the wind (cf. [Turner et al., 2014](#)).

4.5 Summary and Conclusions

In this chapter, I compared the interaction between a shock and a spherical cloud with that of a wind-cloud interaction with similar initial parameters. My motivation was the lack of any paper in the literature that directly compared these two processes and the general supposition that shock-cloud and wind-cloud interactions were broadly comparable. However, I found there to be subtle, but also significant, differences between the two types of interaction.

I first compared my wind-cloud simulations against a shock-cloud simulation with $M = 10$ and $\chi = 10$ (*c1shock*). My standard wind-cloud simulation (*c1wind1*) has the same cloud completely embedded in a (slightly supersonic) wind with exactly the same properties as the post-shock flow in model *c1shock*. I find that the subsequent behaviour of the external medium differs between the two cases. In the particular case of a marginally supersonic wind, an area of low pressure immediately forms downstream behind the cloud (a feature not present in the shock-cloud case). There are also differences in the morphology of the cloud itself. A cloud engulfed by a marginally supersonic wind undergoes less compression than that struck by a shock, because the flow around the cloud is diffracted in a different way to the shock-cloud case. Finally, there are noticeable differences in the initial transmitted shock between the shock-cloud and wind-cloud simulations; the shock in the former is far flatter in shape whereas that in model *c1wind1* curves around the edge of the cloud.

As the effective Mach number of the wind increases, the morphological differences between the wind simulations and the shock simulation become more prominent. The cavitation behind the cloud becomes more highly supersonic and

elongated. The higher Mach number causes a greater density and pressure jump behind the bow shock, leading to reduced normalised post-bow shock gas velocities around the cloud flank. Because of this, KH instabilities become slightly weaker as M_{wind} increases. Another difference is that clouds in simulations with a high wind Mach number do not experience the formation of transmitted shocks on the axis behind the cloud. In addition to the morphological changes, I also showed that the mixing time increases for increasing M_{wind} , which is in contrast to the findings of [Pittard and Parkin \(2016\)](#) with respect to a shock-cloud interaction. My simulations also display Mach scaling in the high Mach number limit. The density jump at the bow shock asymptotes to 4.0 (for $\gamma = 5/3$), and the stand-off distance between the bow shock and the centre of the cloud asymptotes to $1.28 r_c$ (again for $\gamma = 5/3$). The morphology of the cloud and the normalised acceleration and mixing time-scales plateau at high Mach numbers. Moreover, I found that clouds embedded in winds with high M_{wind} survived for longer, and travelled over larger distances, compared to the results of the wind-cloud study by [Scannapieco and Brügger \(2015\)](#).

The models used in this work have several limitations. Firstly, this was a 2D study with imposed axisymmetry. Secondly, I considered only spherical clouds with sharp edges (i.e. my clouds had no distinct core and surrounding envelope but were uniformly dense) and neglected physical processes such as radiative cooling and magnetic fields. Therefore, future comparisons should consider more realistic cloud models and scenarios reflecting a more complex, inhomogenous ISM/intergalactic medium. However, since my work is scale-free my results can be applied to a broad range of problems related to the gas dynamics of the ISM. A follow-up to the present study (see Chapter 5) compared shock-cloud and wind-cloud interactions where the cloud density contrast is higher.

Chapter 5

A comparison of shock-cloud and wind-cloud interactions: effect of increased cloud density contrast on cloud evolution

5.1 Introduction

The ISM is a dynamic entity. Under certain circumstances, flows interacting with clouds can lead to the formation of tail-like morphologies or filamentary structures. Observations have shown these to occur from the small scale, such as comet plasma tails (e.g. [Brandt and Snow, 2000](#); [Buffington et al., 2008](#); [Yagi et al., 2015](#)) to much larger scales, e.g. $H\alpha$ -emitting filaments occurring within galaxies. Tails have been observed in NGC 7293 in the Helix nebula ([O'Dell et al. 2005](#); [Hora et al. 2006](#); [Matsuura et al. 2007](#); [Matsuura et al. 2009](#); [Meaburn and Boumis 2010](#). See also [Dyson et al. \(2006\)](#) for a corresponding numerical study) and also in the Orion Molecular Cloud OMC1 ([Allen and Burton 1993](#); [Schultz et al. 1999](#); [Tedds et al. 1999](#); [Kaifu et al. 2000](#); [Lee and Burton 2000](#)). Tail-like structures have also been

found in Galactic winds (Cecil et al. 2001; Ohyama et al. 2002; Cecil et al. 2002; Crawford et al. 2005; McClure-Griffiths et al. 2012; McClure-Griffiths et al. 2013; Shafi et al. 2015).

Numerical shock/wind-cloud studies which have had either a particular focus on, or have noted, the formation of tails include Cooper et al. (2008, 2009); Pittard et al. (2009, 2010); Strickland and Stevens (2000); and Banda-Barragán et al. (2016), whilst Pittard (2011) investigated the formation of tails in shell-cloud interactions. Pittard et al. (2009, 2010), for example, noted the formation of tail-like structures in 2D shock-cloud interactions where the cloud had a density contrast $\chi = 10^3$ and a high shock Mach number and suggested that this was because the stripping of material was more effective at higher Mach numbers due to the faster growth of KH and RT instabilities. They stated that well-defined tails only formed for density contrasts $\chi \gtrsim 10^3$ but over a variety of Mach numbers.

In contrast, whilst there are a large number of wind-cloud simulations in the literature, very few have considered clouds with density contrasts of 10^3 or greater. Those that have (e.g. Murray et al. 1993; Schiano et al. 1995; Vieser and Hensler 2007; Cooper et al. 2009; Scannapieco and Brüggén 2015; Banda-Barragán et al. 2016) have tended not to vary the wind Mach number. Banda-Barragán et al. (2016), for example, noted the realistic nature of higher cloud density contrasts (i.e. $\chi > 100$) but limited their adiabatic calculations to winds of Mach number 4.

In Chapter 4 I compared shock-cloud and wind-cloud simulations using similar flow parameters for a cloud density contrast $\chi = 10$, and explored the effect of increasing the wind Mach number on the evolution of the cloud. In that chapter, I found there to be significant differences between shock-cloud and wind-cloud interactions in terms of the nature of the shock driven through the cloud and the axial compression of the cloud, and noted that the cloud mixing time normalised to its crushing timescale increased for increasing wind Mach number until it reached a plateau due to Mach scaling. In addition, I also found that clouds in high Mach num-

A comparison of shock-cloud and wind-cloud interactions: effect of increased cloud density contrast on cloud evolution

ber winds were capable of surviving for longer and travelling considerable distances. In the current chapter, I extend my investigation to clouds with a density contrast higher than that of Chapter 4 ($\chi = 10^3$) and again compare between simulations where the wind Mach number is varied. I also make comparisons between the current work and Chapter 4.

The outline of this chapter is as follows: in § 5.2 I briefly introduce the numerical method and the initial conditions, whilst in § 5.3 I present my results. § 5.4 provides a summary of my results and a conclusion.

5.2 The numerical setup and initial conditions

As in Chapter 4, the computations in this chapter were performed using the MG HD code, details of which can be found in Chapter 2. The initial conditions, numerical setup, global quantities, and time-scales are exactly the same as in Chapter 4 except that the density contrast between the cloud and the stationary ambient medium is given by $\chi = 10^3$. Table 5.1 details the grid extent for each of the simulations and values of the wind Mach number. As before, the velocity of the flow, $v_{ps/wind}$, is increased by factors of $\sqrt{10}$, $\sqrt{100}$, and $\sqrt{1000}$ in order to increase $M_{ps/wind}$. Values for the cloud-crushing time-scale for each simulation are given in Table 5.2. In addition, the time-scale for the growth rate of KH instabilities is given by:

$$t_{KH} \sim \frac{(\gamma + 1)M_{wind}^2}{(2M_{wind}^2 - 2)} t_{cc}. \quad (5.1)$$

5.3 Results

In this section I begin by examining the shock-cloud interaction, model *c3shock*, in terms of the morphology of the cloud and then, maintaining the same initial

Table 5.1 The grid extent for each of the simulations presented in this chapter (see § 5.3 for the model naming convention). $M_{ps/wind}$ denotes the effective Mach number of the post-shock flow/wind. Length is measured in units of the initial cloud radius, r_c .

Simulation	$M_{ps/wind}$	R	Z
c3shock	1.36	$0 < R < 20$	$-400 < Z < 5$
c3wind1	1.36	$0 < R < 30$	$-700 < Z < 5$
c3wind1a	4.30	$0 < R < 30$	$-700 < Z < 5$
c3wind1b	13.6	$0 < R < 35$	$-800 < Z < 5$
c3wind1c	43.0	$0 < R < 35$	$-800 < Z < 5$

parameters, compare this to my standard wind-cloud interaction, model *c3wind1*. I then consider the interaction when the Mach number of the wind is increased (models *c3wind1a* to *c3wind1c*).

At the end of this section I explore the impact of the interaction on various global quantities. In Chapter 4 I used a naming convention such that the higher velocity wind-cloud simulations were described from “wind1a” to “wind1c”. Thus, in order to compare between the two chapters I retain a similar naming convention such that *c3shock* refers to a shock-cloud simulation with $\chi = 10^3$. The “1a” in model *c3wind1a*, for example, indicates that the interaction has an increased wind Mach number compared to model *c3wind1*.

5.3.1 Shock-cloud interaction

Figure 5.1 shows plots of the logarithmic density as a function of time for model *c3shock*. The evolution of the cloud broadly proceeds as per model *c1shock* in Chapter 4 (where $M_{shock} = 10$ and $\chi = 10$) in that the cloud is initially struck on its leading edge, causing a shock to be transmitted through the cloud whilst the external shock sweeps around the cloud edge, and a bow shock is formed ahead of the leading edge of the cloud. There are a number of differences between the two models, as detailed below.

The rate at which the transmitted shock progresses through the cloud is considerably slower than the comparable simulation in Chapter 4 ; in that chapter, the shock

A comparison of shock-cloud and wind-cloud interactions: effect of increased cloud density contrast on cloud evolution

was also much flatter whereas model *c3shock* has a semi-flat shock, the end of which curves around the cloud flank (see fourth panel of Fig. 5.1). The slowness of the transmitted shock and its progress through the cloud in the current simulation is attributed to the increased density of the cloud compared to model *c1shock*.

Initially, the slow progress of the transmitted shock through the cloud means that the cloud appears to undergo little immediate compression in either the axial or radial directions, in contrast to the cloud in Chapter 4 which was flattened into an oblate spheroid even as the external shock was sweeping around the outside. However, when this is measured in units of t_{cc} , maximum compression of the cloud in the axial direction takes place by $t \simeq 1 t_{cc}$ (cf. panels 4 and 5 of Fig. 5.1).

The surface of the cloud in the current simulation from the outset is not smooth (compared to the cloud edge in e.g. Pittard et al., 2009, 2010; Pittard and Parkin, 2016). The rapid development of such small instabilities is attributed to the fact that I used a sharp edge to the cloud (see Pittard and Parkin (2016) for a discussion of how soft cloud edges can hinder the growth of KH instabilities). It is also notable that the cloud moves downstream at a slightly slower rate than would be expected in comparison with previous inviscid shock-cloud calculations (cf. figure 4 in Pittard et al. (2009)). This difference is likely to be due to the smooth edge given to the cloud in e.g. Pittard et al. (2009) which results in the cloud having slightly less mass than in my model.

The third panel of Fig. 5.1 shows that the external shock has reached the $r = 0$ axis and cloud material is being ablated from the back of the cloud into the flow. The shear across the surface of the cloud induces the growth of instabilities, leading to a thin layer of material being drawn away from the side of the cloud and funnelled downstream. At this point, the transmitted shock is still progressing through the cloud. With the transmitted shock curving around the edge of the cloud and also moving in from the rear, the cloud begins to exhibit a shell-like morphology, with a shocked denser outer layer encompassing the unshocked interior. This is a relatively

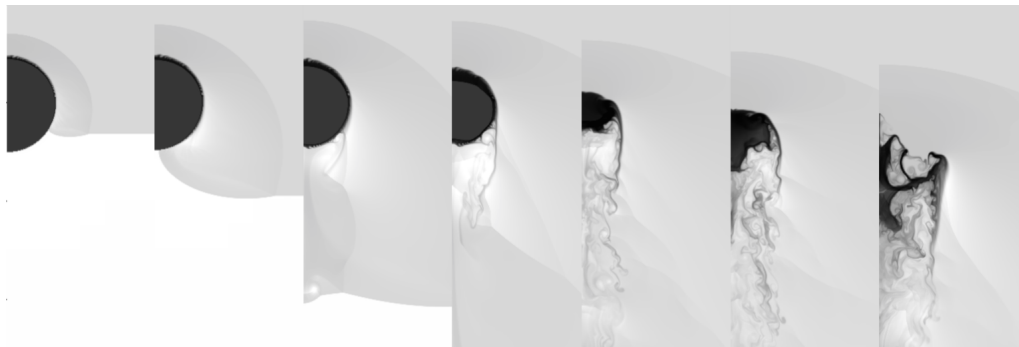


Fig. 5.1 The time evolution of the logarithmic density for model *c3shock*. The greyscale shows the logarithm of the mass density, from white (lowest density) to black (highest density). The density in this and subsequent figures has been scaled with respect to the ambient density, so that a value of 0 represents the value of ρ_{amb} and 1 represents $10 \times \rho_{\text{amb}}$. The density scale used for this figure extends from 0 to 3.8. The evolution proceeds left to right with $t = 0.043 t_{cc}$, $t = 0.084 t_{cc}$, $t = 0.16 t_{cc}$, $t = 0.31 t_{cc}$, $t = 1.2 t_{cc}$, $t = 2.0 t_{cc}$, and $t = 3.6 t_{cc}$. The r axis (plotted horizontally) extends $3 r_c$ off-axis. All frames show the same region ($-5 < z < 2$, in units of r_c) so that the motion of the cloud is clear. Note that in this and similar figures the z axis is plotted vertically, with positive towards the top and negative towards the bottom.

short-lived morphology, since by $t = 1.2 t_{cc}$ the shocked parts of the cloud collapse into each other, and the transmitted shock has exited the cloud and accelerated downstream. Cloud material is then ablated by the flow and expands supersonically downstream, forming a long and turbulent wake. The cloud core, however, remains relatively intact after the formation of the turbulent wake and persists for some time as a distinct clump (until $t \approx 5.2 t_{cc}$, when it starts to become more elongated and drawn-out along the axial direction). This behaviour differs from the $\chi = 10$ cloud investigated in Chapter 4, where the cloud was destroyed much more rapidly. However, it is in better agreement with inviscid simulations presented in [Pittard et al. \(2009\)](#), who showed that clouds with $\chi = 10^3$ and a shock Mach number of 10 form a turbulent wake, and that the mass loss at later times resembles a single tail-like structure (see figures 4 and 7 of that paper).

5.3.2 Wind-cloud interaction

5.3.2.1 Comparison of wind-cloud and shock-cloud interactions

Figure 5.2 shows plots of the logarithmic density as a function of time for the wind-cloud case with $M_{\text{wind}} = 1.36$ (*c3wind1*). Here, the wind density, pressure, and velocity values are exactly the same as the post-shock flow values in model *c3shock*.

As with models *c1shock* and *c1wind1* in Chapter 4, *c3shock* and *c3wind1* show broad similarities (cf. Figs. 5.1 and 5.2). Both clouds have very similar morphologies and there is little to tell them apart, at least initially. However, there are subtle differences between the two models once the initial shock has progressed around the edge of the cloud. For example, the RT instability that develops on the cloud's leading edge behaves differently to that in model *c3shock*. This is due to an area of very low pressure in the shock-cloud case that is situated at the outside (right-hand) edge of the 'finger' of cloud material forming due to the RT instability. This low-pressure area is absent in the wind-cloud case. This means that the RT finger is channelled more upstream in the wind-cloud model but expands more radially in the shock-cloud model (see the last 3 panels in Figs. 5.1 and 5.2). Furthermore, the flow past the cloud in the wind-cloud case is reasonably uniform, whereas that in the shock-cloud case sweeps around the RT finger and helps to push cloud material outwards in the radial direction. This means that the transverse radius of the cloud grows more quickly in model *c3shock* compared to *c3wind1* (see the final panel in Figs. 5.1 and 5.2, and also 5.4e). However, in model *c3shock* the transverse radius of the cloud does not grow any further after $t = 3.6t_{cc}$, whereas in model *c3wind1* it continues to do so and by $t = 5t_{cc}$ it is greater than in model *c3shock*. The continued lateral growth of the cloud in model *c3wind1* coincides with a greater fragmentation of the core and a more rapid reduction in core mass, so that between $t = 5 - 8t_{cc}$ the core mass in *c3wind1* is less than that in *c3shock* (see Fig. 5.4a).

Once the transmitted shock has exited the cloud, the cloud in model *c3wind1* develops a long, low-density, turbulent wake similar to that in model *c3shock* (but much less dense) in the downstream direction.¹ Unlike the cloud in model *c3shock*, the cloud core in model *c3wind1* is not drawn out along the z direction, and once the core fragments the turbulent wake is disrupted by mass-loading of the core into the flow (not shown).

In comparison to model *c1wind1* in Chapter 4, the RT instability in model *c3wind1* expands upstream as opposed to the radial direction. This effect is caused by shock waves moving through the cloud, once the transmitted shocks from the front and rear of the cloud cross each other. Another difference between the *c3wind1* simulation and the *c1wind1* simulation in Chapter 4 is that the rear edge of the cloud is not forced upwards to the same extent due to the action of shocks driven into the back of the cloud (cf. the second panel of Fig. 5.2 at $t = 0.077 t_{cc}$ with the second panel of figure 2 in Chapter 4 at $t = 0.82 t_{cc}$). A turbulent wake is not seen in model *c1wind1* in Chapter 4 .

The evolution of the cloud in model *c3wind1* bears some similarities to the adiabatic spherical cloud in the wind-cloud study by Cooper et al. (2009), where mass is immediately ablated from the back of the cloud in the form of a long sheet of material and moves downstream in a thin, turbulent tail (see the left-hand panels of figure 7 in Cooper et al. (2009) showing the logarithmic density of the cloud, in a $M_{\text{wind}} = 4.6$ and $\chi = 910$ simulation). Their cloud showed a large expansion in the transverse direction, with cloud material being torn away from the core in all directions and mixed in with the flow, i.e. comparable behaviour to my model *c3wind1*. Such fragmentation of the cloud core is dissimilar to the evolution of the cloud in model *c3shock*.

¹At late times an axial artifact develops in models *c3shock* and *c3wind1*. This is visible in the final panels of Figs. 5.1 and 5.2 and is seen protruding upstream. Such artifacts are sometimes seen in 2D axisymmetric simulations and occur purely due to the nature of the scheme (fluid can become ‘stuck’ against the boundary). However, it does not appear to influence the rest of the flow and can be safely ignored in this work.

A comparison of shock-cloud and wind-cloud interactions: effect of increased cloud density contrast on cloud evolution

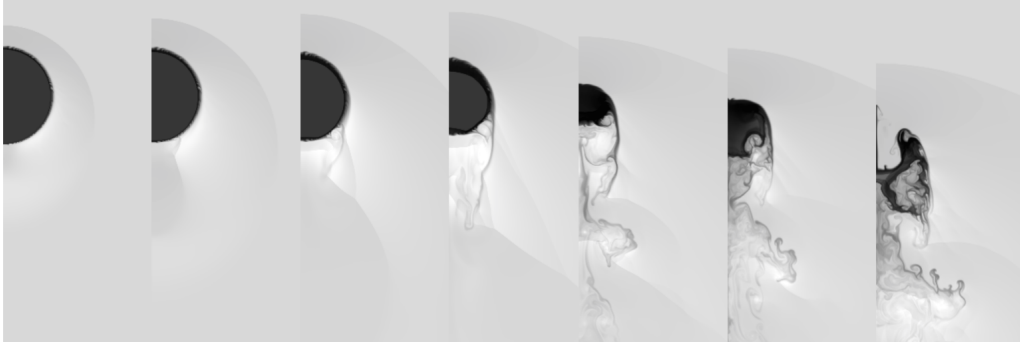


Fig. 5.2 The time evolution of the logarithmic density for model *c3wind1*. The greyscale shows the logarithm of the mass density, scaled with respect to the ambient medium. The density scale used in this figure extends from 0 to 3.8. The evolution proceeds left to right with $t = 0.042t_{cc}$, $t = 0.077t_{cc}$, $t = 0.15t_{cc}$, $t = 0.30t_{cc}$, $t = 1.2t_{cc}$, $t = 2.0t_{cc}$, and $t = 3.6t_{cc}$. All frames show the same region ($-5 < z < 2$, $0 < r < 3$, in units of r_c) so that the motion of the cloud is clear.

5.3.2.2 Effect of increasing M_{wind} on the evolution

Compared to model *c3wind1*, models *c3wind1a*, *c3wind1b*, and *c3wind1c* display a long-lasting and supersonically-expanding cavity located to the rear of the cloud (similar to the higher wind Mach number simulations in Chapter 4) and a reduced stand-off distance between the cloud and the bow shock; these features are due to the increase in wind velocity and Mach number in these models.

There is much greater pressure at the leading edge of the cloud in the higher M_{wind} simulations. The density jump at the bow shock in the higher M_{wind} simulations is also greater, and the stand-off distance between the bow shock and the leading edge of the cloud smaller, than in model *c3wind1*. The greater compression at the bow shock reduces the flow velocity (normalised to $v_{ps/wind}$) around the edge of the cloud, leading to a reduction in the growth rate of instabilities and decreased stripping of cloud material from the side of the cloud (when time is normalised to t_{cc}). The evolution of the cloud in the higher M_{wind} simulations, therefore, is different to that in model *c3wind1*, especially at low values of the cloud-crushing time-scale. As in Chapter 4, the higher M_{wind} simulations have very similar morphologies, at least until around $t \approx 1.8t_{cc}$. This is due to the presence of the highly-supersonic cavity

(as opposed to the area of low pressure behind the cloud in model *c3wind1*) which alters the way the wind flows around the cloud flanks. Instead of being focussed on the $r = 0$ axis immediately behind the cloud as in model *c3wind1*, the flow is deflected further downstream away from the cloud edge leading to a much lower pressure jump behind the cloud and restricting secondary shocks from being driven into the rear of the cloud. Thus, there is less turbulent stripping of cloud material from the rear of the cloud in these simulations compared to model *c3wind1*.

Interestingly, these high- M_{wind} models initially form a thin, compressed, smooth tail of material ablated from the side and rear of the cloud (see panels 2, 3, and 4, corresponding to $t = 0.13, 0.25$, and $0.49t_{cc}$, in each set of Fig. 5.3), whereas, as already noted, the cloud in model *c3wind1* forms instead a low-density turbulent wake. The cause of this is the way the flow moves around the cloud edge. In model *c3wind1* the wind flows much closer to the cloud all the way around its edge. However, in model *c3wind1a* the stronger bow shock deflects some of the flow away from the cloud edge, whilst the cavity serves to restrict the flow immediately behind the cloud. Thus, there is a slower removal of material from the cloud in the latter case. In addition, in model *c3wind1a*, the flow converges on the $r = 0$ axis, which serves to focus cloud material at this point, whereas in model *c3wind1* the flow changes direction and pushes upwards into the rear of the cloud. There is much less focusing of cloud material on the $r = 0$ axis in this case and, thus, the tail of cloud material is much broader. This behaviour also differs from the comparable models in Chapter 4.

The fragments of cloud core in all higher velocity wind models remain encased in the strong bow shock. Furthermore, it is clear from Fig. 5.3 that the cloud core in model *c3wind1c* has travelled much further in the axial direction than that in model *c3wind1a* (cf. the final panel in each set).

A comparison of shock-cloud and wind-cloud interactions: effect of increased cloud density contrast on cloud evolution

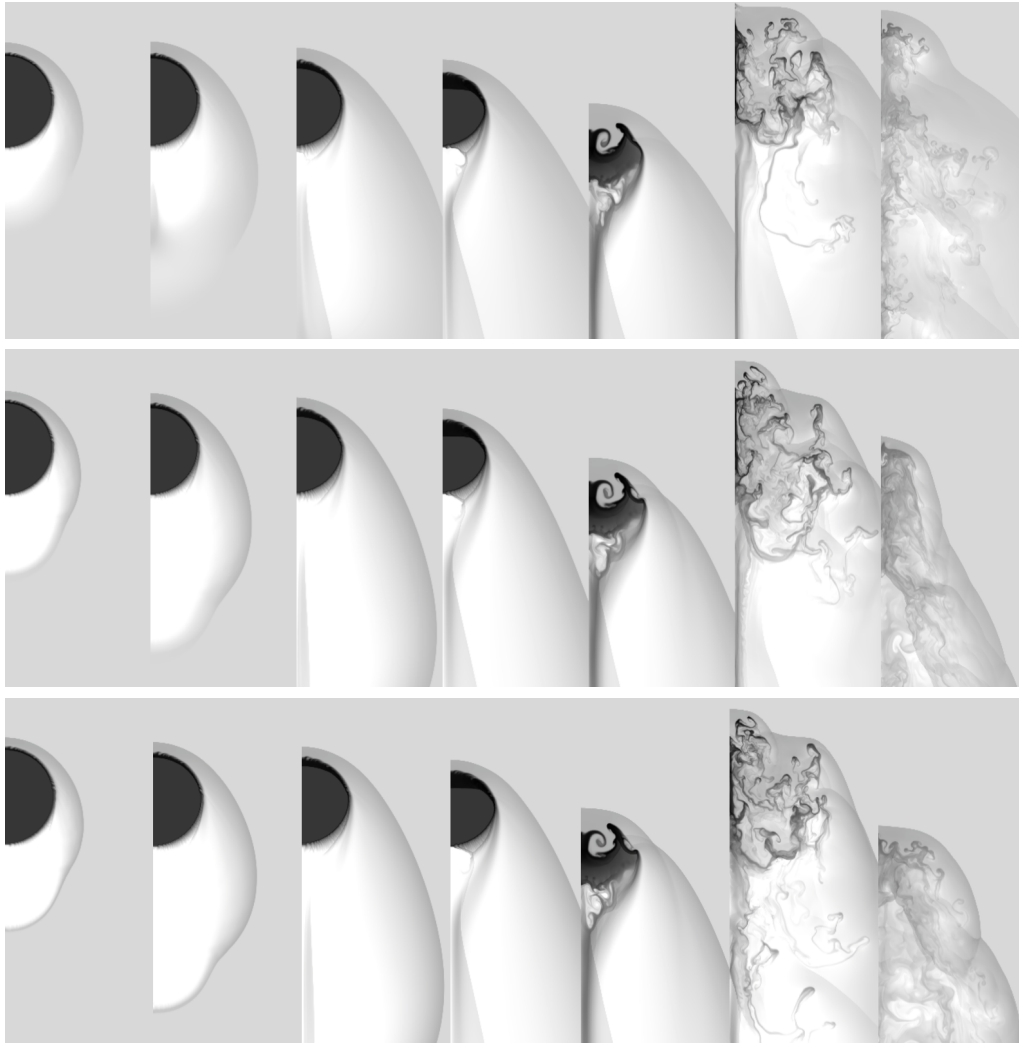


Fig. 5.3 The time evolution of the logarithmic density for models *c3wind1a* (top row), *c3wind1b* (middle row), and *c3wind1c* (bottom row). The greyscale shows the logarithm of the mass density, scaled with respect to the ambient medium. The density scale used in this figure extends from 0 to 3.8. The evolution proceeds left to right with $t = 0.07t_{cc}$, $t = 0.13t_{cc}$, $t = 0.25t_{cc}$, $t = 0.49t_{cc}$, $t = 1.84t_{cc}$, $t = 3.10t_{cc}$, and $t = 5.53t_{cc}$. The first five frames in each set show the same region ($-5 < z < 2$, $0 < r < 3$, in units of r_c) so that the motion of the cloud is clear. The displayed region is shifted in the 6th frame of each set ($-13 < z < -1$, $0 < r < 5$) and the last frame ($-23 < z < -11$, $0 < r < 5$) in order to follow the cloud.

Table 5.2 A summary of the cloud-crushing time, t_{cc} , and key time-scales, in units of t_{cc} , for the simulations investigated in this work. Note that the value for t_{drag} given here is calculated using the definition given in § 4.2.5, whilst t'_{drag} is the time when $\langle v_{z,\text{cloud}} \rangle = v_{ps}/e$, where v_{ps} is the post-shock (or wind) speed in the frame of the unshocked cloud.

Simulation	t_{cc}	t_{drag}	t'_{drag}	t_{mix}	t_{life}
c3shock	2.331	4.86	3.04	4.21	10.2
c3wind1	2.331	4.46	3.69	4.97	10.9
c3wind1a	0.737	4.16	3.40	6.23	11.7
c3wind1b	0.233	4.25	3.43	5.87	17.8
c3wind1c	0.074	4.38	3.53	5.82	17.6

5.3.3 Statistics

I now explore the evolution of various global quantities of the interaction for both the shock-cloud and wind-cloud models. Figure 5.4 shows the time evolution of these key quantities, whilst Table 5.2 lists various time-scales taken from these simulations.

Figure 5.4(a) shows the time evolution of the core mass of the cloud in each of the simulations. It can be seen that models *c3shock* and *c3wind1* are closer in their behaviour than either of them is to the higher wind Mach number simulations (which, however, are more closely converged to each other as expected from Mach scaling considerations). The cloud core in model *c3shock* drops to 50% of its initial value more quickly than that of model *c3wind1* due to the faster transverse expansion of the cloud in the former case. However, the greater lateral expansion of the cloud in model *c3wind1* at later times, and hence its greater effective cross-section, means that it then loses mass from its core at a faster rate, between $t = 5.5$ and $8.3t_{cc}$.

The rate of mass loss of model *c3shock* is considerably faster than the comparable model *c1shock* in Chapter 4 where the cloud core survived until $t \approx 24t_{cc}$. In contrast, the mass loss is very similar between models *c3wind1* and *c1wind1*, the cores of which are both destroyed by $t \approx 15t_{cc}$. In the shock-cloud cases, the turbulent wake evident in model *c3shock* serves to hasten the rate of mass loss, compared to model *c1shock* which lacked such a wake. The cloud core in model *c1wind1* becomes compressed by secondary shocks which travel upwards from the rear of the core, and

A comparison of shock-cloud and wind-cloud interactions: effect of increased cloud density contrast on cloud evolution

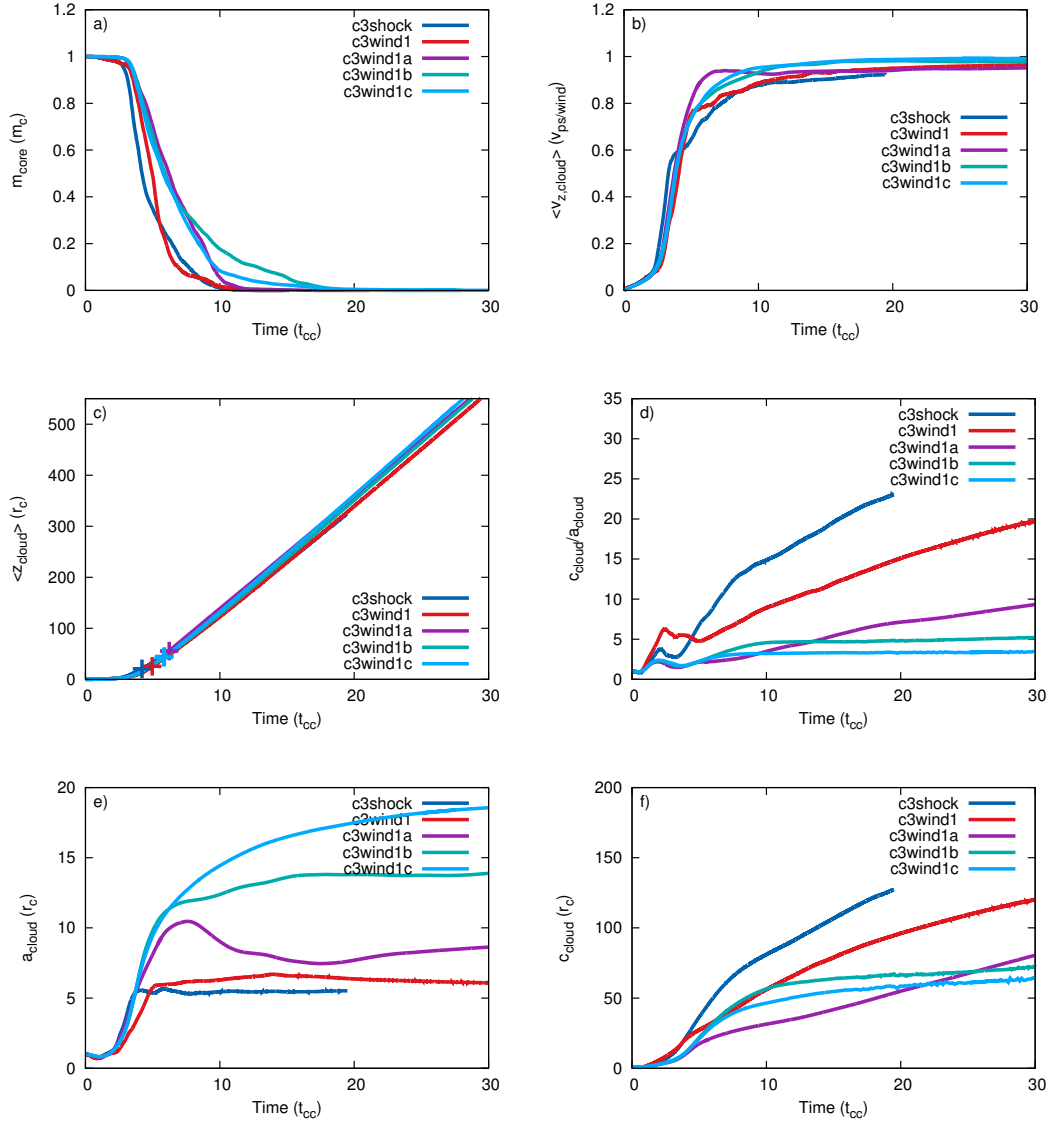


Fig. 5.4 Time evolution of (a) the core mass of the cloud, m_{core} , (b) the mean velocity of the cloud in the z direction, $\langle v_z \rangle$, (c) the centre of mass in the axial direction, $\langle z \rangle$, (d) the ratio of cloud shape in the axial and transverse directions, $c_{\text{cloud}}/a_{\text{cloud}}$, (e) the effective transverse radius of the cloud, a_{cloud} , and (f) the effective axial radius of the cloud c_{cloud} . Note that panel (c) shows the position of the centre of mass of each cloud at $t = t_{\text{mix}}$ (indicated by the respectively-coloured crosses). In addition, the behaviour of the cloud in model *c3shock* after $t \approx 20t_{cc}$ has not been included in any of the above panels since the cloud material drops below the $\beta = 2/\chi$ threshold at late times (see § 4.2.4).

it develops filamentary structures at the rear much earlier than the cloud in model *c1shock*. Thus, the rate of core mass loss in *c1wind1* is quicker than that in model *c1shock*, and comparable to *c3wind1* where the core fragments.

The clouds in models *c3wind1a*, *c3wind1b*, and *c3wind1c* are the slowest of the clouds in Fig. 5.4(a) to lose mass and have a slightly shallower mass-loss curve due to the lack of a turbulent wake prior to core fragmentation. These models have very similar core-mass profiles until $t \simeq 8t_{cc}$, when random fluctuations cause subsequent divergence in the evolution of m_{core} . The mass loss rate is considerably quicker for the wind-cloud models in the current paper than those in Chapter 4 since the former fragment whilst the latter remain much more intact over a longer period before becoming mixed into the flow. Therefore, the cloud cores in the current chapter have much steeper mass loss curves.

The values of t_{life} given in Table 5.2 are further confirmation that the cloud lifetime (normalised by t_{cc}) *increases* with Mach number in wind-cloud interactions (Scannapieco and Brüggén 2015; Chapter 4), as opposed to decreasing with Mach number in shock-cloud interactions (e.g. Pittard et al., 2010; Pittard and Parkin, 2016), until Mach scaling kicks in at high Mach numbers, whereupon t_{life}/t_{cc} approaches a constant value. Previous shock-cloud studies (e.g. Pittard and Parkin, 2016) have shown that at low shock Mach numbers dynamical instabilities on the cloud edge are slow to form; however, such instabilities are more prevalent as the Mach number increases, thus allowing the cloud to be shredded and mixed into the flow more rapidly and reducing the cloud lifetime. However, in the wind-cloud case such instabilities are retarded as the wind Mach number increases, lessening the stripping of cloud material from the edge of the cloud in the higher M_{wind} runs in Chapter 4 and the current chapter. Such dampening of the growth of KH (and RT) instabilities and less effective stripping provide for a longer time-scale over which mass is lost. KH instabilities are able to become independent of the Mach number in wind-cloud simulations owing to the way that the cloud-crushing time-scale is calculated. Here,

A comparison of shock-cloud and wind-cloud interactions: effect of increased cloud density contrast on cloud evolution

the value of t_{cc} is reduced as M_{wind} is increased. Since the calculation of the KH growth rate (see Eq. 5.1) is dependent upon both M_{wind} and t_{cc} , the KH time-scale also varies. Thus, as M_{wind} increases, t_{KH} *decreases* until it levels out at high M_{wind} .

The acceleration of the cloud is shown in Fig. 5.4(b). The cloud in model *c3wind1* has a slightly slower acceleration than that in *c3shock*. Compared to Chapter 4, these two models show a slightly slower initial acceleration, due to the increased density of the cloud in these cases (for instance, the speed of the transmitted shock through the cloud is much slower). In addition, the non-smooth acceleration of both clouds between $t \approx 4 - 15t_{cc}$ acknowledges the change in shape of the cloud core away from the previous near-spherical morphology. The acceleration of the cloud in the higher M_{wind} simulations initially follows that of the cloud in *c3wind1*. The acceleration of the cloud up to the asymptotic velocity is much smoother than seen in models *c3shock* and *c3wind1*. The similar behaviour of the higher M_{wind} simulations, as in Chapter 4, indicates the presence of Mach scaling.

Figure 5.4(c) shows the time evolution of the cloud centre of mass in the axial direction. The movement of the centre of mass of the cloud in models *c3shock* and *c3wind1* is near identical. Models *c3wind1a* to *c3wind1c* differ very slightly in that the plot of the centre of mass of the cloud in these simulations is marginally steeper than that of the other two models from $t \approx 12t_{cc}$, indicating that they have moved downstream slightly further than the clouds in the other two models. Interestingly, this behaviour contrasts with that given in Chapter 4, where models *c3shock* and *c1wind1* had noticeably *steeper* profiles compared to the higher M_{wind} models.

Scannapieco and Brüggén (2015) found that clouds with $\chi \gtrsim 100$ in a high-velocity flow were unable to be accelerated to the wind velocity before being disrupted, with clouds with a lower density contrast embedded in a high-velocity wind attaining much greater velocities. This suggests that clouds with high density contrasts would have difficulty in being moved across large distances before they are disrupted. I find that due to their large reservoir of mass, clouds with an initially high

density contrast are able to significantly “mass-load” the flow, thus generating much longer-lived structures with density substantially greater than that of the background flow (see e.g. the last two time snapshots of each model in Fig. 5.3). These structures are able to move 100s of r_c downstream from the original cloud position and acquire velocities comparable to the background flow speed. I find that this process is facilitated in high-velocity winds: the cloud in model *c3wind1c* accelerates faster and is moved a greater distance than the cloud in model *c3wind1*. I note also that neither the complete mixing of cloud material, nor complete smoothing of the flow, are achieved in any of my simulations.

The time evolution of the shape of the cloud is presented in Fig. 5.4(d-f). In terms of the transverse radius of the cloud, a_{cloud} , the clouds in both *c3shock* and *c3wind1* show a modest expansion until $t \approx 4t_{cc}$ (not dissimilar to models *c1shock* and *c1wind1* in Chapter 4) before levelling out, coinciding with the moderate compression of the cloud in each case by the transmitted shock. The clouds in both models have a much greater expansion in the axial direction (c_{cloud}), coinciding with the formation of their turbulent wakes, in contrast to the behaviour found in Chapter 4 where there was a much more modest axial expansion for the equivalent models (cf. Fig. 5.4(f) with the same figure in that chapter). In contrast, the cloud in *c3wind1c* shows much less expansion in the axial direction (its axial radius nearly plateaus after $t \simeq 10t_{cc}$), whilst its expansion in the transverse direction is $3 - 4\times$ as large as the cloud in *c3shock* and *c3wind1*. This is caused by the pressure and flow gradients resulting from the strong bow shock surrounding the cloud. Again, it can be seen that the cloud in model *c3wind1b* behaves similarly to that in *c3wind1c* in terms of the evolution of c_{cloud} , thus demonstrating Mach scaling.

5.3.4 Time-scales

Table 5.2 provides normalised values for t_{drag} , t_{mix} , and t_{life} for each of the simulations presented in this chapter. Figure 5.5 also shows the normalised values of t'_{drag} and t_{mix} as a function of the Mach number, and also in comparison to 2D inviscid shock-cloud simulations with $\chi = 10^3$. The behaviour of each time-scale is now discussed in turn.

5.3.4.1 t_{drag}

First, I note that the wind-cloud simulations all have $t_{\text{drag}}/t_{\text{cc}} \approx 4.2 - 4.5$ (see Table 5.2). These values are typically slightly greater than the values seen from the lower χ wind-cloud simulations in Chapter 4, which spanned the range 3.3 – 4.3. Thus, clouds with $\chi = 10^3$ are accelerated by a wind slightly more slowly than those with $\chi = 10$. This dependence is consistent with that also found in shock-cloud simulations (see e.g. Pittard et al., 2010), but in both cases the scaling is weaker than the $\chi^{1/2}$ scaling expected from a simple analytical model (Klein et al., 1994; Pittard et al., 2010). I also find barely any Mach-number dependence to the values of $t_{\text{drag}}/t_{\text{cc}}$ in my wind-cloud simulations, when $\chi = 10$ and 10^3 . This contrasts with the behaviour seen in shock-cloud simulations, where $t_{\text{drag}}/t_{\text{cc}}$ rises sharply at low Mach numbers (e.g. Pittard et al., 2010; Pittard and Parkin, 2016).

5.3.4.2 t_{mix}

Table 5.2 and Fig. 5.5 show that $t_{\text{mix}}/t_{\text{cc}}$ is almost independent of Mach number for the $\chi = 10^3$ wind-cloud simulations presented in this chapter. This behaviour contrasts with that from the $\chi = 10$ wind-cloud simulations in Chapter 4, and the results of Scannapieco and Brüggén (2015), where simulations with higher wind Mach numbers had significantly longer mixing times. Both behaviours contrast with the rapid rise in $t_{\text{mix}}/t_{\text{cc}}$ at low Mach numbers in shock-cloud simulations

(Pittard et al., 2010; Pittard and Parkin, 2016)! This clearly reveals very interesting diversity between these various interactions and motivates further studies of them. In particular, it is not clear why Scannapieco and Brüggén (2015) find longer mixing times with higher wind Mach numbers, when the current chapter does not, although there are a number of obvious avenues to investigate, including differences between the initial conditions and physics included, the effects of numerical resolution, and differences in the definition of mixing. As a final point, I note that Mach scaling is demonstrated in all of the relevant work (Pittard et al. 2010; Pittard and Parkin 2016; Chapter 4), including the present chapter.

Interestingly, Fig. 5.5(b) shows that the values of t_{mix}/t_{cc} from the shock-cloud simulations (which *do* show a Mach number dependence) appear to converge towards the Mach number-independent wind-cloud values as $M_{\text{shock/wind}}$ increases. This behaviour, although not quite so clear cut, may also be taking place for t'_{drag}/t_{cc} too (see Fig. 5.5(a). Finally, I note that $t'_{\text{drag}}/t_{\text{mix}} \sim 0.6$ in my $\chi = 10^3$ wind-cloud simulations (see Fig. 5.5).

5.3.5 Comparison to existing literature

As noted in § 5.1, there is a lack of numerical studies in the literature that investigate the Mach-number dependence of wind-cloud interactions at high density contrast ($\chi \gtrsim 10^3$). Studies which consider high values of χ are often limited to a single value of M_{wind} (e.g. Banda-Barragán et al., 2016; Cooper et al., 2009; Vieser and Hensler, 2007). Thus, it is difficult to draw any conclusions from the current literature as to the Mach-number dependence of t_{mix} in wind-cloud simulations at high χ . In fact, the only other wind-cloud study, to my knowledge, to investigate a range of Mach numbers at high χ is by Scannapieco and Brüggén (2015). They find an increasing trend for t_{mix} with M_{wind} , which is in disagreement with the results that I present here. This disagreement is down to the different initial setup (their cloud is

A comparison of shock-cloud and wind-cloud interactions: effect of increased cloud density contrast on cloud evolution

initially assumed to be in pressure equilibrium with the surrounding wind, whereas my cloud is under-pressured) and to the different physics employed (their simulation is radiative, whereas mine is adiabatic). In addition, there are numerical differences (e.g. 2D vs. 3D), and differences in the definition of mixing between their work and mine. Further investigation into the effect of these differences is needed.

In previous shock-cloud studies, [Pittard et al. \(2010\)](#) and [Pittard and Parkin \(2016\)](#) showed that the ratio $t'_{\text{drag}}/t_{\text{mix}}$ was χ -dependent². To first order, the normalised mixing time-scale is independent of χ , while the normalised drag time-scale increases weakly with χ . Thus, clouds with low density contrasts are accelerated more quickly than they mix, while clouds with very high density contrasts tend to mix more efficiently than they are accelerated. At high Mach numbers ($M_{\text{shock}} \gtrsim 10$), [Pittard and Parkin \(2016\)](#) found that $t'_{\text{drag}}/t_{\text{mix}}$ increased from 0.14 when $\chi = 10$, to 0.75 when $\chi = 10^3$. The current chapter now allows me to examine whether such behaviour is displayed in wind-cloud interactions. At high Mach numbers, Chapter 4 showed that for $\chi = 10$, $t'_{\text{drag}}/t_{\text{mix}} \approx 0.1$, while here I find $t'_{\text{drag}}/t_{\text{mix}} \approx 0.6$ for $\chi = 10^3$. Thus, I find that mixing becomes relatively more efficient compared to acceleration for wind-cloud interactions as the cloud density contrast increases, in agreement with the behaviour seen in shock-cloud interactions.

5.4 Summary and Conclusions

This is the second part of a study comparing shock-cloud and wind-cloud interactions and the effect of increasing the wind Mach number on the evolution of the cloud. The first paper (Chapter 4) investigated the morphological differences between clouds of density contrast $\chi = 10$ struck by a shock and those embedded in a wind. Significant differences were found, not only between the morphology of the clouds themselves but also in terms of the behaviour of the external medium in each case. It was also

²In these works, t_{drag} is equivalent to t'_{drag} in the current chapter.

5.4 Summary and Conclusions

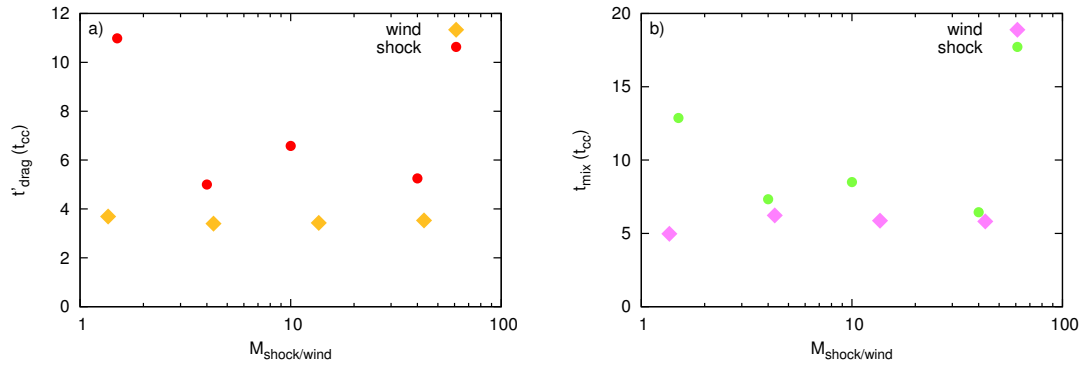


Fig. 5.5 (a) Cloud drag time, t'_{drag} , (gold diamonds) and (b) mixing time of the core, t_{mix} , (pink diamonds) as a function of the wind Mach number, M_{wind} for the wind-cloud simulations. Also shown are the corresponding values from 2D inviscid simulations calculated for a shock-cloud interaction with $\chi = 10^3$ (t_{drag} , red circles; t_{mix} , green circles). Note that in this figure, t'_{drag} is defined as the time at which the mean cloud velocity, $\langle v_{z,\text{cloud}} \rangle = v_{ps}/e$, where v_{ps} is the post-shock (or wind) speed in the frame of the unshocked cloud. This definition is consistent with Pittard et al. (2010), but differs from Klein et al. (1994) and Pittard and Parkin (2016). Thus, $t'_{\text{drag}} < t_{\text{drag}}$. See Table 5.2 for values of t_{drag} calculated according to the definition given in § 4.2.5.

the first work to identify Mach scaling in a wind-cloud simulation and additionally found that clouds embedded in high Mach number winds survived for longer and travelled larger distances.

In this follow-up chapter, I have continued my investigation of shock-cloud and wind-cloud interactions, but this time have focussed on clouds with a density contrast of $\chi = 10^3$. As in Chapter 4, I began my investigation by comparing wind-cloud simulations against a reference shock-cloud simulation with a shock Mach number $M = 10$ (*c3shock*). My standard wind-cloud simulation (*c3wind1*) used exactly the same cloud embedded in the same flow conditions. On comparing the two simulations, I find only minor morphological differences between the clouds in each simulation whilst the transmitted shock progresses through the cloud. After the transmitted shock has exited the cloud, I find that the cloud in both models begins to develop a low-density turbulent wake. The evolution of the two clouds begins to diverge after this time, and the morphology and properties of the cloud become increasingly different with time. For instance, the development of the wake differs

A comparison of shock-cloud and wind-cloud interactions: effect of increased cloud density contrast on cloud evolution

significantly between the two models: the cloud core in model *c3shock* does not fragment but is drawn out along the $r = 0$ axis, whilst that in model *c3wind1* does fragment and eventually disrupts the evolution of the wake.

On increasing the wind Mach number, I find that a supersonically-expanding cavity quickly forms at the rear of the cloud, similar to the higher M_{wind} simulations in Chapter 4. This is followed by a smooth, compressed, thin, but short-lived tail of cloud material which forms behind the cloud. This narrow tail arises from the focusing of the flow around and behind the cloud. Neither the cavity, nor the subsequent narrow tail, are seen in models *c3shock* and *c3wind1*, or the comparable models in Chapter 4 at lower χ . In all of my new wind-cloud simulations, the cloud eventually fragments and mass-loads the flow.

In Chapter 4, I demonstrated the presence of Mach scaling in wind-cloud simulations for the first time. My new results shown here provide further evidence of this effect. For example, the clouds in the higher Mach number simulations are all morphologically very similar (cf. each set of panels in Fig. 5.3), and evolve closely until “random” perturbations caused by the different non-linear development of instabilities from numerical rounding differences in the simulations eventually cause them to diverge.

I also find that clouds with density contrasts $\chi > 100$ can be accelerated up to the velocity of the wind and travel large distances before being disrupted, in contrast to the findings of [Scannapieco and Brüggén \(2015\)](#). For instance, in model *c3wind1a*, the cloud reaches 90% of v_{wind} by $t = t_{\text{mix}}$, at which time it has moved downstream $\approx 50r_c$. However, the flow remains structured and complete mixing is not achieved.

My work has helped to reveal a rich variety of behaviours depending on the nature of the interaction (shock-cloud or wind-cloud) and the cloud density contrast. In shock-cloud interactions, both the normalised cloud mixing and drag times increase at lower Mach numbers, but are independent of Mach number at higher Mach numbers - i.e. they show Mach scaling (see [Klein et al., 1994](#); [Pittard et al., 2010](#);

Pittard and Parkin, 2016). The drag time also increases weakly with χ , but t_{mix}/t_{cc} does not. In contrast, wind-cloud interactions with $\chi = 10$ show an almost Mach-number-independent drag time, but a strong rise in t_{mix}/t_{cc} with Mach number until $M_{\text{wind}} \sim 20$, whereupon t_{mix}/t_{cc} plateaus as Mach-scaling is reached (Chapter 4). My current work reveals another type of behaviour: wind-cloud interactions with $\chi = 10^3$ show almost Mach-number-independent drag and mixing times. Comparison of the current chapter with Chapter 4 also reveals that the normalised cloud mixing time at high Mach numbers is shorter at higher values of χ in my wind-cloud simulations, which is opposite to the χ -dependence seen in shock-cloud interactions where t_{mix}/t_{cc} is essentially independent of χ , and at most very weakly increases with it (Pittard et al., 2010; Pittard and Parkin, 2016). Finally, I find that the Mach number dependent values of t'_{drag} and t_{mix} for shock-cloud simulations at $\chi = 10^3$ converge towards the Mach-number-independent time-scales of comparable wind-cloud simulations.

That shock-cloud and wind-cloud interactions display such richness of behaviour demands further investigation. In particular, there is a need to address some of the discrepancies which currently exist between different studies.

Chapter 6

Isothermal shock-filament interactions

6.1 Introduction

Some filaments are known to collapse under gravity and fragment into star-forming cores. Recent observational studies have further shown that a large number of prestellar cores are found within dense filaments ([André et al., 2010](#); [Arzoumanian et al., 2011](#); [Roy et al., 2015](#)), with some filaments showing several cores strung out along their length ([Schisano et al. 2014](#); [Könyves et al. 2015](#)). In addition, young stellar clusters appear at the intersections of these filaments ([Myers, 2011](#); [Schneider et al., 2012](#)). The presence of cores embedded within filaments suggests a relationship between their formation and the fragmentation of the filaments themselves ([Larson, 1985](#); [Schneider and Elmegreen, 1979](#)). The conditions under which filaments fragment have been probed by various numerical studies (see e.g. [Heigl et al., 2016](#)). [Mellema et al. \(2002\)](#) found that radiative clouds tended to break up rather than become mixed into the background medium, since radiative or isothermal regimes can lead to milder cloud destruction. Radiative cooling can fundamentally alter the

nature of the interaction through the removal of thermal energy and pressure from the cloud. Under certain conditions, this may lead to the formation of dense cores.

Previous papers (Pittard and Goldsmith 2016 and Chapter 3) investigated the adiabatic interaction between a shock and a filament. Here, I extend these studies into the isothermal regime in order to understand the effects of radiative losses on the interaction. In the current study, I limit myself to a purely hydrodynamical scenario with all calculations performed as for a quasi-isothermal gas ($\gamma = 1.01$). The calculations are scale-free and are easily applicable to a broad range of scenarios.

The outline of this chapter is as follows: in § 6.2 I define the isothermal shock-filament problem and review the relevant literature. § 6.3 introduces the numerical method and describes the initial conditions, whilst in § 6.4 I present my results. In § 6.5 I discuss the relevance of a quasi-isothermal regime in my work. § 6.6 provides a summary of the results and a conclusion.

6.2 Problem definition

In this study, I consider the most basic scenario of a shock striking a filament. The simulated cloud is an idealised non-magnetised filament comprising a central cylindrical core of length lr_c (where r_c is the filament radius) and hemispherical caps at each end. Thus, a cloud with $l = 0$ would be a spherical cloud. The total length of the filament is given by $(l + 2)r_c$, and the ratio of the lengths of the major and minor axes is given by $(l + 2)/2$. I am able to vary the aspect ratio and orientation (denoted by the angle, θ , between the leading surface of the shock and the filament's major axis) of the filament in order to investigate how such changes might alter the interaction. Although this is clearly an idealised set-up, it is suitable for my purposes and allows changes to the interaction to be monitored as the shock Mach number, M , cloud density contrast, χ , l , and θ are varied.

Isothermal shock-filament interactions

The filament is assumed to have smooth edges over about 10 per cent of its radius (see § 3.2.1.1). I adopt the density profile given in [Pittard et al. \(2009\)](#) with $p_1 = 10$, in line with a previous HD shock-filament study, [Pittard and Goldsmith \(2016\)](#); this simulates a reasonably sharp-edged cloud. The presence of a soft edge to the filament is expected to retard the formation of HD instabilities (see [Nakamura et al., 2006](#)). HD instabilities are expected to be further suppressed by the use of a quasi-isothermal equation of state. The filament is initially in pressure equilibrium with its surroundings. This work comprises a purely hydrodynamic study, ignoring the effects of thermal conduction, cooling, magnetic fields, and self-gravity. All calculations were performed using a softened equation of state ($\gamma = 1.01$) in order to approximate an isothermal interaction. I have used this value of γ instead of $\gamma = 1.0$ because, owing to the way that the code is written, the internal energy of the system would become infinite if the latter value is used. Since $\gamma = 1.01$ is only 1% away from the purely isothermal value I therefore assume that any differences in the calculations are negligible.

6.2.1 Previous work

Numerical studies investigating the idealised problem of an adiabatic shock or wind interacting with a cloud date back to the 1970s. Since then, more realistic scenarios involving thermal conduction (e.g. [Orlando et al., 2008](#)), turbulence (e.g. [Pittard et al., 2009, 2010](#); [Pittard and Parkin, 2016](#)), and magnetic fields (e.g. [Mac Low et al., 1994](#); [Shin et al., 2008](#)), have been published. In particular, numerical studies of shock-cloud interactions which have included radiative cooling routines include [Mellema et al. \(2002\)](#); [Fragile et al. \(2005, 2004\)](#); [Orlando et al. \(2005\)](#); [Cooper et al. \(2008, 2009\)](#); [Yirak et al. \(2010\)](#); [van Loo et al. \(2010\)](#); [Li et al. \(2013\)](#), and [Johansson and Ziegler \(2013\)](#).

Whilst a full radiative cooling model would provide more realistic results applicable to observations, such models can be computationally costly. Instead, softening the equation of state so that it is isothermal ($\gamma = 1$) or quasi-isothermal can mimic the effects of cooling in the ISM. Several studies have explored the effect of an isothermal equation of state on the interaction between a shock or wind and a cloud. [Klein et al. \(1994\)](#) briefly explored a 2D shock-cloud interaction using $\gamma = 1.1$ for the cloud only and found that a softened equation of state led to greater compression in the cloud, with the cross-section of the radiative cloud much smaller than that of a non-radiative cloud. Moreover, the cloud drag was smaller than when an adiabatic equation of state was used. In addition, they found that isothermal clouds survived for longer due to the higher density of the shocked cloud. [Li et al. \(2003\)](#) explored self-gravitating turbulent clouds over a range of values for γ and found that the ability of interstellar gas clouds to fragment under the action of self-gravity decreased in the range $0.2 < \gamma < 1.4$. [Larson \(2005\)](#), in a review paper, noted that the above result had particular importance for filamentary clouds, and that a value of $\gamma = 1$ denoted a critical value for filament collapse. [Nakamura et al. \(2006\)](#), in their 3D study in which they compared adiabatic and isothermal interactions, used $\gamma = 1.1$ for both the cloud and the intercloud gas. Their results supported those of [Klein et al. \(1994\)](#) and underlined the fact that the cloud experienced much milder destruction by HD instabilities. Finally, [Banda-Barragán et al. \(2016\)](#) briefly explored the effect of a quasi-isothermal equation of state ($\gamma = 1.1$) on a magnetohydrodynamic wind-cloud interaction and noted that an isothermal filament survived for longer than an adiabatic one. Other studies to have utilised an isothermal equation of state for the cloud include [Raga et al. \(2005\)](#) and [Pittard et al. \(2005b\)](#).

Although there is now a comprehensive, and growing, body of work concerning shock-cloud and wind-cloud interactions using spherical clouds (see Chapter 4 for a brief overview), there remains a paucity of work in the current literature concerning interactions where the cloud is non-spherical. HD simulations with

prolate clouds were performed by [Klein et al. \(1994\)](#) and [Xu and Stone \(1995\)](#), whilst [Pittard and Goldsmith \(2016\)](#) investigated idealised filaments. In addition, Chapter 3 studied shock-filament interactions in a magnetised medium. With the exception of [Klein et al. \(1994\)](#), these studies emphasised the influence on the interaction of the alignment or orientation of the cloud with respect to the shock normal. Moreover, Chapter 3 noted that the length of the filament was not as important to the interaction as the filament's orientation. Other studies (e.g. [Cooper et al. 2009](#); [Banda-Barragán et al. 2018, 2016](#)) that have investigated the formation and evolution of filamentary clouds have started from the basis of a spherical cloud (though [Cooper et al. \(2009\)](#) also simulated a fractal cloud).

To my knowledge, there exists no other numerical study of a shock striking a filament in a non-magnetised medium using a softened equation of state. The current work, therefore, extends the study by [Pittard and Goldsmith \(2016\)](#) into a quasi-isothermal regime.

6.3 The numerical setup

The computations in this study were performed on a 3D XYZ Cartesian grid using the MG AMR HD code (see Chapter 2). Each of the simulations was performed at an effective resolution of R_{32} , in line with the results of a resolution test presented in [Pittard and Goldsmith \(2016\)](#). This means that seven grid levels (G^0 to G^6) are used for calculations requiring the finest grid.

The filament is initially centred at the grid origin $(x, y, z) = (0, 0, 0)$ with the planar shock front located at $x = -10$. The shock propagates along the x -axis in the positive x direction. The numerical domain is set so that there is constant inflow from the negative x direction and free inflow/outflow conditions at other boundaries, and is large enough so that the main features of the interaction occur before the shock reaches the downstream boundary of the grid. The setup of the filament

and the ambient medium is exactly the same as that given in Chapter 3, except for the value of γ and the lack of a magnetised ambient medium. The grid extent is determined by the values of M and χ and was $-20 < x < 1500$, $-12 < y < 12$, $-12 < z < 12$ for all simulations. In this study, I define motion in the direction of shock propagation as ‘axial’ and that perpendicular to this as ‘radial’ or ‘transverse’ (this includes motion in both the y and z directions). The pre-shock values of the ambient medium density and pressure are given in § 3.2.1.1. The post-shock density, pressure, and velocity relative to the pre-shock ambient values and to the shock speed are $\rho_{ps/wind}/\rho_{amb} = 8.7$, $P_{ps/wind}/P_{amb} = 9.1$, and $v_{ps/wind}/v_b = 0.88$, respectively.

6.3.1 Diagnostics

Various integrated quantities allow the evolution of the filament to be studied (see § 3.2.1.2).

6.3.2 Dynamical time-scales

The characteristic time-scale for prolate clouds to be crushed by the shock being driven into them, t_{cs} , is used throughout this chapter in line with [Pittard and Goldsmith \(2016\)](#). Several other time-scales (t_{drag} , t_{mix} , and t_{life}) can be obtained, and the definitions of these are given in Chapter 3. Time zero in my calculations is taken to be the time at which the intercloud shock is level with the centre of the filament.

6.4 Results

In this section I begin by examining the morphology of the interaction for my reference simulation, model *m3c2l8s*, and then consider the morphology for simulations with $M = 3$ for clouds of varying length and orientation, comparing against calculations made using a shock of $M = 10$ in an adiabatic regime. At the end of this section,

I explore the impact of the interaction on various global quantities and time-scales. Table 6.1 summarises the calculations performed and provides some key time-scales. I adopt a naming convention such that $m3$ denotes $M = 3$, $c2$ denotes $\chi = 10^2$, $l8$ denotes a filament length of 8, and s refers to a filament orientated sideways to the shock front (sideways filaments have $\theta = 0^\circ$; where the orientation of the filament is other than sideways, the number given in the model name refers to the angle of orientation of the major axis to the shock front).

6.4.1 Interaction of a filament with $\chi = 10^2$ and a sideways orientation with a shock of $M = 3$

I begin by discussing the morphology of the interaction for my reference simulation, where $M = 3$, $\chi = 10^2$, $l = 8$, and the filament is oriented sideways to the shock front. Figure 6.1 shows the mass density as a function of time for the xy and xz planes. The first panel in this, and subsequent figures, shows the initial filament orientation, with the direction of shock propagation running from left to right. I will describe the nature of the interaction and changing morphology with reference to a filament struck by a $M = 10$ adiabatic shock presented in a previous paper (Pittard and Goldsmith, 2016). The rationale for focussing on a filament struck by a $M = 3$ shock instead of that struck by a shock of $M = 10$ is that the former is a more realistic scenario given the near isothermal nature of the interaction.

Figure 6.1 shows the filament being struck by the shock from its side. The second panel, at $t = 0.00t_{cs}$, shows that the external shock has just passed the centre of the filament, whilst at $t = 0.39t_{cs}$ a bow shock has formed on the upstream side of the filament, very close to its upstream edge, in contrast with the $M = 10$ adiabatic simulation where the bow shock is located at a slightly greater distance from the filament (see figure 3 in Pittard and Goldsmith (2016)). The upstream surface of the filament begins to be compressed (as evidenced by an increase in density at this

Table 6.1 A summary of the shock-filament simulations presented in this work, along with key time-scales. M is the shock Mach number, χ is the density contrast of the filament to the surrounding ambient medium, l defines the length of the filament, and θ defines the angle of orientation of the filament between its major-axis and the shock surface (sideways-oriented filaments have $\theta = 0^\circ$). v_b is the shock speed through the inter-cloud medium (in code units). v_{ps} is the post-shock flow velocity, and is given in units of v_b . t_{cc} is the cloud-crushing time-scale of Klein et al. (1994), while t_{cs} is the cloud-crushing timescale for a spherical cloud of equivalent mass introduced by Xu and Stone (1995). Key filament time-scales are additionally noted. † denotes that the true value is unable to be given because the simulation had ended before this point was reached. Note that simulations *m3c2l885*, *m3c3l8s*, and *m10c2l885* were run at a reduced resolution of R_{16} .

Simulation	M	χ	$l (r_c)$	θ ($^\circ$)	v_b	v_{ps}/v_b	t_{cs}/t_{cc}	t_{drag}/t_{cs}	t_{mix}/t_{cs}	t_{life}/t_{cs}
m10c1l8s	10	10	8	sideways	10.6	0.99	1.91	0.61	0.44	—†
m10c2l2s	10	10^2	2	sideways	10.6	0.99	1.36	0.43	0.27	0.50
m10c2l4s	10	10^2	4	sideways	10.6	0.99	1.59	0.36	0.23	0.43
m10c2l8s	10	10^2	8	sideways	10.6	0.99	1.91	0.30	0.19	0.36
m10c2l230	10	10^2	2	30°	10.6	0.99	1.35	0.51	0.27	0.66
m10c2l430	10	10^2	4	30°	10.6	0.99	1.58	0.43	0.23	0.57
m10c2l830	10	10^2	8	30°	10.6	0.99	1.91	0.36	0.19	0.47
m10c2l860	10	10^2	8	60°	10.6	0.99	1.91	0.71	0.41	1.54
m10c2l885	10	10^2	8	85°	10.6	0.99	1.91	1.53	0.98	4.93
m3c1l8s	3	10	8	sideways	3.17	0.88	1.91	0.72	7.06	23.8
m3c2l2s	3	10^2	2	sideways	3.17	0.88	1.36	2.06	3.14	6.54
m3c2l4s	3	10^2	4	sideways	3.17	0.88	1.59	1.76	3.04	6.27
m3c2l8s	3	10^2	8	sideways	3.17	0.88	1.91	1.46	2.82	5.92
m3c2l230	3	10^2	2	30°	3.17	0.88	1.36	3.23	4.14	7.07
m3c2l430	3	10^2	4	30°	3.17	0.88	1.59	2.69	3.61	6.41
m3c2l830	3	10^2	8	30°	3.17	0.88	1.91	2.11	3.12	5.64
m3c2l860	3	10^2	8	60°	3.17	0.88	1.91	5.25	5.93	8.90
m3c2l885	3	10^2	8	85°	3.17	0.88	1.91	6.40	6.81	10.7
m3c3l8s	3	10^3	8	sideways	3.17	0.88	1.91	2.03	2.58	4.52
m1.5c1l8s	1.5	10	8	sideways	1.58	0.55	1.91	2.16	9.26	12.31
m1.5c2l2s	1.5	10^2	2	sideways	1.58	0.55	1.36	8.72	8.98	18.8
m1.5c2l4s	1.5	10^2	4	sideways	1.58	0.55	1.91	6.26	7.53	13.2
m1.5c2l8s	1.5	10^2	8	sideways	1.58	0.55	1.91	5.36	6.61	12.2
m1.5c2l230	1.5	10^2	2	30°	1.58	0.55	1.36	7.73	9.15	17.96
m1.5c2l430	1.5	10^2	4	30°	1.58	0.55	1.36	7.04	8.26	13.33
m1.5c2l830	1.5	10^2	8	30°	1.58	0.55	1.36	6.03	6.85	13.78
m1.5c2l860	1.5	10^2	8	60°	1.58	0.55	1.36	7.50	7.32	14.47
m1.5c2l885	1.5	10^2	8	85°	1.58	0.55	1.36	8.08	7.84	13.66

Isothermal shock-filament interactions

point) by the transmitted shock progressing through it, while the external shock sweeps symmetrically around the outside of the filament and converges at the rear of the cloud, creating a region of higher pressure compared to the pressure of the ambient medium downstream of the cloud. The convergence of the external shock on the $z = 0$ plane forces a secondary shock back through the cloud in the upstream direction.

The filament reaches maximum compression at $t \approx 0.39t_{cs}$. At this point the transmitted shock has travelled through and exited the filament and has propagated downstream, accelerating as it proceeds and dragging filament material with it. As it exits the back of the filament the ends of the filament begin to display the effects of diffracted shocks and some ablation of filament material by the surrounding flow is observed (in line with the sideways filament in the $M = 10$ adiabatic simulation presented in [Pittard and Goldsmith \(2016\)](#)). The ends of the filament at this point are bent in the upstream direction; this bears some similarities with the sideways filament of length $l = 4$ and density contrast $\chi = 10$ embedded in a perpendicular magnetic field in Chapter 3, where it was noted that care ought to be taken from an observational point of view since the interpretation of such a filament might lead to the conclusion that the shock was travelling in the $-x$ direction. After this point (at $t \approx 0.66t_{cs}$), the filament expands due to rarefaction waves within it. A ‘tail shock’ (as noted in [Pittard and Goldsmith 2016](#)) is visible. The filament is then seen to collapse in on itself at $t \approx 0.95t_{cs}$ and become compacted in the direction of shock propagation. Small RT fingers develop on the tips of the filament. Unlike in [Pittard and Goldsmith \(2016\)](#), the upstream edge of the filament displays no obvious KH instabilities at $t = 0.92t_{cs}$ due to the quasi-isothermal nature of the interaction. The filament is also much more compressed than in the aforementioned study and its tail of ablated cloud material is much smoother. As noted in [Pittard and Goldsmith \(2016\)](#), the filament forms a ‘three-rolled’ structure, though this becomes more spread out as the filament material is ablated by the flow.

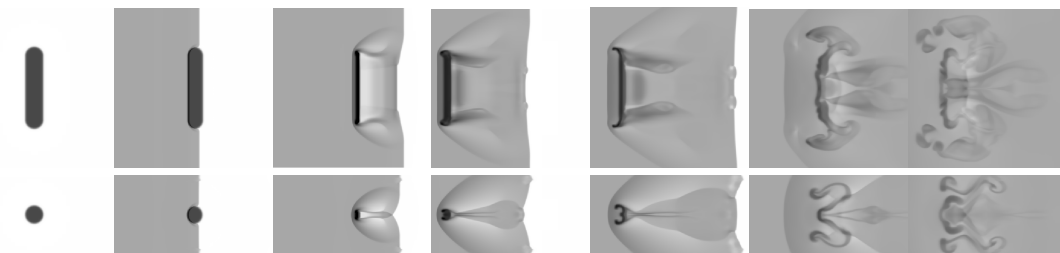


Fig. 6.1 The time evolution of the logarithmic density for model *m3c2l8s* showing the xy (top set of panels) and xz planes (bottom set of panels). The greyscale shows the logarithm of the mass density, from white (lowest density) to black (highest density). The density in this and subsequent figures has been scaled with respect to the ambient density ρ_{amb} , so that a value of 0 represents the value of ρ_{amb} and 1 represents $10 \times \rho_{\text{amb}}$. The density scale used for this figure extends from 0 to 2.8. The first panel on each row shows the setup of the simulation. The evolution proceeds from the second panel onwards, left to right, with $t = 0.00t_{\text{CS}}$, $t = 0.39t_{\text{CS}}$, $t = 0.66t_{\text{CS}}$, $t = 0.95t_{\text{CS}}$, $t = 2.16t_{\text{CS}}$, and $t = 2.82t_{\text{CS}}$. All frames show the same region for y and z ($-10 < y < 10$ and $-5 < z < 5$, in units of r_c). So that the motion of the cloud is clear, the first 3 frames show $-10 < x < 10$. Frames 4-6 show $0 < x < 20$, and the final frame shows $20 < x < 40$. Note that in this and similar figures the y and z axes are plotted vertically, with positive towards the top and negative towards the bottom, whilst the shock is initially located at $x = -10$.

Figure 6.2 shows volumetric density renderings of the filament as a function of time in the xz and xy planes, respectively. Owing to the focus on filament material, this figure (and subsequent similar figures) does not show features such as the bow shock or other elements of the ambient material or flow. The main differences between this figure and figure 1 of [Pittard and Goldsmith \(2016\)](#) are that the entrainment of filament material by the flow is much smoother in the current figure (as expected by the lack of KH instabilities produced by the damping effect of the quasi-isothermal equation of state) and thus there is no turbulent mass of filament material located to the rear of the cloud. Moreover, a short tail of material is observed to form on the axis behind the filament as the simulation progresses. The three-rolled structure identified by [Pittard and Goldsmith \(2016\)](#) is present in this figure (from $t \approx 0.95t_{\text{CS}}$ onwards), though the rolls are less tight and lose cohesion as the filament is ablated by the flow.

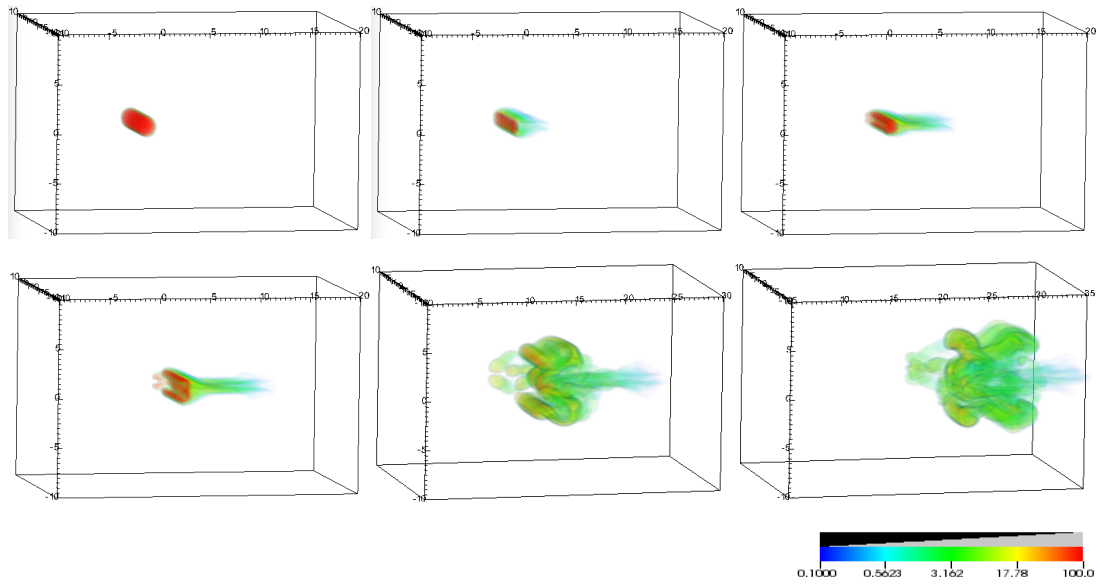


Fig. 6.2 A 3D volumetric rendering of model *m3c2l8s*. From left to right, top to bottom the timings are $t = 0.00t_{CS}$, $t = 0.39t_{CS}$, $t = 0.66t_{CS}$, $t = 0.95t_{CS}$, $t = 2.16t_{CS}$, and $t = 2.82t_{CS}$. The colour scale in this and similar figures indicates the density of the filament, normalised by the density of the ambient medium, with the initial filament density being 100 (or red). The ambient medium is not shown; therefore, the bow shock upstream of the filament is also not visible.

6.4.2 Effect of filament orientation on the interaction

Figure 6.3 shows the interaction of an $M = 3$ shock with an obliquely-oriented filament (i.e. one oriented at $\theta = 30^\circ$ to the shock front). Unlike the sideways filament in Figs 6.1 and 6.2 which was struck from the side, the filament in the current figure is initially struck at its upstream-facing end. The external shock is then channelled around the edge of the filament. At $t = 0.39t_{CS}$ the external shock has become fully diffracted around the filament and converges on the axis behind the filament, interacting and causing shocks to be driven back into the rear of the filament at an angle. At the same time, a transmitted shock is making its way through the filament from the upstream side, leading to that part of the filament becoming compressed and the filament taking on a wedge-shaped appearance. As the shock moves through the filament, the bottom end of the filament expands whilst the top end is steadily compressed ($t \approx 0.66t_{CS}$). Filament material begins to be ablated

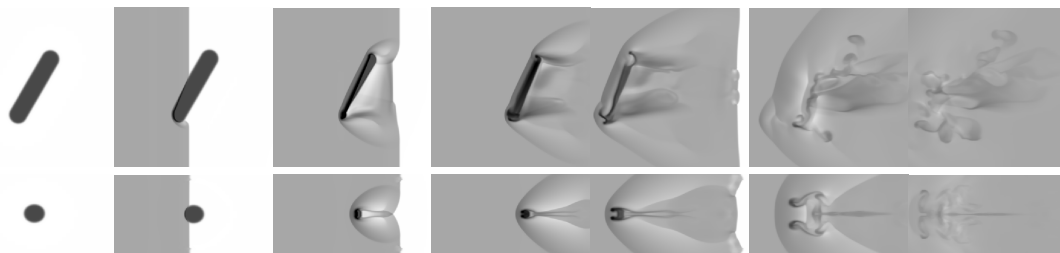


Fig. 6.3 The time evolution of the logarithmic density for model *m3c2l830* showing the xz (top set of panels) and xy planes (bottom set of panels). The greyscale shows the logarithm of the mass density, from white (lowest density) to black (highest density). The density scale used for this figure extends from 0 to 2.8. The first panel on each row shows the setup of the simulation. The evolution proceeds from the second panel onwards, left to right, with $t = 0.00t_{cs}$, $t = 0.39t_{cs}$, $t = 0.66t_{cs}$, $t = 0.95t_{cs}$, $t = 2.16t_{cs}$, and $t = 2.82t_{cs}$. All frames show the same region in y and z ($-5 < y < 5$ and $-10 < z < 10$, in units of r_c). So that the motion of the cloud is clear, the first 4 frames show $-10 < x < 10$. Frame 5 shows $0 < x < 20$, frame 6 shows $5 < x < 25$, and the final frame shows $20 < x < 40$.

from each end of the filament at $t = 0.39t_{cs}$ onwards and a vortex ring is visible at the base of the filament. Meanwhile, an RT finger is evident at the top end of the filament from $t \approx 0.95t_{cs}$. Considerably less turbulent stripping of filament material is evident in the current figure and it is clear that the bow shock is much closer to the upstream edge of the filament compared to the bow shock in figure 7 in [Pittard and Goldsmith \(2016\)](#). Because of the RT finger, the flow of filament material stripped by the surrounding flow is channelled behind and above the filament, though it is much less turbulent. At $t = 2.16t_{cs}$ multiple shocks are present at the location of the bow shock and are caused by shocks propagating back through the filament and accelerating into the surrounding flow. Clumps of filament material are observed to break away from the top of the filament, and the filament core mass has been significantly ablated by the flow, though still retaining its structure. Figure 6.4 shows how the filament forms a short turbulent wake at late times.

The interaction of a shock with a filament oriented at $\theta = 60^\circ$ to the shock front (simulation *m3c2l860*) is shown in Figs 6.5 and 6.6. The initial morphology is not dissimilar to that in simulation *m3c2l830*. However, at later times (from $t = 0.95t_{cs}$ onwards) the filament length becomes compressed until it is less than half its original

Isothermal shock-filament interactions

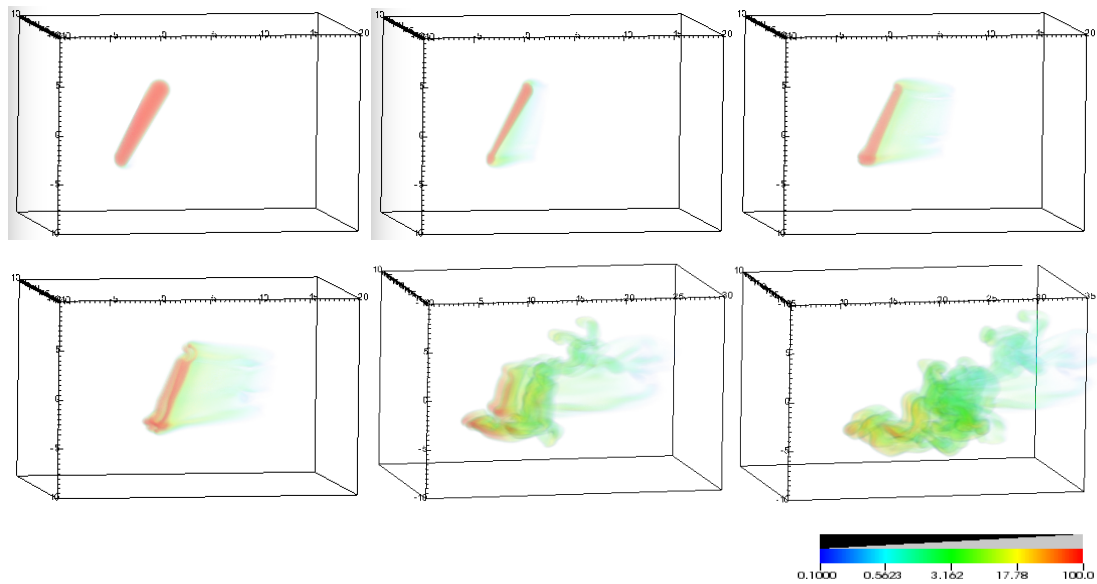


Fig. 6.4 A 3D volumetric rendering of model *m3c2l830*. From left to right, top to bottom the timings are $t = 0.00t_{cs}$, $t = 0.39t_{cs}$, $t = 0.66t_{cs}$, $t = 0.95t_{cs}$, $t = 2.16t_{cs}$, and $t = 2.82t_{cs}$.

length. The vortex ring located at the upstream end of the filament is much larger than before, whilst the RT finger at the top of the filament and its associated wake of filament material extends much further downstream. A double bow shock is observed in the xy panels at later times.

Figures 6.7 and 6.8 show the interaction for simulation *m3c2l885*, a filament lying almost end-on to the shock front. Here, the transmitted shock travels along the entire length of the filament and a small vortex ring is visible at the upstream end. Shocks are transmitted through the sides of the filament as the transmitted and external shocks sweep through and around it. These sideways shocks, however, produce less reverberation within the filament than in the comparable filament in [Pittard and Goldsmith \(2016\)](#) and there is therefore considerably less voiding of the filament in the present figures. There are two main differences between this filament and that in [Pittard and Goldsmith \(2016\)](#). Firstly, the bow shock is located immediately on the upstream edge of the filament and is sharply angled downstream on either side, whereas that in [Pittard and Goldsmith \(2016\)](#) is much more rounded and located at a distance from the filament edge. Secondly, the filament develops a

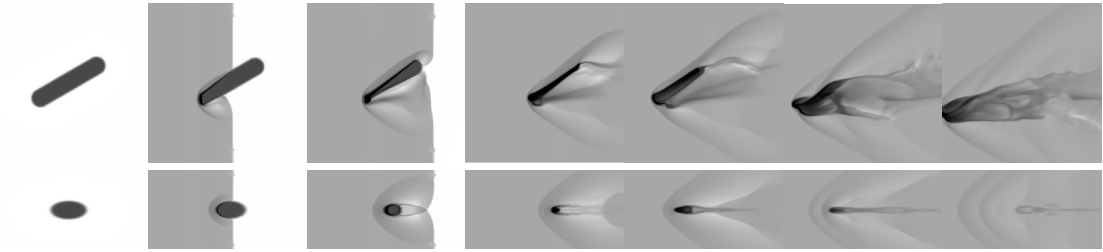


Fig. 6.5 The time evolution of the logarithmic density for model *m3c2l860* showing the xz (top set of panels) and xy planes (bottom set of panels). The greyscale shows the logarithm of the mass density, from white (lowest density) to black (highest density). The density scale used for this figure extends from 0 to 2.8. The first panel on each row shows the setup of the simulation. The evolution proceeds from the second panel onwards, left to right, with $t = 0.00t_{CS}$, $t = 0.39t_{CS}$, $t = 0.66t_{CS}$, $t = 0.95t_{CS}$, $t = 2.16t_{CS}$, and $t = 2.82t_{CS}$. All frames show the same region in y and z ($-5 < y < 5$ and $-10 < z < 10$, in units of r_c). So that the motion of the cloud is clear, the first 4 frames show $-10 < x < 10$. Frame 5 shows $-5 < x < 15$, frame 6 shows $0 < x < 20$, and the final frame shows $5 < x < 25$.

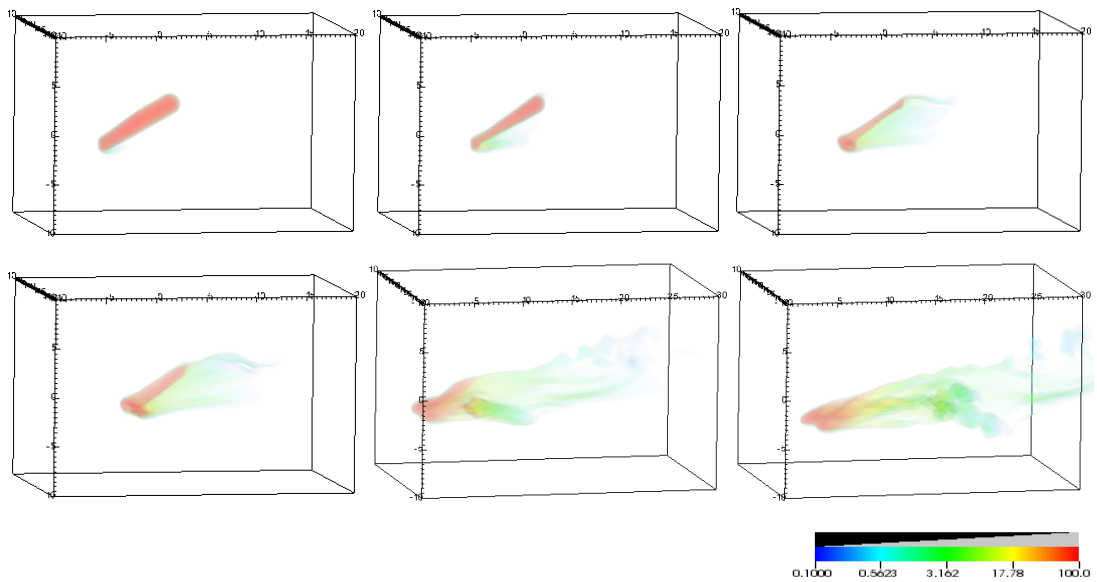


Fig. 6.6 A 3D volumetric rendering of model *m3c2l860*. From left to right, top to bottom the timings are $t = 0.00t_{CS}$, $t = 0.39t_{CS}$, $t = 0.66t_{CS}$, $t = 0.95t_{CS}$, $t = 2.16t_{CS}$, and $t = 2.82t_{CS}$.

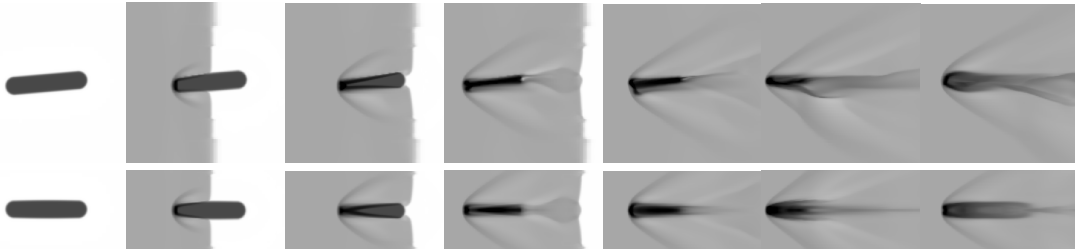


Fig. 6.7 The time evolution of the logarithmic density for model *m3c2l885* showing the xz (top set of panels) and xy planes (bottom set of panels). The greyscale shows the logarithm of the mass density, from white (lowest density) to black (highest density). The density scale used for this figure extends from 0 to 2.8. The first panel on each row shows the setup of the simulation. The evolution proceeds from the second panel onwards, left to right, with $t = 0.00t_{cs}$, $t = 0.39t_{cs}$, $t = 0.66t_{cs}$, $t = 0.95t_{cs}$, $t = 2.16t_{cs}$, and $t = 2.82t_{cs}$. All frames show the same region in y and z ($-5 < y < 5$ and $-10 < z < 10$, in units of r_c). So that the motion of the cloud is clear, the first 3 frames show $-10 < x < 10$. Frames 4 and 5 show $-5 < x < 15$, and the final two frames show $0 < x < 20$. Note that this simulation was run at a slightly lower resolution of R_{16} .

smooth tail of material as the simulation progresses and broadly retains the shape of its core, unlike in the previous paper.

6.4.3 Mach number dependence

The Mach number dependence of the interaction is now explored. Figure 6.9 shows the interaction of a Mach 10 shock with a filament of $\chi = 10^2$ and a sideways orientation (simulation *m10c2l8s*). It is immediately clear that the filament undergoes much greater compression in the x direction compared to the same filament struck by a $M = 3$ shock, and that this compression occurs over a much shorter normalised time-scale. Furthermore, the filament rapidly loses its core mass; much of the core mass has been ablated by the flow by $t \approx 1t_{cs}$. This is a significant finding, and one which is not observed in adiabatic shock-filament interactions for an $M = 10$ shock. It also contradicts the findings of Klein et al. (1994) and Nakamura et al. (2006) in terms of their simulations using $\gamma = 1.1$ for the cloud (though it should be noted that they used a spherical cloud and not a filament). With the bow shock located so close to the upstream edge of the filament, RT fingers at each end of the

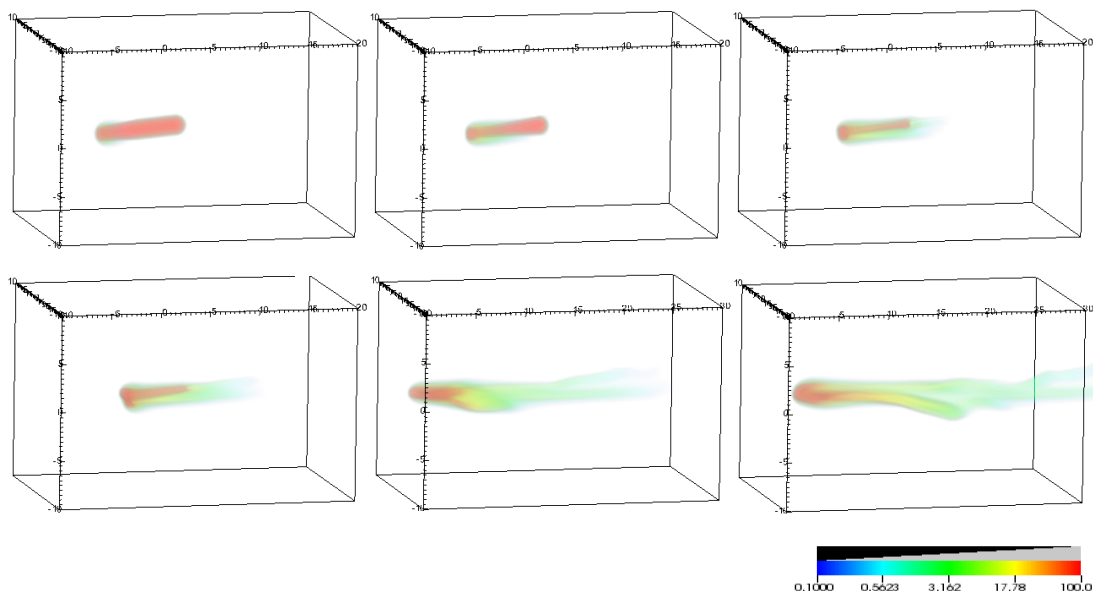


Fig. 6.8 A 3D volumetric rendering of model *m3c2l885*. From left to right, top to bottom the timings are $t = 0.00t_{CS}$, $t = 0.39t_{CS}$, $t = 0.66t_{CS}$, $t = 0.95t_{CS}$, $t = 2.16t_{CS}$, and $t = 2.82t_{CS}$.

filament are less in evidence, though most of the filament material is still lost from the ends of the filament. This filament can also be compared to figs. 1-3 in [Pittard and Goldsmith \(2016\)](#), thus highlighting the effect of only changing γ from $5/3$ to 1.01 . Compared to the adiabatic $M = 10$ simulation, the quasi-isothermal shock in the current figure has a far greater density jump than the adiabatic shock and thus its interaction with the filament is much stronger. For example, it is clear that the filament in figs. 1-3 in [Pittard and Goldsmith \(2016\)](#) is far less compressed compared to that in model *m10c2l8s*. The quasi-isothermal filament also shows no evidence of the ‘three-rolled’ structure present in [Pittard and Goldsmith \(2016\)](#). Moreover, the transmitted shock in Fig. 6.9 travels through the filament much more quickly than in figs. 1-3 mentioned above (cf. the third panel of Fig. 6.9 where the shock has exited the filament by $t = 0.27t_{CS}$ (though the external shock is still sweeping around the edge of the filament) with the fourth panel of figure 3 in [Pittard and Goldsmith \(2016\)](#) which shows the transmitted shock exiting the cloud at $t = 0.53t_{CS}$). Noticeably, the bow shock is located at the upstream edge of the filament, compared to being located some distance away in figure 3 in [Pittard and Goldsmith \(2016\)](#). Moreover,

Isothermal shock-filament interactions



Fig. 6.9 The time evolution of the logarithmic density for model *m10c2l8s* showing the *xy* (top set of panels) and *xz* planes (bottom set of panels). The greyscale shows the logarithm of the mass density, from white (lowest density) to black (highest density). The density scale used for this figure extends from 0 to 2.8. The evolution proceeds, left to right, with $t = 0.05 t_{cs}$, $t = 0.16 t_{cs}$, $t = 0.27 t_{cs}$, and $t = 0.96 t_{cs}$. All frames show the same region in *y* and *z* ($-10 < y < 10$ and $-5 < z < 5$, in units of r_c). So that the motion of the cloud is clear, the first three frames show $-10 < x < 10$. The final frame shows $10 < x < 30$.

the quasi-isothermal filament has lost almost all its core mass by $t = 1 t_{cs}$, whereas the $M = 10$ adiabatic filament still has a significant amount of its core intact by this point.

Figure 6.10 shows the interaction of a filament with a $M = 1.5$ shock (simulation *m1.5c2l8s*). It can be seen that the interaction is more gentle than that in model *m3c2l8s* in that filament material is not strongly stripped from the filament ends and channelled downstream behind the cloud. Instead, filament material is stripped over a longer time-scale by the flow and the filament core remains reasonably intact for much longer than in simulation *m3c2l8s*. Many more instabilities are present on the surface of the filament throughout the simulation particularly during the early stages, compared to the filament in model *m3c2l8s*. Moreover, the RT fingers located at the filament ends are much more pronounced in the current figure and extend behind the filament rather than upstream of it. Some clumps of filament material are observed to break off the main core from around $t = 2.75 t_{cs}$.

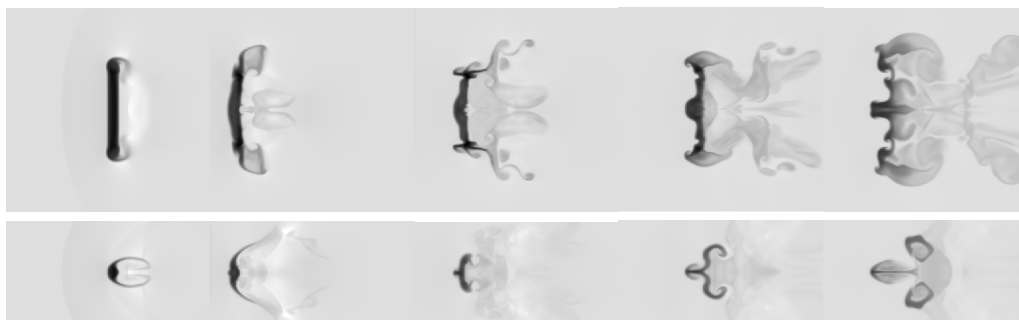


Fig. 6.10 The time evolution of the logarithmic density for model $m1.5c2l8s$ showing the xy (top set of panels) and xz planes (bottom set of panels). The greyscale shows the logarithm of the mass density, from white (lowest density) to black (highest density). The density scale used for this figure extends from 0 to 2.8. The evolution proceeds, left to right, with $t = 0.58t_{cs}$, $t = 1.92t_{cs}$, $t = 2.75t_{cs}$, $t = 3.58t_{cs}$, and $t = 4.35t_{cs}$. All frames show the same region in y and z ($-10 < y < 10$ and $-5 < z < 5$, in units of r_c). So that the motion of the cloud is clear, the first frame shows $-10 < x < 10$. The next three frames show $0 < x < 20$, and the final frame shows $5 < x < 25$.

6.4.4 χ dependence

I now investigate the dependence of the interaction on the filament density contrast. Figure 6.11 shows the effect on the interaction when $\chi = 10^3$. The most obvious contrast between the filament in this simulation and that in $m3c2l8s$ is the thickness of the filament once the transmitted shock has progressed through it. In addition, the filament forms a much more angular shape compared to the previous model. At later times, the filament retains its thin, ‘C’-shaped morphology in the xy plane whilst a considerable density of filament material is present at the rear of the filament forming a long but wide wake. Note that the resolution of this simulation was R_{16} , in contrast with the rest of the simulations.

Figure 6.12 shows the interaction when $\chi = 10$. At $t = 0.74t_{cs}$ the filament is compressed and its filament tips are bent downstream behind the filament, unlike in similar simulations where $\chi = 10^2$ or 10^3 . The bow shock is initially located very close to the filament. However, by $t = 1.56t_{cs}$ it has moved further upstream. Neither this filament nor that in Fig. 6.11 show the three-rolled structure visible in

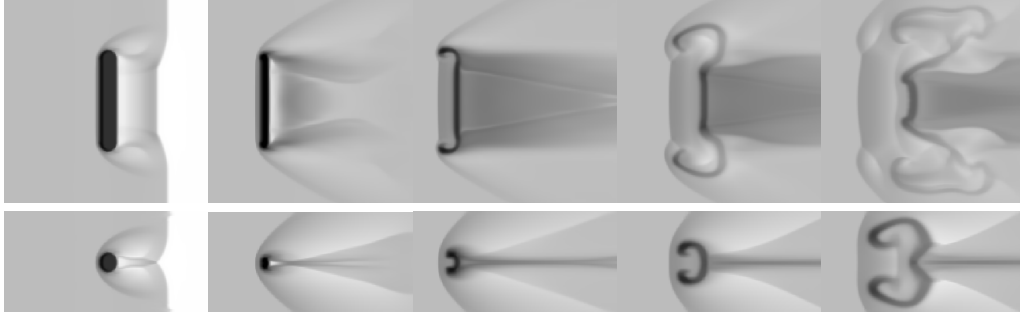


Fig. 6.11 The time evolution of the logarithmic density for model *m3c3l8s* showing the *xy* (top set of panels) and *xz* planes (bottom set of panels). The greyscale shows the logarithm of the mass density, from white (lowest density) to black (highest density). The density scale used for this figure extends from 0 to 3.7. The evolution proceeds, left to right, with $t = 0.10t_{cs}$, $t = 0.29t_{cs}$, $t = 0.87t_{cs}$, $t = 1.15t_{cs}$, and $t = 1.41t_{cs}$. All frames show the same region in *y* and *z* ($-10 < y < 10$ and $-5 < z < 5$, in units of r_c). So that the motion of the cloud is clear, the first frame shows $-10 < x < 10$. Frame 2 shows $-5 < x < 15$, frames 3 and 4 show $0 < x < 20$, and the final frame shows $5 < x < 25$. Note that this simulation was run at a slightly lower resolution of R_{16} .

Fig. 6.2. This result is interesting because the three-rolled structure was seen in the $\chi = 10^3$ simulation presented in figure 24 in [Pittard and Goldsmith \(2016\)](#).

6.4.5 Statistics

I will now explore the evolution of various global quantities of the interaction, starting with the simulations with $M = 3$ and $\chi = 10^2$. I will then consider the Mach- and χ -dependency of the global quantities. Figures 6.13 to 6.16 show the time evolution of these key quantities, whilst Figs 6.19 and 6.20 and Table 6.1 present various time-scales taken from these simulations.

Considering first the evolution of the filament core mass, m_{core} , Fig. 6.13 a) shows the decline in core mass for filaments of differing length with $M = 3$, $\chi = 10^2$, and a sideways orientation. Also shown are the results for a spherical cloud. It can be seen that the time taken for the core mass to be destroyed is very similar for all lengths of filament (circa $t = 7t_{cs}$), though the filament with length $l = 8$ is destroyed slightly faster. Figure 6.13 b), where the filament is orientated at $\theta = 30^\circ$ to the shock front, shows some slight variation, with shorter filaments surviving for slightly longer

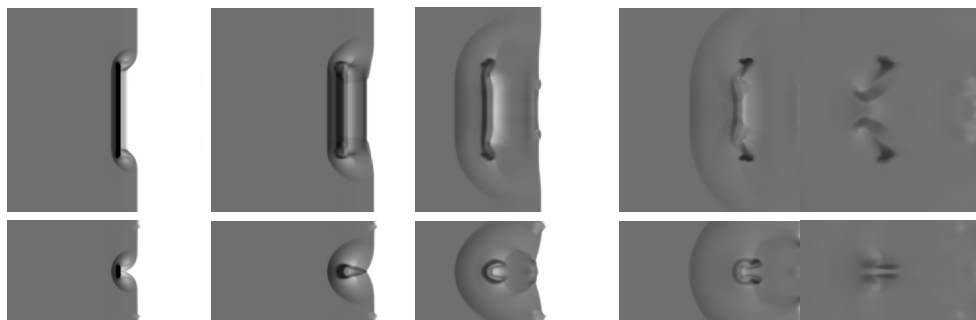


Fig. 6.12 The time evolution of the logarithmic density for model $m3c1l8s$ showing the $x-y$ (top set of panels) and $x-z$ planes (bottom set of panels). The greyscale shows the logarithm of the mass density, from white (lowest density) to black (highest density). The density scale used for this figure extends from 0 to 1.7. The evolution proceeds, left to right, with $t = 0.33t_{cs}$, $t = 1.05t_{cs}$, $t = 1.90t_{cs}$, $t = 2.95t_{cs}$, and $t = 6.28t_{cs}$. All frames show the same region in y and z ($-10 < y < 10$ and $-5 < z < 5$, in units of r_c). So that the motion of the cloud is clear, the first 2 frames show $-10 < x < 10$. Frame 3 shows $0 < x < 20$, frame 4 shows $20 < x < 40$, and the final frame shows $30 < x < 50$.

normalised times than longer ones, though interestingly the spherical cloud mirrors the behaviour of the filament with length $l = 8$, which is odd given the greater mass of the filament compared to the spherical cloud. However, when these two figures are compared with Fig. 6.13 c), which presents filaments with various orientations but a length of $l = 8$, it can be seen that there is much more variety in the rate of mass loss. Filaments aligned more closely to the shock front (i.e. filaments at $\theta = 0^\circ$ and 30°) lose mass much more quickly than those oriented more ‘end-on’ to the shock. Indeed, the filaments with very small angles of orientation have near-identical profiles, in contrast to the results presented in [Pittard and Goldsmith \(2016\)](#). It is interesting to note that my results differ slightly from those in [Pittard and Goldsmith \(2016\)](#), where the filament orientated at $\theta = 60^\circ$ had the slowest degree of mass loss, in that the filament orientated at $\theta = 85^\circ$ took the longest to be destroyed in my work. The spread in the rate of mass loss with orientation angle is also much greater than shown in figure 28 in [Pittard and Goldsmith \(2016\)](#) for filaments with $M = 10$ and $\gamma = 5/3$.

Figure 6.14 shows the time evolution of the x and z centre-of-mass positions of the filament for simulations with $M = 3$ and $\chi = 10^2$. When considering first the x

Isothermal shock-filament interactions

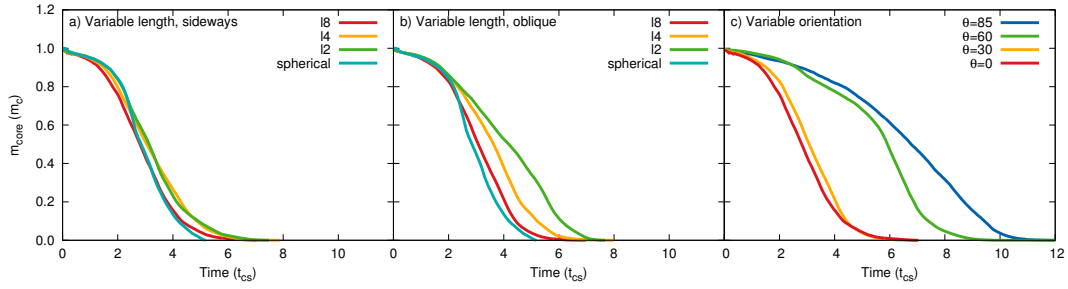


Fig. 6.13 Time evolution of the core mass, m_{core} , normalised to its initial value, for various simulations with $M = 3$ and $\chi = 10^2$. The left-hand panels are for ‘sideways’ simulations, the centre panels are for simulations with $\theta = 30^\circ$, while the right-hand panels are for filaments with $l = 8$.

centre of mass the variation of the results in both panels a) and b) is immediately clear. This shows that filaments of increasing length are accelerated downstream at a much faster velocity than shorter filaments, agreeing with the results presented in [Pittard and Goldsmith \(2016\)](#). However, compared to the results in that paper, the simulations in Fig. 6.14 a) and b) show that the acceleration of all filaments is nearly half as much as rapid again. Some uniformity in filament acceleration/position of the centre of mass is found in panel c), at least in terms of filaments of orientation $\theta \leq 30^\circ$. However, there is also a clear gap between filaments with $\theta = 0 - 30^\circ$ and those with $\theta = 60 - 85^\circ$. This may be because the latter present less of their surface area to the shock front. This also agrees with the results of [Pittard and Goldsmith \(2016\)](#).

Considering the time evolution of the filament centre of mass in the z -direction (Figs 6.14 d-f), no movement of the filament is observed in the z -direction for filaments with a sideways orientation. This is due to the effects of symmetry. When considering panel e), though, it is clear that these filaments are pushed downwards after the shock has overrun them; the filament with length $l = 8$ shows far greater displacement than that with length $l = 2$ because there is more cloud material present to feel the effects of the shock. In comparison with the adiabatic simulations in [Pittard and Goldsmith \(2016\)](#), where the longest filament with an orientation of

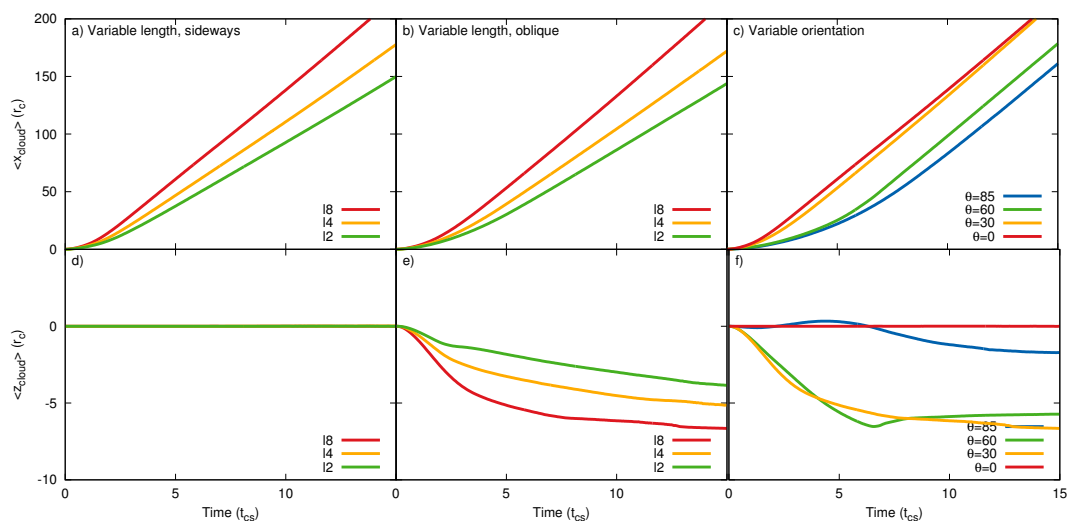


Fig. 6.14 The time evolution of the x and z centre-of-mass position of the filament for various simulations (the same simulations as in Fig. 6.13). The middle panels show simulations with $\theta = 30^\circ$, while the right-hand panels are for filaments with $l = 8$.

$\theta = 30^\circ$ experienced a displacement of up to $10 r_c$ at later times, the filaments in my simulations are displaced by between $3.5 - 6.5 r_c$, and thus experience much less displacement. In Fig. 6.14 f) it can be seen that the orientation of the filament has a much larger impact on the displacement of the filament in the z -direction. In contrast to the results presented in Pittard and Goldsmith (2016), the filament with an orientation of $\theta = 60^\circ$ shows as much displacement as a filament with $\theta = 30^\circ$. However, the uplift observed in the filament orientated at $\theta = 85^\circ$ is similar but this time occurs at around $t \approx 5 t_{cs}$ (as opposed to $t \approx 1 t_{cs}$ in the $M = 10$, $\gamma = 5/3$ case). This filament is also displaced much more in the z direction. There is also much more of a downward push in this panel for filaments orientated at $\theta = 30^\circ$ and $\theta = 60^\circ$ compared to the other two filaments.

The time evolution of the mean filament velocity in the direction of shock propagation is shown in Fig. 6.15 a) to c). All panels show that the asymptotic velocity reached by the filaments is very similar, though there is some variation within this in that longer filaments accelerate faster than spherical clouds. The asymptotic velocity is reached by $t \approx 5 t_{cs}$ in the first two panels. Filaments which are sideways

Isothermal shock-filament interactions

to the shock front or orientated at $\theta = 30^\circ$ have near identical acceleration, though again there is some variation according to filament length with shorter filaments accelerated more slowly than longer ones. Moreover, the spherical cloud is shown to accelerate faster than the filaments between $t \approx 2 - 3 t_{cs}$. When the filament length $l = 8$ and the filament orientation is varied there is much greater variance in filament acceleration and a clear split is observed between filaments with small angles of orientation and those with large angles of orientation; the latter are accelerated up to the ambient flow velocity at a much slower rate whilst the sideways filament shows the fastest acceleration. This split is far less pronounced when $M = 10$ and $\gamma = 5/3$ (cf. figure 30 in (Pittard and Goldsmith, 2016)).

In terms of the mean velocity perpendicular to the direction of shock propagation, Fig. 6.15 d) shows no movement for filaments oriented sideways to the shock (cf. with Pittard and Goldsmith (2016) where there was slight oscillation about zero v_b). However, for obliquely-oriented filaments and filaments with $l = 8$ and variable orientations there is considerable variety (panels e and f, respectively). When the filament orientation is $\theta = 30^\circ$ (panel e), the maximum velocity increases with increasing filament length (with the filament with $l = 8$ attaining a maximum absolute velocity of almost $+0.1v_b$) owing to the fragmentation of the filament core in the transverse direction. This maximum velocity soon drops back to zero again for all filaments once the filament core has been ablated by the flow and is unable to significantly fragment any further. However, in panel f) the picture is much more complex. The filament orientated at $\theta = 85^\circ$ shows a small net positive velocity but then oscillates between negative and zero z -velocities until reaching an equilibrium at zero. Meanwhile, the filament with $\theta = 30^\circ$ exhibits the greatest negative z -velocity (reaching $v_z \approx -0.08v_b$), in agreement with the comparable filament in Pittard and Goldsmith (2016) (cf. with their figure 30).

Figure 6.16 shows the filament velocity dispersion in each direction. There is reasonable agreement between the simulations when the cloud is orientated sideways

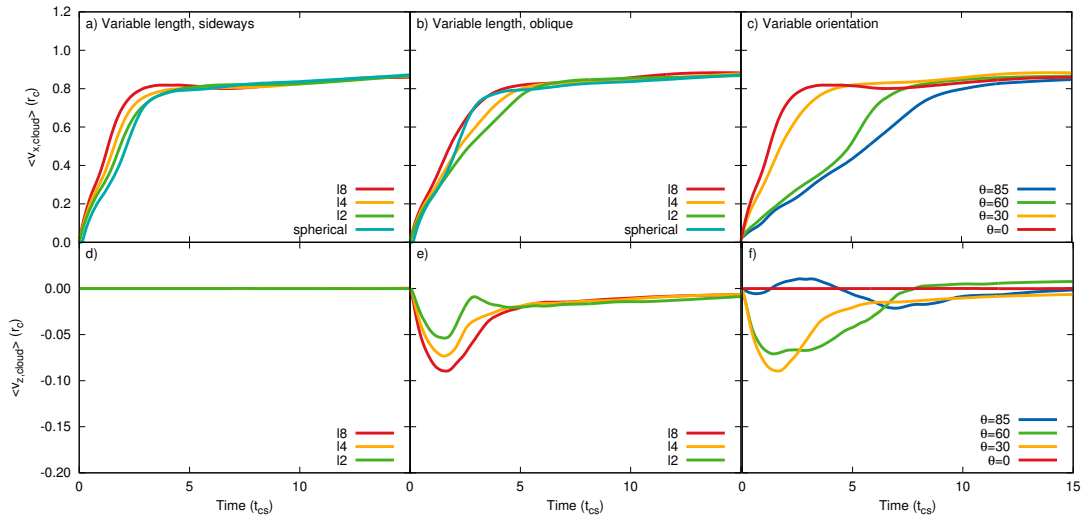


Fig. 6.15 As Fig. 6.13 but showing the time evolution of the filament mean velocity in the direction of shock propagation ($\langle v_{x,cloud} \rangle$) and in the z -direction ($\langle v_{z,cloud} \rangle$). The middle panels again show simulations with $\theta = 30^\circ$, while the right-hand panels are for filaments with $l = 8$.

or obliquely to the shock, and the maximum peak velocity distribution is almost homogenous with a peak at between 0.06 and $0.17 v_b$. In contrast, panels c), f), and i) show much greater variance in the velocity distribution in all directions and far less uniformity. The greatest maximum velocity distribution is in $\delta v_{x,cloud}$ where the filament oriented $\theta = 60^\circ$ to the shock normal reaches just over $0.20 v_b$. Compared to figure 31 in Pittard and Goldsmith (2016), panels f) and i) have much more variation between the models, with the filaments oriented $\theta = 30^\circ$ and $\theta = 0^\circ$ achieving peak velocity dispersion in the y - and z -directions at earlier times.

The Mach dependence of m_{core} , $\langle v_{x,cloud} \rangle$, and $\langle x_{cloud} \rangle$ for filaments with $l = 8 r_c$ and oriented sideways to the shock front is now investigated. Figure 6.17 shows these global quantities for simulations with $\chi = 10$ and 10^2 . In line with Pittard and Goldsmith (2016) I find that m_{core} declines much more slowly as M is reduced (with filaments in simulations with $M = 10$ declining extremely rapidly in $< t_{cs}$, in contrast to the aforementioned paper and also in contrast to the findings of Nakamura et al. (2006) with respect to their two simulations where $\gamma = 1.1$), and that the acceleration and centre of mass position of the filament, as evidenced by $\langle v_{x,cloud} \rangle$ and $\langle x_{cloud} \rangle$,

Isothermal shock-filament interactions

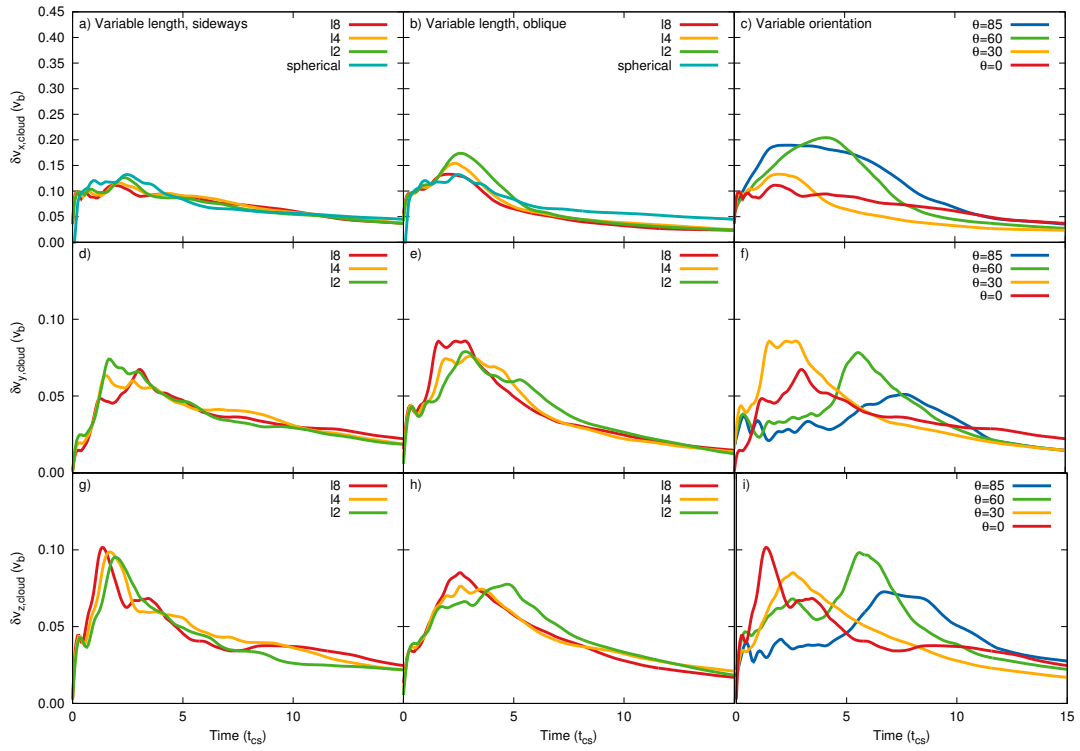


Fig. 6.16 As Fig. 6.13 but showing the time evolution of the filament velocity dispersion in each direction. The middle panels again show simulations with $\theta = 30^\circ$, while the right-hand panels are for filaments with $l = 8$.

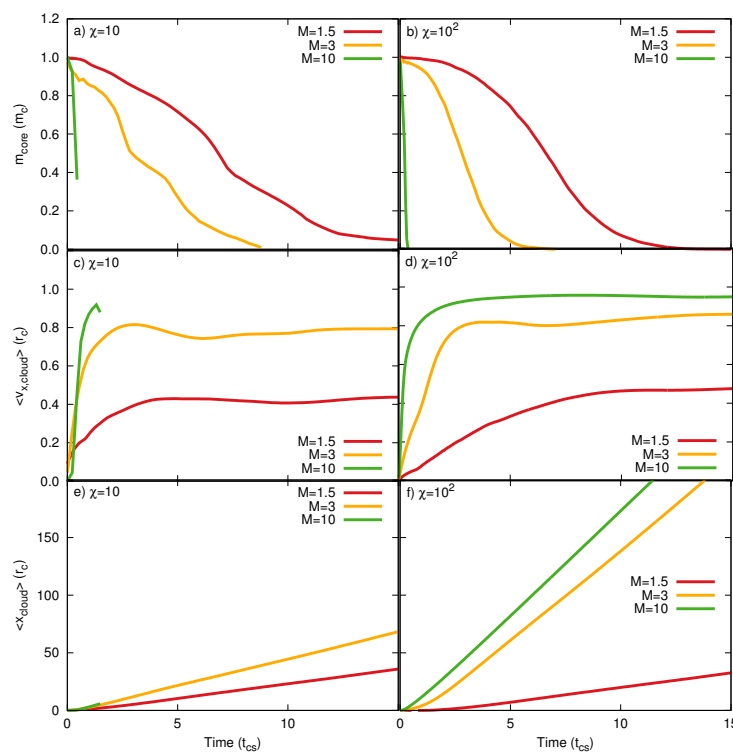


Fig. 6.17 The Mach number dependence of the evolution of m_{core} , $\langle v_{x,\text{cloud}} \rangle$, and $\langle x_{\text{cloud}} \rangle$, for filaments with $l = 8 r_c$ and oriented sideways to the shock front.

both reduce as M decreases. Panel f) shows that the filament centre of mass is moved downstream slightly more slowly when $M = 3$ compared to when $M = 10$, though there is a clear difference between these two filaments and that when $M = 1.5$, where the centre of mass is extremely slow to move downstream.

Figure 6.18 shows the χ dependence of m_{core} , $\langle v_{x,\text{cloud}} \rangle$, and $\langle x_{\text{cloud}} \rangle$ for simulations with $M = 3$ and filaments with $l = 8 r_c$ and oriented sideways to the shock.

In terms of $\langle v_{x,\text{cloud}} \rangle$ (panel b) of Fig. 6.18) the lower χ filament experiences a faster acceleration up to the asymptotic velocity of the flow but, in comparison with the other two filaments which show very similar profiles, its velocity then drops below the asymptotic value before very slowly climbing back up again. Filaments with a lower density contrast are also slower to lose mass compared to those with a higher density contrast. Panel c) shows great variation between all filaments in the movement of the filament centre of mass downstream. When $\chi = 10^3$ the filament

Isothermal shock-filament interactions

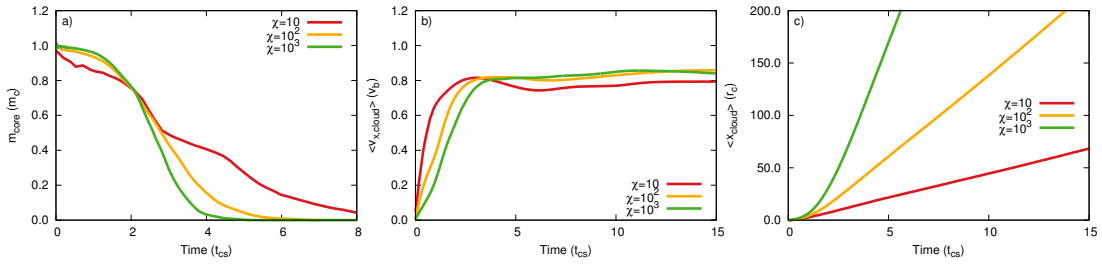


Fig. 6.18 The χ dependence of the evolution of m_{core} , $\langle v_{x,\text{cloud}} \rangle$, and $\langle x_{\text{cloud}} \rangle$, for $M = 3$ and filaments with $l = 8 r_c$ and oriented sideways to the shock front.

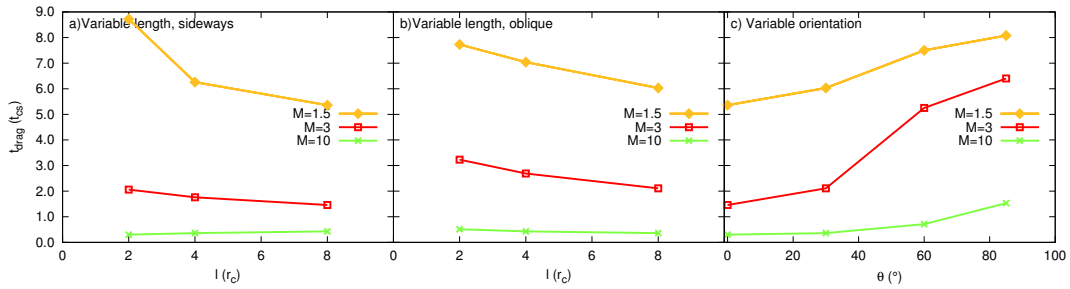


Fig. 6.19 t_{drag} as a function of the filament length (left-hand and middle panels) and orientation (right-hand panel), from simulations with varying Mach number and $\chi = 10^2$. The ‘oblique’ simulation results noted in the middle panel are for $\theta = 30^{\circ}$, while the right-hand panel is for filaments with $l = 8$.

experiences a rapid acceleration of its centre of mass, whereas that when $\chi = 10$ is far slower to move downstream (normalised to t_{cs}). Again, this figure compares well to figure 33 in [Pittard and Goldsmith \(2016\)](#).

6.4.5.1 Time-scales

Figures 6.19 and 6.20 show values of t_{drag} and t_{mix} , respectively, for simulations with $M = 1.5$, $M = 3$, and $M = 10$ and $\chi = 10^2$, as a function of both the filament length and orientation. Panel a) of each figure shows values taken from simulations where the filament is oriented sideways to the shock front and where the filament length is varied. Panel b) of each figure shows values taken from simulations where the filament is oriented obliquely (i.e. at $\theta = 30^{\circ}$) and the length varied. Panel c) shows values taken from simulations where the filament has length $l = 8$ but its angle

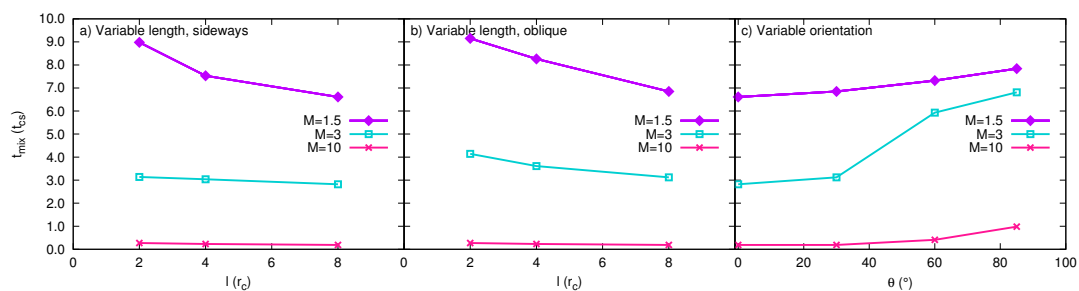


Fig. 6.20 t_{mix} as a function of the filament length (left-hand and middle panels) and orientation (right-hand panel), from simulations with varying Mach number and $\chi = 10^2$. The ‘oblique’ simulation results noted in the middle panel are for $\theta = 30^\circ$, while the right-hand panel is for filaments with $l = 8$.

of orientation is varied. Values for both time-scales (along with the filament lifetime) are also noted in Table 6.1.

Figure 6.19 a) and b) shows that filaments in quasi-isothermal simulations with $M = 3$ and $M = 10$ have smaller values of t_{drag} compared to those in the adiabatic $M = 10$ simulations presented in Pittard and Goldsmith (2016), indicating that filaments in the former simulations are accelerated at a faster rate. However, when the Mach number is 1.5 in the quasi-isothermal simulations the values of t_{drag} much greater. There is also a trend in both sets of results for t_{drag} to decrease as the filament length increases, though this effect is most visible in the $M = 1.5$ quasi-isothermal simulations. Filaments orientated at $\theta = 30^\circ$ to an $M = 3$ shock front show a clear difference to those oriented sideways, with the latter showing greater acceleration than the former. However, those in simulations with $M = 10$ and $M = 1.5$ are broadly similar. Panel c) shows that t_{drag} increases with increasing angle of orientation for simulations with $M = 1.5$ and $M = 3$ until $\theta = 60^\circ$ when it begins to tail off broadly in line with the results presented in Pittard and Goldsmith (2016). However, the results for simulations with $M = 10$ do not exhibit such a tailing-off. It is clear that filaments in simulations where $M = 10$ have very rapid acceleration regardless of the orientation or length of the filament, with the exception of filaments oriented at

$\theta = 60^\circ$ and $\theta = 85^\circ$, though even these results are significantly different to those where the Mach number is different.

Figure 6.20 a) and b) shows a general trend for t_{mix} to decrease with increasing filament length for sideways and oblique filaments in simulations where $M = 1.5$ and $M = 3$. Sideways-orientated filaments experience mixing of core material on a slightly shorter time-scale compared to obliquely-orientated filaments but there is less variation in the results, indicating that the length of the sideways filaments is of less importance for t_{mix} compared to when the filament has an orientation of $\theta = 30^\circ$. Panel c) shows that t_{mix} increases with the angle of orientation, though it shows far less of a reduction when the filament is oriented at $\theta = 85^\circ$ compared to the adiabatic results (see figure 34 in [Pittard and Goldsmith \(2016\)](#)). In this panel the $M = 3$ simulations show far more variety in mixing times compared to simulations with different Mach numbers. It is noticeable that the mixing times of filaments in simulations with $M = 10$ are far more linear and the values extremely low, indicating that neither filament length nor an orientation at an oblique angle are important for the mixing time, but that the filament core is mixed very rapidly. It is only as the angle of orientation of the filament becomes $\theta > 30^\circ$ that there is any increase in t_{mix} for these filaments.

6.5 Discussion

Isothermal filaments, and particularly their fragmentation, have been well studied on a theoretical basis in previous years. However, such studies have tended to assume an isothermal filament of infinite length, which is unrealistic. The assumption of isothermality on its own, however, may be reasonable under certain circumstances. For example, [Heigl et al. \(2016\)](#) discuss the use of isothermality as a valid approach in the case of the L1517 dark cloud in Taurus which contains filamentary structure punctuated by dense cores. In this case, the density profiles appear to match the

isothermal profile and the profile of three of the four studied filaments could be reproduced by that of an isothermal cylinder. In contrast, [Hosseinirad et al. \(2018\)](#) found that more recent observations of filamentary molecular clouds indicate filament properties which deviate from those described by an isothermal equation of state. They therefore compared the gravitational instability of a filamentary molecular cloud under both isothermal and softer non-isothermal equations of state and found that the filament was more unstable with the latter equation of state. In addition, [Di Cintio et al. \(2018\)](#) found that although earlier observations of filaments showed density profiles consistent with those of an isothermal cylinder, more recent observations are again better described by power laws even softer than the isothermal case; thus, such filaments can be considered to have a non-thermal state (see also [Toci and Galli \(2015\)](#)). The use of an isothermal cylinder was first proposed by [Ostriker \(1964\)](#); however, this may no longer be a reasonable approach when studying the fragmentation of filaments ([Chira et al., 2018](#)). The filaments in the current chapter deviate from the constraints of an isothermal cylinder since they have quantifiable lengths and rounded ends; thus some of the caution exercised by the above studies may be relaxed in my case. Moreover, although my study was intended to represent an idealised scenario rather than one directly comparable to specific cases through the use of an isothermal equation of state, the findings of [Heigl et al. \(2016\)](#) are encouraging when considering the relevance of my work to observations.

Apart from those numerical studies noted in Tables 1.1 and 1.2 in Chapter 1, there have been very few numerical studies of shock-filament/wind-filament interactions in the literature in the last couple of years. Studies which have been published tend to include MHD and self-gravity, neither of which are pertinent to the current research in this chapter, and are specific to particular astrophysical environments. Other studies include cloud-cloud collisions which lead to filament formation ([Inoue et al., 2018](#)) and wind-cloud interactions which evolve to form filaments ([Banda-Barragán et al., 2018](#)). There are, to my knowledge, no other recent scale-free numerical

studies which have investigated the evolution of a filament interacting with either a shock or a wind. This, therefore, precludes any detailed comparison with my work.

6.6 Summary and Conclusions

In this chapter, I investigated the hydrodynamic interaction of a quasi-isothermal shock with a filament in a non-magnetised medium. This work extends the work previously presented in [Pittard and Goldsmith \(2016\)](#) into an isothermal regime where $\gamma = 1.01$, and complements the MHD adiabatic shock-filament results presented in Chapter 3. I performed 3D calculations in which I varied the filament length and angle of orientation to the shock front and I investigated the nature of the interaction when the shock Mach number or cloud density contrast were varied. My focus was on the interaction of a Mach 3 shock with a filament since this was a more realistic case for an isothermal shock than a Mach 10 shock. Although this chapter is a work in progress, the following main conclusions can be noted.

i) Only sideways-oriented filaments with $\chi = 10^2$ form a three-rolled structure, dissimilar to the findings of [Pittard and Goldsmith \(2016\)](#). Filaments oriented at other angles to the shock front instead form elongated structures with turbulent wakes and their morphology is dominated by the formation of a vortex ring at the upstream edge of the filament, whilst filaments with different values of χ are bent into a ‘C’ shape;

ii) The greater the angle of orientation, the longer and less turbulent the wake, with the filament core in model *m3c2l885* becoming highly elongated and remaining relatively intact for some considerable time. Such filaments do not spill turbulent core material from their upper edge but rather lose material smoothly from the filament edges;

iii) Most filaments showed a tendency for turbulent stripping of cloud material and the loss of clumps of material to the flow during the initial stages of the

interaction. However, the filament oriented at $\theta = 85^\circ$ shows no such tendency towards fragmentation in the early stages (up until at least $t \approx 3t_{cs}$), thus indicating the longer-lived nature of this filament;

iv) I find that filament length is not important for mass loss when the filament is oriented sideways. However, there is a clear differentiation when the angle of orientation is varied, with those filaments oriented at angles $\theta \geq 60^\circ$ much slower to lose mass than those with smaller angles of orientation. This split between small and large angles of orientation is also evident in the movement of the core centre of mass in the x direction and in the average velocity in the x direction;

v) Values of t_{drag} for sideways and oblique filaments decline as the filament length increases. Filaments in a quasi-isothermal interaction have smaller values of t_{drag} (i.e. are accelerated faster) than filaments in an adiabatic interaction. Moreover, considering only the filaments struck by a quasi-isothermal shock, sideways filaments are accelerated much faster than obliquely oriented ones. When the filament angle of orientation is varied, t_{drag} increases as the angle is increased, until the value of t_{drag} begins to plateau, indicating the possible beginning of Mach scaling. t_{mix} shows similar results to the above;

vi) The normalised evolution of the filament becomes significantly more rapid at high Mach numbers ($M = 10$) and there is far more variation with Mach number compared to adiabatic simulations.

As noted above, the work contained in this chapter is ongoing and is therefore a work in progress. Future work should therefore include much more detailed discussion of these results as well as a dedicated 3D MHD study of an isothermal shock striking a filament.

Chapter 7

Conclusions

7.1 Summary

The work presented in this thesis has added to the body of literature on shock-cloud/shock-filament and wind-cloud interactions and has furthered our understanding of such interactions in three main ways: 1) it has pinpointed the most favourable conditions for the survival of filaments in a magnetised medium; 2) it has highlighted discrepancies between shock-cloud and wind-cloud simulations; and 3) it has noted the huge variation in filament evolution between high and low Mach numbers in isothermal simulations. I summarise below the main results from my work, followed by a brief discussion of potential future work and some concluding remarks.

In Chapter 3 I investigated the interaction between a filament embedded within a magnetised medium and a shock wave and used a large parameter space to explore the various conditions that would influence the evolution and destruction of the filament. I found that the orientation of the magnetic field (parallel or perpendicular) to the shock normal has a major impact on the interaction, though (as also noted in [van Loo et al. \(2010\)](#)) the field orientated at 45° to the shock leads to behaviour similar to that produced by the perpendicular field. A parallel field allows the field lines to penetrate into the filament, hastening its destruction, whilst perpendicular

field lines are dragged around the leading edge of the filament, shielding it from the full effects of the post-shock flow and allowing the flow to move along the field lines. Secondary to the orientation of the field, the orientation of the filament itself to the shock front has a large effect on the interaction. However, changes to the aspect ratio of the filament are less important in terms of the filament mass-loss rate, unless the aspect ratio is very small, in which case the filament begins to resemble a spherical cloud.

In a parallel field, filaments orientated ‘end on’ (or at $\theta = 90^\circ$) to the shock front are destroyed more quickly than those oriented ‘broadside’ ($\theta = 0^\circ$), though the filament lifetime remains greater than that of the hydrodynamical case due to the action of the field lines in resisting the compression of the filament by the converging flow. However, only end on filaments develop significant, well-defined linear structures (‘flux ropes’) on the downstream axis; this is caused by compression of the field lines at this point which increases the magnetic pressure and prevents the post-shock flow from entering the area. Varying the cloud density contrast between the filament and the surrounding medium influences the lifetime of the filament. High density contrasts lead to the rapid destruction of the cloud through the formation of turbulent instabilities on the filament edge which help to tear it apart, subsequently mass-loading the flow with cloud material. The increase in the density contrast is, therefore, linked to the growth of hydrodynamic instabilities in the parallel field case. Low Mach numbers (i.e. a milder shock) can prevent the filament from being destroyed, and the filament retains its initial morphology over a long time-scale. Thus, the lower the Mach number, the longer the filament lifetime. In terms of the acceleration of the filament to the velocity of the post-shock flow, filaments orientated broadside to the shock front are initially accelerated faster than those orientated more end on due to the greater surface area presented to the shock front. In addition, filaments orientated at $\theta = 30^\circ$ and 90° overshoot and then decelerate to the value of the post-shock flow velocity, possibly due to the release of

Conclusions

built-up tension in the field lines. Finally, filaments in a parallel field are compressed into a disc-like shape when observed in 3D.

A perpendicular (or oblique, 45°) field is more conducive to extending the lifetime of the filament since the field lines wrap themselves around the leading edge of the filament and reduce the penetration of the post-shock flow into the cloud. The snapping back of the field lines as they release tension, as well as the build up in magnetic pressure on the upstream side of the filament, allows filaments in such field orientations to be more rapidly accelerated to the post-shock flow velocity. Moreover, filaments in these fields remain at a higher density for longer and are drawn into long, smooth tendrils. However, flux ropes do not form behind end on clouds in these field orientations, in agreement with earlier studies. Unusually, the filament orientated broadside to the shock front is bent into a ‘C’ shape when viewed in the xz plane, with the ends of the ‘C’ unusually facing back upstream. This may have implications with respect to interpretation of the data from an observational point of view as it suggests that the filament may have been struck from its rear side, rather than the upstream side as in my work. Unlike in the parallel field case, increasing the cloud density contrast does not lead to the rapid destruction of the cloud. Conversely, it provides more favourable conditions for the damping of the formation of turbulent instabilities on the filament’s surface, allowing the filament to be stretched downstream and survive for a considerable time. Dissimilar to the parallel field case, filaments in a perpendicular or oblique field are compressed into a sheet-like shape in 3D. As before, a low shock Mach number significantly prolongs the lifetime of the filament.

Given the above, the conditions that best extend the lifetime of a filament embedded in a magnetised medium are a combination of a mild shock (e.g. of Mach number = 1.5), a filament orientation of $\theta = 45^\circ$ to the shock front, and a strong magnetic field with a perpendicular or oblique orientation. These conditions can lead to the indefinite survival of the cloud.

In Chapters 4 and 5, I conducted a 2D comparison of shock-cloud and wind-cloud simulations using a spherical cloud in a non-magnetised medium. My motivation was to explore the degree to which wind-cloud studies could be described as a particular case of the shock-cloud problem where the cloud is embedded in a post-shock flow without the initial shock. A comparison of both types of interaction using a cloud density contrast of 10 revealed there to be significant morphological differences between the two interactions. Firstly, clouds embedded in a mildly supersonic wind form lower density, low-pressure regions on their downstream axis formed by the initial motion of the wind removing gas from behind the cloud - a feature not observed in shock-cloud simulations. Secondly, clouds interacting with winds also undergo less compression in the axial direction during the initial stages of the interaction than equivalent clouds that are struck by a shock. The cloud in the wind-cloud case retains a more rounded shape compared to the cloud in the shock-cloud case which forms an oblate spheroid. This contrast is due to the different ways that the flow is diffracted around the cloud in each case. Finally, there are large differences in the manner in which the shock that is transmitted through the cloud behaves. In the shock-cloud case, the transmitted shock is much flatter than that in the wind-cloud case. Increases to the effective Mach number of the wind (M_{wind}) lead to further morphological differences not only between the shock-cloud simulation but also among the wind-cloud simulations themselves. As M_{wind} increases, the region of low pressure behind the cloud in the low-Mach-number wind-cloud case becomes a highly supersonic cavity and expands rapidly in the direction of wind propagation, elongating as it does so. Moreover, the density jump just behind the bow shock increases towards the high Mach number limit and the stand-off distance between the bow shock and the leading edge of the cloud decreases, leading to a reduction in the normalised velocity of the shocked gas around the cloud's flanks due to the higher compression at the bow shock and reducing the growth of KH instabilities.

Conclusions

Remaining with the $\chi = 10$ simulations, differences between the two interaction types are also evident from the statistics. For example, as M_{wind} increases, the cloud mixing time also increases up to the high Mach number limit (i.e. $M_{\text{wind}} \gtrsim 10$), which is in contrast to the results of a previous shock-cloud study and is due to the less effective stripping of cloud material by the flow. In addition, clouds embedded in winds with high M_{wind} survived for much longer and travelled over greater distances (up to $47 r_c$ for the highest M_{wind} simulation by the time the core mass had reduced by half) than previous wind-cloud studies had shown. My work is also the first to display Mach scaling in the high Mach number limit for a wind-cloud simulation. For example, I found that the density jump asymptotes to 4.0 for $\gamma = 5/3$, whilst the stand-off distance between the bow shock and the cloud centre asymptotes to $1.28 r_c$.

When χ is increased to 10^3 , only minor morphological differences are noted between the low M_{wind} wind-cloud and shock-cloud simulations whilst the transmitted shock progresses through the cloud, in contrast to the above. However, once the shock has exited the rear of the cloud a long, low-density turbulent wake is formed in both cases, though whilst the cloud core in the case of the shock remains relatively intact and is drawn out along the $r = 0$ axis, that in the case of the wind fragments in all directions, mass-loading the flow, and the evolution of the turbulent wake is severely disrupted. As M_{wind} increases, a smooth, thin tail of cloud material drawn from the rear and side of the core forms in the wind-cloud case, dissimilar to the turbulent wake created in the shock-cloud case. However, this tail is short-lived. When the statistics are taken into account, it is found that high-density clouds are capable of being moved many 100s of r_c downstream of the original cloud position, in contrast to previous wind-cloud studies, due to their large reservoir of mass which is able to generate longer-lived structures. Moreover, the normalised cloud lifetime is found to increase with increasing M_{wind} . However, in contrast to the findings of Chapter 4, the normalised cloud mixing time is shorter at higher values of χ . Moreover, there is no clear evidence of Mach number dependence for either the mixing time or the

cloud drag time. Interestingly, these two time-scales for comparable shock-cloud simulations that do show a Mach number dependence appear to converge towards the Mach number-independent wind-cloud time-scales as the Mach number is increased.

Chapter 6 presented the results of 3D isothermal shock-filament interactions in a non-magnetised medium. As with the MHD simulations presented in Chapter 3 I was able to vary a large number of parameters pertaining to the filament and surrounding flow/shock. The main (and most surprising) result is that the evolution (normalised to t_{cs}) of sideways-oriented filaments with length $l = 8$ is significantly more rapid at high Mach numbers ($M = 10$), with the filament core mass almost completely destroyed by $t \approx 1 t_{cs}$. This contrasts with the behaviour of comparable filaments in previous adiabatic simulations and contradicts the results of previous shock-cloud simulations where $\gamma = 1.1$ for the cloud. This behaviour arises from the greater interaction between the shock and the filament caused by an increase in the density jump of the shock in isothermal simulations. The χ dependence of the interaction for filaments with $l = 8$ and $M = 3$ shows that only filaments with $\chi = 10^2$ form the three-rolled structure seen in [Pittard and Goldsmith \(2016\)](#). Moreover, when the angle of orientation of the filament's major axis to the shock front is varied, filaments which are created at an oblique angle to the shock form instead a long and turbulent wake on their downstream edge, with clumps of core material breaking away from the flow of material originating from the filament ends. However, as the filament orientation becomes more 'end on' to the shock front, the wake becomes much more smooth and the core longer-lived. I find that values of t_{drag} and t_{mix} for sideways and oblique filaments with $M = 3$ decline as the filament length increases. Filaments in an isothermal interaction have smaller values of t_{drag} (i.e. are accelerated faster) and t_{mix} than filaments in an adiabatic interaction. When the filament angle of orientation is varied, t_{drag} and t_{mix} increase as the angle is increased (i.e. the filament becomes more 'end-on').

7.2 Future work

The work presented in Chapters 3 and 6 provides a relatively comprehensive study of shock-filament interactions. However, although I included the approximated effects of radiative cooling using a softened equation of state in an HD shock-filament study, inclusion of an isothermal MHD study in the literature would be of great interest, particularly since the effects of an isothermal MHD wind-cloud interaction leading to the formation of a filament have previously been explored ([Banda-Barragán et al., 2016](#)). Given that Chapter 6 showed that an isothermal interaction leads to more rapid destruction of the cloud as the Mach number is increased it would be of interest to explore this effect in a more detailed study.

Although the simulations presented in Chapters 3 and 6 were performed in 3D, those in Chapters 4 and 5 were instead performed in 2D. A 3D study would, however, provide greater realism for simulations extending for many cloud-crushing times (t_{cc}) (particularly since a previous study noted the presence of some differences between 2D and 3D simulations after about $3.66t_{cc}$). In addition, a number of previous wind-cloud studies have included radiative cooling models and have noted the strong effect such models have on the results. Therefore, the inclusion of radiative losses in the calculations in the above two chapters would again render the simulations more realistic.

Although scale-free, the above idealised studies are of great use in isolating the effects of specific processes on the interaction. However, closer comparison with observations would also be of use. In particular, the production of synthetic simulations of observational data relating to filaments would give a more complete picture of filament formation and evolution in the ISM.

7.3 Concluding remarks

This thesis presents the first simulations of a shock-filament interaction in both magnetised and isothermal media. Moreover, it presents the first comparison between shock-cloud and wind-cloud studies. The simulations are intentionally simplified and scale-free and, as such, are unable to be directly compared to observations. Nonetheless, I believe that the results presented in this thesis will help to further our understanding of the processes driving and shaping the interstellar medium and will lay the ground-work for future, complex studies.

References

- Abramson, A. and Kenney, J. D. P. (2014). Hubble Space Telescope Imaging of Decoupled Dust Clouds in the Ram Pressure Stripped Virgo Spirals NGC 4402 and NGC 4522. *AJ*, 147:63.
- Alūzas, R., Pittard, J. M., Falle, S. A. E. G., and Hartquist, T. W. (2014). Numerical simulations of a shock interacting with multiple magnetized clouds. *MNRAS*, 444:971–993.
- Alūzas, R., Pittard, J. M., Hartquist, T. W., Falle, S. A. E. G., and Langton, R. (2012). Numerical simulations of shocks encountering clumpy regions. *MNRAS*, 425:2212–2227.
- Alfvén, H. (1942). Remarks on the Rotation of a Magnetized Sphere with Application to Solar Rotation. *Arkiv for Astronomi*, 28:1–9.
- Allen, D. A. and Burton, M. G. (1993). Explosive ejection of matter associated with star formation in the Orion nebula. *Nature*, 363:54–56.
- André, P., Di Francesco, J., Ward-Thompson, D., Inutsuka, S.-I., Pudritz, R. E., and Pineda, J. E. (2014). From Filamentary Networks to Dense Cores in Molecular Clouds: Toward a New Paradigm for Star Formation. *Protostars and Planets VI*, pages 27–51.
- André, P., Men’shchikov, A., Bontemps, S., Könyves, V., Motte, F., Schneider, N., Didelon, P., Minier, V., Saraceno, P., Ward-Thompson, D., di Francesco, J., White, G., Molinari, S., Testi, L., Abergel, A., Griffin, M., Henning, T., Royer, P., Merín, B., Vavrek, R., Attard, M., Arzoumanian, D., Wilson, C. D., Ade, P., Aussel, H., Baluteau, J.-P., Benedettini, M., Bernard, J.-P., Blommaert, J. A. D. L., Cambrésy, L., Cox, P., di Giorgio, A., Hargrave, P., Hennemann, M., Huang, M., Kirk, J., Krause, O., Launhardt, R., Leeks, S., Le Penec, J., Li, J. Z., Martin, P. G., Maury, A., Olofsson, G., Omont, A., Peretto, N., Pezzuto, S., Prusti, T., Roussel, H., Russeil, D., Sauvage, M., Sibthorpe, B., Sicilia-Aguilar, A., Spinoglio, L., Waelkens, C., Woodcraft, A., and Zavagno, A. (2010). From filamentary clouds to prestellar cores to the stellar IMF: Initial highlights from the Herschel Gould Belt Survey. *A&A*, 518:L102.
- Arzoumanian, D., André, P., Didelon, P., Könyves, V., Schneider, N., Men’shchikov, A., Sousbie, T., Zavagno, A., Bontemps, S., di Francesco, J., Griffin, M., Hennemann, M., Hill, T., Kirk, J., Martin, P., Minier, V., Molinari, S., Motte, F., Peretto, N., Pezzuto, S., Spinoglio, L., Ward-Thompson, D., White, G., and Wilson, C. D. (2011). Characterizing interstellar filaments with Herschel in IC 5146. *A&A*, 529:L6.

- Baade, W. and Minkowski, R. (1954). Identification of the Radio Sources in Cassiopeia, Cygnus A, and Puppis A. *ApJ*, 119:206.
- Ballesteros-Paredes, J. and Hartmann, L. (2007). Remarks on Rapid vs. Slow Star Formation. *Rev. Mexicana Astron. Astrofis.*, 43:123–136.
- Ballesteros-Paredes, J. and Mac Low, M.-M. (2002). Physical versus Observational Properties of Clouds in Turbulent Molecular Cloud Models. *ApJ*, 570:734–748.
- Banda-Barragán, W. E., Federrath, C., Crocker, R. M., and Bicknell, G. V. (2018). Filament formation in wind-cloud interactions- II. Clouds with turbulent density, velocity, and magnetic fields. *MNRAS*, 473:3454–3489.
- Banda-Barragán, W. E., Parkin, E. R., Federrath, C., Crocker, R. M., and Bicknell, G. V. (2016). Filament formation in wind-cloud interactions - I. Spherical clouds in uniform magnetic fields. *MNRAS*, 455:1309–1333.
- Banerjee, R., Vázquez-Semadeni, E., Hennebelle, P., and Klessen, R. S. (2009). Clump morphology and evolution in MHD simulations of molecular cloud formation. *MNRAS*, 398:1082–1092.
- Barnes, J. E., Wood, K., Hill, A. S., and Haffner, L. M. (2014). Photoionization and heating of a supernova-driven turbulent interstellar medium. *MNRAS*, 440:3027–3035.
- Benedettini, M., Schisano, E., Pezzuto, S., Elia, D., André, P., Könyves, V., Schneider, N., Tremblin, P., Arzoumanian, D., di Giorgio, A. M., Di Francesco, J., Hill, T., Molinari, S., Motte, F., Nguyen-Luong, Q., Palmeirim, P., Rivera-Ingraham, A., Roy, A., Rygl, K. L. J., Spinoglio, L., Ward-Thompson, D., and White, G. J. (2015). Filaments in the Lupus molecular clouds. *MNRAS*, 453:2036–2049.
- Benjamin, R. A., Churchwell, E., Babler, B. L., Bania, T. M., Clemens, D. P., Cohen, M., Dickey, J. M., Indebetouw, R., Jackson, J. M., Kobulnicky, H. A., Lazarian, A., Marston, A. P., Mathis, J. S., Meade, M. R., Seager, S., Stolovy, S. R., Watson, C., Whitney, B. A., Wolff, M. J., and Wolfire, M. G. (2003). GLIMPSE. I. An SIRTf Legacy Project to Map the Inner Galaxy. *PASP*, 115:953–964.
- Bergeron, J. (1986). The MG II absorption system in the QSO PKS 2128-12 - A galaxy disc/halo with a radius of 65 KPC. *A&A*, 155:L8–L11.
- Blitz, L. and Stark, A. A. (1986). Detection of clump and interclump gas in the Rosette Molecular Cloud Complex. *ApJ*, 300:L89–L93.
- Bohlin, R. C. (1975). Copernicus observations of interstellar absorption at Lyman alpha. *ApJ*, 200:402–414.
- Bolatto, A. D., Warren, S. R., Leroy, A. K., Walter, F., Veilleux, S., Ostriker, E. C., Ott, J., Zwaan, M., Fisher, D. B., Weiss, A., Rosolowsky, E., and Hodge, J. (2013). Suppression of star formation in the galaxy NGC 253 by a starburst-driven molecular wind. *Nature*, 499:450–453.
- Brackbill, J. U. and Barnes, D. C. (1980). The effect of nonzero product of magnetic gradient and B on the numerical solution of the magnetohydrodynamic equations. *Journal of Computational Physics*, 35:426–430.

References

- Brandt, J. C. and Snow, M. (2000). Heliospheric Latitude Variations of Properties of Cometary Plasma Tails: A Test of the Ulysses Comet Watch Paradigm. *Icarus*, 148:52–64.
- Brüggen, M. and Scannapieco, E. (2016). The Launching of Cold Clouds by Galaxy Outflows. II. The Role of Thermal Conduction. *ApJ*, 822:31.
- Bruhweiler, F. C., Freire Ferrero, R., Bourdin, M. O., and Gull, T. R. (2010). The Young Interstellar Bubble Within the Rosette Nebula. *ApJ*, 719:1872–1883.
- Buffington, A., Bisi, M. M., Clover, J. M., Hick, P. P., Jackson, B. V., and Kuchar, T. A. (2008). Analysis of Plasma-Tail Motions for Comets C/2001 Q4 (NEAT) and C/2002 T7 (LINEAR) Using Observations from SMEI. *ApJ*, 677:798–807.
- Burstein, D. (2003). Line-of-Sight Reddening Predictions: Zero Points, Accuracies, the Interstellar Medium, and the Stellar Populations of Elliptical Galaxies. *AJ*, 126:1849–1860.
- Canning, R. E. A., Fabian, A. C., Johnstone, R. M., Sanders, J. S., Crawford, C. S., Ferland, G. J., and Hatch, N. A. (2011). A deep spectroscopic study of the filamentary nebulosity in NGC 4696, the brightest cluster galaxy in the Centaurus cluster. *MNRAS*, 417:3080–3099.
- Carey, S. J., Noriega-Crespo, A., Mizuno, D. R., Shenoy, S., Paladini, R., Kraemer, K. E., Price, S. D., Flagey, N., Ryan, E., Ingalls, J. G., Kuchar, T. A., Pinheiro Gonçalves, D., Indebetouw, R., Billot, N., Marleau, F. R., Padgett, D. L., Rebull, L. M., Bressert, E., Ali, B., Molinari, S., Martin, P. G., Berriman, G. B., Boulanger, F., Latter, W. B., Miville-Deschenes, M. A., Shipman, R., and Testi, L. (2009). MIPS GAL: A Survey of the Inner Galactic Plane at 24 and 70 μm . *PASP*, 121:76.
- Cecil, G., Bland-Hawthorn, J., and Veilleux, S. (2002). Tightly Correlated X-Ray/ $H\alpha$ -emitting Filaments in the Superbubble and Large-Scale Superwind of NGC 3079. *ApJ*, 576:745–752.
- Cecil, G., Bland-Hawthorn, J., Veilleux, S., and Filippenko, A. V. (2001). Jet- and Wind-driven Ionized Outflows in the Superbubble and Star-forming Disk of NGC 3079. *ApJ*, 555:338–355.
- Chandrasekhar, S. (1961). Hydrodynamic and hydromagnetic stability. In *International Series of Monographs on Physics*, Oxford: Clarendon.
- Chen, H.-W., Helsby, J. E., Gauthier, J.-R., Shectman, S. A., Thompson, I. B., and Tinker, J. L. (2010). An Empirical Characterization of Extended Cool Gas Around Galaxies Using Mg II Absorption Features. *ApJ*, 714:1521–1541.
- Chevalier, R. A. and Imamura, J. N. (1982). Linear analysis of an oscillatory instability of radiative shock waves. *ApJ*, 261:543–549.
- Chira, R.-A., Kainulainen, J., Ibáñez-Mejía, J. C., Henning, T., and Mac Low, M.-M. (2018). On the fragmentation of filaments in a molecular cloud simulation. *A&A*, 610:A62.

- Churchwell, E., Babler, B. L., Meade, M. R., Whitney, B. A., Benjamin, R., Indebetouw, R., Cyganowski, C., Robitaille, T. P., Povich, M., Watson, C., and Bracker, S. (2009). The Spitzer/GLIMPSE Surveys: A New View of the Milky Way. *PASP*, 121:213.
- Close, J. L., Pittard, J. M., Hartquist, T. W., and Falle, S. A. E. G. (2013). Ram pressure stripping of the hot gaseous haloes of galaxies using the k- ϵ sub-grid turbulence model. *MNRAS*, 436:3021–3030.
- Colín, P., Vázquez-Semadeni, E., and Gómez, G. C. (2013). Molecular cloud evolution - V. Cloud destruction by stellar feedback. *MNRAS*, 435:1701–1714.
- Conselice, C. J., Gallagher, III, J. S., and Wyse, R. F. G. (2001). On the Nature of the NGC 1275 System. *AJ*, 122:2281–2300.
- Cooper, J. L., Bicknell, G. V., Sutherland, R. S., and Bland-Hawthorn, J. (2008). Three-Dimensional Simulations of a Starburst-driven Galactic Wind. *ApJ*, 674:157–171.
- Cooper, J. L., Bicknell, G. V., Sutherland, R. S., and Bland-Hawthorn, J. (2009). Starburst-Driven Galactic Winds: Filament Formation and Emission Processes. *ApJ*, 703:330–347.
- Courtois, H. M., Zaritsky, D., Sorce, J. G., and Pomarède, D. (2015). Giant disc galaxies: where environment trumps mass in galaxy evolution. *MNRAS*, 448:1767–1778.
- Cowie, L. L., McKee, C. F., and Ostriker, J. P. (1981). Supernova remnant evolution in an inhomogeneous medium. I - Numerical models. *ApJ*, 247:908–924.
- Cox, D. P. (2005). The Three-Phase Interstellar Medium Revisited. *ARA&A*, 43:337–385.
- Crawford, C. S., Hatch, N. A., Fabian, A. C., and Sanders, J. S. (2005). The extended H α -emitting filaments surrounding NGC 4696, the central galaxy of the Centaurus cluster. *MNRAS*, 363:216–222.
- Dash, S. M. and Wolf, D. E. (1983). Shock-capturing parabolized Navier Stokes model (SCIPVIS) for the analysis of turbulent underexpanded jets. 8th Aeroacoustics Conference (AIAA, Atlanta, GA, USA, April 1983), AIAA Paper 83-0704.
- Dedner, A., Kemm, F., Kröner, D., Munz, C.-D., Schnitzer, T., and Wesenberg, M. (2002). Hyperbolic Divergence Cleaning for the MHD Equations. *Journal of Computational Physics*, 175:645–673.
- Di Cintio, P., Gupta, S., and Casetti, L. (2018). Dynamical origin of non-thermal states in galactic filaments. *MNRAS*, 475:1137–1147.
- Dopita, M. A., Calzetti, D., Maíz Apellániz, J., Blair, W. P., Long, K. S., Mutchler, M., Whitmore, B. C., Bond, H. E., MacKenty, J., Balick, B., Carollo, M., Disney, M., Frogel, J. A., O’Connell, R., Hall, D., Holtzman, J. A., Kimble, R. A., McCarthy, P., Paresce, F., Saha, A., Walker, A. R., Silk, J., Sirianni, M., Trauger, J., Windhorst, R., and Young, E. (2010). Supernova remnants, planetary nebulae and the distance to NGC 4214. *Ap&SS*, 330:123–131.

References

- Draine, B. T. (1978). Photoelectric heating of interstellar gas. *ApJS*, 36:595–619.
- Draine, B. T. (2010). *Physics of the Interstellar and Intergalactic Medium, Princeton Series in Astrophysics, 1st edn.* Princeton University Press.
- Draine, B. T. and Lee, H. M. (1984). Optical properties of interstellar graphite and silicate grains. *ApJ*, 285:89–108.
- Draine, B. T. and Li, A. (2007). Infrared Emission from Interstellar Dust. IV. The Silicate-Graphite-PAH Model in the Post-Spitzer Era. *ApJ*, 657:810–837.
- Drew, J. E., Greimel, R., Irwin, M. J., Aungwerojwit, A., Barlow, M. J., Corradi, R. L. M., Drake, J. J., Gänsicke, B. T., Groot, P., Hales, A., Hopewell, E. C., Irwin, J., Knigge, C., Leisy, P., Lennon, D. J., Mampaso, A., Masheder, M. R. W., Matsuura, M., Morales-Rueda, L., Morris, R. A. H., Parker, Q. A., Phillipps, S., Rodriguez-Gil, P., Roelofs, G., Skillen, I., Sokoloski, J. L., Steeghs, D., Unruh, Y. C., Viironen, K., Vink, J. S., Walton, N. A., Witham, A., Wright, N., Zijlstra, A. A., and Zurita, A. (2005). The INT Photometric H α Survey of the Northern Galactic Plane (IPHAS). *MNRAS*, 362:753–776.
- Duarte-Cabral, A., Chrysostomou, A., Peretto, N., Fuller, G. A., Matthews, B., Schieven, G., and Davis, G. R. (2012). The molecular gas content of the Pipe Nebula. I. Direct evidence of outflow-generated turbulence in B59? *A&A*, 543:A140.
- Duarte-Cabral, A., Dobbs, C. L., Peretto, N., and Fuller, G. A. (2011). Was a cloud-cloud collision the trigger of the recent star formation in Serpens? *A&A*, 528:A50.
- Dyson, J. E., Arthur, S. J., and Hartquist, T. W. (2002). The evolution of mass loaded supernova remnants. I. Constant and Mach Number dependent mass injection rates. *A&A*, 390:1063–1074.
- Dyson, J. E., Pittard, J. M., Meaburn, J., and Falle, S. A. E. G. (2006). The tails in the Helix Nebula NGC 7293. *A&A*, 457:561–567.
- Elmegreen, B. G. (1993). *Protostars and Planets III.* ed. Levy, E. H. & Lunine, J. I., University of Arizona Press, Tucson.
- Elmegreen, B. G. (1998). Observations and Theory of Dynamical Triggers for Star Formation. In Woodward, C. E., Shull, J. M., and Thronson, Jr., H. A., editors, *Origins*, volume 148 of *Astronomical Society of the Pacific Conference Series*, page 150.
- Elmegreen, B. G. and Lada, C. J. (1977). Sequential formation of subgroups in OB associations. *ApJ*, 214:725–741.
- Elmegreen, B. G. and Scalo, J. (2004). Interstellar Turbulence I: Observations and Processes. *ARA&A*, 42:211–273.
- Falle, S. A. E. G. (1975). Numerical calculation of thin shell formation in supernova remnants. *MNRAS*, 172:55–84.
- Falle, S. A. E. G. (1994). The Effect of Turbulence on the Largescale Structure of Radio Jets. *MNRAS*, 269:607.

- Falle, S. A. E. G. and Komissarov, S. S. (1999). On the Inadmissibility of Non-evolutionary Shocks. *ArXiv e-prints*.
- Falle, S. A. E. G., Komissarov, S. S., and Joarder, P. (1998). A multidimensional upwind scheme for magnetohydrodynamics. *MNRAS*, 297:265–277.
- Farris, M. H. and Russell, C. T. (1994). Determining the standoff distance of the bow shock: Mach number dependence and use of models. *J. Geophys. Res.*, 99:17.
- Federrath, C. (2016). On the universality of interstellar filaments: theory meets simulations and observations. *MNRAS*, 457:375–388.
- Federrath, C. and Klessen, R. S. (2012). The Star Formation Rate of Turbulent Magnetized Clouds: Comparing Theory, Simulations, and Observations. *ApJ*, 761:156.
- Federrath, C., Roman-Duval, J., Klessen, R. S., Schmidt, W., and Mac Low, M.-M. (2010). Comparing the statistics of interstellar turbulence in simulations and observations. Solenoidal versus compressive turbulence forcing. *A&A*, 512:A81.
- Ferrière, K. M. (2001). The interstellar environment of our galaxy. *Reviews of Modern Physics*, 73:1031–1066.
- Field, G. B., Goldsmith, D. W., and Habing, H. J. (1969). Cosmic-Ray Heating of the Interstellar Gas. *ApJ*, 155:L149.
- Field, G. B., Somerville, W. B., and Dressler, K. (1966). Hydrogen Molecules in Astronomy. *ARA&A*, 4:207.
- Forman, W., Jones, C., Churazov, E., Markevitch, M., Nulsen, P., Vikhlinin, A., Begelman, M., Böhringer, H., Eilek, J., Heinz, S., Kraft, R., Owen, F., and Pahre, M. (2007). Filaments, Bubbles, and Weak Shocks in the Gaseous Atmosphere of M87. *ApJ*, 665:1057–1066.
- Fragile, P. C., Anninos, P., Croft, S., Lacy, M., and Witry, J. W. L. (2017). Numerical Simulations of a Jet-Cloud Collision and Starburst: Application to Minkowski’s Object. *ArXiv e-prints*.
- Fragile, P. C., Anninos, P., Gustafson, K., and Murray, S. D. (2005). Magneto-hydrodynamic Simulations of Shock Interactions with Radiative Clouds. *ApJ*, 619:327–339.
- Fragile, P. C., Murray, S. D., Anninos, P., and van Breugel, W. (2004). Radiative Shock-induced Collapse of Intergalactic Clouds. *ApJ*, 604:74–87.
- Gilra, D. P. (1972). Collective Excitations and Dust Particles in Space. In Code, A. D., editor, *Scientific results from the orbiting astronomical observatory (OAO-2)*, volume 310 of *NASA Special Publication*, page 295.
- Godunov, S. K. (1959). A Finite Difference Method for the Computation of Discontinuous Solutions of the Equations of Fluid Dynamics. *Mat. Sb.*, 47:357.
- Goldsmith, P. F. (1987). Molecular clouds - an overview. In Hollenbach, D. J. and Thronson, Jr., H. A., editors, *Interstellar Processes*, volume 134 of *Astrophysics and Space Science Library*, pages 51–70.

References

- Goodson, M. D., Heitsch, F., Eklund, K., and Williams, V. A. (2017). A systematic comparison of two-equation Reynolds-averaged Navier-Stokes turbulence models applied to shock-cloud interactions. *MNRAS*, 468:3184–3201.
- Gregori, G., Miniati, F., Ryu, D., and Jones, T. W. (1999). Enhanced Cloud Disruption by Magnetic Field Interaction. *ApJ*, 527:L113–L116.
- Gregori, G., Miniati, F., Ryu, D., and Jones, T. W. (2000). Three-dimensional Magnetohydrodynamic Numerical Simulations of Cloud-Wind Interactions. *ApJ*, 543:775–786.
- Hansen, J. F., Robey, H. F., Klein, R. I., and Miles, A. R. (2007). Experiment on the Mass Stripping of an Interstellar Cloud Following Shock Passage. *ApJ*, 662:379–388.
- Hartmann, J. (1904). Investigations on the spectrum and orbit of delta Orionis. *ApJ*, 19.
- Hartquist, T. W., Dyson, J. E., Pettini, M., and Smith, L. J. (1986). Mass-loaded astronomical flows. I - General principles and their application to RCW 58. *MNRAS*, 221:715–726.
- Heckman, T. M., Lehnert, M. D., Strickland, D. K., and Armus, L. (2000). Absorption-Line Probes of Gas and Dust in Galactic Superwinds. *ApJS*, 129:493–516.
- Heesen, V., Beck, R., Krause, M., and Dettmar, R.-J. (2011). Cosmic rays and the magnetic field in the nearby starburst galaxy NGC 253 III. Helical magnetic fields in the nuclear outflow. *A&A*, 535:A79.
- Heigl, S., Burkert, A., and Hacar, A. (2016). Non-linear dense core formation in the dark cloud L1517. *MNRAS*, 463:4301–4310.
- Heiles, C. and Troland, T. H. (2003). The Millennium Arecibo 21 Centimeter Absorption-Line Survey. II. Properties of the Warm and Cold Neutral Media. *ApJ*, 586:1067–1093.
- Hennebelle, P. (2013). On the origin of non-self-gravitating filaments in the ISM. *A&A*, 556:A153.
- Hennebelle, P. and Falgarone, E. (2012). Turbulent molecular clouds. *A&A Rev.*, 20:55.
- Henning, T., Linz, H., Krause, O., Ragan, S., Beuther, H., Launhardt, R., Nielbock, M., and Vasyunina, T. (2010). The seeds of star formation in the filamentary infrared-dark cloud G011.11-0.12. *A&A*, 518:L95.
- Hoang, T. and Lazarian, A. (2008). Radiative torque alignment: essential physical processes. *MNRAS*, 388:117–143.
- Hollenbach, D. and Salpeter, E. E. (1971). Surface Recombination of Hydrogen Molecules. *ApJ*, 163:155.
- Hora, J. L., Latter, W. B., Smith, H. A., and Marengo, M. (2006). Infrared Observations of the Helix Planetary Nebula. *ApJ*, 652:426–441.

- Hosseinirad, M., Abbassi, S., Roshan, M., and Naficy, K. (2018). Gravitational instability of filamentary molecular clouds, including ambipolar diffusion; non-isothermal filament. *MNRAS*, 475:2632–2641.
- Imamura, J. N., Wolff, M. T., and Durisen, R. H. (1984). A numerical study of the stability of radiative shocks. *ApJ*, 276:667–676.
- Inoue, T., Hennebelle, P., Fukui, Y., Matsumoto, T., Iwasaki, K., and Inutsuka, S.-i. (2018). The formation of massive molecular filaments and massive stars triggered by a magnetohydrodynamic shock wave. *PASJ*, 70:S53.
- Jenkins, E. B. and Savage, B. D. (1974). Ultraviolet photometry from the Orbiting Astronomical Observatory. XIV. An extension of the survey of Lyman-alpha absorption from interstellar hydrogen. *ApJ*, 187:243–255.
- Johansson, E. P. G. and Ziegler, U. (2013). Radiative Interaction of Shocks with Small Interstellar Clouds as a Pre-stage to Star Formation. *ApJ*, 766:45.
- Jones, T. W., Ryu, D., and Tregillis, I. L. (1996). The Magnetohydrodynamics of Supersonic Gas Clouds: MHD Cosmic Bullets and Wind-swept Clumps. *ApJ*, 473:365.
- Kacprzak, G. G., Churchill, C. W., Steidel, C. C., and Murphy, M. T. (2008). Halo Gas Cross Sections and Covering Fractions of Mg II Absorption Selected Galaxies. *AJ*, 135:922–927.
- Kaifu, N., Usuda, T., Hayashi, S. S., Itoh, Y., Akiyama, M., Yamashita, T., Nakajima, Y., Tamura, M., Inutsuka, S., Hayashi, M., Maihara, T., Iwamuro, F., Motohara, K., Iwai, J., Tanabe, H., Taguchi, T., Hata, R., Terada, H., Goto, M., Ando, H., Aoki, T., Chikada, Y., Doi, M., Ebizuka, N., Fukuda, T., Hamabe, M., Hasegawa, T., Horaguchi, T., Ichikawa, S., Ichikawa, T., Imanishi, M., Imi, K., Inata, M., Isobe, S., Iye, M., Kamata, Y., Kanzawa, T., Karoji, H., Kashikawa, N., Kataza, H., Kato, T., Kobayashi, N., Kobayashi, Y., Kodaira, K., Kosugi, G., Kurakami, T., Mikami, Y., Miyama, S. M., Miyashita, A., Miyata, T., Miyazaki, S., Mizumoto, Y., Nakagiri, M., Nakajima, K., Nakamura, K., Nariai, K., Nishihara, E., Nishikawa, J., Nishimura, S., Nishimura, T., Nishino, T., Noguchi, K., Noguchi, T., Noumaru, J., Ogasawara, R., Okada, N., Okita, K., Omata, K., Oshima, N., Osubo, M., Sasaki, G., Sasaki, T., Sekiguchi, M., Sekiguchi, K., Shelton, I., Simpson, C., Suto, H., Takami, H., Takata, T., Takato, N., Tanaka, K., Tanaka, W., Tomono, D., Torii, Y., Waseda, K., Watanabe, J., Watanabe, M., Yagi, M., Yamashita, Y., Yasuda, N., Yoshida, M., Yoshida, S., and Yutani, M. (2000). The First Light of the Subaru Telescope: A New Infrared Image of the Orion Nebula. *PASJ*, 52:1.
- Katushkina, O. A., Alexashov, D. B., Gvaramadze, V. V., and Izmodenov, V. V. (2018). An astrosphere around the blue supergiant κ Cas: possible explanation of its filamentary structure. *MNRAS*, 473:1576–1588.
- Kawachi, T. and Hanawa, T. (1998). Gravitational Collapse of Filamentary Clouds. *PASJ*, 50:577–586.
- Kenney, J. D. P., Abramson, A., and Bravo-Alfaro, H. (2015). Hubble Space Telescope and HI Imaging of Strong Ram Pressure Stripping in the Coma Spiral NGC 4921: Dense Cloud Decoupling and Evidence for Magnetic Binding in the ISM. *AJ*, 150:59.

References

- Kimoto, P. A. and Chernoff, D. F. (1997). Radiative Instabilities in Simulations of Spherically Symmetric Supernova Blast Waves. *ApJ*, 485:274–284.
- Kirk, H., Klassen, M., Pudritz, R., and Pillsworth, S. (2015). The Role of Turbulence and Magnetic Fields in Simulated Filamentary Structure. *ApJ*, 802:75.
- Klein, R. I., Budil, K. S., Perry, T. S., and Bach, D. R. (2000). Interaction of Supernova Remnants with Interstellar Clouds: From the Nova Laser to the Galaxy. *ApJS*, 127:379–383.
- Klein, R. I., Budil, K. S., Perry, T. S., and Bach, D. R. (2003). The Interaction of Supernova Remnants with Interstellar Clouds: Experiments on the Nova Laser. *ApJ*, 583:245–259.
- Klein, R. I., McKee, C. F., and Colella, P. (1994). On the hydrodynamic interaction of shock waves with interstellar clouds. 1: Nonradiative shocks in small clouds. *ApJ*, 420:213–236.
- Klessen, R. S. and Burkert, A. (2000). The Formation of Stellar Clusters: Gaussian Cloud Conditions. I. *ApJS*, 128:287–319.
- Knacke, R. F. and Thomson, R. K. (1973). Infrared Extinction Cross Sections of Silicate Grains. *PASP*, 85:341.
- Koenig, X. P., Leisawitz, D. T., Benford, D. J., Rebull, L. M., Padgett, D. L., and Assef, R. J. (2012). Wide-field Infrared Survey Explorer Observations of the Evolution of Massive Star-forming Regions. *ApJ*, 744:130.
- Könyves, V., André, P., Men’shchikov, A., Palmeirim, P., Arzoumanian, D., Schneider, N., Roy, A., Didelon, P., Maury, A., Shimajiri, Y., Di Francesco, J., Bontemps, S., Peretto, N., Benedettini, M., Bernard, J.-P., Elia, D., Griffin, M. J., Hill, T., Kirk, J., Ladjelate, B., Marsh, K., Martin, P. G., Motte, F., Nguyễn Luong, Q., Pezzuto, S., Roussel, H., Rygl, K. L. J., Sadavoy, S. I., Schisano, E., Spinoglio, L., Ward-Thompson, D., and White, G. J. (2015). A census of dense cores in the Aquila cloud complex: SPIRE/PACS observations from the Herschel Gould Belt survey. *A&A*, 584:A91.
- Koo, B.-C., Moon, D.-S., Lee, H.-G., Lee, J.-J., and Matthews, K. (2007). [Fe II] and H₂ Filaments in the Supernova Remnant G11.2-0.3: Supernova Ejecta and Presupernova Circumstellar Wind. *ApJ*, 657:308–317.
- Koo, B.-C., Rho, J., Reach, W. T., Jung, J., and Mangum, J. G. (2001). Shocked Molecular Gas in the Supernova Remnant HB 21. *ApJ*, 552:175–188.
- Landau, L. D. and Lifshitz, E. M. (1987). Fluid Mechanics, 2nd ed.
- Langer, S. H., Chanmugam, G., and Shaviv, G. (1981). Thermal instability in accretion flows onto degenerate stars. *ApJ*, 245:L23–L26.
- Lanzetta, K. M. and Bowen, D. V. (1992). The kinematics of intermediate-redshift gaseous galaxy halos. *ApJ*, 391:48–72.
- Larson, R. B. (1981). Turbulence and star formation in molecular clouds. *MNRAS*, 194:809–826.

- Larson, R. B. (1985). Cloud fragmentation and stellar masses. *MNRAS*, 214:379–398.
- Larson, R. B. (2005). Thermal physics, cloud geometry and the stellar initial mass function. *MNRAS*, 359:211–222.
- Lee, J.-K. and Burton, M. G. (2000). An infrared proper motion study of the Orion bullets. *MNRAS*, 315:11–20.
- Levenson, N. A., Graham, J. R., and Walters, J. L. (2002). Shell Shock and Cloud Shock: Results from Spatially Resolved X-Ray Spectroscopy with Chandra in the Cygnus Loop. *ApJ*, 576:798–805.
- Li, S., Frank, A., and Blackman, E. G. (2013). Magnetohydrodynamic Shock-Clump Evolution with Self-contained Magnetic Fields. *ApJ*, 774:133.
- Li, Y., Klessen, R. S., and Mac Low, M.-M. (2003). The Formation of Stellar Clusters in Turbulent Molecular Clouds: Effects of the Equation of State. *ApJ*, 592:975–985.
- Lim, A. J., Falle, S. A. E. G., and Hartquist, T. W. (2005). The Production of Magnetically Dominated Star-forming Regions. *ApJ*, 632:L91–L94.
- Mac Low, M.-M. and Klessen, R. S. (2004). Control of star formation by supersonic turbulence. *Reviews of Modern Physics*, 76:125–194.
- Mac Low, M.-M., McKee, C. F., Klein, R. I., Stone, J. M., and Norman, M. L. (1994). Shock interactions with magnetized interstellar clouds. 1: Steady shocks hitting nonradiative clouds. *ApJ*, 433:757–777.
- Mallick, K. K., Kumar, M. S. N., Ojha, D. K., Bachiller, R., Samal, M. R., and Pirogov, L. (2013). The W40 Region in the Gould Belt: An Embedded Cluster and H II Region at the Junction of Filaments. *ApJ*, 779:113.
- Marcolini, A., Strickland, D. K., D’Ercole, A., Heckman, T. M., and Hoopes, C. G. (2005). The dynamics and high-energy emission of conductive gas clouds in supernova-driven galactic superwinds. *MNRAS*, 362:626–648.
- Martin, C. L. (2005). Mapping Large-Scale Gaseous Outflows in Ultraluminous Galaxies with Keck II ESI Spectra: Variations in Outflow Velocity with Galactic Mass. *ApJ*, 621:227–245.
- Martin, C. L., Kobulnicky, H. A., and Heckman, T. M. (2002). The Metal Content of Dwarf Starburst Winds: Results from Chandra Observations of NGC 1569. *ApJ*, 574:663–692.
- Martin, C. L., Shapley, A. E., Coil, A. L., Kornei, K. A., Bundy, K., Weiner, B. J., Noeske, K. G., and Schiminovich, D. (2012). Demographics and Physical Properties of Gas Outflows/Inflows at $0.4 < z < 1.4$. *ApJ*, 760:127.
- Mathis, J. S., Rumpl, W., and Nordsieck, K. H. (1977). The size distribution of interstellar grains. *ApJ*, 217:425–433.

References

- Matsuura, M., Speck, A. K., McHunu, B. M., Tanaka, I., Wright, N. J., Smith, M. D., Zijlstra, A. A., Viti, S., and Wesson, R. (2009). A “Firework” of H₂ Knots in the Planetary Nebula NGC 7293 (The Helix Nebula). *ApJ*, 700:1067–1077.
- Matsuura, M., Speck, A. K., Smith, M. D., Zijlstra, A. A., Viti, S., Lowe, K. T. E., Redman, M., Wareing, C. J., and Lagadec, E. (2007). VLT/near-infrared integral field spectrometer observations of molecular hydrogen lines in the knots of the planetary nebula NGC 7293 (the Helix Nebula). *MNRAS*, 382:1447–1459.
- McClure-Griffiths, N. M., Dickey, J. M., Gaensler, B. M., Green, A. J., Green, J. A., and Haverkorn, M. (2012). The Australia Telescope Compact Array H I Survey of the Galactic Center. *ApJS*, 199:12.
- McClure-Griffiths, N. M., Green, J. A., Hill, A. S., Lockman, F. J., Dickey, J. M., Gaensler, B. M., and Green, A. J. (2013). Atomic Hydrogen in a Galactic Center Outflow. *ApJ*, 770:L4.
- McCourt, M., O’Leary, R. M., Madigan, A.-M., and Quataert, E. (2015). Magnetized gas clouds can survive acceleration by a hot wind. *MNRAS*, 449:2–7.
- McCray, R., Kafatos, M., and Stein, R. F. (1975). Thermal instability in supernova shells. *ApJ*, 196:565–570.
- McCray, R. and Snow, Jr., T. P. (1979). The violent interstellar medium. *ARA&A*, 17:213–240.
- McKee, C. F. (1995). The Multiphase Interstellar Medium. In Ferrara, A., McKee, C. F., Heiles, C., and Shapiro, P. R., editors, *The Physics of the Interstellar Medium and Intergalactic Medium*, volume 80 of *Astronomical Society of the Pacific Conference Series*, page 292.
- McKee, C. F. (1999). The Dynamical Structure and Evolution of Giant Molecular Clouds. In Lada, C. J. and Kylafis, N. D., editors, *NATO Advanced Science Institutes (ASI) Series C*, volume 540 of *NATO Advanced Science Institutes (ASI) Series C*, page 29.
- McKee, C. F. and Cowie, L. L. (1975). The interaction between the blast wave of a supernova remnant and interstellar clouds. *ApJ*, 195:715–725.
- McKee, C. F. and Ostriker, E. C. (2007). Theory of Star Formation. *ARA&A*, 45:565–687.
- McKee, C. F. and Ostriker, J. P. (1977). A theory of the interstellar medium - Three components regulated by supernova explosions in an inhomogeneous substrate. *ApJ*, 218:148–169.
- Meaburn, J. and Boumis, P. (2010). Flows along cometary tails in the Helix planetary nebula NGC 7293. *MNRAS*, 402:381–385.
- Melioli, C., de Gouveia dal Pino, E. M., and Raga, A. (2005). Multidimensional hydrodynamical simulations of radiative cooling SNRs-clouds interactions: an application to starburst environments. *A&A*, 443:495–508.

- Mellema, G., Kurk, J. D., and Röttgering, H. J. A. (2002). Evolution of clouds in radio galaxy cocoons. *A&A*, 395:L13–L16.
- Men'shchikov, A., André, P., Didelon, P., Könyves, V., Schneider, N., Motte, F., Bontemps, S., Arzoumanian, D., Attard, M., Abergel, A., Baluteau, J.-P., Bernard, J.-P., Cambrésy, L., Cox, P., di Francesco, J., di Giorgio, A. M., Griffin, M., Hargrave, P., Huang, M., Kirk, J., Li, J. Z., Martin, P., Minier, V., Miville-Deschênes, M.-A., Molinari, S., Olofsson, G., Pezzuto, S., Roussel, H., Russeil, D., Saraceno, P., Sauvage, M., Sibthorpe, B., Spinoglio, L., Testi, L., Ward-Thompson, D., White, G., Wilson, C. D., Woodcraft, A., and Zavagno, A. (2010). Filamentary structures and compact objects in the Aquila and Polaris clouds observed by Herschel. *A&A*, 518:L103.
- Miniati, F., Jones, T. W., and Ryu, D. (1999). On the Exchange of Kinetic and Magnetic Energy between Clouds and the Interstellar Medium. *ApJ*, 517:242–255.
- Moeckel, N. and Burkert, A. (2015). The Formation of Filamentary Bundles in Turbulent Molecular Clouds. *ApJ*, 807:67.
- Molinari, S., Swinyard, B., Bally, J., Barlow, M., Bernard, J.-P., Martin, P., Moore, T., Noriega-Crespo, A., Plume, R., Testi, L., Zavagno, A., Abergel, A., Ali, B., Anderson, L., André, P., Baluteau, J.-P., Battersby, C., Beltrán, M. T., Benedettini, M., Billot, N., Blommaert, J., Bontemps, S., Boulanger, F., Brand, J., Brunt, C., Burton, M., Calzoletti, L., Carey, S., Caselli, P., Cesaroni, R., Cernicharo, J., Chakrabarti, S., Chrysostomou, A., Cohen, M., Compiegne, M., de Bernardis, P., de Gasperis, G., di Giorgio, A. M., Elia, D., Faustini, F., Flagey, N., Fukui, Y., Fuller, G. A., Ganga, K., Garcia-Lario, P., Glenn, J., Goldsmith, P. F., Griffin, M., Hoare, M., Huang, M., Ikhenade, D., Joblin, C., Joncas, G., Juvela, M., Kirk, J. M., Lagache, G., Li, J. Z., Lim, T. L., Lord, S. D., Marengo, M., Marshall, D. J., Masi, S., Massi, F., Matsuura, M., Minier, V., Miville-Deschênes, M.-A., Montier, L. A., Morgan, L., Motte, F., Mottram, J. C., Müller, T. G., Natoli, P., Neves, J., Olmi, L., Paladini, R., Paradis, D., Parsons, H., Peretto, N., Pestalozzi, M., Pezzuto, S., Piacentini, F., Piazzi, L., Polychroni, D., Pomarès, M., Popescu, C. C., Reach, W. T., Ristorcelli, I., Robitaille, J.-F., Robitaille, T., Rodón, J. A., Roy, A., Royer, P., Russeil, D., Saraceno, P., Sauvage, M., Schilke, P., Schisano, E., Schneider, N., Schuller, F., Schulz, B., Sibthorpe, B., Smith, H. A., Smith, M. D., Spinoglio, L., Stamatellos, D., Strafella, F., Stringfellow, G. S., Sturm, E., Taylor, R., Thompson, M. A., Traficante, A., Tuffs, R. J., Umana, G., Valenziano, L., Vavrek, R., Veneziani, M., Viti, S., Waelkens, C., Ward-Thompson, D., White, G., Wilcock, L. A., Wyrowski, F., Yorke, H. W., and Zhang, Q. (2010). Clouds, filaments, and protostars: The Herschel Hi-GAL Milky Way. *A&A*, 518:L100.
- Motte, F., Zavagno, A., Bontemps, S., Schneider, N., Hennemann, M., di Francesco, J., André, P., Saraceno, P., Griffin, M., Marston, A., Ward-Thompson, D., White, G., Minier, V., Men'shchikov, A., Hill, T., Abergel, A., Anderson, L. D., Aussel, H., Balog, Z., Baluteau, J.-P., Bernard, J.-P., Cox, P., Csengeri, T., Deharveng, L., Didelon, P., di Giorgio, A.-M., Hargrave, P., Huang, M., Kirk, J., Leeks, S., Li, J. Z., Martin, P., Molinari, S., Nguyen-Luong, Q., Olofsson, G., Persi, P., Peretto, N., Pezzuto, S., Roussel, H., Russeil, D., Sadavoy, S., Sauvage, M., Sibthorpe, B., Spinoglio, L., Testi, L., Teyssier, D., Vavrek, R., Wilson, C. D., and Woodcraft,

References

- A. (2010). Initial highlights of the HOBYS key program, the Herschel imaging survey of OB young stellar objects. *A&A*, 518:L77.
- Murray, S. D., White, S. D. M., Blondin, J. M., and Lin, D. N. C. (1993). Dynamical instabilities in two-phase media and the minimum masses of stellar systems. *ApJ*, 407:588–596.
- Myers, P. C. (1987). Observations of molecular cloud structure and internal motions. In Hollenbach, D. J. and Thronson, Jr., H. A., editors, *Interstellar Processes*, volume 134 of *Astrophysics and Space Science Library*, pages 71–86.
- Myers, P. C. (2011). Filamentary Condensations in a Young Cluster. *ApJ*, 735:82.
- Nakamura, F., McKee, C. F., Klein, R. I., and Fisher, R. T. (2006). On the Hydrodynamic Interaction of Shock Waves with Interstellar Clouds. II. The Effect of Smooth Cloud Boundaries on Cloud Destruction and Cloud Turbulence. *ApJS*, 164:477–505.
- Niederhaus, J. H. J. (2007). PhD thesis, Univ. Wisconsin-Madison.
- Nittmann, J., Falle, S. A. E. G., and Gaskell, P. H. (1982). The dynamical destruction of shocked gas clouds. *MNRAS*, 201:833–847.
- Nynka, M., Hailey, C. J., Zhang, S., Morris, M. M., Zhao, J.-H., Goss, M., Bauer, F. E., Boggs, S. E., Craig, W. W., Christensen, F. E., Gotthelf, E. V., Harrison, F. A., Mori, K., Perez, K. M., Stern, D., and Zhang, W. W. (2015). G359.97-0.038: A Hard X-Ray Filament Associated with a Supernova Shell-Molecular Cloud Interaction. *ApJ*, 800:119.
- O’Dea, C. P., Baum, S. A., Tremblay, G. R., Kharb, P., Cotton, W., and Perley, R. (2013). Hubble Space Telescope Observations of Dusty Filaments in Hercules A: Evidence for Entrainment. *ApJ*, 771:38.
- O’Dell, C. R., Henney, W. J., and Ferland, G. J. (2005). A Multi-Instrument Study of the Helix Nebula Knots with the Hubble Space Telescope. *AJ*, 130:172–187.
- Ohyama, Y., Taniguchi, Y., Iye, M., Yoshida, M., Sekiguchi, K., Takata, T., Saito, Y., Kawabata, K. S., Kashikawa, N., Aoki, K., Sasaki, T., Kosugi, G., Okita, K., Shimizu, Y., Inata, M., Ebizuka, N., Ozawa, T., Yadoumaru, Y., Taguchi, H., and Asai, R. (2002). Decomposition of the Superwind in M 82. *PASJ*, 54:891–898.
- Orlando, S., Bocchino, F., Reale, F., Peres, G., and Pagano, P. (2008). The Importance of Magnetic-Field-Oriented Thermal Conduction in the Interaction of SNR Shocks with Interstellar Clouds. *ApJ*, 678:274–286.
- Orlando, S., Peres, G., Reale, F., Bocchino, F., Rosner, R., Plewa, T., and Siegel, A. (2005). Crushing of interstellar gas clouds in supernova remnants. I. The role of thermal conduction and radiative losses. *A&A*, 444:505–519.
- Ostriker, J. (1964). The Equilibrium of Polytropic and Isothermal Cylinders. *ApJ*, 140:1056.
- Padoan, P., Cambr esy, L., Juvela, M., Kritsuk, A., Langer, W. D., and Norman, M. L. (2006). Can We Trust the Dust? Evidence of Dust Segregation in Molecular Clouds. *ApJ*, 649:807–815.

- Padoan, P., Federrath, C., Chabrier, G., Evans, II, N. J., Johnstone, D., Jørgensen, J. K., McKee, C. F., and Nordlund, Å. (2014). The Star Formation Rate of Molecular Clouds. *Protostars and Planets VI*, pages 77–100.
- Panopoulou, G. V., Tassis, K., Goldsmith, P. F., and Heyer, M. H. (2014). ^{13}CO filaments in the Taurus molecular cloud. *MNRAS*, 444:2507–2524.
- Patnaude, D. J. and Fesen, R. A. (2005). Model Simulations of a Shock-Cloud Interaction in the Cygnus Loop. *ApJ*, 633:240–247.
- Patnaude, D. J., Fesen, R. A., Raymond, J. C., Levenson, N. A., Graham, J. R., and Wallace, D. J. (2002). An Isolated, Recently Shocked ISM Cloud in the Cygnus Loop Supernova Remnant. *AJ*, 124:2118–2134.
- Peebles, M. S., Werk, J. K., Tumlinson, J., Oppenheimer, B. D., Prochaska, J. X., Katz, N., and Weinberg, D. H. (2014). A Budget and Accounting of Metals at $z \sim 0$: Results from the COS-Halos Survey. *ApJ*, 786:54.
- Peretto, N., André, P., Könyves, V., Schneider, N., Arzoumanian, D., Palmeirim, P., Didelon, P., Attard, M., Bernard, J. P., Di Francesco, J., Elia, D., Hennemann, M., Hill, T., Kirk, J., Men'shchikov, A., Motte, F., Nguyen Luong, Q., Roussel, H., Sousbie, T., Testi, L., Ward-Thompson, D., White, G. J., and Zavagno, A. (2012). The Pipe Nebula as seen with Herschel: formation of filamentary structures by large-scale compression? *A&A*, 541:A63.
- Peters, T., Schleicher, D. R. G., Klessen, R. S., Banerjee, R., Federrath, C., Smith, R. J., and Sur, S. (2012). The Impact of Thermodynamics on Gravitational Collapse: Filament Formation and Magnetic Field Amplification. *ApJ*, 760:L28.
- Pettini, M., Shapley, A. E., Steidel, C. C., Cuby, J.-G., Dickinson, M., Moorwood, A. F. M., Adelberger, K. L., and Giavalisco, M. (2001). The Rest-Frame Optical Spectra of Lyman Break Galaxies: Star Formation, Extinction, Abundances, and Kinematics. *ApJ*, 554:981–1000.
- Pittard, J. M. (2011). Tails of the unexpected: the interaction of an isothermal shell with a cloud. *MNRAS*, 411:L41–L45.
- Pittard, J. M., Arthur, S. J., Dyson, J. E., Falle, S. A. E. G., Hartquist, T. W., Knight, M. I., and Pexon, M. (2003). The evolution of mass loaded supernova remnants. II. Temperature dependent mass injection rates. *A&A*, 401:1027–1038.
- Pittard, J. M., Dobson, M. S., Durisen, R. H., Dyson, J. E., Hartquist, T. W., and O'Brien, J. T. (2005a). The shocking properties of supersonic flows: Dependence of the thermal overstability on M , α , and T_c / T_0 . *A&A*, 438:11–21.
- Pittard, J. M., Dyson, J. E., Falle, S. A. E. G., and Hartquist, T. W. (2005b). Dynamical and pressure structures in winds with multiple embedded evaporating clumps - I. Two-dimensional numerical simulations. *MNRAS*, 361:1077–1090.
- Pittard, J. M., Falle, S. A. E. G., Hartquist, T. W., and Dyson, J. E. (2009). The turbulent destruction of clouds - I. A k - ϵ treatment of turbulence in 2D models of adiabatic shock-cloud interactions. *MNRAS*, 394:1351–1378.

References

- Pittard, J. M. and Goldsmith, K. J. A. (2016). Numerical simulations of a shock-filament interaction. *MNRAS*, 458:1139–1163.
- Pittard, J. M., Hartquist, T. W., and Falle, S. A. E. G. (2010). The turbulent destruction of clouds - II. Mach number dependence, mass-loss rates and tail formation. *MNRAS*, 405:821–838.
- Pittard, J. M. and Parkin, E. R. (2016). The turbulent destruction of clouds - III. Three-dimensional adiabatic shock-cloud simulations. *MNRAS*, 457:4470–4498.
- Poludnenko, A. Y., Frank, A., and Blackman, E. G. (2002). Hydrodynamic Interaction of Strong Shocks with Inhomogeneous Media. I. Adiabatic Case. *ApJ*, 576:832–848.
- Poludnenko, A. Y., Frank, A., and Mitran, S. (2004). Strings in the η Carinae Nebula: Hypersonic Radiative Cosmic Bullets. *ApJ*, 613:387–392.
- Polychroni, D., Schisano, E., Elia, D., Roy, A., Molinari, S., Martin, P., André, P., Turrini, D., Rygl, K. L. J., Di Francesco, J., Benedettini, M., Busquet, G., di Giorgio, A. M., Pestalozzi, M., Pezzuto, S., Arzoumanian, D., Bontemps, S., Hennemann, M., Hill, T., Könyves, V., Men'shchikov, A., Motte, F., Nguyen-Luong, Q., Peretto, N., Schneider, N., and White, G. (2013). Two Mass Distributions in the L 1641 Molecular Clouds: The Herschel Connection of Dense Cores and Filaments in Orion A. *ApJ*, 777:L33.
- Raga, A. C., Esquivel, A., Riera, A., and Velázquez, P. F. (2007). The Three-dimensional Structure of a Radiative, Cosmic Bullet Flow. *ApJ*, 668:310–315.
- Raga, A. C., Steffen, W., and González, R. F. (2005). 3D Simulations of the Fragmentation of Photoevaporating Clumps Embedded in a Stellar Wind. *Rev. Mexicana Astron. Astrofis.*, 41:45–55.
- Rayner, T. S. M., Griffin, M. J., Schneider, N., Motte, F., Könyves, V., André, P., Di Francesco, J., Didelon, P., Pattle, K., Ward-Thompson, D., Anderson, L. D., Benedettini, M., Bernard, J.-P., Bontemps, S., Elia, D., Fuente, A., Hennemann, M., Hill, T., Kirk, J., Marsh, K., Men'shchikov, A., Nguyen Luong, Q., Peretto, N., Pezzuto, S., Rivera-Ingraham, A., Roy, A., Rygl, K., Sánchez-Monge, Á., Spinoglio, L., Tigé, J., Treviño-Morales, S. P., and White, G. J. (2017). Far-infrared observations of a massive cluster forming in the Monoceros R2 filament hub. *A&A*, 607:A22.
- Reynolds, R. J. (1987). A view of the galactic H-alpha background - L = 208-218 deg, B = -2 to +8 deg. *ApJ*, 323:118–128.
- Reynolds, R. J., Haffner, L. M., and Tufte, S. L. (1999). The Gaseous ISM: Observations with the Wisconsin H α Mapper (WHAM). In Taylor, A. R., Landecker, T. L., and Joncas, G., editors, *New Perspectives on the Interstellar Medium*, volume 168 of *Astronomical Society of the Pacific Conference Series*, page 149.
- Roesler, F. L., Reynolds, R. J., Scherb, F., and Ogden, P. M. (1978). Instrumental Aspects of the Wisconsin Interstellar Emission Line Program. In Hack, M., editor, *High resolution spectrometry*, page 600.

- Rogers, H. and Pittard, J. M. (2013). Feedback from winds and supernovae in massive stellar clusters - I. Hydrodynamics. *MNRAS*, 431:1337–1351.
- Rosen, P. A., Foster, J. M., Wilde, B. H., Hartigan, P., Blue, B. E., Hansen, J. F., Sorce, C., Williams, R. J. R., Coker, R., and Frank, A. (2009). Laboratory experiments to study supersonic astrophysical flows interacting with clumpy environments. *Ap&SS*, 322:101–105.
- Roy, A., André, P., Arzoumanian, D., Peretto, N., Palmeirim, P., Könyves, V., Schneider, N., Benedettini, M., Di Francesco, J., Elia, D., Hill, T., Ladjelate, B., Louvet, F., Motte, F., Pezzuto, S., Schisano, E., Shimajiri, Y., Spinoglio, L., Ward-Thompson, D., and White, G. (2015). Possible link between the power spectrum of interstellar filaments and the origin of the prestellar core mass function. *A&A*, 584:A111.
- Rupke, D. S., Veilleux, S., and Sanders, D. B. (2002). Keck Absorption-Line Spectroscopy of Galactic Winds in Ultraluminous Infrared Galaxies. *ApJ*, 570:588–609.
- Sales, L. V., Navarro, J. F., Schaye, J., Dalla Vecchia, C., Springel, V., and Booth, C. M. (2010). Feedback and the structure of simulated galaxies at redshift $z = 2$. *MNRAS*, 409:1541–1556.
- Scalo, J. and Elmegreen, B. G. (2004). Interstellar Turbulence II: Implications and Effects. *ARA&A*, 42:275–316.
- Scannapieco, E. and Brügger, M. (2015). The Launching of Cold Clouds by Galaxy Outflows. I. Hydrodynamic Interactions with Radiative Cooling. *ApJ*, 805:158.
- Schiano, A. V. R., Christiansen, W. A., and Knerr, J. M. (1995). Interstellar clouds in high-speed, supersonic flows: Two-dimensional simulations. *ApJ*, 439:237–255.
- Schisano, E., Rygl, K. L. J., Molinari, S., Busquet, G., Elia, D., Pestalozzi, M., Polychroni, D., Billot, N., Carey, S., Paladini, R., Noriega-Crespo, A., Moore, T. J. T., Plume, R., Glover, S. C. O., and Vázquez-Semadeni, E. (2014). The Identification of Filaments on Far-infrared and Submillimeter Images: Morphology, Physical Conditions and Relation with Star Formation of Filamentary Structure. *ApJ*, 791:27.
- Schlegel, D. J., Finkbeiner, D. P., and Davis, M. (1998). Maps of Dust Infrared Emission for Use in Estimation of Reddening and Cosmic Microwave Background Radiation Foregrounds. *ApJ*, 500:525–553.
- Schneider, N., Bontemps, S., Simon, R., Jakob, H., Motte, F., Miller, M., Kramer, C., and Stutzki, J. (2006). A new view of the Cygnus X region. KOSMA ^{13}CO 2 to 1, 3 to 2, and ^{12}CO 3 to 2 imaging. *A&A*, 458:855–871.
- Schneider, N., Csengeri, T., Hennemann, M., Motte, F., Didelon, P., Federrath, C., Bontemps, S., Di Francesco, J., Arzoumanian, D., Minier, V., André, P., Hill, T., Zavagno, A., Nguyen-Luong, Q., Attard, M., Bernard, J.-P., Elia, D., Fallscheer, C., Griffin, M., Kirk, J., Klessen, R., Könyves, V., Martin, P., Men'shchikov, A., Palmeirim, P., Peretto, N., Pestalozzi, M., Russeil, D., Sadavoy, S., Sousbie,

References

- T., Testi, L., Tremblin, P., Ward-Thompson, D., and White, G. (2012). Cluster-formation in the Rosette molecular cloud at the junctions of filaments. *A&A*, 540:L11.
- Schneider, S. and Elmegreen, B. G. (1979). A catalog of dark globular filaments. *ApJS*, 41:87–95.
- Schultz, A. S. B., Colgan, S. W. J., Erickson, E. F., Kaufman, M. J., Hollenbach, D. J., O’Dell, C. R., Young, E. T., and Chen, H. (1999). NICMOS Narrowband Images of OMC-1. *ApJ*, 511:282–288.
- Sgro, A. G. (1975). The collision of a strong shock with a gas cloud - A model for Cassiopeia A. *ApJ*, 197:621–634.
- Shafi, N., Oosterloo, T. A., Morganti, R., Colafrancesco, S., and Booth, R. (2015). The ‘shook up’ galaxy NGC 3079: the complex interplay between H I, activity and environment. *MNRAS*, 454:1404–1415.
- Shin, M.-S., Stone, J. M., and Snyder, G. F. (2008). The Magnetohydrodynamics of Shock-Cloud Interaction in Three Dimensions. *ApJ*, 680:336–348.
- Shopbell, P. L. and Bland-Hawthorn, J. (1998). The Asymmetric Wind in M82. *ApJ*, 493:129–153.
- Shull, J. M. and Beckwith, S. (1982). Interstellar molecular hydrogen. *ARA&A*, 20:163–190.
- Soto, K. T. and Martin, C. L. (2012). Gas Excitation in ULIRGs: Maps of Diagnostic Emission-line Ratios in Space and Velocity. *ApJS*, 203:3.
- Spitzer, Jr., L. (1982). Acoustic waves in supernova remnants. *ApJ*, 262:315–321.
- Spitzer, Jr., L. (1990). Theories of the hot interstellar gas. *ARA&A*, 28:71–101.
- Steidel, C. C., Dickinson, M., and Persson, S. E. (1994). Field galaxy evolution since Z approximately 1 from a sample of QSO absorption-selected galaxies. *ApJ*, 437:L75–L78.
- Steidel, C. C., Erb, D. K., Shapley, A. E., Pettini, M., Reddy, N., Bogosavljević, M., Rudie, G. C., and Rakic, O. (2010). The Structure and Kinematics of the Circumgalactic Medium from Far-ultraviolet Spectra of $z \sim 2-3$ Galaxies. *ApJ*, 717:289–322.
- Steidel, C. C., Kollmeier, J. A., Shapley, A. E., Churchill, C. W., Dickinson, M., and Pettini, M. (2002). The Kinematic Connection between absorbing Gas toward QSOs and Galaxies at Intermediate Redshift. *ApJ*, 570:526–542.
- Stone, J. M. and Norman, M. L. (1992). The three-dimensional interaction of a supernova remnant with an interstellar cloud. *ApJ*, 390:L17–L19.
- Strickland, D. K., Heckman, T. M., Colbert, E. J. M., Hoopes, C. G., and Weaver, K. A. (2004). A High Spatial Resolution X-Ray and $H\alpha$ Study of Hot Gas in the Halos of Star-forming Disk Galaxies. I. Spatial and Spectral Properties of the Diffuse X-Ray Emission. *ApJS*, 151:193–236.

- Strickland, D. K. and Stevens, I. R. (2000). Starburst-driven galactic winds - I. Energetics and intrinsic X-ray emission. *MNRAS*, 314:511–545.
- Strickland, R. and Blondin, J. M. (1995). Numerical Analysis of the Dynamic Stability of Radiative Shocks. *ApJ*, 449:727.
- Tedds, J. A., Brand, P. W. J. L., and Burton, M. G. (1999). Shocked H₂ and Fe⁺ dynamics in the Orion bullets. *MNRAS*, 307:337–356.
- Toci, C. and Galli, D. (2015). Polytropic models of filamentary interstellar clouds - I. Structure and stability. *MNRAS*, 446:2110–2117.
- Toro, E. F. (2009). *Riemann Solvers and Numerical Methods for Fluid Dynamics: A Practical Introduction*. Springer, Berlin, 3rd Edn.
- Trumpler, R. J. (1930). Preliminary results on the distances, dimensions and space distribution of open star clusters. *Lick Observatory Bulletin*, 14:154–188.
- Tumlinson, J., Thom, C., Werk, J. K., Prochaska, J. X., Tripp, T. M., Katz, N., Davé, R., Oppenheimer, B. D., Meiring, J. D., Ford, A. B., O’Meara, J. M., Peebles, M. S., Sembach, K. R., and Weinberg, D. H. (2013). The COS-Halos Survey: Rationale, Design, and a Census of Circumgalactic Neutral Hydrogen. *ApJ*, 777:59.
- Turner, M. L., Schaye, J., Steidel, C. C., Rudie, G. C., and Strom, A. L. (2014). Metal-line absorption around $z \approx 2.4$ star-forming galaxies in the Keck Baryonic Structure Survey. *MNRAS*, 445:794–822.
- van den Bergh, S. (1971). Optical Studies of Cassiopeia a. III. Spectra of the Supernova Remnant. *ApJ*, 165:457.
- van Loo, S., Falle, S. A. E. G., and Hartquist, T. W. (2010). Shock-triggered formation of magnetically dominated clouds - II. Weak shock-cloud interaction in three dimensions. *MNRAS*, 406:1260–1268.
- van Loo, S., Falle, S. A. E. G., Hartquist, T. W., and Moore, T. J. T. (2007). Shock-triggered formation of magnetically-dominated clouds. *A&A*, 471:213–218.
- Vazquez-Semadeni, E., Banerjee, R., Klessen, R., and Ballesteros-Paredes, J. (2007). Molecular Cloud Formation III. Influence of the Magnetic Field. In *American Astronomical Society Meeting Abstracts*, volume 39 of *Bulletin of the American Astronomical Society*, page 984.
- Veilleux, S., Cecil, G., and Bland-Hawthorn, J. (2005). Galactic Winds. *ARA&A*, 43:769–826.
- Vieser, W. and Hensler, G. (2007). The evolution of interstellar clouds in a streaming hot plasma including heat conduction. *A&A*, 472:141–153.
- Vig, S., Testi, L., Walmsley, M., Molinari, S., Carey, S., and Noriega-Crespo, A. (2007). IRAS 18511+0146: a proto Herbig Ae/Be cluster? *A&A*, 470:977–989.
- Vogt, F. and Dopita, M. A. (2011). The 3D structure of N132D in the LMC: a late-stage young supernova remnant. *Ap&SS*, 331:521–535.

References

- Wareing, C. J., Pittard, J. M., and Falle, S. A. E. G. (2017). Magnetohydrodynamic simulations of mechanical stellar feedback in a sheet-like molecular cloud. *MNRAS*, 465:2757–2783.
- Werk, J. K., Prochaska, J. X., Thom, C., Tumlinson, J., Tripp, T. M., O’Meara, J. M., and Peebles, M. S. (2013). The COS-Halos Survey: An Empirical Description of Metal-line Absorption in the Low-redshift Circumgalactic Medium. *ApJS*, 204:17.
- Werk, J. K., Prochaska, J. X., Tumlinson, J., Peebles, M. S., Tripp, T. M., Fox, A. J., Lehner, N., Thom, C., O’Meara, J. M., Ford, A. B., Bordoloi, R., Katz, N., Tejos, N., Oppenheimer, B. D., Davé, R., and Weinberg, D. H. (2014). The COS-Halos Survey: Physical Conditions and Baryonic Mass in the Low-redshift Circumgalactic Medium. *ApJ*, 792:8.
- Westmoquette, M. S., Slavin, J. D., Smith, L. J., and Gallagher, III, J. S. (2010). VLT/FLAMES-ARGUS observations of stellar wind-ISM cloud interactions in NGC 6357. *MNRAS*, 402:152–160.
- Westmoquette, M. S., Smith, L. J., and Gallagher, III, J. S. (2011). Spatially resolved optical integral field unit spectroscopy of the inner superwind of NGC 253. *MNRAS*, 414:3719–3739.
- White, R. L. and Long, K. S. (1991). Supernova remnant evolution in an interstellar medium with evaporating clouds. *ApJ*, 373:543–555.
- Wolfire, M. G., Hollenbach, D., McKee, C. F., Tielens, A. G. G. M., and Bakes, E. L. O. (1995). The neutral atomic phases of the interstellar medium. *ApJ*, 443:152–168.
- Wolfire, M. G., McKee, C. F., Hollenbach, D., and Tielens, A. G. G. M. (2003). Neutral Atomic Phases of the Interstellar Medium in the Galaxy. *ApJ*, 587:278–311.
- Woodward, P. R. (1976). Shock-driven implosion of interstellar gas clouds and star formation. *ApJ*, 207:484–501.
- Xu, J. and Stone, J. M. (1995). The Hydrodynamics of Shock-Cloud Interactions in Three Dimensions. *ApJ*, 454:172.
- Yagi, M., Koda, J., Furusho, R., Terai, T., Fujiwara, H., and Watanabe, J.-I. (2015). Initial Speed of Knots in the Plasma Tail of C/2013 R1(Lovejoy). *AJ*, 149:97.
- Yirak, K., Frank, A., and Cunningham, A. J. (2010). Self-convergence of Radiatively Cooling Clumps in the Interstellar Medium. *ApJ*, 722:412–424.
- Zhang, D., Thompson, T. A., Quataert, E., and Murray, N. (2015). Entrainment in Trouble: Cool Cloud Acceleration and Destruction in Hot Supernova-Driven Galactic Winds. *ArXiv e-prints*.
- Zhou, X., Yang, J., Fang, M., and Su, Y. (2014). Discovery of a Pre-existing Molecular Filament Associated with Supernova Remnant G127.1+0.5. *ApJ*, 791:109.
- Zibetti, S., Ménard, B., Nestor, D. B., Quider, A. M., Rao, S. M., and Turnshek, D. A. (2007). Optical Properties and Spatial Distribution of Mg II Absorbers from SDSS Image Stacking. *ApJ*, 658:161–184.